Analysis of Trace Gas Heterogeneity using In-Situ and Remote Sensing Measurement Techniques

Jeffrey D. Earley

Dissertation submitted to the Faculty of the

Virginia Polytechnic Institute and State University

in partial fulfillment of the requirements for the degree of

Doctor of Philosophy

in

Electrical Engineering

Elena S. Lind, Chair

Scott M. Bailey

Hosein Foroutan

Gabriel Isaacman-Van Wertz

Yizheng Zhu

October 20, 2025

Blacksburg, Virginia

Keywords: Mobile DOAS, Remote Sensing, Satellite DOAS, Radiative Transfer, Atmospheric Measurement

Copyright 2025, Jeffrey D. Earley

Analysis of Trace Gas Heterogeneity using In-Situ and Remote Sensing Measurement Techniques

Jeffrey D. Earley

(ABSTRACT)

Differential Optical Absorption Spectroscopy (DOAS) is a remote sensing spectroscopic technique capable of retrieving vertical column densities of trace gases in the atmosphere. While the technique can be used to retrieve vertical profiles of trace gases this retrieval is not applicable to Mobile-DOAS measurements due to the lengthy measurement times. In addition, the requirement for rapid measurements for Mobile-DOAS application prevents a single instrument from retrieving information about the horizontal trace gas distributions around the instrument, in addition to the lack of vertical distribution information. However, with the addition of collocated in-situ measurements of surface concentration, as well as the use of Multi Axis DOAS (MAX-DOAS) measurements taken from multiple azimuth viewing directions, it is possible to estimate these distributions using a minimal amount of measurements, allowing this gap in mobile DOAS measurements to be filled.

The relationship between the vertical column density measured by Mobile Zenith-DOAS and in-situ surface concentration is first explored using measurements made during the first TRACER-AQ field campaign. This relationship, expressed as the column to surface ratio, is then used to identify trace gas plumes and other transport patterns that can be separated from local, vehicular emission based on this ratio during two case days, in order to determine the origin of the high Ozone event that was observed on both days. In addition, the effect of the trace gas vertical distribution on satellite-based DOAS measurements is also

determined, where it is found that the column to surface ratio is proportional to worsening agreement between Mobile Zenith-DOAS and TROPOMI Satellite-Based DOAS, however the relationship is only somewhat correlated ($r^2 = 0.3$), indicating that other factors are a greater influence on the ability of Ground-Based DOAS and Satellite-Based DOAS to agree.

During the second TRACER-AQ field campaign, the column to surface ratio was combined with analysis of MAX-DOAS measurements in order to determine both the vertical and horizontal distributions of trace gas around the instruments. This analysis of the horizontal distribution is expressed with the Horizontal Heterogeneity Index, which is a comparison between two MAX-DOAS azimuth viewing directions, behind and to the right of the moving vehicle, with the Zenith DOAS measurements each MAX-DOAS instrument is making. The analysis of both distributions is then used to pinpoint the potential sources giving rise to two more high Ozone events during two more case days during the second field campaign. In addition, the horizontal trace gas distribution was also compared to TROPOMI validation, and was found to correlate more strongly than the vertical distribution ($r^2 = 0.69$), showing that while there are many issues with satellite validation, the horizontal distribution is most likely responsible for deviations between Ground-Based and Satellite-Based DOAS measurements.

Finally, analysis of trace gas distributions requires low uncertainty retrievals of Zenith DOAS VCD's. This is typically performed using radiative transfer simulations, but which require information of the aerosol scattering properties that are not retrievable from a mobile platform. In order to perform these simulations, a novel technique of averaging the aerosol conditions as measured by a network of six AERONET aerosol measuring instruments was investigated through a series of sensitivity studies. These studies analyzed the effect of potential errors in the aerosol properties on the resulting Air Mass Factor estimations, in order to determine how these errors effect Air Mass Factor uncertainty. The studies showed that

the total error introduced into the model through potential errors in aerosol properties, as well as through errors in the assumption of an a priori trace gas profile used to retrieve the Air MAss Factors, was less than 20% for AMF retrievals in Visible light and 25% for UV retrievals, approximately the same level of uncertainty used for Zenith AMF retrievals in other studies, demonstrating that this averaging technique is capable of retrieving sufficiently low uncertainty AMF estimations.

Analysis of Trace Gas Heterogeneity using In-Situ and Remote Sensing Measurement Techniques

Jeffrey D. Earley

(GENERAL AUDIENCE ABSTRACT)

Differential Optical Absorption Spectroscopy (DOAS) is a remote sensing technique capable of measuring trace gas amounts in the atmosphere. However, DOAS measurements taken onboard vehicles have remained limited in scope due to the limited amount of time Mobile DOAS instruments spend in a measurement area. In order to expand the applications of Mobile DOAS, this dissertation combines Multi-Axis DOAS (MAX-DOAS) measurements with Zenith DOAS, or DOAS measurements taken directly vertical, with in-situ measurements of surface concentrations to analyze both the horizontal and vertical distributions of trace gases around the instruments. While this technique does not provide as much information as similar techniques for stationary DOAS instruments, the technique is used to analyze the sources contributing to multiple high Ozone events observed in Houston, Texas during the Tracking Aerosol Convection Experiment-Air Quality (TRACER-AQ) field campaigns held during 2021 and 2022. In addition, the effect of the vertical and horizontal trace gas distributions on Satellite-Based DOAS instruments is evaluated, in order to determine if the trace gas distribution is contributing to errors in Satellite-Based DOAS validation. Finally, due to the need for low uncertainty Zenith DOAS Vertical Column Densities, a novel technique of estimating Air Mass Factors radiative transfer simulations based on the mean aerosol conditions observed by six Aerosol Robotic Network (AERONET) is explored with a series of sensitivity studies. These studies isolate each potential source of error due to uncertain radiative transfer inputs, and are used to both determine how much uncertainty is introduced

into the Air Mass Factor estimation due to errors in the aerosol properties, as well as prove that these uncertainties are sufficiently small that the estimated aerosol properties are valid inputs.

Dedication

This Dissertation is dedicated in memory of my grandfather, Thomas Henry Earley

Acknowledgments

I would like to first express my gratitude to my principal advisor, Dr. Elena Lind, for her support during both my PhD experience as well as my Masters program. I would also like to thank my other committee member, Dr. Scott Bailey, Hosein Foroutan, Gabriel Isaacman-Van Wertz, and Yizheng Zhu for their insight and recommendations during my research.

I would also like to thank the University of Houston research team, headed by James Flynn, including Subin Yoon, Travis Griggs, and Sergio Alvarez, for their hard work in planning and executing both TRACER-AQ field campaigns, as well as their insight and assistance in interpreting results from both field campaigns. I would also like to thank James Flynn for his effort in establishing and maintaining the Aldine, Liberty, Sugarland the UH Coastal Research Center, and the University of Houston Main Campus sites, as well as Rick Wagener and Lynn Ma for their effort in establishing and maintaining the La Porte Airport site.

Finally, I would like to thank both my friends and family, for their love and support all throughout my graduate programs. I would especially like to thank them for making my transition from Blacksburg back to Decatur, Alabama, as quick and painless as possible.

Contents

List of Figures xiii

List of Tables xxix

1 Introduction 1

1.1 Dissertation Goals and Objectives 1

1.2 Dissertation Organization 3

2 Trace Gases 5

2.1 Nitrogen Oxides (NO/NO_2) 5

2.1.1 Stratospheric NO_2 6

2.1.2 Tropospheric NO_2 9

2.2 Formaldehyde ($HCHO$) 11

3 Radiative Transfer 14

3.1 Introduction 14

3.1.1 Absorption 14

3.1.2 Scattering 15

3.1.3 Emission 16

3.2 The Radiative Transfer Equation . . . 17
3.2.1 Streaming Term . . . 18
3.2.2 Source Term . . . 20
3.2.3 Radiative Transfer Solutions . . . 22
3.3 Radiative Transfer Simulations . . . 24
3.4 Air Mass Factors . . . 25

4 Differential Optical Absorption Spectroscopy 28

4.1 Introduction . . . 28
4.2 DOAS Technique . . . 29
4.2.1 DOAS retrieval algorithm . . . 31
4.3 Passive DOAS . . . 34
4.3.1 Multi-Axis DOAS . . . 36
4.3.2 Zenith Scattered Light DOAS . . . 39
4.4 DOAS Measurement Platforms . . . 43
4.4.1 Ground-Based DOAS . . . 44
4.4.2 Satellite-DOAS . . . 53
4.4.3 Mobile-DOAS . . . 56

5 Mobile Zenith DOAS Measurements of NO_2 and $HCHO$, and their Relationship to Collocated In-Situ measurements 61

5.1 Introduction . . . 61
5.2 TRACER-AQ1 Overview . . . 62
5.3 Methodology . . . 65
5.3.1 DOAS Analysis . . . 65
5.3.2 Ancillary Instrumentation . . . 71
5.3.3 Column to Surface Ratio . . . 72
5.4 DOAS results . . . 74
5.5 Case Studies . . . 77
5.5.1 September 6th . . . 77
5.5.2 September 9th . . . 82
5.6 Satellite Validation . . . 87
5.7 Error Estimation . . . 91
5.8 Discussion . . . 93

6 Mobile MAX-DOAS measurements made during TRACER-AQ2 96

6.1 Introduction . . . 96
6.2 TRACER-AQ2 Overview . . . 97
6.3 Methodology . . . 100
6.3.1 Zenith DOAS Analysis . . . 100
6.3.2 MAX-DOAS Analysis . . . 104

6.3.3 Horizontal Heterogeneity Index . . . 107
6.4 Results . . . 109
6.5 Case Studies . . . 113
6.5.1 September 10 . . . 113
6.5.2 September 21 . . . 117
6.6 Satellite Validation . . . 124
6.7 Discussion . . . 129

7 Radiative Transfer Simulations **132**
7.1 Introduction . . . 132
7.2 Data Preparation . . . 133
7.3 Effect of Single Scatter Albedo & Asymmetry Parameter . . . 139
7.4 Effect of the Aerosol Profile . . . 142
7.5 Effect of the A Priori Profile . . . 144
7.6 Discussion . . . 148

8 Conclusions **151**

Appendices **156**

Appendix A Additional Figures **157**

Bibliography **180**

List of Figures

2.1 Stratospheric profiles of various NO_y mixing ratios. Each line is the result of calculations assuming photochemical steady state over 24 hours. (Image adopted from Seinfeld and Pandis 2016[1]) 8

2.2 Climatological estimations of the NO_2 Stratospheric VCD for various latitudes, and months of the year, as a function of local time. (Image adopted from Cede 2021 [2] 9

3.1 Box Air Mass Factors for a Zenith facing instrument in a Rayleigh Atmosphere. 27

4.1 Diagram of the Beer-Lambert Law demonstrating how light originating from a source ($I_0(\lambda)$) is lost due to scattering and absorption before it reaches the detector ($I(\lambda)$). Image adopted from Platt & Stutts (2008)[3] 29

4.2 The differential absorption cross-sections of various nonocyclic aromatic species, as well as O_2 and O_3 as a function of wavelength. Each spectrum, regardless of similarity in the absorption cross-section, posseses unique differential absorption structures that can be used to retrieve trace gas amounts. Image adopted from Platt & Stutts (2008)[3] 32

4.3 The Ring pseudo-cross section calculated through the QDOAS software for the TRACER-AQ2 field campaign 35

4.4 The Ring pseudo-cross section calculated through the QDOAS software for the TRACER-AQ2 field campaign 36

4.5 Diagram of the MAX-DOAS viewing geometry showing 3 measurements and a reference measurement at 90° zenith. Image adopted from Platt & Stutts (2008)[3] 37

4.6 Diagram of the ZSL-DOAS viewing geometry showing 3 measurements, all of which at different SZAs but measured at 90° zenith. Image adopted from Platt & Stutts (2008)[3] 40

4.7 Plot depicting the Minimum Langley Extrapolation technique. Differential Slant Column Densities are plotted according to their air mass factor, then binned according to air mass factor. A linear fit is performed on the minimum value of each bin to extrapolate the minimum dSCD at an air mass factor of 0 42

4.8 Map of the Installed Pandora instruments including those associated with the PGN (green) and those that are not (purple). Image Courtesy of the Pandonia Global Network[2]. 46

4.9 Example Pandora instrument set up on the roof of Whittemore Hall in November, 2021. 48

4.10 Pandora Instrument set up for radiometric calibration. 49

4.11 Pandora Instrument set up for wavelength calibration using a Neon spectral lamp. 50

5.1 Map depicting the greater Houston Area with major roads and coastlines outlined in black, major waterways in cyan. Each path the mobile DOAS vehicle traveled during the campaign is outlined in red. The star represents la Porte airport, where the instruments remained stationary when not driving 64

5.2 NO_2 differential slant column densities retrieved at 460 nm from measurements on the reference day, September 21, plotted as a function of the NO_2 AMF's retrieved at 460 nm from September 21. Each red dot represents the minimum ΔSCD in each bin which is used for a linear fit (red line) which is used for Minimum Langley Extrapolation. The reference column of NO_2 was estimated to be $6.17 \times 10^{15} \frac{Molecules}{cm^2}$ 68

5.3 $HCHO$ differential slant column densities retrieved at 460 nm from measurements on the reference day, September 22, plotted as a function of the NO_2 AMF's retrieved at 340 nm from September 22. Each red dot represents the minimum ΔSCD in each bin which is used for a linear fit (red line) which is used for Minimum Langley Extrapolation. The reference column of $HCHO$ was estimated to be $4.51 \times 10^{15} \frac{Molecules}{cm^2}$. 69

5.4 Time series of daily O_2O_2 differential slant column densities during the TRACER-AQ field campaign. 70

5.5 Time series scatter plots of the NO_2 Visible (blue) and UV(orange) retrieved VCDs, and the in-situ NO_2 surface concentration, in black. All data shown is presented as 1 minute averages. 74

5.6 Time series scatter plots of the $HCHO$ retrieved VCDs, in blue, and the in-situ $HCHO$ surface concentration, in black. All data shown is presented as 1 minute averages. 76

5.7 A scatter plot depicting the $HCHO/NO_2$ ratio for the VCDs retrieved on September 6, in black and the in-situ ozone concentration observed onboard MAQL1, in red. All data shown is presented as 1 minute averages. 78

5.8 Top: The diurnal averaged Boundary Layer Height (green) on September 6. Bottom: The $HCHO$ Tropospheric Vertical Column Density (red) Aside from the boundary layer height, which is the diurnal variation averaged every 10 minutes, all data shown is presented as 1 minute averages. 79

5.9 Top: The column to surface ratio of NO_2 (black) and corresponding diurnal averaged Boundary Layer Height (green) on September 6. Bottom: The NO_2 Tropospheric Vertical Column Density (red) and the in-situ surface concentration (blue). Aside from the boundary layer height, which is the diurnal variation averaged every 10 minutes, all data shown is presented as 1 minute averages. 80

5.10 HYSPLIT [4] modeled 3 hour back-trajectory showing the path air masses at 17:00 (red), 16:00 (blue), 15:00 (green), and 14:00 (cyan) took to arrive at the la Porte Airport (starred) with an end altitude of 500m. 82

5.11 The driving route of MAQL1 on September 9 during the locally observed high Ozone event. In addition, the maps show the Zenith NO_2(a) and $HCHO$(b) VCDs retrieved during this time frame. The arrows in the bottom right of each plot shows the average wind direction collected from 5 airports located in the vicinity of the driving path. The average wind speed during this period was 3.56 m/s. All data shown is presented as 1 minute averages. 83

5.12 A scatter plot depicting the $HCHO/NO_2$ ratio for the VCDs retrieved on September 9. Each point is color coded to the Ozone surface concentration. All data shown is presented as 1 minute averages. 84

5.13 Top: The column to surface ratio of $HCHO$ (black) and corresponding diurnal averaged Boundary Layer Height (green) on September 9. Bottom: The $HCHO$ Tropospheric Vertical Column Density (red) and the in-situ surface concentration (blue). Aside from the boundary layer height, which is the diurnal variation averaged every 10 minutes, all data shown is presented as 1 minute averages. 85

5.14 Top: The column to surface ratio of NO_2 (black) and corresponding diurnal averaged Boundary Layer Height (green) on September 9. Bottom: The NO_2 Tropospheric Vertical Column Density (red) and the in-situ surface concentration (blue). Aside from the boundary layer height, which is the diurnal variation averaged every 10 minutes, all data shown is presented as 1 minute averages. 86

5.15 Time series plots of the TROPOMI NO_2 VCD (black) nearest the Pandora instrument and the Pandora NO_2 VCD, color coded to the column to surface ratio. The selected days correspond to days where the average column to surface ratio is larger than 1Km. All data shown is presented as 1 minute averages. 88

5.16 Time series plots of the TROPOMI NO_2 VCD (black) nearest the Pandora instrument and the Pandora NO_2 VCD, color coded to the column to surface ratio. The selected days correspond to days where the average column to surface ratio is less than 1Km. All data shown is presented as 1 minute averages. 89

5.17 Correlation plot comparing the difference between the TROPOMI and Pandora NO_2 VCD and the column to surface ratio. All Pandora data is averaged per 1 minute. 90

6.1 Map depicting the greater Houston Area with major roads and coastlines outlined in black, major waterways in cyan. Each path the mobile DOAS vehicle traveled during the campaign is outlined in red. The star represents la Porte airport, where the insturments remained stationary when not driving. 98

6.2 Diagram of the measuring directions of the two MAX-DOAS instruments mounted onboard MAQL1. 99

6.3 NO_2 differential slant column densities retrieved at 460 nm from measurements on the reference day, September 28, plotted as a function of the NO_2 AMF's retrieved at 460 nm from September 28. Each red dot represents the minimum ΔSCD in each bin which is used for a linear fit (red line) which is used for Minimum Langley Extrapolation. The reference column of NO_2 was estimated to be $8.72 \times 10^{15} \frac{Molecules}{cm^2}$ 102

6.4 A histogram showing the results of the Bootstrap method for $HCHO$ from TRACER-AQ2. The second percentile is used as the estimated $HCHO$ reference column. 103

6.5 A diagram depicting the measurement schedule for the MAX-DOAS measurements over one cycle. 105

6.6 Comparison of NO_2 Tropospheric VCDs measured by both Pandora instruments, as well as columns retrieved from Zenith measurements for the Intensive Operations period of TRACER-AQ2. Time is given in local time (CDT), and columns in $\times 10^{16} \frac{Molecules}{cm^2}$ 110

6.7 Comparison of $HCHO$ Tropospheric VCDs measured by both Pandora instruments, as well as columns retrieved from Zenith measurements for the Intensive Operations period of TRACER-AQ2. Time is given in local time (CDT), and columns in $\times 10^{16} \frac{Molecules}{cm^2}$ 112

6.8 Time series of the $HCHO/NO_2$ Ratio for the Zenith DOAS (a) and MAX-DOAS datasets (b) (c). Each point is color coded to the local Ozone surface concentration($\times 10^{11} \frac{Molecules}{cm^3}$) recorded onboard MAQL1 on September 10. . 114

6.9 a) The 1-minute average HCHO in-situ concentrations measured on September 10 between 14:00 and 15:00 CST by the mobile lab in $\frac{Molecules}{cm^3}$ plotted at the corresponding latitude and longitude. b) The 1 minute average Pandora 148 HCHO columns plotted at the corresponding latitude and longitude. c) The 1 minute average Pandora 168 HCHO columns plotted at the corresponding latitude and longitude. d)The 1 minute average Pandora HCHO Zenith columns plotted at the corresponding latitude and longitude. e) The column to surface ratio between in-situ and Pandora Zenith columns. f) The heterogeneity index calculated from both MAX-DOAS instruments as well as Zenith columns. 116

6.10 a) The 1-minute average NO_2 in-situ concentrations measured on September 10 between 14:00-15:00 CST by the mobile lab in $\frac{Molecules}{cm^3}$ b) The 1 minute average Pandora 148 NO_2 columns c) The 1 minute average Pandora 168 NO_2 columns d)The 1 minute average Pandora NO_2 Zenith columns e) The column to surface ratio between in-situ and Pandora Zenith columns. f) The heterogeneity index calculated from both MAX-DOAS instruments as well as Zenith columns. 117

6.11 HYSPLIT modeled 3 hour back-trajectory showing the path air masses at 21:00 (red), 20:00 (blue), 19:00 (green), and 18:00 (cyan) took to transport into the high Ozone area observed, with an end altitude of 500m. 118

6.12 Time series of the $HCHO/NO_2$ Ratio for MAX-DOAS and Zenith DOAS datasets. Each point is color coded to the local Ozone surface concentration on September 21 119

6.13 a) The 1-minute average HCHO in-situ concentrations measured on September 21 between 14:00 and 15:00 CDT while the Pandora instruments are in the proximity of the WA Parrish Power Plant (starred) by the mobile lab in $\frac{Molecules}{cm^3}$ b) The 1 minute average Pandora 148 HCHO columns c) The 1 minute average Pandora 168 HCHO columns d)The 1 minute average Pandora HCHO Zenith columns e) The column to surface ratio between in-situ and Pandora Zenith columns. f) The heterogeneity index calculated from both MAX-DOAS instruments as well as Zenith columns. 120

6.14 a) The 1-minute average HCHO in-situ concentrations measured on September 21 between 14:00 and 15:00 CDT while the Pandora instruments are in the proximity of the WA Parrish Power Plant (starred) by the mobile lab in $\frac{Molecules}{cm^3}$ b) The 1 minute average Pandora 148 HCHO columns c) The 1 minute average Pandora 168 HCHO columns d)The 1 minute average Pandora HCHO Zenith columns e) The column to surface ratio between in-situ and Pandora Zenith columns. f) The heterogeneity index calculated from both MAX-DOAS instruments as well as Zenith columns. 122

6.15 HYSPLIT modeled 3 hour back-trajectory showing the path air masses at 21:00 (red), 20:00 (blue), 19:00 (green), and 18:00 (cyan) took to transport into the high Ozone area observed at an altitude of 500m. 123

6.16 (Left) A collection of Scatter plots on days with a column to surface ratio >1Km comparing TROPOMI NO_2 VCDs (black) to Zenith DOAS VCDs, color coded to each measurement's column to surface ratio. (Right) A collection of Scatter plots on days with a column to surface ratio <1Km comparing TROPOMI NO_2 VCDs (black) to Zenith DOAS VCDs, color coded to each measurement's column to surface ratio 124

6.17 Correlation plot showing the linear relationship between the Column to Surface Ratio and the difference between the TROPOMI and Zenith DOAS VCDs during TROPOMI overpass. The correlation coefficient of this linear fit is r=0.42. 126

6.18 (Left) A collection of Scatter plots on days with a column to Horizontal heterogeneity Index $> 0.25 \times 10^{16} \frac{Molecules}{cm^2}$ comparing TROPOMI NO_2 VCDs (black) to Zenith DOAS VCDs, color coded to each measurement's column to surface ratio. (Right) A collection of Scatter plots on days with a Horizontal heterogeneity Index $< 0.25 \times 10^{16} \frac{Molecules}{cm^2}$ comparing TROPOMI NO_2 comparing TROPOMI NO_2 VCDs (black) to Zenith DOAS VCDs, color coded to each measurement's column to surface ratio 127

6.19 Correlation plot showing the linear relationship between the Horizontal heterogeneity Index and the difference between the TROPOMI and Zenith DOAS VCDs during TROPOMI overpass.The correlation coefficient of this linear fit is r=0.78. 128

7.1 Map showing the AERONET instruments in operation around the Houston-Galveston-Brazoria area during TRACER-AQ1&2. 134

7.2 Hourly averaged L2 Aerosol Optical Depth values retrieved at 870nm from six AERONET sites in the Houston-Galveston-Brazoria area during TRACER-AQ 135

7.3 Daily mean values for single scatter albedo(a) and asymmetry parameter(b) retrieved from six AERONET instruments at 440nm in the Houston-Galveston-Brazoria area during September 2021. 136

7.4 Four backscatter profiles (blue) temporally averaged over a one hour period. The red line represents the corrected backscatter profile, where further smoothing has been applied, and the bottom 40m has been corrected by linearly extrapolating the backscatter signal in the 100-40m range. 137

7.5 The aerosol extinction profiles of the four corrected backscatter profiles from Figure 7.4, scaled to 477nm (blue), 460nm (red), 360nm (red) and 340nm (green). 138

7.6 The AMF for O_2O_2 as the single scatter albedo was increased from 0.7 to 1.0, for 477nm(a) and 360nm(c), as well as AMFs for O_2O_2 as the asymmetry parameter was increased from 0.625 to 0.8 for 477nm(b) and 360nm(d). Each line corresponds to the solar zenith angle used to retrieve AMFS, from 0° to 70° in 10° increments. 141

7.7 The absolute difference between O_2O_2 Air Mass Factors retrieved from high and mean aerosol conditions (blue) and from low and mean aerosol conditions (orange) plotted as a function of O_2O_2 Air Mass Factor retrieved from mean aerosol conditions for 477nm retrievals(a) and 360nm retrievals(b). 144

7.8 The vertical profiles used in the 2019 MAX-DOAS profile inter-comparison study[5]. These profiles serve as the basis for the profile-based prtion of the sensitivity study. Details on the profile shape are provided in Table 7.1. In addition, the vertical profile of O_2O_2 (black) is included, which is derived from the mean atmospheric conditions measured by balloon sondes launched during TRACER-AQ. 145

7.9 The diurnal average of uncorrected differences between the air mass factors retrieved from the seven profiles and the O_2O_2 profile in the UV band (a) and Visible band (b), as well as the diurnal average of corrected differences between the air mass factors retrieved from the seven profiles and the O_2O_2 profile at 360nm(c) 477nm(d). 146

7.10 Linear fits of the air mass factors retrieved from the seven profiles and the air mass factors retrieved from the O_2O_2 profile at 360nm(column a) and 477nm(column b) 150

A.1 Comparison of O_2O_2 dSCDs retrieved from Zenith measurements for the Intensive Operations period of TRACER-AQ2. Time is given in local time (CST), and columns in $\times 10^{43} \frac{Molecules^2}{cm^5}$ 157

A.2 a) The 1-minute average HCHO in-situ concentrations measured on September 21 by the mobile lab in $\frac{Molecules}{cm^3}$ b) The 1 minute average Pandora 148 HCHO columns c) The 1 minute average Pandora 168 HCHO columns d)The 1 minute average Pandora HCHO Zenith columns e) The column to surface ratio between in-situ and Pandora Zenith columns. f) The heterogeneity index calculated from both MAX-DOAS instruments as well as Zenith columns. . . 158

A.3 a) The 1-minute average HCHO in-situ concentrations measured on September 21 by the mobile lab in $\frac{Molecules}{cm^3}$ b) The 1 minute average Pandora 148 HCHO columns c) The 1 minute average Pandora 168 HCHO columns d)The 1 minute average Pandora HCHO Zenith columns e) The column to surface ratio between in-situ and Pandora Zenith columns. f) The heterogeneity index calculated from both MAX-DOAS instruments as well as Zenith columns. . . 159

A.4 HYSPLIT [4] modeled 3 hour back-trajectory showing the path air masses at 17:00 (red), 16:00 (blue), 15:00 (green), and 14:00 (cyan) took to arrive at the la Porte Airport (starred) with an end altitude of 250m. 160

A.5 HYSPLIT [4] modeled 3 hour back-trajectory showing the path air masses at 17:00 (red), 16:00 (blue), 15:00 (green), and 14:00 (cyan) took to arrive at the la Porte Airport (starred) with an end altitude of 750m. 161

A.6 The Horizontal heterogeneity Index of each day's set of measurements for the Intensive Operations period of TRACER-AQ2. Time is given in local time (CST), and index in $\times 10^{16} \frac{Molecules}{cm^2}$ 162

A.7 The Horizontal heterogeneity Index of each day's set of measurements for the Intensive Operations period of TRACER-AQ2. Time is given in local time (CST), and index in $\times 10^{16} \frac{Molecules}{cm^2}$ 163

A.8 a) The 1-minute average NO_2 in-situ concentrations measured on September 10 by the mobile lab in ppb plotted at the corresponding latitude and longitude. b) The 1 minute average Pandora 148 NO_2 columns plotted at the corresponding latitude and longitude. c) The 1 minute average Pandora 168 NO_2 columns plotted at the corresponding latitude and longitude. d)The 1 minute average Pandora NO_2 Zenith columns plotted at the corresponding latitude and longitude. e) The column to surface ratio between in-situ and Pandora Zenith columns. f) The heterogeneity index calculated from both MAX-DOAS instruments as well as Zenith columns. 164

A.9 a) The 1-minute average $HCHO$ in-situ concentrations measured on September 10 by the mobile lab in ppb plotted at the corresponding latitude and longitude. b) The 1 minute average Pandora 148 $HCHO$ columns plotted at the corresponding latitude and longitude. c) The 1 minute average Pandora 168 $HCHO$ columns plotted at the corresponding latitude and longitude. d)The 1 minute average Pandora $HCHO$ Zenith columns plotted at the corresponding latitude and longitude. e) The column to surface ratio between in-situ and Pandora Zenith columns. f) The heterogeneity index calculated from both MAX-DOAS instruments as well as Zenith columns. 165

A.10 a) The 1-minute average NO_2 in-situ concentrations measured on September 21 by the mobile lab in ppb b) The 1 minute average Pandora 148 NO_2 columns c) The 1 minute average Pandora 168 NO_2 columns d)The 1 minute average Pandora NO_2 Zenith columns e) The column to surface ratio between in-situ and Pandora Zenith columns. f) The heterogeneity index calculated from both MAX-DOAS instruments as well as Zenith columns. 166

A.11 a) The 1-minute average $HCHO$ in-situ concentrations measured on September 21 by the mobile lab in ppb b) The 1 minute average Pandora 148 $HCHO$ columns c) The 1 minute average Pandora 168 $HCHO$ columns d)The 1 minute average Pandora $HCHO$ Zenith columns e) The column to surface ratio between in-situ and Pandora Zenith columns. f) The heterogeneity index calculated from both MAX-DOAS instruments as well as Zenith columns. . . 167

A.12 a) The 1-minute average NO_2 in-situ concentrations measured on September 10 between 12:00-13:00 CST by the mobile lab b) The 1 minute average Pandora 148 NO_2 columns c) The 1 minute average Pandora 168 NO_2 columns d)The 1 minute average Pandora NO_2 Zenith columns e) The column to surface ratio between in-situ and Pandora Zenith columns. f) The heterogeneity index calculated from both MAX-DOAS instruments as well as Zenith columns. 168

A.13 a) The 1-minute average HCHO in-situ concentrations measured on September 10 between 12:00-13:00 CST by the mobile lab b) The 1 minute average Pandora 148 HCHO columns c) The 1 minute average Pandora 168 HCHO columns d)The 1 minute average Pandora HCHO Zenith columns e) The column to surface ratio between in-situ and Pandora Zenith columns. f) The heterogeneity index calculated from both MAX-DOAS instruments as well as Zenith columns. 169

A.14 a) The 1-minute average NO_2 in-situ concentrations measured on September 10 between 13:00-14:00 CST by the mobile lab b) The 1 minute average Pandora 148 NO_2 columns c) The 1 minute average Pandora 168 NO_2 columns d)The 1 minute average Pandora NO_2 Zenith columns e) The column to surface ratio between in-situ and Pandora Zenith columns. f) The heterogeneity index calculated from both MAX-DOAS instruments as well as Zenith columns. 170

A.15 a) The 1-minute average HCHO in-situ concentrations measured on September 10 between 13:00-14:00 CST by the mobile lab b) The 1 minute average Pandora 148 HCHO columns c) The 1 minute average Pandora 168 HCHO columns d)The 1 minute average Pandora HCHO Zenith columns e) The column to surface ratio between in-situ and Pandora Zenith columns. f) The heterogeneity index calculated from both MAX-DOAS instruments as well as Zenith columns. 171

A.16 (Left) A collection of Scatter plots on days with a column to Horizontal heterogeneity Index $> 0.25 \times 10^{16} \frac{Molecules}{cm^2}$ comparing TROPOMI NO_2 VCDs (black) to Pandora 148 MAX-DOAS VCDs, color coded to each measurement's column to surface ratio. (Right) A collection of Scatter plots on days with a Horizontal heterogeneity Index $< 0.25 \times 10^{16} \frac{Molecules}{cm^2}$ comparing TROPOMI NO_2 VCDs (black) to Pandora 148 MAX-DOAS VCDs, color coded to each measurement's column to surface ratio 172

A.17 Correlation plot showing the linear relationship between the Horizontal heterogeneity Index and the difference between the TROPOMI and Pandora 148 MAX-DOASS VCDs during TROPOMI overpass.The correlation coefficient of this linear fit is r=0.30. 173

A.18 (Left) A collection of Scatter plots on days with a column to Horizontal heterogeneity Index $> 0.25 \times 10^{16} \frac{Molecules}{cm^2}$ comparing TROPOMI NO_2 VCDs (black) to Pandora 168 MAX-DOAS VCDs, color coded to each measurement's column to surface ratio. (Right) A collection of Scatter plots on days with a Horizontal heterogeneity Index $< 0.25 \times 10^{16} \frac{Molecules}{cm^2}$ comparing TROPOMI NO_2 VCDs (black) to Pandora 168 MAX-DOAS VCDs, color coded to each measurement's column to surface ratio 174

A.19 Correlation plot showing the linear relationship between the Horizontal heterogeneity Index and the difference between the TROPOMI and Pandora 168 MAX-DOASS VCDs during TROPOMI overpass.The correlation coefficient of this linear fit is r=0.37. 175

A.20 HYSPLIT modeled 3 hour back-trajectory showing the path air masses at 21:00 (red), 20:00 (blue), 19:00 (green), and 18:00 (cyan) took to transport into the high Ozone area observed, with an end altitude of 250m. 176

A.21 HYSPLIT modeled 3 hour back-trajectory showing the path air masses at 21:00 (red), 20:00 (blue), 19:00 (green), and 18:00 (cyan) took to transport into the high Ozone area observed, with an end altitude of 750m. 177

A.22 HYSPLIT modeled 3 hour back-trajectory showing the path air masses at 21:00 (red), 20:00 (blue), 19:00 (green), and 18:00 (cyan) took to transport into the high Ozone area observed at an altitude of 250m. 178

A.23 HYSPLIT modeled 3 hour back-trajectory showing the path air masses at 21:00 (red), 20:00 (blue), 19:00 (green), and 18:00 (cyan) took to transport into the high Ozone area observed at an altitude of 750m. 179

List of Tables

4.1 Pandora DOAS retrieval steps 51

4.2 Summery of correction steps to convert L0 into L1 data. 53

5.1 DOAS fitting parameters used to retrieve $HCHO$, NO_2, and O_2O_2 ΔSCD from Pandora zenith sky measurements. The fitting windows are ordered starting with $HCHO$, NO_2 Ultraviolet, then NO_2 Visible retrievals. 66

5.2 Summary of Error Sources for Visible NO_2 and $HCHO$VCDs 93

6.1 DOAS fitting parameters used to retrieve $HCHO$, NO_2, and O_2O_2 ΔSCD from Pandora zenith sky measurements. 101

6.2 Absorption Cross-Sections used for MAX-DOAS Analysis 106

7.1 Description of trace gas profiles used for sensitivity study 145

List of Abbreviations

(C_5H_8) Isoprene

CH_3OOH Methyl hydroperoxide

$HCHO$ Formaldehyde

HNO_3 Nitric acid

HO_2 Hydroperoxyl Radical

HO_x $OH + HO_2$

N_2O Nitrous Oxide

NO Nitrogen Monoxide

NO_2 Nitrogen Dioxide

NO_3 Nitate radical

NO_x Nitrogen Oxides

$O(^1D)$ First excited state of atomic oxygen

OH Hydroxyl Radical

AOD Aerosol Optical Depth

ARM Atmospheric Radiation Management

ASY Asymmetry parameter

BREDOM Bremen DOAS Network for Atmospheric Measurements

DOAS Differential Optical Absorption Spectroscopy

dSCD Differential Slant Column Density

EPA Environmental Protection Agency

ESA European Space Agency

FTIR Fourier Transfer Infrared

FWHM Full Width at Half Maximum

GCAS GEO-CAPE Airborne Spectrometer

GEO-CAPE Geostationary Coastal and Air Pollution Events

GOME Global Ozone Monitoring Instrument

GPS Global Positioning System

HYSPLIT Hybrid Single-Particle Lagrangian Integrated Trajectory

LIDAR Light Detection And Ranging

MADRAS MAX-DOAS instruments in Russia and ASia

MAX-DOAS Multi-Axis DOAS

NASA National Aeronotics and Space Agency

NDACC Network for the Detection of Atmospheric Composition and Change

NOVAC Network for Observation of Volcanic and Atmospheric Change

OMI Ozone Monitoring Instrument

PGN Pandonia Global Network

SCD Slant Column Density

SCIAMACHY Scanning Imaging Absorption Spectrometer for Atmospheric Cartography

SHARP Study of Houston Atmospheric Radical Precursors

SSA Single Scatter Albedo

SZA Solar Zenith Angle

TCEQ Texas Commission on Environmental Quality

TEMPO Tropospheric Emissions: Monitoring of Pollution

TEXAQ Texas Air Quality Field Campaign

TRACER-AQ1 Tracking Aerosol Convection Experiment-Air Quality 2021

TROPOMI Tropospheric Monitoring Instrument

UTSC University of Science and Technology of China

UV-VIS-NIR Ultraviolet-Visible-Near Infrared

VCD Vertical Column Density

VOC Volitile Organic Compound

ZSL-DOAS Zenith Scattered Light DOAS

Chapter 1

Introduction

1.1 Dissertation Goals and Objectives

The primary goal of this dissertation is to advance the capabilities of Mobile DOAS measurements. In particular, analysis of mobile DOAS measurements made in the zenith direction (Zenith DOAS) is improved to provide Vertical Column Densities (VCD) of Mobile Zenith DOAS measurements for comparisons to mobile Multi-Axis DOAS (MAX-DOAS) and in-situ measurements of surface concentration to describe the horizontal and vertical distributions of trace gas in the measurement area.

This dissertation presents an improved methodology for mobile DOAS measurements to achieve the following goals:

1. Develop a methodology for estimating the Air Mass Factor (AMF) of Zenith DOAS measurements using an average of aerosol optical properties retrieved from aerosol measuring instruments present within a measurement area. The AMF estimation allows for Mobile Zenith DOAS measurements to be converted into VCDs, which is typically the final data product for DOAS measurements. In addition, the uncertainty added into each measurement from this methodology must also be characterized.

2. Utilize Zenith DOAS VCDs and in-situ surface concentrations to identify local sources and estimate their impact on local Ozone production.

3. Analyze the horizontal heterogeneity present within a measurement area and use areas of high heterogeneity to identify emissions transport patterns an nearby sources, as well as determine the effect of these sources on local Ozone production.

4. Improve validation of Satellite-Based DOAS measurements using Ground-Based DOAS techniques

Objective 1 is accomplished through the simulation of box Air Mass Factors through radiative transfer simulations. These simulations are used to perform sensitivity studies in order to determine the effect of averaging together aerosol optical properties on the uncertainty of each measurement is addressed. These sensitivity studies primarily focused on the following's impact on AMF uncertainty:

1. Daily averages of Single Scatter Albedo and Asymmetry Parameter

2. Hourly Averages of Aerosol Optical Depth and the assumed Aerosol Profile

3. The assumed trace gas a priori profile.

Objective 2 is accomplished by comparing the Zenith VCDs, retrieved through the results of **Objective 1**, to in-situ surface concentrations measured by instruments onboard the same mobile platform as the Zenith DOAS instrument. This comparison, known as the column to surface ratio, provides a general description of the effective mixing layer height of a trace gas, and is used to identify areas where the mixing layer height is much larger than expected.

Objective 3 is accomplished through the development of the Horizontal heterogeneity Index, a numerical value of how representative MAX-DOAS measurements made in differing directions are to Zenith DOAS measurements. Areas identified as high heterogeneity are combined with weather data and the column to surface ratio to determine the origin of these high heterogeneity areas.

Objective 3 is accomplished by utilizing both the column to surface ratio and Horizontal Heterogeneity Index to identify the relationship between these values and the ability of Ground-Based DOAS instruments to validate Satellite-Based DOAS instruments.

1.2 Dissertation Organization

This dissertation is organized as follows:

1. Chapter 1 introduces the major goals of this dissertation and its organization.

2. Chapter 2 describes the trace gases of interest to this work, explaining their formation, destruction, and transport behaviors in both the troposphere and stratosphere.

3. Chapter 3 explains the radiative transfer principles used to retrieve Air Mass Factors, as well as the equations used by radiative transfer simulators to trace light paths through the atmosphere.

4. Chapter 4 introduces the underlying principles of Differential Optical Absorption Spectroscopy (DOAS) as well as their practical implementation in the field, explaining the operating principles behind both Zenith and Multi-Axis DOAS. In addition, the DOAS instruments used for this dissertation, the Pandora spectrometer, is discussed in detail.

5. Chapter 5 presents the results from the mobile Zenith DOAS instrument measured during the Tracking Aerosol and Convection Experiment (Air Quality) (TRACER-AAQ) field campaign held in Houston, Tx. These results are compared to co-located in-situ measurements to identify the impact of two major sources in Houston on Ozone formation within two measurement areas, as well as determine how the vertical distribution of trace gas affects the Zenith DOAS's ability to validate OMI (a Satellite-Based

DOAS instrument) data products.

6. Chapter 6 presents the MAX-DOAS and Zenith DOAS results from the TRACER-AQ2 field campaign, also held in Houston. These results are used to develop the horizontal heterogeneity index. This index is then used to identify transport patterns of two more sources in Houston and their impact on nearby Ozone formation, as well as how effective MAX-DOAS and Zenith DOAS is effective in validating OMI data products at different heterogeneity levels.

7. Chapter 7 presents the comcusions from this dissertation.

Chapter 2

Trace Gases

2.1 Nitrogen Oxides (NO/NO_2)

Nitrogen Oxides ($NO_x = NO + NO_2$) are two trace gases that are critical contributors to atmospheric chemistry in troposphere as well as the stratosphere. The primary anthropogenic source of NO_x is the combustion process, which is dominated by vehicle emissions, as well as industrial emissions, especially from fossil fuel power generators [6]. At urban locations, these emissions reach concentrations high enough to pose a negative impact on human health [7]. Because of this NO_2 has been classified as one of the six criteria pollutants regulated by the EPA [8]. The short lifetime of tropospheric NO_2 [9] means that NO_2 will be measured close to its source, and can therefore be used as an effective method to track pollution sources of NO_2, as well as other trace gases produced by combustion reactions.

In addition, NO_x plays an important role in Ozone chemistry, both in the stratosphere, as well in the troposphere. While Ozone destruction in the stratosphere causes an increase in near UV solar radiation at the Earth's surface, causing increased health risk due to skin exposure to this light. In the troposphere, inhalation of Ozone can exacerbate respiratory illness and increase a person's susceptibility to allergies and asthma. Due to the high spatial and temporal variability of NO_x anthropogenic emissions, estimating Ozone related chemistry can be very difficult, and is compounded by other trace gases, such as Volatile Organic Compounds (VOCs) present in the troposphere.

2.1.1 Stratospheric NO_2

Stratospheric NO_2 Source

The primary source of stratospheric NO_2 arises from the vertical transport of nitrous oxide (N_2O) into the stratosphere. N_2O is primarily emitted by soil nitrifying bacteria, and is primarily associated with fertilizer enrichment and use in agriculture. Due to the long lifetime of N_2O (120 years)[10] the trace gas is able to be vertically transported into the stratosphere where it is photolyzed and oxidized to produce NO

$$N_2O + h\nu \rightarrow N_2 + O(^1D) \tag{2.1}$$

$$N_2O + O(^1D) \rightarrow NO + NO \tag{2.2}$$

$$N_2O + O(^1D) \rightarrow N_2 + O_2 \tag{2.3}$$

Where Equation 2.2 is the primary source of NO_x in the stratosphere. The NO produced by the photolysis of N_2O is the primarily responsible for the destruction of stratospheric ozone as part of the NO_x cycle. In addition to being the primary driver of stratospheric NO_x, N_2O is also a greenhouse gas, and one of the primary drivers of radiative forcing [11]. In addition, the lifetime of N_2O has been shown to be decreasing at a rate of -2.1% per decade [10] indicating that decreases in the trace gas has led to an increase in its rate of destruction in the stratosphere, hastening the repair of the ozone layer.

Stratospheric NO_2 Chemistry

Stratospheric NO_x chemistry can be separated into to cycles: one that requires the presence of oxygen atoms and one that does not. In the upper stratosphere, photolysis of NO_2

provides an abundance of oxygen atoms, due to the abundance of UV solar radiation in the upper stratosphere, this cycle dominates the upper stratosphere.

$$NO_2 + hv \rightarrow NO + O \tag{2.4}$$

$$NO + O_3 \rightarrow NO_2 + O_2 \tag{2.5}$$

$$NO_2 + O \rightarrow NO + O_2 \tag{2.6}$$

In the lower stratosphere, reduced UV radiation leads to a reduction of atomic oxygen in the stratosphere, and as such a second cycle, one that does not rely on the presence of atomic oxygen, dominates the NO_x cycle.

$$NO + O_3 \rightarrow NO_2 + O_2 \tag{2.7}$$

$$NO_2 + O_3 \rightarrow NO_3 + O_2 \tag{2.8}$$

$$NO_3 + hv \rightarrow NO + NO_2 \tag{2.9}$$

$$NO_3 + hv \rightarrow NO_2 + O_2 \tag{2.10}$$

$$NO_3 + hv \rightarrow NO + NO_2 \tag{2.11}$$

During daylight hours, NO_3 is destroyed through photolysis, as shown in formulae 2.10 and 2.11, with formula 2.10 having about an 8 times higher rate than formula 2.11. At night, NO_3 is not destroyed, and instead reacts with NO_2 and water vapor formed on the surface of aerosol particles to form nitric acid (HNO_3)

$$NO_3 + NO_2 + M \rightarrow N_2O_5 + M \tag{2.12}$$

$$N_2O_5 + H_2O(s) \rightarrow 2HNO_3 \tag{2.13}$$

Due to the difference in NO_x cycle reactions at different altitudes in the stratosphere, as

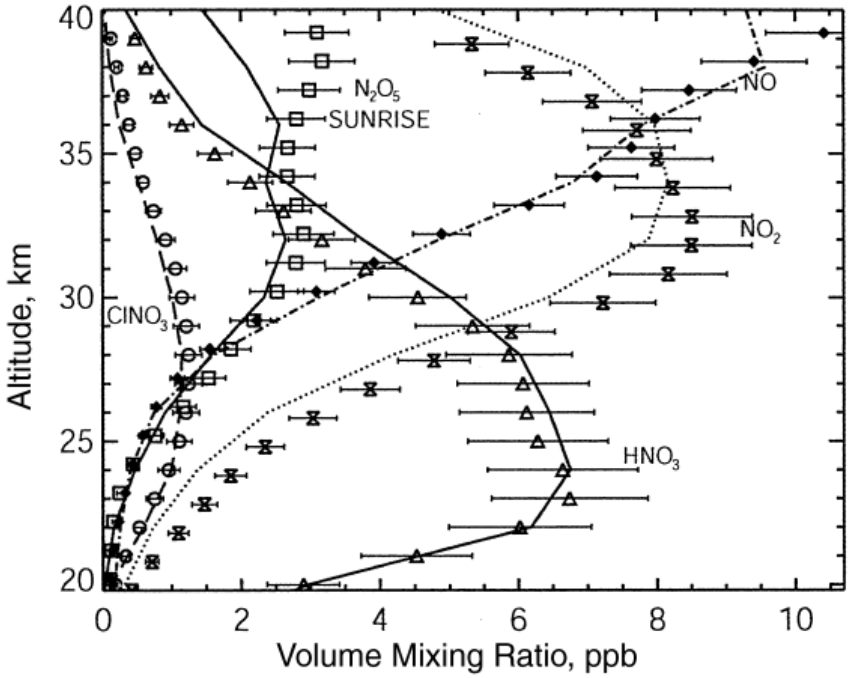


Figure 2.1: Stratospheric profiles of various NO_y mixing ratios. Each line is the result of calculations assuming photochemical steady state over 24 hours. (Image adopted from Seinfeld and Pandis 2016[1])

well as the decrease in stratospheric aerosols at higher altitudes, the stratospheric profile of NO_x, as well as N_2O_5 and HNO_2 are not constant, and vary with altitude, as can be seen in Figure 2.1. Efforts to measure the stratospheric profiles of trace gases include solar occultation flux measurements both onboard satellites [12][13][14] as well as ground [15]ballon-bourne instruments [16]. Due to the increase in UV radiation at the upper portions of the stratosphere the NO profile increases exponentially as a function of altitude, peaking at around 38 Km. On the other hand, HNO_3's reliance on stratospheric aerosols to form leads to it being concentrated in the lower portions of the stratosphere, where the majority of stratospheric aerosols are concentrated in, peaking in concentration at around 25 Km. In

between 30 to 35 Km, where HNO_3 and NO are less concentrated NO_2 is the major NO_y compound.

In addition, due to the NO_x cycle's dependency on the amount of solar radiation present in the stratosphere, the reactions of NO_2 are governed by latitude, time of day, as well as season. Figure 2.2 shows the variation of the NO_2 stratospheric Vertical Column Density (VCD) as a function of local time for various latitudes and seasons. As can be seen, the diurnal pattern of the NO_2 stratospheric column is heavily dependent on the latitude of the measurement, with the sensitivity to the time of year increasing and sensitivity to the time of day decreasing at higher latitudes.

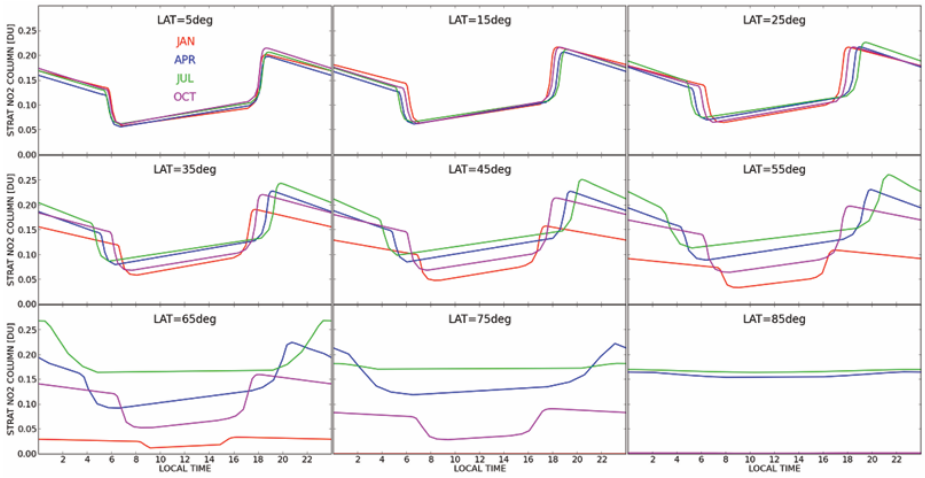


Figure 2.2: Climatological estimations of the NO_2 Stratospheric VCD for various latitudes, and months of the year, as a function of local time. (Image adopted from Cede 2021 [2]

2.1.2 Tropospheric NO_2

Tropospheric NO_2 chemistry undergoes a similar NO_x cycle to stratospheric NO_2 chemistry; however, the presence of Volatile Organic Compounds (VOC) in the surface layer, anthropogenic sources of NO_x, and variations in solar radiation due to tropospheric aerosols and

clouds further complicates tropospheric NO_x chemistry. NO_x is primarily removed from the troposphere during daylight hours through the oxidation of NO_2 into nitric acid.

$$OH + NO_2 + M \rightarrow HNO_3 + M \tag{2.14}$$

At night, NO reacts rapidly with O_3 to form NO_2, while NO_2 is unable to photolyze into NO, leaving the vast majority of night time NO_x as NO_2. Night time NO_2 is then removed from the troposphere in a similar manner as in the lower stratosphere, where NO_2 is converted into NO_3 following formula 2.8, which then according to formula 2.12reacts again with NO_2 to form N_2O_5. N_2O_5 then reacts with water vapor through particle phase hydrolysis to form nitric acid, as shown in Formula 2.13.

Anthropogenic NO_2 is primarily formed through the combustion of fossil fuels. This leads to the primary anthropogenic sources of NO_2 including vehicles, power plants, airplanes, as well as some industry. Additional NO_2 can be formed through biomass burning. Anthropogenic sources typically lead to a heterogeneous distribution of NO_2, especially when sources are concentrated together, such as around industrial parks and along major highways. Anthropogenic NO_2 sources are responsible for approximately 75% of global tropospheric NO_2 emissions [17]. On the other hand, NO_2 can also be produced through the nitrification of soil, as well as lightning strikes and natural cases of biomass burning. These natural sources account for the remaining 25% of NO_2 emissions.

The heterogeneous distribution of tropospheric NO_2 can not only arise due to concentrations of NO_x sources, but also due to other factors such as transport, and variations in removal rate due to changes in weather patterns. NO_2 has lifetimes ranging between 1 to 6 hours, which is largely dependent on time of day, season, and amount of NO_x present [18]. The heterogeneity of NO_2 gives rise to significantly different profiles depending on proximity to

sources as well as the type of source present. For instance, NO_2 profiles measured near roads will see the largest distribution close to the surface, while industrial sites, which make use of smokestacks and flares to emit NO_2, will have profiles which are more evenly distributed across the first few hundred meters off the ground.

Tropospheric NO_2 is also one of the leading drivers of tropospheric ozone formation. Tropospheric ozone is also one of the leading causes of negative respiratory health outcomes [19], and is one of the primary sources of the Hydroxyl radical, OH, which is responsible for the oxidation of trace gas species in the troposphere[20]. Tropospheric ozone formation can also be affected by the presence of VOC's, with formation being dependent on the ratio between NO_x and VOC's[21].

2.2 Formaldehyde ($HCHO$)

Formaldehyde ($HCHO$) is one of the most abundant Volatile Organic Compounds (VOC) in the troposphere[22]. $HCHO$, like other VOCs, contribute to tropospheric Ozone production in the NO_x cycle. In addition, $HCHO$ is carcinogenic, genotoxic, and can be found in both molecular and particulate forms [23].

The majority of formaldehyde that is present in the atmosphere is not directly emitted, but rather is the result of oxidation of other VOCs, such as methane and isoprene[24]. For instance, Formaldehyde is formed through the oxidation of methyl hydroperoxide (CH_3OOH), which is an intermediate product of methane oxidation.

$$CH_3OOH + OH \rightarrow H_2O + CH_2OOH \rightarrow_{Fast} HCHO + OH \tag{2.15}$$

Methane, as well as isoprene, each constitute approximately one third of total VOC production[25],

and as such both are responsible for most secondary formation of formaldehyde. Methane is a long lived VOC, with a lifetime of 9 years, which allows for formaldehyde production in remote parts of the world[26], as well as the free troposphere.

Isoprene C_5H_8, on the other hand, is a much shorter lived trace gas(1-2 hours) however it is emitted primarily from plant life[27], namely deciduous trees, during daylight hours. This gives isoprene a homogeneous distribution, especially across the continental United States, where around one third of its land mass is covered in forests. Due to isoprene being most commonly emitted in daylight hours, formaldehyde is most commonly produced from isoprene through it's oxidation[28], with a lifetime against oxidation of 1.7 hours. Because of the relation between formaldehyde and isoprene, satellite-based measurements of formaldehyde have been used to identify the presence of formaldehyde precursors, namely isoprene, present over the continental United States[29][30]

In addition to secondary formation, formaldehyde is known t be produced as a result of combustion reactions, similar to NO_2. This leads to industrial sites, especially petrochemical facilities [31], and vehicles[32]. However, emissions from petrochemical facilities dominates primary formaldehyde emissions.

Once in the atmosphere, formaldehyde plays a crucial role in HO_x. Both the oxidation and photolysis of formaldehyde produce radicals that then form OH and HO_2.

$$HCHO + hv \rightarrow H + HCO \tag{2.16}$$

$$HCHO + hv \rightarrow H_2 + CO \tag{2.17}$$

$$HCHO + OH \rightarrow HCO + H_2O \tag{2.18}$$

$$HCO + O_2 \rightarrow HO_2 + CO \tag{2.19}$$

$$H + O_2 + M \rightarrow HO_2 + M \tag{2.20}$$

Due to this behavior, formaldehyde is directly linked to the oxidation capacity of the atmosphere, with an increase in formaldehyde leading to an increase in oxidation rates. At night, formaldehyde is removed from the atmosphere through both dry and wet deposition, as well as oxidation through NO_3, however the lifetime of formaldehyde against these processes is much longer than OH oxidation and photolysis, and as such residual formaldehyde can remain in the atmosphere overnight.

$$HCHO + NO_3 \rightarrow HNO_3 + HCO \tag{2.21}$$

Chapter 3

Radiative Transfer

3.1 Introduction

As light propagates through the vacuum of space between the sun and Earth, very few interactions occur, with only the attenuation of the light affecting transmission. However, as light enters the Earth's atmosphere, it begins to interact with the molecules and particles in the atmosphere before reaching the surface. This process is called radiative transfer and these interactions separated into three groups: scattering, absorption, and emission.

3.1.1 Absorption

Electromagnetic radiation can be absorbed by molecules in the atmosphere which transfers the energy into the molecule, typically causing electrons within the molecule to change energy levels. Due to the quantized nature of the molecular energy levels, electrons can only change energy levels when specific amounts of energy are inputted into the molecule. As such, due to the relationship between electromagnetic energy and wavelength, only specific wavelengths can be absorbed by a molecule, and each molecule absorbs different wavelengths of light at different efficiencies. This unique absorption is described by each molecule's absorption cross-section, $\sigma(\lambda)$, and are determined through extensive laboratory measurements of the behavior of light as it passes through set amounts of each molecule. This behavior is described by the

Beer-Lambert law, which describes light extinction both due to absorption and scattering:

$$I(\lambda) = I_o(\lambda)e^{\sigma(\lambda)\int_0^L Nds} \tag{3.1}$$

where N is the number density of a given molecule, $sigma(\lambda)$ is the absorption cross section of the molecule, and L is the path length of the measured light (I) from its source (I_o) This process and the information that can be retrieved from measurements of absorbed light is covered in more detain in Chapter 4.

3.1.2 Scattering

When light interacts with a particle or molecule but is unable to be absorbed, a scattering event occurs instead. In a scattering event, the photon collides with a particle or molecule, and reflects off the surface.

When the scattered light retains its original wavelength of the incident light while maintaining photon energy; this process is called elastic scattering. There are two major regimes of elastic scattering, Rayleigh and Mie Scattering. The Rayleigh regime of elastic scattering occurs when the wavelength of light is much larger than the size of the scattering particle. As such, this regime is typically associated with molecules and is also known as molecular scattering. Rayleigh scattering efficiency is also inversely proportional to the wavelength of the scattered light; this behavior as well as the abundance of blue light emitted from the sun leads to the distinct blue color of Earth's atmosphere on a typical day.

Mie scattering, on the other hand, occurs when the scattering particle is comparable in size or larger than the wavelength of the scattered light. As such aerosols aerosols, especially those found close to the surface, Mie scatter more efficiently than molecules. In addition, Mie scattering has a large angular dependency, in particular Mie scattering is highly efficient at

forward scattering, and is more efficient at larger wavelengths. These three properties combine to dominate scattering events at sunrise and sunset, where the light path of unscattered light includes large portions of the lower troposphere where there are large quantities of dust, smoke, and other aerosols.

Finally, elastic scattering, also known as Raman scattering, occurs when the scattered light does not retain the wavelength of the incident light. This leads to either an increase in energy, known as Stokes scattering, or a decrease in energy, known as anti-Stokes scattering, of the scattered light. Elastic scattering is much less efficient than elastic scattering, however, and as such

3.1.3 Emission

When light is absorbed by a molecule, an electron is elevated to a higher energy level. When this happens, the electron remains unstable and will eventually return to its rest state. When this happens, light is emitted from the molecule at the same frequency of light that was originally absorbed.

In addition, due to the thermal energy present in all particles and molecules, they will emit electromagnetic radiation isotopically and in all wavelengths, with the intensity of the emitted light proportional to the temperature of the molecule. However, this emission is negligible with regards to radiative transfer in Earth's atmosphere, and will be ignored for the remainder of this paper.

3.2 The Radiative Transfer Equation

The previous processes described in the previous section can be described through a single unified equation, named the radiative transfer equation. While it is possible to derive this equation based only on Maxwell's equations [33], an alternate method can be performed using the Boltzmann Equation[34], given in Equation 3.2:

$$\frac{\partial f}{\partial t} + \nabla_r(vf) + \nabla_p(\mathbf{F}f) = Q(\mathbf{r}, \hat{n}, \nu, t) \tag{3.2}$$

Where $f(\mathbf{r}, \hat{n}, \nu, t)$ is the photon distribution function, and is dependent on photon position ($\mathbf{r}$), direction of propagation ($\hat{n}$), frequency (ν), ant time (t). The photon distribution function is defined such that the number of photons passing through a differential surface over a differential time can be defined as the following:

$$dN = f(\mathbf{r}, \hat{n}, \nu, t)c\hat{n} \cdot d\mathbf{S}d\Omega d\nu dt \tag{3.3}$$

Which describes the number of photons with frequencies between ν and $\nu+d\nu$passing through a surface $d\mathbf{S}$ in the $\hat{n}$ direction at a solid angle of $d\Omega$ in time dt, and where c is the speed of light. The photon distribution function has the units of $cm^{-3}sr^{-1}Hz^{-1}$. $Q(\mathbf{r}, \hat{n}, \nu, t)$ is the source term, which represents the sources and sinks that can be present due to production and loss in the atmosphere, while $\mathbf{F}(\mathbf{r}, \hat{n}, \nu, t)$ represents any external force applied to the photons. In addition, ∇_r and ∇_p are the divergence operators for the configuration and momentum spaces, respectfully.

When no external force is applied to the photons, which would be the case in the absence of relativistic effects, and if the photons propagate in straight lines between collisions ($\mathbf{V} = c\hat{n}$),

then Equation 3.2 can be simplified:

$$\frac{\partial f}{\partial t} + c(\hat{n} \cdot \nabla_r) f = Q(\mathbf{r}, \hat{n}, \nu, t) \tag{3.4}$$

Using the Equation3.5:

$$\nabla_r(vf) = f\nabla_r v + v \cdot \nabla_r f = v \cdot \nabla_r f \tag{3.5}$$

From here, the differential energy of the photons can be computed by combining Equation 3.3 with the Planck relation:

$$dE = h\nu c f(\mathbf{r}, \hat{n}, \nu, t)\hat{n} \cdot d\mathbf{S} d\Omega d\nu dt \tag{3.6}$$

Likewise, the intensity of the photons, $I(\mathbf{r}, \hat{n}, \nu, t)$ is defined by Equation 3.7:

$$dE = I(\mathbf{r}, \hat{n}, \nu, t) dS cos(\theta) d\Omega d\nu dt \tag{3.7}$$

Such that $\hat{n} \cdot d\mathbf{S} = cos(\theta) dS$. Combining Equations 3.6 and 3.7 gives Equation 3.8:

$$I(\mathbf{r}, \hat{n}, \nu, t) = h\nu c f(\mathbf{r}, \hat{n}, \nu, t) \tag{3.8}$$

Equation 3.8 allows for Equation 3.4 to be rewritten as Equation 3.9 under steady state conditions:

$$(\hat{n} \cdot \nabla_r) I(\mathbf{r}, \hat{n}, \nu) = h\nu Q(\mathbf{r}, \hat{n}, \nu) \tag{3.9}$$

3.2.1 Streaming Term

The streaming term $(\hat{n} \cdot \nabla_r)$, defines the geometry of the radiative transfer problem. Typically, this geometry is presented under cartesian or spherical coordinates when dealing with

radiative transfer in Earth's atmosphere.

The streaming term represented in cartesian coordinates is given in Equation 3.10:

$$\hat{n} \cdot \nabla_r = n_x \frac{\partial}{\partial x} + n_y \frac{\partial}{\partial y} + n_z \frac{\partial}{\partial z} = cos(\phi)\sqrt{1-\mu^2}\frac{\partial}{\partial x} + sin(\phi)\sqrt{1-\mu^2}\frac{\partial}{\partial y} + \mu\frac{\partial}{\partial z} \tag{3.10}$$

Where $\mu = cos(\theta)$, (n_x, n_y, n_z) are the components of the unit vector $\hat{n}$, and ϕ is the azimuth angle. When using cartesian coordinates, typically the plane parallel approximation is used. This allows for the atmosphere to be divided into parallel layers in the x and why directions. This assumption leads to no change in the x and y directions, and as such both terms can be ignored under the plane parallel approximation. As such, the streaming term under plane parallel geometry is given by equation 3.11

$$\hat{n} \cdot \nabla_r = \mu\frac{\partial}{\partial z} \tag{3.11}$$

On the other hand, the streaming term under spherical geometry can be given by Equation 3.12:

$$\hat{n}\cdot\nabla_r = \mu\frac{\partial}{\partial r} + \frac{1-\mu^2}{r}\frac{\partial}{\partial \mu} + \frac{\sqrt{1-\mu^2}\sqrt{1-\mu_0^2}}{r}[cos(\phi-\phi_0)\frac{\partial}{\partial \mu_0} + \frac{\mu_0}{1-\mu_0^2}sin(\phi-\phi_0)\frac{\partial}{\partial(\phi-\phi_0}))] \tag{3.12}$$

Assuming that Earth's atmosphere is spherically symmetric, i.e. a spherical shell, then Equation 3.12 reduces to:

$$\hat{n} \cdot \nabla_r = \mu\frac{\partial}{\partial r} + \frac{1-\mu^2}{r}\frac{\partial}{\partial \mu} \tag{3.13}$$

It has been shown [35] that for solar zenith angles less than or equal to 90°, only the first term in Equation 3.13 should be considered. Therefore,

$$\hat{n} \cdot \nabla_r = \mu\frac{\partial}{\partial r} \tag{3.14}$$

This is the pseudo-spherical approximation, which holds as long as the direct beam is also calculated in spherical geometry.

3.2.2 Source Term

The right hand side of Equation 3.9 consists of all of the losses and gains of radiation in the radiative transfer system, and is known as the source term. Given polar coordinates, the source term can be written as:

$$h\nu Q(\mathbf{r},\hat{n},\nu) = h\nu Q(\mathbf{r},\theta,\phi,\nu) = -\beta^{ext}(r,\nu)I(\mathbf{r},\hat{n},\nu) + \frac{1}{4\pi}\int_0^{\infty}\beta^{sca}(r,\nu,\nu')\int_0^{2\pi}d\phi'\int_0^{\pi}d\theta' p(r,\theta,\phi;\theta',\phi')I(\mathbf{r},\theta',\phi',\nu')d\nu' + \beta^{abs}(r,\nu)B[T(r)] \quad (3.15)$$

The first term in Equation 3.15 represents loss due to extinction; that is, absorption and scattering. The second term describes photons which have been scattered into the direction of propagation from all other directions, which is describing the additive effect of multiple scattering. Finally, the third term describes the addition of photons due to thermal emission. Separating the extinction coefficient into absorption and scattering coefficients, Equations 3.17 and 3.18 are obtained:

$$\beta^{ext}(r,\nu) = \beta^{abs}(r,\nu) + \beta^{sca}(r,\nu) \quad (3.16)$$

$$\beta^{abs}(r,\nu) = \sum_i \beta_i^{abs}(r,\nu) \quad (3.17)$$

$$\beta^{sca}(r,\nu) = \sum_i \beta_i^{sca}(r,\nu) \tag{3.18}$$

Both Equations 3.17 and 3.18 represent the total absorption and scattering, respectfully, of i different species of molecule that exist along the photon path. Each species' absorption and scattering is a function of the number density of said species ($n_i(r)$, and absorption and scattering cross sections ($\sigma_i^{abs}(\nu), \sigma_i^{sca}(\nu)$)

$$\beta_i^{abs}(r,\nu) = n_i(r)\sigma_i^{abs} \tag{3.19}$$

$$\beta_i^{sca}(r,\nu) = n_i(r)\sigma_i^{sca} \tag{3.20}$$

Next, the phase function can be described by Equation 3.21:

$$p(r,\theta,\phi;\theta',\phi',\nu) = \frac{\Sigma_i \beta_i^{sca}(r,\nu) p_i(r,\theta,\phi;\theta',\phi',\nu)}{\Sigma_i \beta_i^{sca}(r,\nu)} \tag{3.21}$$

Where $p_i(r,\theta,\phi;\theta',\phi',\nu)$ is the phase function for each species and is defined as:

$$p_i(r,\theta,\phi;\theta',\phi',\nu) = p_i(cos(\Theta),\nu) = \frac{\sigma_i^{sca}(\nu, cos(\Theta)}{\int_{4\pi} d\Omega \sigma_i^{sca}(\nu, cos(\Theta))} \tag{3.22}$$

Where Θ is the scattering angle. The scattering angle is then defined by Equation 3.23

$$Cos(\Theta) = cos(\theta)cos(\theta') + sin(\theta)sin(\theta')cos(\phi - \phi') \tag{3.23}$$

3.2.3 Radiative Transfer Solutions

Assuming plane parallel geometry and monochromatic light, the 1 dimensional radiative transfer equation can be written as follows:

$$-\mu\frac{dI(z,\mu,\phi)}{\beta^{ext}dz} = I(z,\mu,\phi) - \frac{\omega(z)}{4\pi}\int_0^{2\pi} d\phi' \int_{-1}^{1} d\mu' p(z,\mu,\phi;\mu',\phi') I(z,\mu',\phi') - (1-\omega(z))B[T(z)] \tag{3.24}$$

Where $\omega(z)$ corresponds to the 1D single scatter albedo, described by Equation 3.25:

$$\omega(z) = \omega(z,\nu) = \frac{\beta_i^{sca}(z,\nu)}{\beta_i^{ext}(z,\nu)} = \frac{\beta_i^{sca}(z,\nu)}{\beta_i^{abs}(z,\nu) + \beta_i^{sca}(z,\nu)} \tag{3.25}$$

Solving Equation 3.24 with the appropriate boundary conditions will give the incident radiation at the surface of the Earth. At the top of the atmosphere ($z = z_{top}$), an incident beam of solar radiation can be assumed to be parallel with a magnitude I^0 and direction μ_0:

$$I(z_{top},\mu) = I^0\delta(\mu - \mu_0) \tag{3.26}$$

Where $\delta(\mu - \mu_0)$ is the Dirac delta function. Equation **??** can then be decomposed into direct and diffuse (scattered) photon beams:

$$I(z,\mu,\phi) = I^{dir}(z,\mu_0,\phi_0) + I^{sca}(z,\mu,\phi) \tag{3.27}$$

Where μ_0 and ϕ_0 are the solar zenith and solar azimuth angles, respectively. Inserting Equation 3.27 into Equation 3.9, the terms corresponding to scattered and direct light can

be treated separately. Focusing on the direct beam only:

$$-\mu\frac{dI^{dir}(z,\mu_0,\phi_0)}{\beta^{ext}dz} = -\mu\frac{dI^{dir}(z,\mu_0,\phi_0)}{d\tau} = I^{dir}(z,\mu_0,\phi_0) \tag{3.28}$$

Where $\tau = \beta^{ext}dz$ is the optical depth. The solution for this problem is the Beer-Lambert law, Equation 3.29:

$$I^{dir}(\tau,\mu_0) = e^{-\tau/\mu_0} \tag{3.29}$$

On the other hand, the scattered terms take the form of the 1D radiative transfer equation:

$$\begin{aligned} -\mu\frac{dI^{sca}(\tau,\mu,\phi)}{d\tau} &= I^{sca}(\tau,\mu,\phi) \\ &\quad - \frac{\omega(r)}{4\pi}\int_0^{2\pi} d\phi' \int_{-1}^{1} d\mu' p(\tau,\mu,\phi;\mu',\phi')I^{sca}(\tau,\mu,\phi) \\ &\quad - (1-\omega(\tau))B[T(\tau)] \\ &\quad - \frac{\omega(\tau)I^0}{4\pi}p(\tau,\mu,\phi;\mu_0,\phi_0)e^{-\tau/\mu_0)} \end{aligned} \tag{3.30}$$

In order to solve for the scattered intensity, the pseudo-spherical approximation must be used. This approximation replaces the extinction path (τ/μ_0) with the Chapman function, given in Equation 3.31:

$$ch(r_0,\mu_0) = \int_{r_0}^{\infty} \frac{\beta^{ext}(r,\nu)dr}{\sqrt{1-(\frac{R+r_0}{R+r})(1-\mu_0^2)}} \tag{3.31}$$

Where R corresponds to the radius of the Earth, and r_0 the altitude of the beam above the surface of the Earth. Now considering the boundary conditions of the equations, the intensity at the top of the atmosphere and at the surface of the Earth must be satisfied. At

the top of the atmosphere, the boundary condition is given by:

$$I^{sca}(\tau = 0, -\mu, \phi) = 0 \tag{3.32}$$

Which shows that at the top of the atmosphere, there is no diffuse radiation. At the surface, diffuse radiation is also generated by surface reflectivity, which is an additional term that must be considered. This reflectivity can be described in terms of a bidirectional reflectivity, $\rho(\mu, \phi; -\mu', \phi')$, and directional emissivity $\epsilon(\mu)$:

$$I^{sca}(\tau = \tau_g, \mu, \phi) = \epsilon(\mu)B[T(\tau_g)] + \frac{1}{\pi}\mu_0 I_0 e^{\tau_g/\mu_0}\rho(\mu, \phi; -\mu', \phi') + \frac{1}{\pi}\int_o^{2\pi} d\phi' \int_0^1 \rho(\mu, \phi; -\mu', \phi') I^{sca}(\tau, \mu', \phi')\mu' d\mu' \tag{3.33}$$

Where $T(\tau_g)$ is the temperature at the Earth's surface. The first term represents the emission of light from the Earth, while the second and third terms represent the reflection of the direct beam and reflection of diffuse radiation, respectively.

3.3 Radiative Transfer Simulations

Now that the radiative transfer problem has been set up, the resulting diffuse and direct radiation can now be found. This is typically achieved through simulation of the radiative transfer problem, with the output of said simulations being the direct radiance ($I^{dir}(z, \mu_0, \phi_0)$ and diffuse radiance ($I^{sca}(z, \mu, \phi)$. Multiple radiative transfer solvers have been developed, which make use of different techniques to solve the radiative transfer problem.

The Discrete Ordinate approach (cite chandrasekhar, stamnes 88 and 01) is a 1-Dimensional radiative transfer simulation algorithm that, due to the assumed 1D nature of the problem,

is able to assume that the scattering phase function depends only on the angle θ between the incident and scattered beams. Because of this, the azimuthal dependence of the phase function can be separated from the rest of the radiative transfer equation. This is achieved through a series of Legendre polynomials in $cos(\phi)$ while the intensity is expanded in a Fourier cosine series. This process leads to a set of integro-differential equations, which when integrated over the angular space using a quadrature rule, the intensity of a specific stream, or direction, can be obtained.

The adding-doubling method(cite Hulst, de haan), on the other hand, takes the geometric ray tracing approach. The interactions between each neighboring atmospheric layer is modeled, for both reflection and transmission, with this process continuing over all layers until all light is absorbed by air molecules, reflected into space, or reaches the surface of the Earth.

The Monte Carlo method (cite kuscer, deutchmann, domke), on the other hand, randomized the scattering and absorption events in the atmosphere by treating the phase function as a probability distribution function, and the single scatter albedo as the probability that an interaction results in scattering. This allows for a stochastic approach to solving the radiative transfer problem. Typically, between 10^5 and 10^10 simulations of photon paths are used in order to properly converge on the most likely solution to the radiative transfer problem. Technically, due to the modeled photons starting at the top of the atmosphere and ending at the simulated instrument, the process is called Backwards Monte Carlo method.

3.4 Air Mass Factors

In addition to the change in radiance in each atmospheric layer, radiative transfer simulations can determine the effect the light path had on the simulated photons. This effect, known as the air mass factor and discussed in further detail in Chapter 4, is a vital component to

determining the vertical column density of the trace gas that is being measured. However, the air mass factor can be difficult to calculate for measurements of scattered light without the aid of radiative transfer simulations.

$$AMF_i = \frac{ln(\frac{I}{I_0})}{VCD_i \cdot \sigma} \tag{3.34}$$

As shown in Equation 3.34, for each run of the radiative transfer simulator, the radiance is determined both with and without the presence of the absorbing trace gas ($I\&I_0$) in each atmospheric layer, along with the partial vertical column density (VCD_i) for the trace gas of interest in each atmospheric layer and the trace gas's absorption cross-section (σ). This results in an air mass factor for each of the atmospheric layer, known as a box air mass factor.

An example of a set of box air mass factors can be seen in Figure 3.1, where the box air mass factors for NO_2 are shown for the lowest 40Km of the Earth's atmosphere increasing solar zenith angles from 0° to 90° Due to the configuration of the surface instrument being zenith facing, the box air mass factors are much larger in the upper troposphere and stratosphere than close to the surface; in addition, the box air mass factors at 90° are much larger than the other solar zenith angles. This behavior has made measurements of stratospheric trace gases using zenith facing instruments at twilight a popular measurement technique [**?**].

$$AMF = \frac{\Sigma_i^{TOA} VCD_i AMF_i}{\Sigma_i^{TOA} VCD_i} \tag{3.35}$$

The box air mass factors can then be used to retrieve the box air mass factor of each measurement simulated. Equation 3.35 shows the conversion process of box Air Mass Factors into Air Mass Factors. Each set of box Air Mass Factors is combined with the partial vertical column density (VCD_i) that is based on an a priori trace gas profile. That is, an assumed

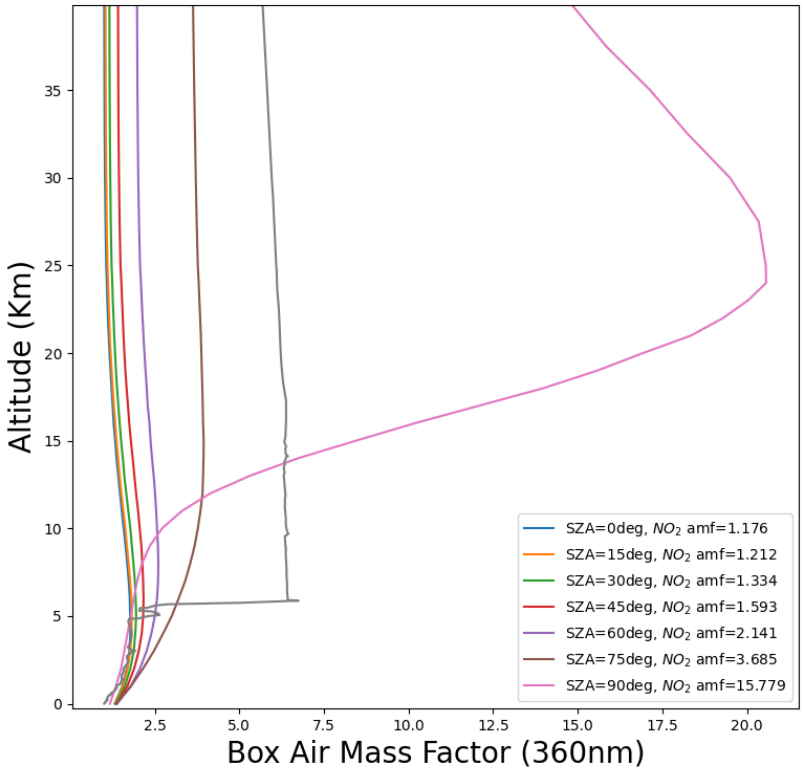


Figure 3.1: Box Air Mass Factors for a Zenith facing instrument in a Rayleigh Atmosphere.

trace gas profile that most likely fits the trace gas distribution that was measured. Typically, this profile is simply a best guess as to the vertical distribution of the trace gas. The effect of the a priori profile on the air mass factor is discussed further in Chapter 7.

Chapter 4

Differential Optical Absorption Spectroscopy

4.1 Introduction

Differential Optical Absorption Spectroscopy (DOAS)[36] [3]is a remote sensing technique that is capable of retrieving information about trace gas amounts in the atmosphere based on the absorption of light as it passes from source to detector. The earliest uses of the DOAS technique made heavy use of artificial light sources to determine concentrations of nitrous acid[37][38] and the hydoxyl radical[39] at low altitudes, as well as Nitrogen Dioxide in the stratosphere using measurements of scattered sunlight at twilight[40]. However, as spectrometer technology improved, measurements of sunlight, both scattered and direct, became more common. Today, most DOAS measuring instruments collect sunlight either using direct-sun measuring techniques, measurements of scattered sunlight at particular angles, MAX-DOAS, or scattered sunlight exclusively in the zenith direction, Zenith Scattered Light DOAS. In addition, many DOAS instruments are operated onboard airplanes, satellites, boats, and ground vehicles, in addition to the typical stationary DOAS instrument. The DOAS method is particularly sensitive to the differential absorption of trace gas species, which when combined with careful selection of retrieval wavelengths allows for the absorption contribution of individual trace gases to be separated from other trace gases.

This chapter is organized as follows: First, the mathematical principle of the DOAS technique is described and discussed. Next, the viewing geometries and the retrieval techniques used in this dissertation are described, as well as the various platforms used. Finally, the error sources present in the viewing geometries are discussed.

4.2 DOAS Technique

The Basic operating principle of Differential Optical Absorption Spectroscopy is derived from the Beer-Lambert Law, given in Equation 3.29 in Chapter 3 and shown in Figure 4.1. As light propagates through some medium from source to detector, the light is absorbed by the molecules present. This behavior can be analyzed to determine what molecules and at what concentration were responsible for the loss of light intensity.

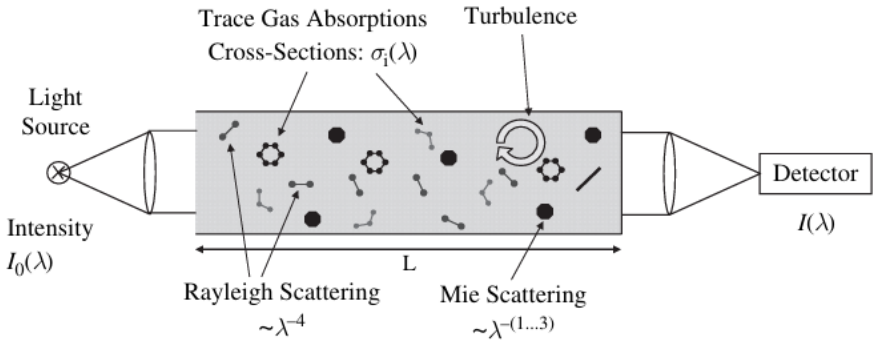


Figure 4.1: Diagram of the Beer-Lambert Law demonstrating how light originating from a source ($I_0(\lambda)$) is lost due to scattering and absorption before it reaches the detector ($I(\lambda)$). Image adopted from Platt & Stutts (2008)[3]

Equation 4.2 gives the modified Beer-Lambert law, which includes all scattering and absorption effects that can be present in the atmosphere. Instrumental effects and atmospheric turbulence are approximated by an attenuation function $A(\lambda)$.

$$I(\lambda) = I_0(\lambda)e^{-L\Sigma(\sigma_j(\lambda)c_j)+\epsilon_r(\lambda)+\epsilon_m(\lambda)} \cdot A(\lambda) \tag{4.1}$$

Where $\epsilon_r(\lambda)$ and $\epsilon_m(\lambda)$ are the scattering effects under the Rayleigh and Mie regimes, respectively, and $\Sigma(\sigma_j(\lambda)c_j)$ represents the absorption effects from all molecules present along the light path, L. This modification of the Beer-Lambert law is the basis for classical absorption spectroscopy, however due to the complexities of Earth's atmosphere, this technique has only ever been used to quantify major absorbers, such as Carbon Dioxide [41][42] and Ozone.[43][44]

Differential Optical Absorption Spectroscopy solves this problem by separating wide-band extinction effects, such as most scattering processes and parts of the absorption cross-section ($\sigma_j(\lambda)$) from the narrowband extinction effects, which are only the narrowband portions of absorption.

$$I(\lambda) = I_0(\lambda)e^{-L\Sigma(\sigma'_j(\lambda)c_j)} \cdot e^{L\Sigma(\sigma_{j0}(\lambda)c_j)+\epsilon_r(\lambda)+\epsilon_m(\lambda)} \cdot A(\lambda) \tag{4.2}$$

Where now $\sigma'_j(\lambda)$ and $\sigma_{j0}(\lambda)$ are the narrow-band and wide-band components of the absorption cross section, respectively. This separation is typically performed through filtering, which is capable of separating the components of the absorption cross-section which vary rapidly in λ from the components that vary slowly in λ. Next, the non-differential absorption, $I'_0(\lambda)$ is defined as the attenuation of light from the wide-band extinction effects, and is described by Equation 4.3:

$$I'_0(\lambda) = I_0(\lambda)e^{L\Sigma(\sigma_{j0}(\lambda)c_j)+\epsilon_r(\lambda)+\epsilon_m(\lambda)} \cdot A(\lambda) \tag{4.3}$$

Typically, the spectroscopic measurements made for both classical and differential absorption spectroscopy are made over multiple, continuous wavelengths. This allows for the non-differential portion of the absorption cross-section, as well as the scattering effects, to be approximated as a low order polynomial, typically between the 3rd and 5th order, in order

to simplify Equation 4.2:

$$ln(\frac{I(\lambda)}{I_0(\lambda)}) = -L(\Sigma(\sigma'_j(\lambda)c_j) + \Sigma(\sigma_{j0}(\lambda)c_j) + \epsilon_r(\lambda) + \epsilon_m(\lambda) \cdot A(\lambda)) \tag{4.4}$$

$$= -L(\Sigma(\sigma'_j(\lambda, p)c_j) + L\Sigma(\sigma_{j0}(\lambda, p)c_j) + \epsilon_r(\lambda) + \epsilon_m(\lambda) \cdot A(\lambda)) \tag{4.5}$$

$$= -L\Sigma(\sigma'_j(\lambda, p)c_j) - \Sigma_{m=0}^{p}\alpha_m \cdot \lambda^m \tag{4.6}$$

Where p is the polynomial order used to approximate the wide-band extinction effects, and α_m is the scaling factor of the polynomial. By isolating the differential absorption effects, the trace gas absorption contribution to the overall extinction that would be otherwise difficult to retrieve can now more easily be singled out, as can be seen by the differential absorption cross-sections shown in Figure 4.2. In addition, certain trace gases exhibit little to no differential absorption at certain wavelengths they are otherwise strong absorbers in. By selecting wavelength bands where only certain traces show strong differential absorption, the absorption of these trace gases can more easily be analyzed, with only a small handful of other trace gas species needing to be analyzed alongside the species of interest in order to retrieve information about the primary species.

4.2.1 DOAS retrieval algorithm

The DOAS technique is typically not performed numerically, but through an least squares fitting process to estimate what combination of slant column densities of the trace gases of interest result in the absorption observed. While Equation 4.6 is a linear equation, several effects, namely the shifting and stretching of wavelength between measurements of I and I_0, as well as instrument effects requiring an additional offset, adding an additional offset

($offset(\lambda)$ and shift and stretch $\Delta(\lambda)$ to the first term in Equation 4.6:

$$ln(\frac{I(\lambda - \Delta(\lambda)) - offset(\lambda)}{I_0(\lambda)}) + L\Sigma(\sigma'_j(\lambda, p)c_j) + \Sigma^p_{m=0}\alpha_m \cdot \lambda^m = 0 \tag{4.7}$$

Due to the non-linear nature of Equation 4.7 a non-linear least squares fitting procedure first

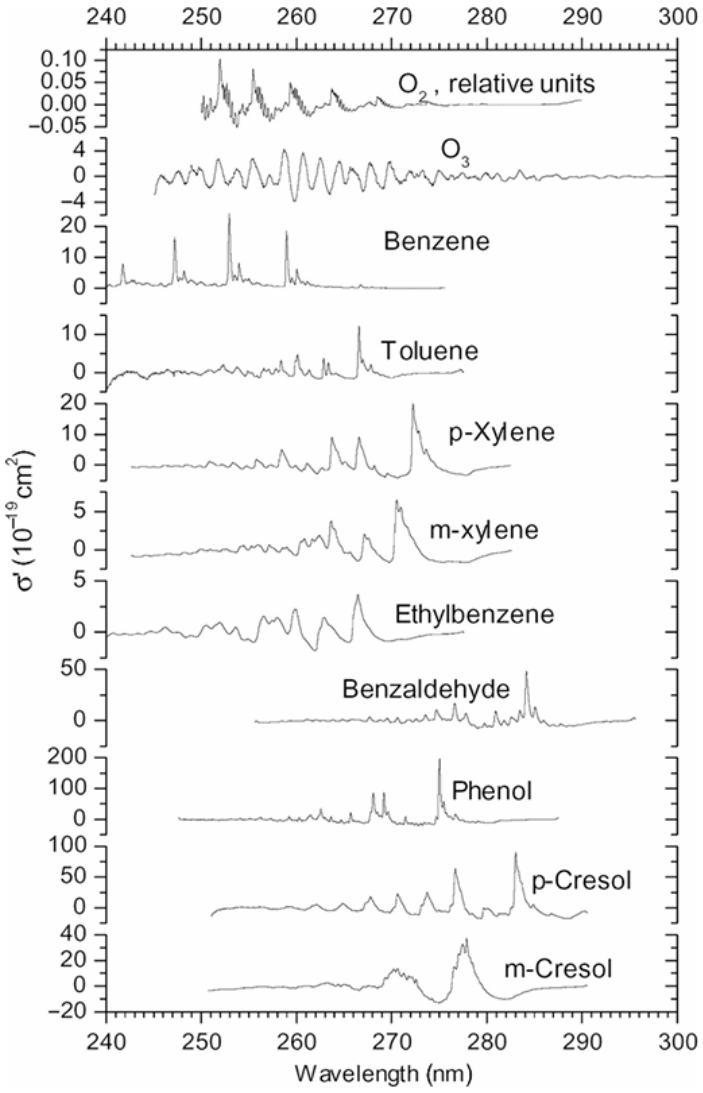


Figure 4.2: The differential absorption cross-sections of various nonocyclic aromatic species, as well as O_2 and O_3 as a function of wavelength. Each spectrum, regardless of similarity in the absorption cross-section, posseses unique differential absorption structures that can be used to retrieve trace gas amounts. Image adopted from Platt & Stutts (2008)[3]

must be used to optimize the non-linear portion of the problem. Typically, the Marquardt-Levenberg Algorithm, which makes use of both gradient descent and Gauss-Newton based steps to efficiently minimize a wide range of optimization problems, including the DOAS fit. The Marquardt-Levenberg Algorithm is typically implemented in a DOAS fit to find the set of input parameters which minimized the sum of the weighted squares:

$$F(\vec{\alpha}) = \frac{1}{2}\Sigma_{i=1}^{M}(\frac{f^i(\vec{\alpha})}{S^i})^2 \tag{4.8}$$

$$= \frac{1}{2}\Sigma_{i=1}^{M}(\frac{ln(I^i(\vec{a}) + \Sigma_{j=1}^{n}\sigma^{ij}c_j + \Sigma_{k=0}^{d}(b_k(\lambda_i)^k - ln(I_0^i)}{S^i})^2 \tag{4.9}$$

Where $\vec{\alpha} = (\vec{a}, \vec{b}, \vec{c})$ is the vector containing all fitted parameters: $\vec{a}$: the set of parameters describing the shift, stretch and offset of the measured spectrum, b_k: the polynomial coefficients, and c_j are the fitted slant column densities ($SCD = L \cdot c_j$). λ_i represents the wavelength grid of I_0, and has the limits of the fitting window selected for the DOAS fitting procedure, and S^i is the measurement error at wavelength λ_i. Each iteration sees new values for each parameter estimated through the Marquardt-Levenberg process, converging upon the minimum value of F when F is less than the predefined success criterion ϵ.

Once the non-linear parameters are estimated, they can be used to correct the spectrum $I(\lambda)$ and return the problem to a linear one. this allows Equation 4.9 to be rewritten as the following:

$$F = \frac{1}{2}\Sigma_{i=1}^{M}(\frac{ln(\frac{I^i(\vec{a})}{I_0^i}) + (A \cdot \vec{x})^i}{S^i})^2 \tag{4.10}$$

Where A is a matrix containing the polynomial basis $(\lambda_i)^k$ and the absorption cross-sections σ^{ij} and $\vec{x}$ represents the combined parameters $\vec{b}$ and $\vec{c}$. This technique allows for the linear parameters to be rapidly updated once the non-linear parameters are estimated, which greatly reduces computation time.

4.3 Passive DOAS

While the previous sections describe the theoretical basis of the DOAS Technique, the actual implementation of the technique is largely based on the remote sensing techniques used to collect the spectral measurements used. For instance, most uses of the DOAS technique in a laboratory setting make use of artificial light sources; these types of DOAS systems are known as active DOAS systems. Active DOAS systems provide the benefit of absolute calibration; that is, an accurate measurement of the light leaving the source which can be used to measure the average concentration of trace gas along the light path. However, this technique is limited in the parts of the atmosphere, with only surface and near-surface concentrations being measurable[45][46]. In addition, light paths in the field tend to require long path lengths or a system of mirrors to reflect light over a target area, in order to ensure enough absorption occurs that the trace gas is measurable.

On the other hand, DOAS systems in the field can make use of sunlight, moonlight, and even light from other stars as a natural light source. These systems, known as passive DOAS systems, are able to measure trace gases far higher into the atmosphere than active DOAS systems are capable of. In addition, the use of natural sources creates a more compact and versatile measurement system, allowing for passive DOAS to be used in more remote locations and on many different platforms. However, due to the lack of knowledge of the spectrum at its source, only the difference in the measurement and reference measurement's trace column amounts can be retrieved from the DOAS technique. This quantity, known as the differential slant column density represents the difference in average concentration, integrated along two separate light paths for the two measurements. Because the differential slant column density is a relative measurement, it holds little value when used to describe trace gas amounts in the atmosphere. As such, differential slant column densities require

additional analysis, typically either geometric or radiative transfer calculations, in order to convert them to other, more relevant quantities such as the tropospheric vertical column density, representing the average concentration integrated from the surface to the top of the troposphere. An example of the full DOAS retrieval process for two measurements of scattered sunlight, Multi Axis DOAS and Zenith Sky DOAS, is shown in Figure 4.3.

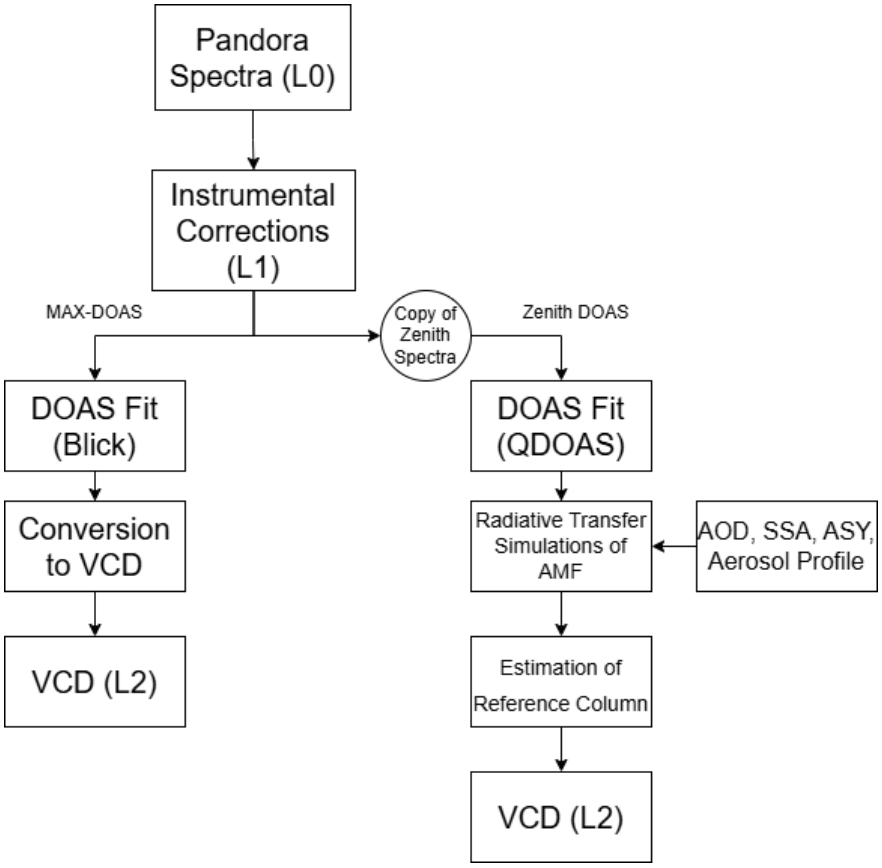


Figure 4.3: The Ring pseudo-cross section calculated through the QDOAS software for the TRACER-AQ2 field campaign

Another complication with passive DOAS systems is due to the unique behavior of the solar spectrum. Because of the hydrogen present in the solar atmosphere, photons matching the absorption lines of Hydrogen are absorbed before exiting the sun. These lines, called Fraunhofer absorption lines, can significantly impact DOAs retrievals in wavelength windows

that include these lines. However, when dealing with measurements of scattered sunlight, the intensity of the Fraunhofer lines are not constant with line depth and broadening observed when compared to direct sun measurements. This behavior, known as the Ring Effect[47], has been attributed to rotational Raman scattering by air molecules[48]. In order to account for the Ring Effect, this absorption can be treated as a pseudo-absorber during DOAS analysis. The Ring cross-section used for this dissertation was calculated following the method described by Chance and Spur[49][50] using the QDOAS software and can be seen in Figure 4.5.

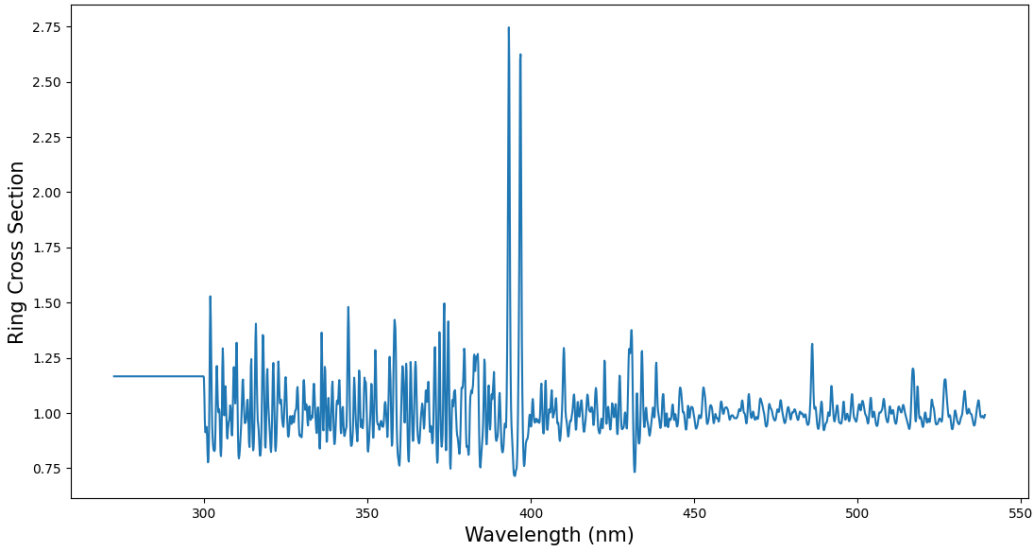


Figure 4.4: The Ring pseudo-cross section calculated through the QDOAS software for the TRACER-AQ2 field campaign

4.3.1 Multi-Axis DOAS

Within Passive DOAS systems, there are multiple viewing geometries which dictate the measurement direction of the instrument. For instance, measurements of direct sunlight can

provide information on trace gases throughout the atmosphere and can be easily converted into vertical column densities, however this viewing geometry is limited by the solar position in the local air masses it can measure, and can be blocked by clouds.

Measurements of scattered sunlight, on the other hand, offer a more complete view of the local troposphere which only must avoid the sun when taking measurements. The most general form of scattered sunlight measurement is known as Multi Axis DOAS (MAX-DOAS)[51][45]. Typically, the reference measurement for a MAX-DOAS instrument is collected at 90° zenith, which provides a differential slant column density representing the difference in trace gas in some direction away from the instrument and trace gas directly above the instrument. This technique allows for reference measurements to be made for each measurement, minimizing the uncertainty present in the reference measurement when compared to other viewing geometries, such as Direct Sun measurements, which require a single reference measurement for an entire dataset.

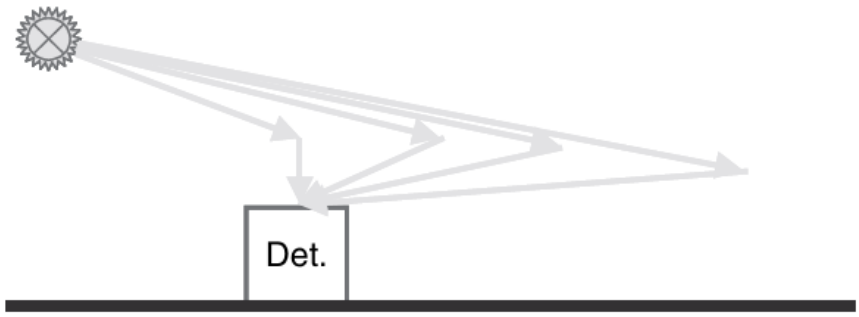


Figure 4.5: Diagram of the MAX-DOAS viewing geometry showing 3 measurements and a reference measurement at 90° zenith. Image adopted from Platt & Stutts (2008)[3]

However, due to the complexity of the scattering processes present, MAX-DOAS dSCDs cannot be easily converted into a VCD as with Direct Sun measurements and in the past have required radiative transfer simulations to estimate the air mass factor of each measurement[52][53]. More recently, however, multiple retrieval algorithms have been developed to bypass the need

to consider radiative transfer when converting MAX-DOAS measurements into VCDs.

One such method is the retrieval of vertical profiles from multiple MAX-DOAS measurements at successive zenith angles [54][55][56]. This method uses the set of measurements to retrieve the most likely profile that would generate the differential slant column densities measured at each viewing zenith angle. In practice, profile retrieval involves the optimization of a forward model ($\mathbf{F}(\mathbf{x}, \mathbf{b})$) as shown in Equation 4.11:

$$\mathbf{y} = \mathbf{F}(\mathbf{x}, \mathbf{b}) + \epsilon \tag{4.11}$$

Where $\mathbf{y}$ is the measurement vector containing the dSCDs measured for one cycle, $\mathbf{x}$ is the state vector representing the atmospheric profile, $\mathbf{b}$ is the vector containing the forward model parameter, and ϵ is the error between measurement vector and forward model. Typically, this inversion problem is solved through the Optimal Estimation method or Parameterization method. Typically, each profile inversion algorithm requires between 10-20 zenith angles to be measured in order to retrieve a profile. As such this technique can produce typically only one profile every 15-20 minutes.

In addition, a real-time algorithm which provides a semi-analytical approach to profile retrieval have also been developed, known as the Air-Sky Ratio algorithm[5][2][57] to quickly estimate the vertical profile based on meteorological measurements and radiative transfer simulations of a Rayleigh atmosphere. This method first retrieves the Vertical Column Density according to Equation 4.12:

$$q_T = \frac{(qs_{75} - qs_0) \cdot q_{CLIM,AIR}}{qs_{75,AIR} - qs_{60,AIR} + 2 \cdot q_{CLIM,AIR}} = \frac{\Delta qs_{75} \cdot q_{CLIM,AIR}}{\Delta qs_{75,AIR} - \Delta qs_{60,AIR} + 2 \cdot q_{CLIM,AIR}} \tag{4.12}$$

Where q_T is the tropospheric Vertical Column Density for the trace gas of interest, $(qs_{75} - qs_0) = \Delta qs_{75}$ is the differential slant column density of the trace gas of interest, $qs_{60,AIR}$ and $qs_{75,AIR}$ are the differential slant column densities of air, which are calculated based on the retrieval of an "air-gas", typically either O_2 or O_2O_2, and $q_{CLIM,AIR}$ is a climatological estimation of the total vertical column density of air, which is based on the effective height of air, $h_{EFF,AIR}$ and an estimated concentration at the surface, $n_{SURF,AIR}$:

$$q_{CLIM,AIR} = n_{SURF,AIR} \cdot h_{EFF,AIR} \tag{4.13}$$

What is interesting here is that the Vertical Column Density is first calculated before the profile, rather than integrating the vertical profile to find the Vertical Column Density as with other profile retrieval techniques. In addition, only three viewing zenith angles are required to retrieve the Vertical Column Density, assuming the vertical profile is not a desirable quantity. This not only reduces the time required to convert the differential slant column densities into a vertical column density, but also reduces the number of measurement direction required to 3, allowing for Vertical Column Densities to be retrieved on a per minute basis, a much faster pace than other inversion algorithms.

4.3.2 Zenith Scattered Light DOAS

Measurements of scattered sunlight can also be made exclusively at zenith as well; this viewing geometry is known as Zenith Scattered Light DOAS, or ZSL-DOAS. ZSL-DOAS has the advantage of rapid measurement: due to the consistent viewing geometry, a single measurement is all that is required to produce a VCD. As such, the ZSL-DOAS technique,s cycle time is limited only on the measurement speed of the instrument. However, due to the lack of other measurement directions, ZSL-DOAS requires radiative transfer simulations

in order to calculate its air mass factors. Spectroscopic measurements of zenith scattered

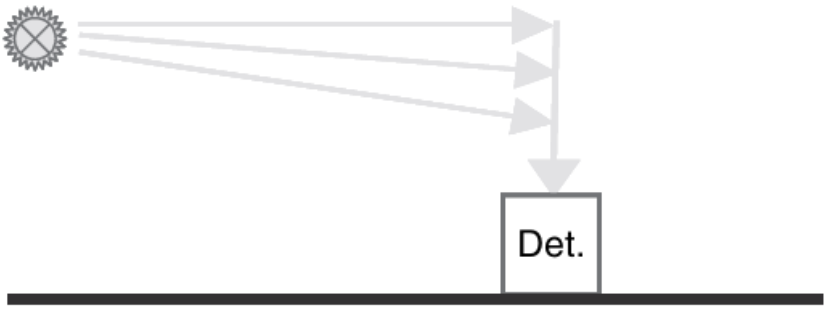


Figure 4.6: Diagram of the ZSL-DOAS viewing geometry showing 3 measurements, all of which at different SZAs but measured at 90° zenith. Image adopted from Platt & Stutts (2008)[3]

light predate the DOAS technique, with several studies measuring NO_2 concentrations in the stratosphere[58][40]. This is largely due to the sensitivity of ZSL measurements to stratospheric concentrations of trace gases, in particular at twilight as the majority of the light path travels through the stratosphere, making trace gases at these altitudes easier to measure with the instrumentation available at the time. Even after the development of the DOAS technique, ZSL measurements remained popular for understanding the interaction of stratospheric trace gases with ozone formation and depletion[59][60][61][62]. However, recent studies have used ZSL measurements to measure tropospheric columns of trace gases, ignoring any stratospheric component present in the measurement[63][64]. While ZSL measurements are not as sensitive to the tropospheric column, ZSL measurements have the advantage of directly measuring the tropospheric trace gas overhead,allowing for a more direct measurement of the VCD than with the MAX-DOAS viewing geometry.

Due to the limitations on viewing geometry, the ZSL-DOAS measurement cannot be converted to a VCD through profile inversions or comparisons with the dSCD of air, as with MAX-DOAS measurements, or through geometric approximations as with measurements of

direct sunlight. Instead, after DOAS fitting the tropospheric component of the ZSL VCD must be retrieved according to Equation 4.14:

$$VCD = \frac{dSCD + SCD_{ref}}{AMF} - VCD_{strat} \tag{4.14}$$

Where SCD_{ref} is the slant column density of the reference measurement used for the DOAS fit, AMF is the Air Mass Factor of the measurement, and VCD_{strat} is the stratospheric component of the total Vertical Column Density. While the Air Mass Factor can be geometrically approximated as 1, due to the direct measurement of the column directly vertical, the Air Mass Factor is influenced both by the solar zenith angle changing both the light path as well as the assumed last scattering altitude, and scattering due to aerosols and large particles. As such, radiative transfer simulations are required to estimate the light path of the measured light, as well as the impact of local aerosols on said light path. More information of these simulations is given in Chapter 7.

Once the Air Mass Factor of each measurement is estimated, the differential slant column density must first be converted into an abolute slant column density before the VCD can be retrieved. This is due to the AMF and VCD being absolute quantities, i.e. neither represents the difference between two measurements. However, because the dSCD represents the difference between two measurements, it is not a relaable quanity to the VCD or AMF. Therefore, the slant column that was measured for the reference spectrum must first be estimated and discounted from the dSCD.

Typically, ZSL-DOAS measurements will select a reference measurement that is the average of several low trace gas days that are also cloud-free and with small minimum zenith angles, in order for the reference to be as close to a true unscattered zenith measurement as possible. This also means that the time periods used for this average are limited to roughly solar noon.

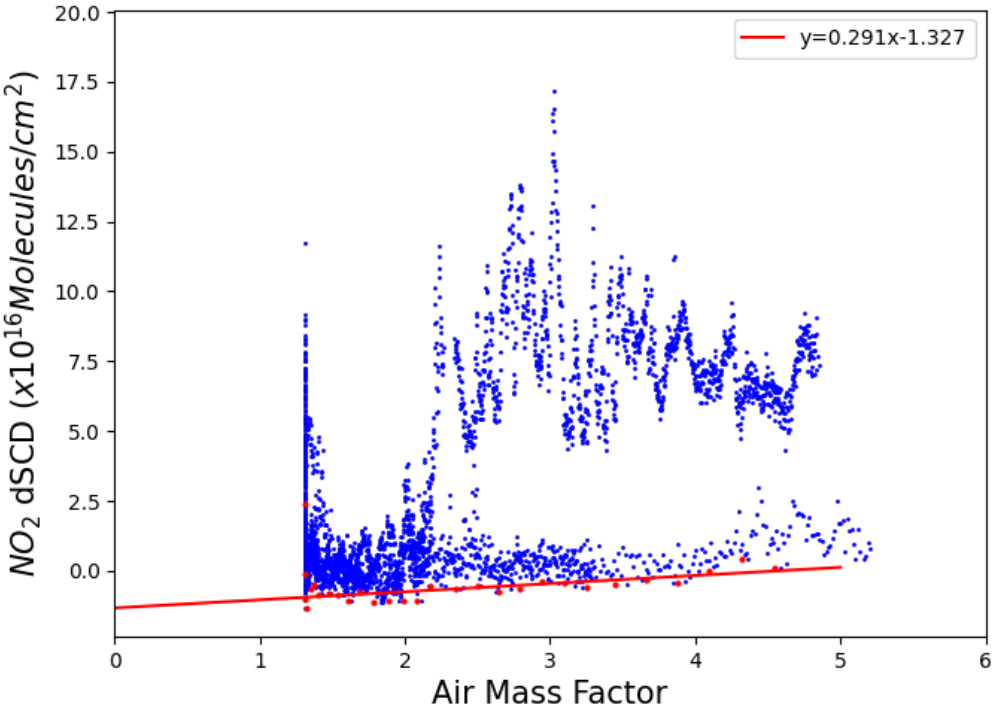


Figure 4.7: Plot depicting the Minimum Langley Extrapolation technique. Differential Slant Column Densities are plotted according to their air mass factor, then binned according to air mass factor. A linear fit is performed on the minimum value of each bin to extrapolate the minimum dSCD at an air mass factor of 0

However, in the case of shorter term projects, instruments have been moved away from areas of interest into emissions-free areas[65], where a reference measurement with a small slant column can be taken over a shorter time period.

However, even when minimizing this reference column, its presence can still be significant and must be removed. In order to estimate this column amount, Minimum-Langley Extrapolation can be used to estimate this column. Figure 5.2 shows an example of Minimum-Langley Extrapolation. In this technique, each dSCD measured on the reference days is plotted against its respective AMF. In addidiot, the dSCDs are binned by their AMFs and the smallest dSCD in each bin is used to perform a linear fit, which is used to extrapolate the

minimum dSCD at an AMF of 0. As can be seen in Figure 5.2, AMFs do not decrease below 1, and in fact the minimum AMF for a zenith measurement remains around 1.2. An AMF of 0 would represent the complete absense of both scattering and absorption, such as in space, and if there were no reference column present in the dSCDs, this extrapolated value should be 0. But, as can be seen in Figure 5.2, the extrapolated dSCD at an AMF of 0 is present, and negative, indicating that the dSCDs are biased by this amount. This negative value is taken as the estimation of the trace gas column that was present in the reference spectrum, and used to convert all dSCDs into the absolute SCD, which is combined with the AMF to produce a total Vertical Column Density.

In the case of trace gases that have significant quantities present in both the Troposphere and Stratosphere, such as NO_2 and O_3, it is useful to separate the Vertical Column Density into Stratospheric and Tropospheric components, in order to analyze one or both separately. The stratospheric column can typically be directly measured by limiting the measurement time to twilight, when the light path passes mostly through the stratosphere, and as such most of the measured absorption occurs at these altitudes. However,when trying to isolate the tropospheric column, it is not possible to simply take measurements when the ZSL measurement is sufficiently sensitive to the Tropospheric column. Instead, the Stratospheric column must either be measured[66], or estimated through chemical transport modelling[67][68][69], or climatologies [14]. Once estimated, this value can be removed from the total VCD to obtain an exclucively Tropospheric VCD.

4.4 DOAS Measurement Platforms

Due to the versatility of passive DOAS systems, these instruments can be used in a wide variety of applications. These include stationary applications, as well as mobile platforms

which are capable of measuring on a local, national, and global scale.

4.4.1 Ground-Based DOAS

Ground-Based DOAS instruments are best characterized by the fact that they remain stationary at fixed locations. This allows for these instruments to focus on one specific location over a long period of time, with many semi-autonomous Ground-Based DOAS instruments remaining in the field for years at a time, only being moved for calibration or maintenance purposes. However, due to their fixed location, the trace gas that these instruments can measure is limited by atmospheric scattering. Even in a Rayleigh atmosphere and under a single scattering approximation, there is some distance away from the instrument where all light that is being measured can be expected to have been scattered before. The presence of aerosols and multi-scattering further limit this distance, to where typical distances range between 8-20Km depending on aerosol conditions and viewing geometries.

Because of this behavior, these instruments typically measure trace gases within major cities and industrial sites, to track long term emissions trends in these areas. However, one other major application of Ground-Based DOAS instruments is in the field of satellite validation. While there are numerous satellites currently in orbit capable of performing DOAS measurements, and will be discussed further in Section 4.4.2, there is a need on the ground to ensure that these Satellite-Based DOAS instruments are reporting accurate results. The long term measurements of Ground-Based DOAS instruments allows for daily, monthly and yearly trends in both Ground-Based and Satellite-Based DOAS measurements to be analyzed and compared, in order to identify both when and why these two instrument types agree and do not.

Measurements of direct sunlight have been used for satellite validation[70][71] and show

good agreement between measurement sets, however Satellite-Based DOAS instruments consistently underestimate trace gas amounts when compared to Ground-Based DOAS instruments. This is possibly due to the limitations on viewing geometry of the direct sun technique limiting parts of the atmosphere that are measurable within the short overpass time leading to biased measurements on the ground. In order to limit this, multiple studies have made use of the MAX-DOAS viewing geometry[72][73][74] and have performed measurements focused on measuring the area around the instrument as completely as possible. However, even MAX-DOAS viewing geometries see Satellite-Based DOAS instruments under reporting trace gas amounts when compared to Ground-Based DOAS instruments, usually by around 30%.

In order to better coordinate measurements of trace gases on the ground as well as improve satellite validation efforts, numerous instrument networks have been formed. These networks consist both of DOAS and non-DOAS remote sensing instruments, and are coordinated by a central authoority. For Instance, the Network for the Detection of Atmospheric Composition and Change (NDACC)[75][76] is one such network, which has combined the use of DOAS instruments with other remote sensing techniques, such as LIDAR Fourier Transform Infrared (FTIR) remote sensing techniques as well as atmospheric soundings to measure atmospheric composition across the globe. In addition, there are several nationally sponsored networks such as the Chinese University of Science and Technology of China DOAS Network (USTC)[77], the MAX-DOAS instruments in Russia and ASia (MADRAS)[78] based in Russia, the Bremen DOAS Network for Atmospheric Measurements (BREDOM) in Germany[79], and Network for Observation of Volcanic and Atmospheric Change (NOVAC) in Sweden[80]. These national networks typically have a smaller scope than the NDACC either being dedicated to a measurements in a single country or to measure a specific atmospheric quantity.

Pandonia Global Network

Another instrument network that is particularly associated with this dissertation is the Pandonia Global Network (PGN)[81][2]. The PGN is an international program maintained by both NASA and the ESA that maintain over 200 Ground-Based DOAS instruments stationed all over the globe, as seen in Figure 4.8. These instruments are capable of taking measurements in all viewing geometries, and long-term data on trace gas trends in their areas of interest. The primary retrievals of the instruments are VCDs of NO_2 and $HCHO$, however the instruments are also able to provide secondary measurements of O_2O_2, H_2O, O_3, as well as SO_2 as an experimental, non-validated data product.

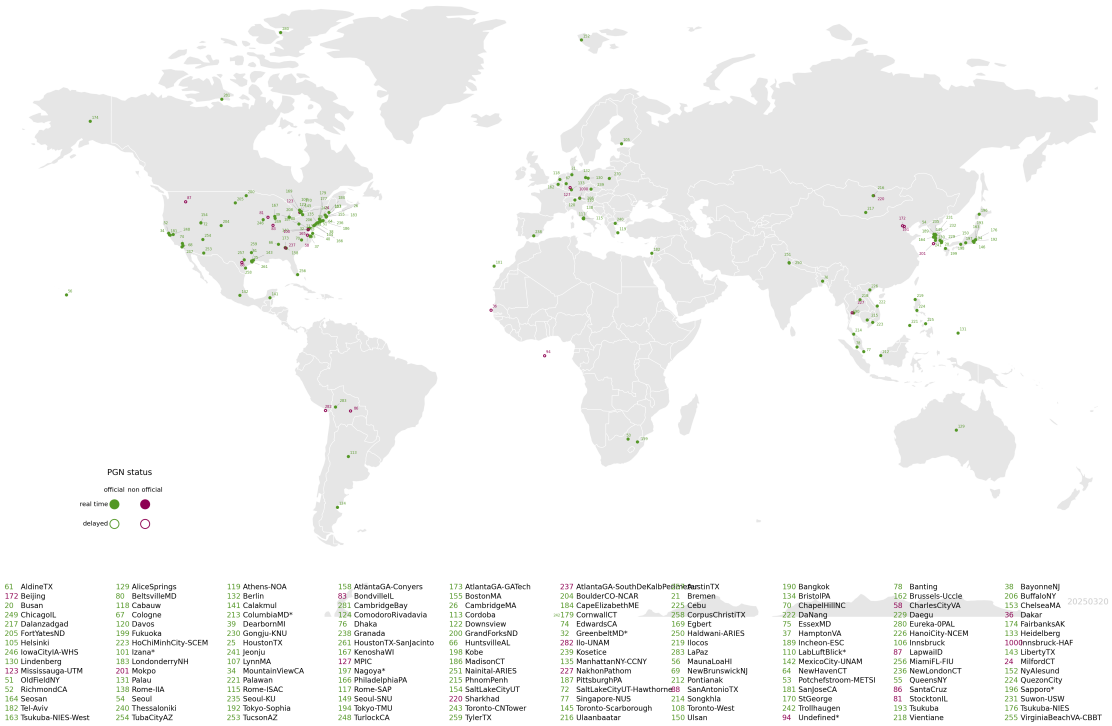


Figure 4.8: Map of the Installed Pandora instruments including those associated with the PGN (green) and those that are not (purple). Image Courtesy of the Pandonia Global Network[2].

The primary mission of the Pandonia Global Network is to assist in validation efforts of the

many Satellite-Based DOAS instruments that both NASA and the ESA have in orbit around Earth. This includes both short term field campaigns focused on identifying particular cases where measurements do not align[82][83][84] and long term projects where trends over multiple years can be compared[85]. In addition to satellites, Pandora systems have been used to compare airborne DOAS measurements[86], which rely on a similar measuring strategy to Satellite-Based DOAS instruments.

While the first Pandora instruments were in development as early as 2005, The Pandonia Global Network was formally established in 2018. During this time, extensive validation efforts have taken place to ensure Pandora instruments maintain the highest quality of measurements, with multiple studies looking at both the agreement of Pandora measurements with measurements of other DOAS instruments[87][88] as well as comparisons of Pandora and other instruments' ability to validate satellite data[89].

Pandora Spectrometer

An example of a Pandora instrument is shown in Figure 4.11. The Pandora instrument consists of five main components: the Sensor Head, Tracker, optical fiber, spectrometer, and computer. The filter head consists of a collimating tube, which both limits the introduction of stray light into the optical fiber and prevents most debris from blocking the optical window, and two sets of filters consisting of various neutral density filters and cutoff filters to limit the light entering the system, as well as a diffuser filter meant to improve field of view of the instrument when making measurements of direct sunlight, and opaque filters for measurements of dark signal. The typical field of view of the instrument is 1.6°, however use of the diffuser filter increases this to 2.1° at the cost of most of the measured sunlight, hence its limitation to measurements of direct sunlight. The sensor head is directly connected to a 400μm optical fiber which is typically between 3 and 20m, depending on the location the

instrument is deployed in. Instrument pointing is performed by a tracker, which is capable of 360° of azimuthal pointing and 180° of zenith pointing with 0.2° pointing accuracy, well withing the instrument's field of view.



Figure 4.9: Example Pandora instrument set up on the roof of Whittemore Hall in November, 2021.

The spectrometer itself is an Avantes spectrometer with a dynamic range between 280 and 525nm and a resolution of 0.6nm FWHM, however this can vary as some instruments may have other spectrometer models than the typical instrument. The spectrometer sits on top of a TE Tech cold plate cooling module, which ensures the spectrometer remains at a constant temperature as well as temperature stability while in operation. Control of the instrument's operation is handled by the Blick Operational (BlickO) software included with

Pandora instruments. This software is capable of managing the instrument autonomously, only requiring regular inspections to ensure no operational errors have taken place. In addition, BlickO supports manual control of the instrument, and allows for user control over all facets of the instrument.

In order to ensure consistency of measurement between field campaigns the Pandora instruments used in this dissertation underwent calibration procedures. This includes radiometric calibration, wavelength calibration, and temperature calibration. Temperature calibration of the instruments is ensured by performing the calibration procedures while the spectrometer is at three steady state temperatures: the operating temperature as well as 7° above and below this temperature. This procedure allows for the effect of the instrument's temperature dependence to be characterized and its effect to be removed from the spectral measurements.

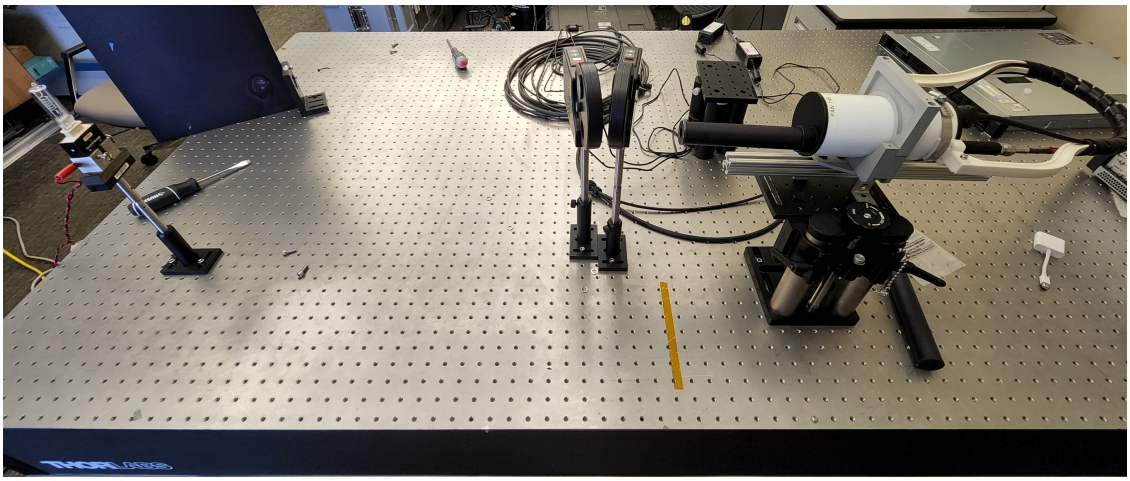


Figure 4.10: Pandora Instrument set up for radiometric calibration.

Radiometric calibration consists of

On the other hand, the purpose of wavelength calibration is to characterize any changes to the instrument's dynamic range or spectral resolution that might have occurred during field

operations. This is accomplished by measuring a series of spectral lamps; for this dissertation Helium, Neon, Xenon, Krypton, Mercury lamps were used, however any spectral lamp with significant emission within the instrument's dynamic range could be used. The emission lines of these elements are well characterized, and their spectral location well known. As such, The spectrometer pixels can be easily aligned to the wavelength of the emission line that they align with.

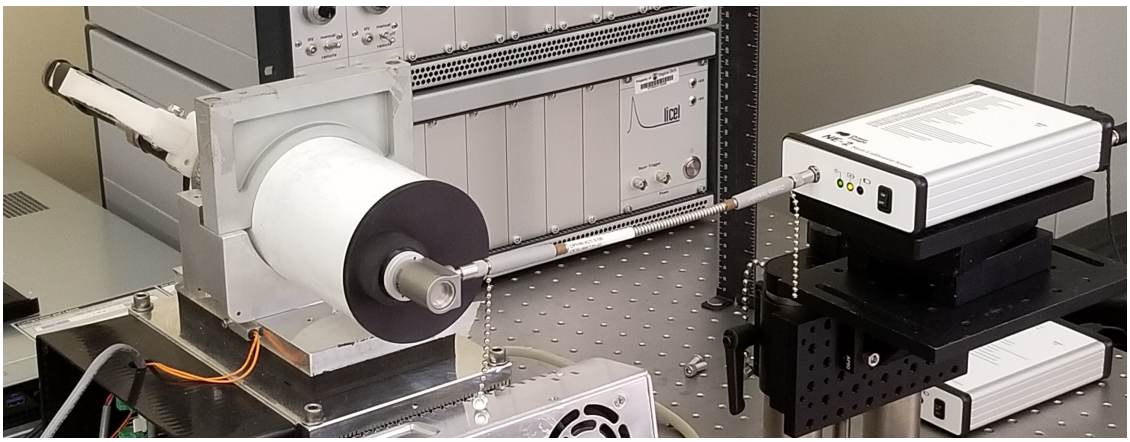


Figure 4.11: Pandora Instrument set up for wavelength calibration using a Neon spectral lamp.

The results of calibration are used to correct the raw spectra after collection. While the raw spectra can be used to perform the DOAS fit, correcting spectra will both limit the errors present in uncorrected spctra as well as ensure a better fit is performed, in which the residuals of the DOAS fit are further minimized. This step of the rocess is known as conversion of L0 data into L1 data, as shown in Table 4.1. After conversion to L1 data, the actual DOAS fit is performed on the corrected sectra, converting them into L2Fit data, or the differential Slant column Densities. These dSCDs are then converted into VCDs, or L2 data, through the processes described previously in this chapter.

The L0 data corrections are summarized in Table 4.2. In short, each of these corrections is required in order to discount various instrumental effects, such that two seperate instruments

Table 4.1: Pandora DOAS retrieval steps

Data Level	Description
L0	Raw Spectra
L1	Corrected Spectra
L2Fit	differential Slant Column Densities after DOAS fit
L2	Vertical Column Densities

performing the same measurement at the same location should result in the same corrected spectrum.

The Dark Current represents the thermal noise of the spectrometer, one of the largest sources of retrieval uncertainty. The dark current is removed from the spectrum by subtracting a "dark measurement". This measurement is made immediately after each measurement, and is done under the same integration time and number of repetitions but while an opaque filter is blocking all light from entering the sensor head. This dark measurement represents the mean thermal noise of each pixel present in the original measurement and is subtracted from the measurement.

The non-linearity of image sensors, while a consistent phenomenon, is not consistent between sensors. Using the results from radiometric calibration, the nonlinearity is fitted to a curve based on dark corrected counts, then based on the counts of the initial measurement, each pixel's value is adjusted.

The latency of a spectrometer refers to the bias of successive measurements. For example, multiple high count measurements followed by low count measurements will bias the low measurements high. This bias is typically determined during radiometric calibration, and the bias gain and decay for each measurement that is preceded by high and low measurements, respectively, is used to correct the spectrum.

Pixel response non-uniformity correction, also known as flat-field correction, is needed due to the inconsistency of each pixel when measuring. This leads to individual pixels, even when illuminated by the same light level, return different values; this effect is caused by physical differences in the pixels both due to their fabrication as well as being subject to slightly different conditions while the instrument is deployed in the field. This non-uniformity is determined during radiometric calibration, where the consistent light source is used to identify inconsistencies in pixels, and is then used to correct the measured spectra.

The temperature effect on the spectrometer, while limited by the temperature control systems in the instrument, is still present due to the influence of ambient temperature. As such, the spectrometer temperature, while stable over minute scales, will still shift during the day as the temperature controller maintains a constant output to ensure temperature stability over consistency. As such, the results of temperature calibration are used to determine the sensitivity of the instrument to changes in temperature, then this sensitivity is used to correct the spectrum.

Finally, stray light, which is light that reaches the detector pixels without traveling along the expected optical path, must be quantified and its effect minimized. Typically, this is performed through stray light calibrations in the field, where measurements of light below 290nm is used as an estimate for the stray light present. In lieu of dark current, which has already been minimuzed, there should be only minute amounts of light below 290nm on the Earth's surface, due to the presence of Ozone and Oxygen absorbing light below this wavelength. As such, it is reasonable to conclude that any light below this wavelength that is measured is due to light travelling through the optical system outside the expected optical path, and illuminating parts of the detector that does not match the stray light's wavelength. Typically, the mean value of the light detected under 290nm, averaged over multiple days in the field, is used as the estimate for stray light present in the spectrometer, and is subtracted

from the spectrum to finish the corrections of the L0 data.

Table 4.2: Summery of correction steps to convert L0 into L1 data.

Name	Description
Dark Current	Limit the effects of thermal noise
Non-Linearity	Account for non-linearity of detector
Latency	Prevent influence of previously measured detector pixels
Pixel Response Non-Uniformity	Account for physical differences in detector pixels
Temperature	Eliminate temperature dependence of the spectrometer
Stray Light	Remove contribution of stray light from spectra

4.4.2 Satellite-DOAS

As previously mentioned, there are many DOAS instruments operating onboard satellites currently orbiting Earth. These instruments are typically placed in sun-synchronous orbits, measuring a wide swath of the Earth's atmosphere as it passes across the light side of the Earth. These orbits are oriented such that the light side is measured at approximately solar noon, and as such the instrument's orbits have an orbital period of one hour.

The Satellite-Based DOAS instruments collect light that has been scattered off the surface of the Earth, and because of this, conversion of Satellite-Based dSCDs to VCDs is more complicated than with Ground-Based DOAS instruments, leading to higher uncertainty in the VCD retrieval. In addition, Satellite-Based DOAS instruments have limited resolution, with individual measurement pixels corresponding to, at minimum, a 2Kmx4Km swath at the surface; it is because of these drawbacks that so many Ground-Based DOAS instruments, including those of the Pandonia Global Network, are focused on validating satellite data products.

The Global Ozone Monitoring Experiment (GOME-1&2)[90][91][92] [93]instruments are some of the first Satellite-Based DOAS instruments, which were launched in 1995 and 2006, re-

spectively, by the ESA. Due to instrument constraints, GOME-1 had limited resolution, with its 960Km swath being measured by a single 320Km by 40Km pixel, which over the course of three orbital cycles, or three days, could cover the entirety of the Earth. GOME-2 used lessons learned from the first satellite and improved upon the design, improving resolution to 80x20Km. The first attempts to validate GOME products came in the form of ZSL-DOAS measurements of NO_2 at twilight in remote locations[94], where the stratospheric column could be measured and compared. For GOME-2, however, the newly developed MAX-DOAS viewing geometry was used to compare tropospheric columns of NO_2[70][95].

Another satellite launched by the ESA is the SCanning Imaging Absorption spectroMeter for Atmospheric CartograpHY (SCIAMACHY)[96][97].Launched in 2002, SCIAMACHY is unique among Satellite-Based DOAS instruments in that the instrument is able to change its measuring geometry. While most Satellite-Based DOAS instruments perform scans at nadir, SCIAMACHY is able to also perform limb scanning as well as solar and lunar occultation measurements. At Nadir, SCIAMACY's resolution is reported to be 30x3Km.

The Ozone Monitoring Instrument (OMI)[98][99][100] is a NASA-based instrument launched in 2004. The instrument provides a resolution of 13x24Km and covers a swath of 2600Km, much larger than the 960Km of both GOME and SCIAMACHY. Validation of OMI products is typically carried out by validation networks, and is one of the original missions of the Pandonia Global Network.

The Tropospheric Monitoring Instrument (TROPOMI)[101][102][103] is one of the most recently launched sun-synchronous satellites to date. Launched in 2017, TROPOMI maintains an orbital period of 100 minutes, which allows the instrument to overpass the equator at 13:30 local time. The TROPOMI instrument has a 2600Km swath, with a resolution of 3.5x7Km. Because of TROPOMI's focus on tropospheric trace gases, and in particular tropospheric NO_2[18], most validation efforts have been directed toward the MAX-DOAS

viewing geometry. However, numerous studies have reported TROPOMI underestimating VCDs when compared to Ground-Based DOAS measurements, with around a 30% underestimation being reported. As such, numerous validation studies have been performed, both for TROPOMI[72][73][104] as well as GOME[95] and OMI[70], in order to mitigate this discrepancy, most notably through adjustments to the measurement directions in order to perform a more comprehensive measurement of the atmosphere that the nearest TROPOMI pixel is measuring. However, discrepancies still remain, which suggest that the issues in TROPOMI retrieval are not simply due to the measurement strategies used on the ground.

While the previous Satellite-Based DOAS instruments were all placed in sun-synchronous orbits, newer Satellite-Based DOAS instruments have been designed for geosynchronous orbits instead. For instance, the Tropospheric Emissions: Monitoring of Pollution (TEMPO)[105][106] instrument is a NASA funded Satellite-Based DOAS instrument designed for geosynchronous orbits. Launched in the spring of 2023, this instrument is currently in orbit over the continental United States, with much of Canada and Mexico within its field of regard. One major advantage of geo-synchronous satellites over sun-synchronous satellites is that the instruments never leave their field of regard. This means that measurements can be made at a more rapid pace. In TEMPO's case, the instrument is capable of measuring its field of regard once an hour during daylight, where its sweep broom style optics scan from East to West. This gives TEMPO an hourly temporal resolution to observe how trace gases evolve throughout the day, where sun-synchronous satellites could only compare between different days. One major drawback to the geosynchronous orbit, however, is its much higher altitude of 35,786Km as opposed to the sun-synchronous orbital altitude of 824Km. This make achieving high spatial resolution measurement much more difficult, however TEMPO boasts a pixel resolution of 2.1x4.4Km, a slight improvement over TROPOMI.

4.4.3 Mobile-DOAS

While Ground-Based DOAS instruments are typically installed in fixed locations, some DOAS applications have these instruments also placed on moving platforms. This application is known as Mobile DOAS, and serves as a compromise between the rapid pace of measurement provided by Ground-Based DOAS instruments, and the high spatial coverage of Satellite-Based DOAS instruments. Mobile DOAS also has the ability to travel into areas of interest, in order to more directly measure high trace gas amounts, as opposed to Ground-Based DOAS instruments needing the trace gas to transport into its area of regard or Satellite-Based DOAS instruments being unable to spatially resolve the true trace gas location.

The primary platform from which mobile DOAS measurements are performed are ground vehicles. These are typically smaller vehicles, from compact cars to research vans, that are just large enough to mount a DOAS instrument on top of the vehicle while its operations are controlled from inside.

Mobile DOAS measurements made using the ZSL-DOAS viewing geometry are one of the most common applications of mobile DOAS. This is due to the convenience of not requiring instrument pointing: this means that the sensor head can be mounted in a fixed direction and is not expected to move during measurements. However, due to the viewing geometry, these ZSL-DOAS are limited to measuring trace gases directly above the roads they are traveling on, limiting the applications of the technique. One such application is in tracking vehicle emissions in high traffic density areas. One example of this can be seen in Wang et. al.[107], where mobile DOAS measurements performed in Shanghai, China, are compared between 2009 and 2010. The decrease in NO_x VCDs between these two years indicated that rules limiting traffic volume were successful in limiting vehicular emissions. On the other

hand, long range mobile DOAS studies have been conducted, where the instrument measures through multiple major cities and the rural areas between them, in order to quantify the emissions gradient, both from vehicles as well as urban emissions. Two examples of this can be seen in two studies in the Balkan peninsula: Constantin et. al.[108] in 2013, and its follow-up in 2017[109]. These two studies showed that while the high VCDs measured inside major cities indicated anthropogenic emissions from both industry and vehicles being responsible for high VCDs, these emissions were not present immediately outside the city, with most NO_2 dissipating in adjacent suburban areas. In addition, almost no NO_2 is present in rural areas, with the stratospheric NO_2 column comprising most of the NO_2 measured; however, in the proximity of large sources, such as isolated power plants, the NO_2 columns rose well above background levels, indicating sensitivity to nearby sources.

Mobile ZSL-DOAS measurements can also be combined with data on wind patterns in order to estimate the amount of trace gas moving into and out of a region. This technique is known as emissions flux[110][111], and can estimate the amount of trace gas travelling out of a particular area, such as around an industrial complex, or into and out of an entire city. However, this technique requires information about the wind profile above the instrument at the time of measurement. This information is functionally impossible to obtain due to the amount of time required to gather the information. Typically these studies have relied on atmospheric soundings made at set times during the day, combined with local ground measurements of wind speed and direction to estimate the overall wind profile.

On the other hand, mobile DOAS measurements made using the MAX-DOAS viewing geometry offer a more versitile set of viewing directions, capable of measuring both emissions on road as well as off road. This also means that the viewing geometry is more sensitive to off road emissions than the ZSL-DOAS viewing geometry, with sources in front of or behind the vehicle being measured in addition to vehicular emissions present around the vehicle.

This leads to a greater emphasis on stationary sources, and less on vehicular emissions.

For example, Wagner et. al.[112] performed mobile MAX-DOAS measurements in rural Belgium and Germany. During this trip, the MAX-DOAS instrument was capable of identifying a local power plant near the vehicle, which greatly increased NO_2 VCDs compared to the surrounding area. In addition, a comparison of viewing zenith angles revealed that higher viewing zenith angles resulted in larger VCDs measured, indicating that the NO_2 measured is likely elevated both from the elevated smokestack of the power plant and from vertical mixing. Mobile MAX-DOAS measurements can also be used to measure the trace gas gradient from isolated regions into cities. For instance, Cheng et. al.[113] measured NO_2 and $HCHO$ in the Tibetian Plateau in Western China. Due to the remoteness of the region, the only sources of NO_2 repent are in towns and cities, predominantly from household heating. This as well as large changes in altitude, allowed for the study to measure both the horizontal gradient as well as vertical gradient of background NO_2 and $HCHO$ present.

In addition, mobile MAX-DOAS measurements can be used to perform emissions flux studies, similar to mobile ZSL-DOAS measurements. The difference in viewing geometries, however, leads to vehicular emissions along a larger portion of the road being measured, and can serve as a spatially averaged estimation of overall vehicular emissions in an area. However, one must take care to measure along a long and straight enough road, or else the measurements will be influenced by stationary sources. For instance, both Ibrahim et. al.[114] and Tan et. al.[115] both performed flux measurements along ring roads surrounding the twin cities of Mannheim and Ludwigshafen, Germany, and Hefei, China. Both loops were sufficiently large, with arii well above 20Km, such that the influence of surrounding stationary sources on the measurements were minimal, and the contributions of vehicular emissions, as well as long term transport from the urban core of both cities could be studied.

Mobile DOAS techniques can also be used to perform satellite validation[116][117][118].

Because of the mobile nature of these measurements, mobile DOAS is capable of covering more area than stationary DOAS measurements, and therefore is able to compare to a larger number of satellite pixels each day when compared to a stationary instrument. However, due to the fewer number of measurements that are made for each individual pixel during a satellite overpass, satellite validation using mobile DOAS tends to have greater amounts of uncertainty than a stationary instrument. Therefore, satellite validation using mobile DOAS is best used to identify areas where mobile DOAS and Satellite-Based DOAS measurements disagree which can better guide validation efforts using longer-term Ground-Based DOAS instrument.

Mobile DOAS instruments have also been placed onboard airborne platforms[119][120][121][122]. These plane based instruments perform measurements in a similar format as Satellite-Based DOAS instruments, but due to its much lower altitude, airborne DOAS instruments can achieve a much higher resolution than Satellite-Based DOAS instruments. In addition, airborne DOAS instruments are not bound by a gravitational orbit, and therefore can measure particular air masses at any given time, but also repeat any measurements throughout daylight hours as neccessary. One major downside to airborne DOAS, however, is the high costs required to operate the plane the instrument is installed on. This typically limits airborne DOAS applications to short-term field campaigns, and is usually operated in tandem with other field instruments onboard.

In addition, due to the similarities between Satellite-Based DOAS and airborne DOAS measurements techniques, airborne DOAS has also been used to validate Stellite-Based DOAS instruments. For instance, Tang et. al.[123] made use of airborne DOAS measurements made during the 2016 KORUS-AQ and 2017 SARP field campaigns in South Korea and Los Angeles, respectively, to both validate TROPOMI and OMI data products, as well as analyze the variability of the smaller airborne DOAS pixels within each TROPOMI pixel. This

study found that in polluted environments, the variability of airborne DOAS pixels within a satellite pixel increased, regardless of the study location. In addition, this high variability was a useful indicator of poor satellite validation, both from airborne DOAS instruments as well as other Ground-Based DOAS instruments in use at the time.

One other form of mobile DOAS measurement platforms are aquatic vessels. These vessels range from small single perfom craft to large container ships, usually used for shipping. Shipboard DOAS instruments are capable of performing measurements over deep ocean, in some of the most remote locations in the World[124][125]. These types of measurements are effective in measuring the stratospheric NO_2 column without being limited by the solar zenith angle, and can also help estimate global transport of trace gases. These types of studies are typically long term, taking place over multiple ocean crossing voyages over multiple years. On the other hand, shipboard DOAS can also provide additional perspectives on trace gas emissions from coastal and riverside cities[126][127]. These studies are typically performed in conjunction with ground and airborne field campaigns, and offer DOAS measurements from locations a stationary instrument could not be mounted at.

Chapter 5

Mobile Zenith DOAS Measurements of NO_2 and $HCHO$, and their Relationship to Collocated In-Situ measurements

5.1 Introduction

While NO_2 and $HCHO$ are well characterized on a global scale thanks to measurement coverage provided by Satellite-Based DOAS instruments, the low spatial resolution of the instruments prevents them from locating major sources influencing measurements, especially in heterogeneous environments such as cities. In addition, this lack of resolution can also mask other underlying issues in this area impacting the formation of other trace gases, such as ozone which is typically formed in the troposphere through interactions between NO_x and VOC's. This can lead to difficulties in pinpointing the cause of many high ozone events, and, especially in the case of cities where ozone is consistently high, results in a lack of impaction policy containing Ozone formation. However, Through the use of Mobile DOAS, in-situ, and meteorological measurements, the conditions that give rise to these high ozone events can be studied in more detail, in order to better understand how to limit ozone formation within

major cities.

With this in mind, the goal of this analysis is to use the combination of measurements made onboard MAQL1, a mobile laboratory used during the Tracking Aerosol Convection Experiment-Air Quality 2021(TRACER-AQ1), in Houston Texas to determine the origin of high ozone events identified during the field campaign. To achieve this, (1) DOAS analysis is performed on ZSL-DOAS measurements made onboard MAQL1 to find VCDs of NO_2 and $HCHO$; (2) The DOAS VCDs are compared to their respective in-situ measurements to determine the column to surface ratio of each trace gas, which represents an estimation of the vertical distribution of trace gas, which is used to determine the impact of various sources on the VCDs; (3) the NO_2 and $HCHO$ columns are compared to each other to determine what combination of NO_2 and $HCHO$ and their interactions are giving rise to observed high ozone events and, through the column to surface ratio and meteorological measurements and modeling, the origin of the trace gas and likely origin of the high ozone event is identified.

In addition, the effect of the vertical distribution of trace gas is used to estimate the efficacy of satellite validation when using ZSL-DOAS measurements. This is done through comparisons between TROPOMI satellite measurements and the ZSL-DOAS measurements made onboard MAQL1. The column to surface ratio is used to screen the ZSL-DOAS data and find the optimal column to surface ratio where both instruments agree with each other.

5.2 TRACER-AQ1 Overview

The Houston-Galveston-Brazoria area, encompassing metropolitan Houston as well as the cities of Brazoria to the Southwest and Galveston to the Southeast, is one of the most polluted regions in the United States, having been classified as a "Severe Non-attainment"[128] area for Ozone, indicating consistant days throughout each year where the average ozone

concentrations in the region were over 70ppb. With the expected attainment date in Fall 2027 quickly approaching, both local and Texas state officials have taken great lengths to further understand the complex factors that give rise to the high ozone events (>80ppb) that regularly occur in the city. One such method is the organization of the TRACER field campaign. Funded by the department of Energy, this field campaign focused on the meteorological factors that could be contributing to Houston's Ozone non-attainment. Due to Houston's proximity to Galveston Bay and the Gulf of Mexico, the city's wind patterns regularly shift between sea, bay, and land breezes, which could potentially combine transport trace gas around the city, causing different gases to mix and produce Ozone.

In order to augment these efforts, NASA also planned a second field campaign, TRACER-AQ, which aimed to focus on the trace gas emissions around Houston that could give rise to these high Ozone events. With additional knowledge on trace gas emissions and transport behaviors within the non-attainment area, both field campaigns could arive at a more comprehensive understanding of Houston's ozone problem.

Prior to the TRACER-AQ1 field campaign, multiple field campaigns have taken place in the same area. The Texas Air Quality Study 1[129] and 2[130][131] (TEXAQ 1 and 2) were two of the first field campaings looking to tackle the high ozone events in Houston, back in 2004 and 2006, respectively. The Study of Houston Atmospheric Radical Precursors (SHARP) [132], was another field campaign held in 2009. This field campaign built off the legacy of both TEXAQ, focusing more on the VOC precursors that give rise to ozone formation. All three of these field campaigns made use of both in-situ as well as remote sensing instruments on a myriad of measurement platforms in order to characterize the air quality of Houston with time scales ranging from a few months to a few years. Using these three field campaigns as models, the TRACER-AQ field campaign was formulated to find the trace gas contributions to ozone formation in Houston.

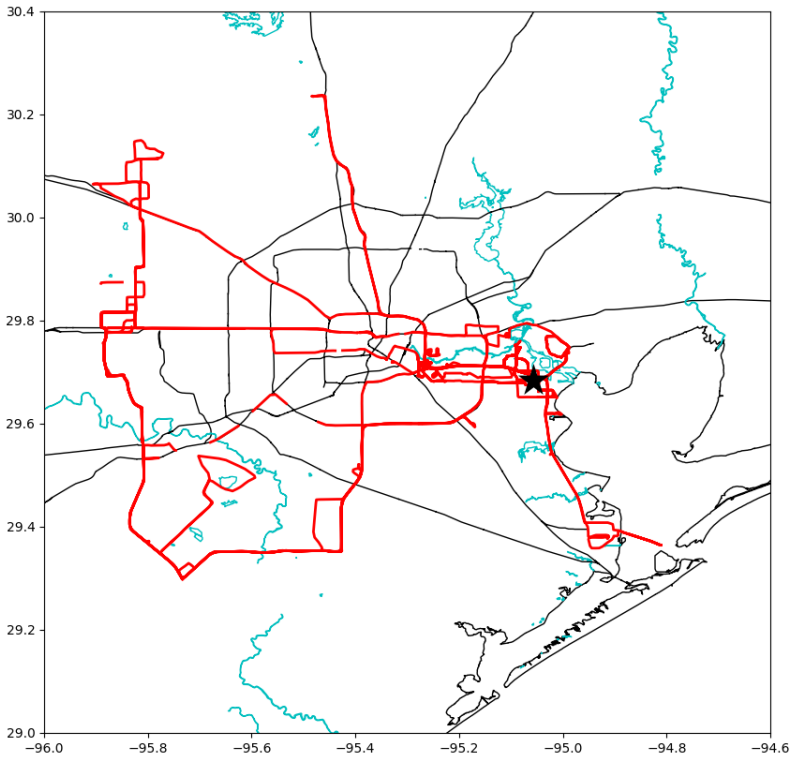


Figure 5.1: Map depicting the greater Houston Area with major roads and coastlines outlined in black, major waterways in cyan. Each path the mobile DOAS vehicle traveled during the campaign is outlined in red. The star represents la Porte airport, where the instruments remained stationary when not driving

While both field campaigns operated in tandem for most of 2021, TRACER-AQ had designated September as a period dedicated to more intensive measurements. This is due to a bimodal peak of Ozone exceedance around this time. Due to the larger number of expected ozone exceedance days measurements made during this period were expected to yield more interesting results. While the typical operations of TRACER-AQ included researchers from the EPA, the Texas Commission on Environmental Quality (TCEQ), and the University of Houston, the intensive operations were expanded to include numerous other researchers

from Virginia Tech, Baylor University, and St Edwards University, each bringing their unique trace gas measuring techniques to enhance the September measurements.

At the core of both typical and intensive measurement periods were the use of a local network of both in-situ and Pandora instruments, providing information on trace gas amounts throughout the region. During the intensive operations however, MAQL1, a vehicular mobile laboratory operated by the University of Houston, made multiple trips throughout the area, as can be seen in Figure 5.1. MAQL1 carried one of the Pandora instruments installed by Virginia tech, mounted in the Zenith direction to measure VCDs of NO_2 and $HCHO$, as well as numerous other in-situ and meteorological instruments in order to understand conditions on the ground. In addition, a DC-8 Gulfstream aircraft make multiple flights over Houston, where the Geostationary Coastal and Air Pollution Events (GEO-CAPE) Airborne Spectrometer (GCAS) ultraviolet-visible-near infrared (UV-VIS-NIR) airborne spectrometer, an airborne DOAS instrument, operated. In addition, multiple in-situ instruments were operated onboard small research watercraft in Galveston Bay and the Houston Ship Channel. Finally, multiple ozonesondes were launched at regular intervals on most days in order to measure vertical profiles of trace gases, wind, and air conditions.

5.3 Methodology

5.3.1 DOAS Analysis

DOAS fitting of NO_2 and $HCHO$ dSCDs was performed using the QDOAS software, version 3.4.5. The fitting procedure was separated into 3 fitting windows, which closely follow the protocols established in Kreher et. al.[133]: NO_2 was fitted in the visible spectrum between 425 and 490nm, and in the UV spectrum between 338 and 370nm. Formaldehyde, on the

other hand, was only fitted in a UV window, between 336.5 and 359. The absorption cross-sections for all of these windows are summarized in Table 6.1. Please note that some of these cross-sections are used for multiple fitting windows.

Table 5.1: DOAS fitting parameters used to retrieve $HCHO$, NO_2, and O_2O_2 ΔSCD from Pandora zenith sky measurements. The fitting windows are ordered starting with $HCHO$, NO_2 Ultraviolet, then NO_2 Visible retrievals.

Fitting Windows: HCHO (336.5-359 nm), NO_2 (UV: 338-370 nm), NO_2 (VIS: 425-490 nm)
Polynomial Order: 5
Offset and wavelength shift polynomial order: 1

Trace Gas	Temperature (K)	Source	Fitting Windows
NO_2	294, 220	Vandaele et. al.[134]	HCHO, NO_2 (UV, VIS)
H_2O	290	Rothman et. al.[135]	NO_2 (VIS)
O_3	243, 223	Serdyuchenko et. al.[136]	HCHO, NO_2 (UV, VIS)
O_2O_2	293	Thalman et. al.[137]	HCHO, NO_2 (UV, VIS)
$HCHO$	297	Meller and Moorgat[138]	HCHO, NO_2 (UV)
BrO	224	Fleischmann et. al[139]	HCHO
Ring	270	Chance and Spurr[49]	HCHO, NO_2 (UV, VIS)

In order to correct for the difference between laboratory and field cross-sections of NO_2 and O_3, I_o correction was performed on all four cross-sections, with an estimated SCD of 10^{20} for O_3, and 10^{17} for NO_2. This issue leads to the incomplete removal of the Frounhofer structures from the solar reference spectrum[140], and can be corrected by correcting the solar reference spectrum with a simulated absorption spectrum generated from a given slant column density and absorption cross-sections. A Ring pseudo cross-section was generated using the Ring tool provided with the QDOAS software. A fifth order polynomial was used to estimate the wideband absorption effects, and a nonlinear shift of the measured spectrum was performed to align it with the other inputs.

The reference measurement was generated from the mean of measurements made around solar noon on September 21. On this day, the instrument was stationed on the Texas City Dike, which can be seen as the furthest Southeast point that MAQL1 traveled in Figure 5.1.

This location is isolated and upwind from the industrial sources present in Texas city on the mainland, which means that the only source that could be present in the measurement are individual commercial ships as they pass by. While the reference spectrum was measured in a relatively remote and trace gas free location, there still remains a residual amount of trace gas in this spectrum that must be removed. The NO_2 reference column was estimated using Minimum Langely Extrapolation, an example of which is shown in Figure 5.2. The reference column estimated for the Visible NO_2 retrievals was $6.17 \times 10^{15} \frac{Molecules}{cm^2}$ the UV NO_2 retrievals was found to be $4.28 \times 10^{15} \frac{Molecules}{cm^2}$, and the $HCHO$ retrieval was found to be $4.51 \times 10^{15} \frac{Molecules}{cm^2}$.

The stratospheric component of the NO_2 column was estimated through the climatological model described by Brohede et. al.[14], which estimates stratospheric NO_2 columns based on latitude, time of day, and season. This model is provided with DOAS analysis performed by BlickP, the Pandora data processing software.

Air Mass Factors were generated through radiative transfer simulations, which are further described in Chapter 7. The resulting box AMFs are used to generate AMFs of NO_2 and $HCHO$ using an exponential profile with an effective height of 250m and a peak concentration matching the mean concentration measured by in-situ instruments onboard MAQL1, while a box profile with a 2Km height and concentration matching the mean in-situ measurement measured by instruments onboard MAQ1 was used for HCHO. Air Mass Factors were simulated once an hour from sunrise to sunset, generating around 12 AMFs for each day. These AMFs were then linearly interpolated to match the time of each dSCD, creating a matching AMF dataset for the dSCDs.

In order to ensure high data quality, the uncertainty of each VCD was screened before use. The error of each VCD is further discussed in Section 5.7. While Pandora measurements with an uncertainty greater than 30% of the final VCD are typically considered as poor quality

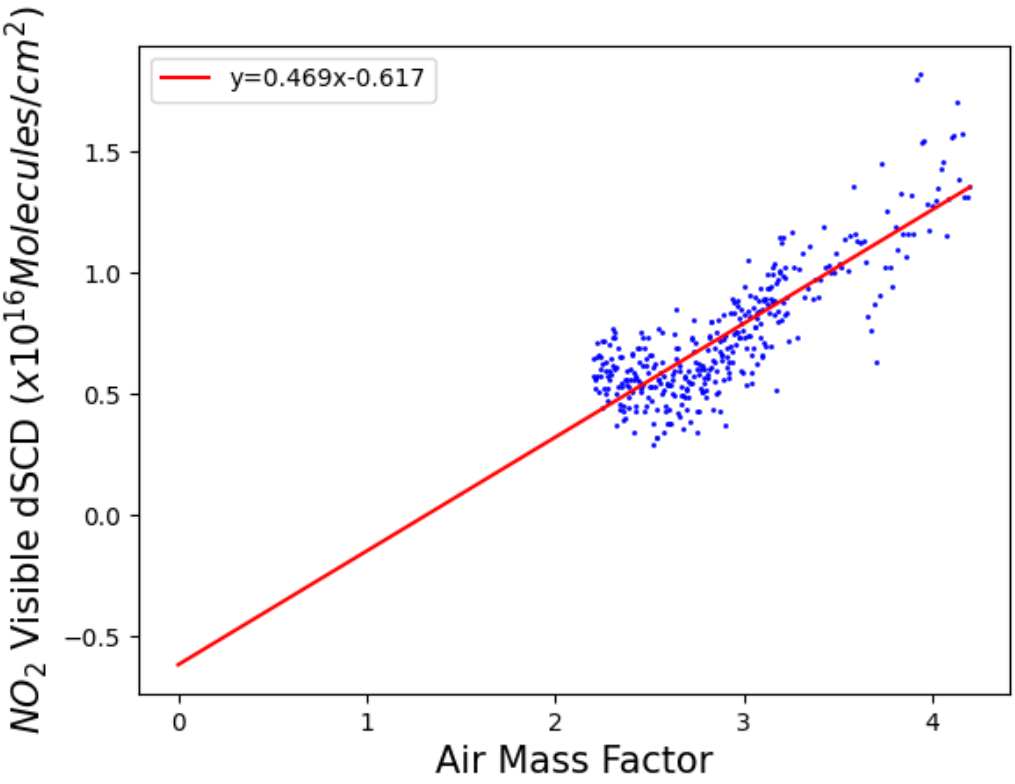


Figure 5.2: NO_2 differential slant column densities retrieved at 460 nm from measurements on the reference day, September 21, plotted as a function of the NO_2 AMF's retrieved at 460 nm from September 21. Each red dot represents the minimum ΔSCD in each bin which is used for a linear fit (red line) which is used for Minimum Langley Extrapolation. The reference column of NO_2 was estimated to be $6.17 \times 10^{15} \frac{Molecules}{cm^2}$

data, the additional uncertainties that arise due to the behavior of mobile measurements requires a higher threshold. Instead, measurements with uncertainty greater than 50% are considered as poor data quality and removed from the VCD datasets.

In addition, Zenith DOAS measurements are very sensitive to the presence of clouds, which can increase the effective path length of the measured photons far beyond what is being estimated by radiative transfer simulations. This results in increased dSCDs when measurements are under the influence of clouds, which without proper screening can be misinterpreted as a plume or other elevated concentration of trace gas. Take for instance the O_2O_2 dSCDs

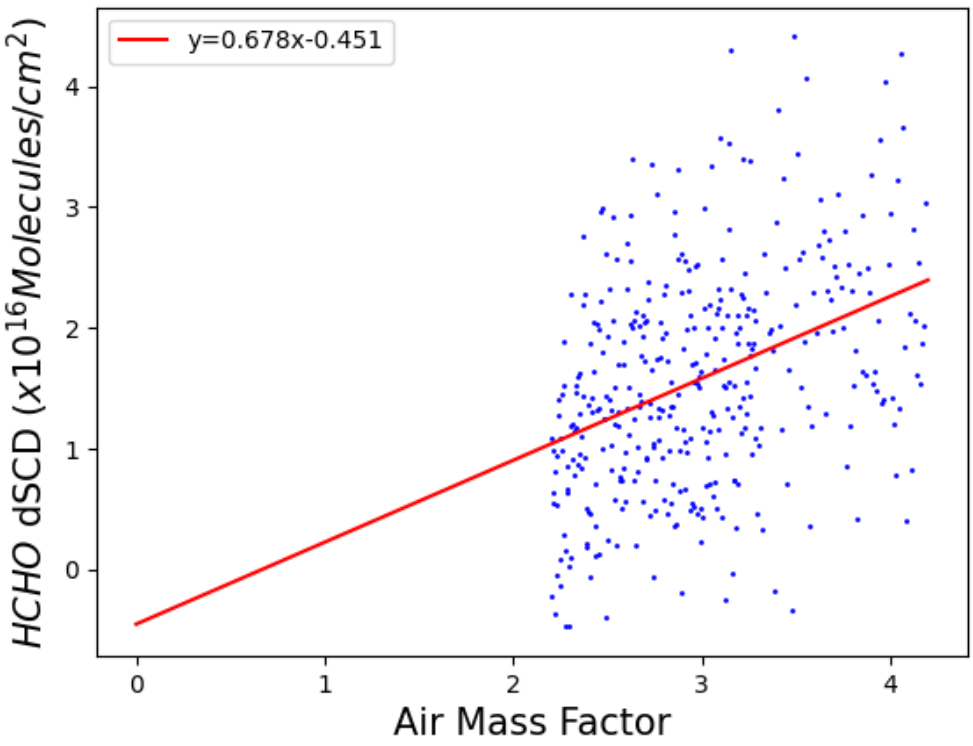


Figure 5.3: $HCHO$ differential slant column densities retrieved at 460 nm from measurements on the reference day, September 22, plotted as a function of the NO_2 AMF's retrieved at 340 nm from September 22. Each red dot represents the minimum ΔSCD in each bin which is used for a linear fit (red line) which is used for Minimum Langley Extrapolation. The reference column of $HCHO$ was estimated to be $4.51 \times 10^{15} \frac{Molecules}{cm^2}$.

measured during TRACER-AQ1, as seen in Figure 5.4: on September 1, 2,3, and 28, there are numerous points on the time series when the dSCD of O_2O_2 increases before dropping back down to previous levels. O_2O_2, also known as the Oxygen Collisional Complex, is a trace gas that is formed entirely through physical processes: the collision of two Oxygen atoms. As such, the physical reaction is proportional to the vertical profile of Oxygen, and therefore the vertical profile of air. The air profile is a very consistant profile, and is only influenced by changes in air temperature, pressure, and relative humidity[141], and as such the O_2O_2 dSCD should only shift slightly throughout the day as these quanitities change.

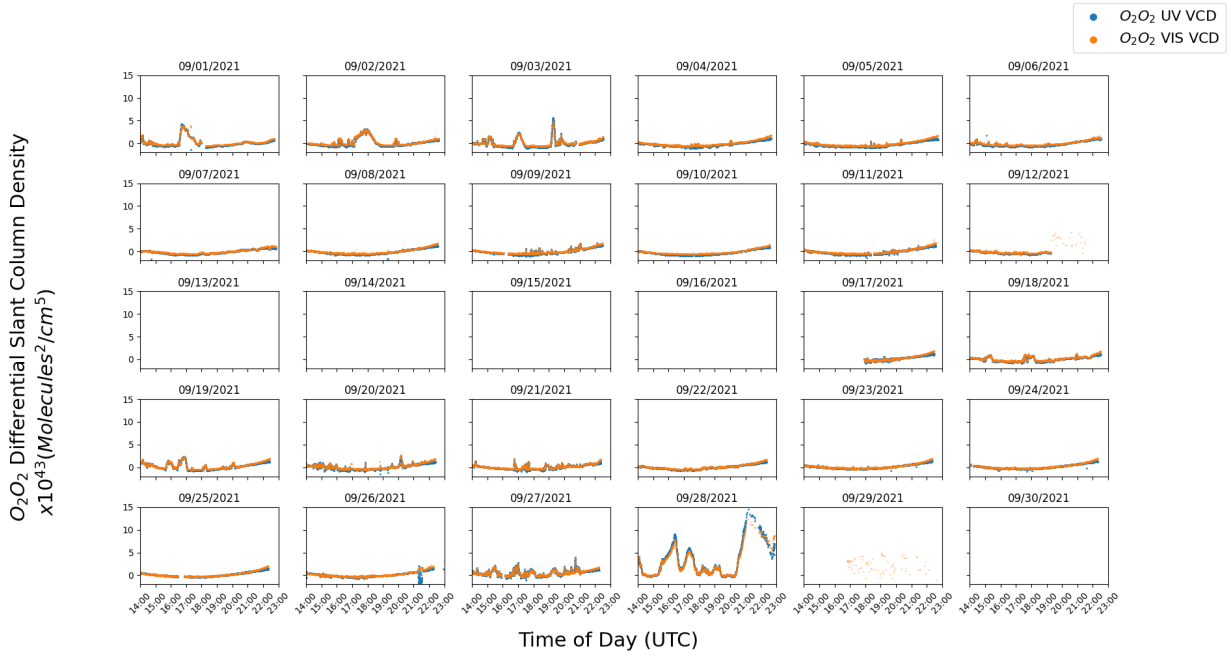


Figure 5.4: Time series of daily O_2O_2 differential slant column densities during the TRACER-AQ field campaign.

However, the light path also influences the dSCD, which for Zenith measurements is largely dependant on the solar zenith angle. Under clear sky conditions, this creates a slight U shape, as sunrise and sunset approach, light travels more and more through the stratosphere and parts of the troposphere before the final scattering event, causing the dSCD to increase as well. However, the path length can also be increased by the presence of clouds, which can cause multiple scattering events as light travels inside cloud layers, creating enhanced dSCDs much larger than can be seen through most of the day.

In order to correct for cloudy conditions, the data was screened for clouds using a color index comparing the radiance measured at 320nm to 440nm and the temporal smoothness of the color index to filter small, scattered and optically thin clouds, and the differential AMF of O_2O_2[142] to filter optically thick clouds. To screen for clouds, a clear sky reference was developed to compare to. This reference was developed from measurements made between

September 22-26, a period of five days with no significant deviations of the O_2O_2 dSCDs. The clear sky reference was converted from individual date-times to each measurement's solar zenith angles and grouped accordingly. The clear sky reference was then interpolated to the solar zenith angle of each measurement, which gives the expected clear sky reference at each measurement's solar position. Color index values, after normalization to the reference, less that 0.5 with a temporal smoothness indicator, normalized to each measurement period, less than $1 \times 10^{-5} s^{-1}$, were flagged as optically thin or scattered clouds and removed from the dataset. In addition, measurements where the dAMF of O_2O_2, normalized to the clear sky reference, was less than 0.8 were flagged as optically thick clouds and removed from the dataset.

5.3.2 Ancillary Instrumentation

In addition to the Pandora instrument onboard the vehicle, there were numerous other meteorological and in-situ instruments dedicated to measuring air in the immediate vicinity of the vehicle. The two in-situ instruments of primary interest for this study are the NO_x and $HCHO$ measuring instruments, both of which were operated by the University of Houston. Concentrations of $HCHO$ were obtained onboard the mobile lab from an Aero-laser GmbH AL4021 $HCHO$ Analyzer. This instrument provides concentrations averaged over 10 second measuring periods through the liquid-phase reaction and fluorescence ligh technique. On the other hand, measurements of NO_2 were made using a Thermo Scientific 42i-TL NO_X analyzer, which also provided a 10 second averaged product of NO_2 concentrations retrieved through the chemiluminescence technique.

In addition to the in-situ instruments, the vehicle carried a GPS and meteorological instruments providing latitude and longitude, as well as local air pressure, temperature, relative

humidity, wind speed and wind direction. In addition, an onboard LIDAR instrument provided profile of atmospheric backscatter, which were used to estimate the height of the Planetary Boundary Layer.

5.3.3 Column to Surface Ratio

Due to the proximity of both in-situ and Pandora measurements, it can be expected that air measured by in-situ instruments is also being partly measured by the Pandora. There have already been numerous studies focused on the relationship between the VCD from DOAS instruments and trace gas concentrations measured by in-situ instruments. In particular, attempts have been made to identify the relationship between VCD and surface concentration so that one can estimate the other[143][144]. In addition, Pandora instruments have been previously compared to in-situ measurements[145], however the purpose was to compare estimations of near-surface concentrations derived from Pandora measurements to measured in-situ concentrations. Many of these studies have tried to link in-situ surface measurements with Satellite-Based DOAS measurements, in order to take advantage of large in-situ measurement networks for the purpose of satellite validation[76][146][147]. These studies rely on an assumed vertical profile that is scaled to match the Satellite-Based DOAS VCD to estimate the concentration at the surface, Other studies, however, looked instead to the impact of meteorology in vertical mixing[83][148], using local weather patterns to identify vertical mixing regimes.

However, there is a clear relationship between VCD and surface concentration in previous studies. This relationship is due to the fact that whatever vertical profile Pandora instruments measure includes the concentration at the surface, even in the instrument is not sensitive to the surface concentration; this relationship, therefore can be described by the

column to surface ratio, which is simply the ratio between VCD and surface concentration for each measurement. Because the column to surface ratio is the ratio between a VCD and concentration, the column to surface ratio results in an altitude; this is due to VCDs representing a path averaged concentration, given in $\frac{Molecules}{cm^2}$ when dividing by an absolute concentration, with units $\frac{Molecules}{cm^3}$, the resulting units are the averaging path. In addition, the proximity to trace gas sources can significantly impact the relationship between VCD and surface concentration[149]. This means that the column to surface ratio can be used to estimate the location of certain trace gas sources depending on the behavior of the column to surface ratio.

Take for instance vehicular traffic, which should be the typical source affecting both in-situ and Pandora measurements on a mobile platform. Because the measured sources are emitting at the surface, the column to surface ratio should be at an altitude close to the surface. On the other hand, an elevated profile, such as a plume where the peak concentration is well above the surface, would result in a column to surface ratio well above the surface. Finally, a well mixed profile, where there are no nearby sources, should result in moderate column to surface ratio altitude, representing the well mixed nature of the vertical profile measured.

The behavior of the column to surface ratio can be further constrained through measurements of the boundary layer height. The Boundary Layer is the highest point of the surface layer, a sublayer of the troposphere where due to temperature inhomogeneity and surface roughness, trace gas vertical transport is not adiabatic, and is instead transported through local turbulence. As such, short lived trace gases like NO_2 and $HCHO$ are not expected to rise far above this point. As such the measurements of the boundary layer height can be used as an assumed maximum real altitude for these trace gases. Any column to surface ratio significantly below this altitude can be assumed to be indicating surface sources are influencing measurements, while column to surface ratios well above this altitude indicate

elevated profiles, where the peak concentrations are not located at the surface. Finally, in the case where column to surface ratios are approximately the height of the boundary layer, then the VCDs that are measured are well-mixed, where the column from the surface to the top of the surface layer has a single, consistent concentration.

5.4 DOAS results

The mobile Pandora was in continuous operation during daylight hours from September 1 to midday September 12, then from midday September 17 until September 28. Due to the low data quality of September 26, 27, 28, these days were omitted from the days shown in Figures 5.5 and 5.6. During September 12-17, a hurricane prevented operations, and as such no data was able to be collected during these times.

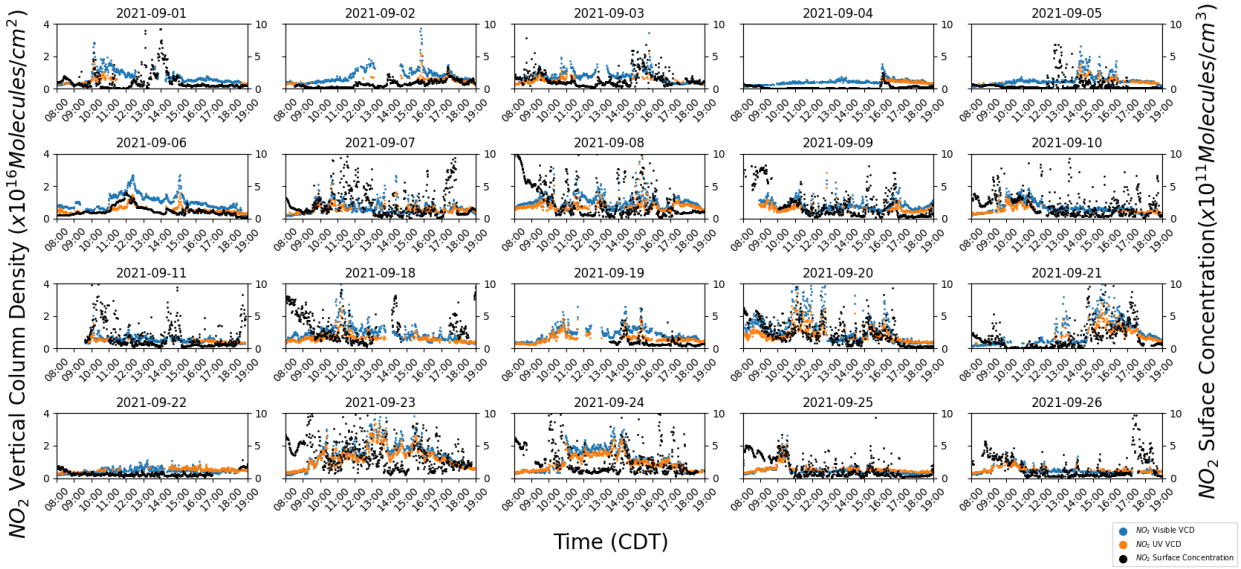


Figure 5.5: Time series scatter plots of the NO_2 Visible (blue) and UV(orange) retrieved VCDs, and the in-situ NO_2 surface concentration, in black. All data shown is presented as 1 minute averages.

As shown in Figure 5.5, the NO_2 VCD retrieved from the Visible (blue scatter points) and

UV (orange scatter points) remained between $0.5 - 2 \times 10^{16} \frac{molecules}{cm^2}$ for most of the month, with peaks in the NO_2 reaching $4 \times 10^{16} \frac{molecules}{cm^2}$. The NO_2 VCDs show good agreement with prior DOAS studies performed in Houston[111][150] as well as Mexico City[151] which has been shown to have similar trace gas behaviors as Houston. This puts Houston as a more polluted environment than the typical European city[112][108] but less than those in China[107][152]. Both datasets show good agreement, and as such the behavior of one dataset should be consistent with the other. Therefore, further analysis of NO_2 VCDs is performed only on the Visible dataset.

On the 2nd, 4th, 6th, 17th, 18th, 19th, 22nd, and the 28th of September, the mobile lab remained parked at the La Porte Municipal Airport (29.6698N, -95.0595W), which is located in the Southeastern portion of Houston's Urban Core, and less than a Kilometer South of the Houston Ship Channel, where numerous industrial sites and ship logistical facilities are located, making the site optimal for measuring any local transport events that might arise from the channel. On the other days, the Pandora instrument operated as a Mobile DOAS instrument. This can be easily seen in the in-situ measurements in Figure 5.5, where on mobile days the surface concentration can vary non-continuously like on stationary days. This is due to the heterogeneity of vehicular emissions on roads leading to variations in the in-situ measurements.

Formaldehyde, on the other hand, is much more well mixed during the field campaign than NO_2 This is largely due to the production of $HCHO$, especially in Houston's urban core and surrounding industrial sites where the Pandora spent most of the month driving through, being reliant on secondary formation from other VOC's emitted by Houston's oil refining and plastic production industries. The presence of secondary $HCHO$ formation also gives the $HCHO$ VCDs a inverse relationship to the solar zenith angle. radiative forcing reaches its maximum at solar noon, increasing the photolysis rate of VOCs into $HCHO$ creating

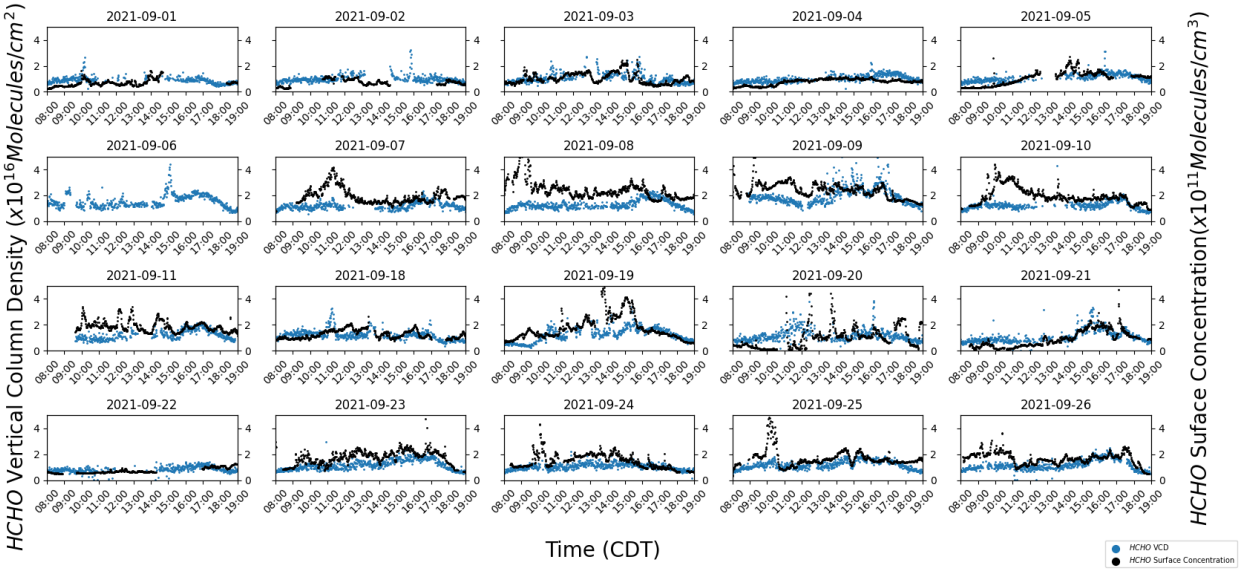


Figure 5.6: Time series scatter plots of the $HCHO$ retrieved VCDs, in blue, and the in-situ $HCHO$ surface concentration, in black. All data shown is presented as 1 minute averages.

the inverse U shape of the $HCHO$ VCDs in the absence of large sources. Near sources of both VOCs and $HCHO$, the $HCHO$ VCDs peak to $5 \times 10^{16} \frac{molecules}{cm^2}$ with typical values ranging between $0.5 - 3 \times 10^{16} \frac{molecules}{cm^2}$. In addition, some of the peaks in the $HCHO$ VCD are not seen by the surface measurements, and vice versa. For example, on September 9, the $HCHO$ VCD from 13:00 to 15:00 CST remains elevated at $4 \times 10^{16} \frac{molecules}{cm^2}$, however during this period there was no increase in the $HCHO$ surface concentration; in fact, the surface concentration showed a gradual decreasing trend over this period. On the other hand, on September 19, a spike in both quantities was recorded around 12:30, however at 14:00 the in-situ $HCHO$ concentration increased from $2-4 \times 10^{11} \frac{molecules}{cm^3}$ while much smaller increase in the $HCHO$ VCD was recorded, from $1.8-2 \times 10^{16} \frac{molecules}{cm^2}$. This behavior suggests that there were multiple plumes, both elevated above the surface as well as very close to the surface, that the instruments passed through during the field campaign. While passing through these plumes, the sensitivity of each instrument prevented one instrument from measuring what the other observed.

5.5 Case Studies

Many of the high ozone events that occurred during the TRACER-AQ1 field campaign coincide with many interesting events occurring between the NO_2 and $HCHO$ VCDs and surface concentrations. These behaviors can be used to identify the particular causes of these events, which can be traced back to probable emissions locations.

Firstly, the behavior of the NO_2 and $HCHO$ VCDs are compared to the local ozone production, measured through an in-situ ozone instrument also onboard the mobile platform. The $NO_2/HCHO$ ratio can give further insight to the behavior of both trace gases during the observed high ozone events. Based on this behavior, analysis of the column to surface ratio can help to better understand what factors, for instance a plume traveling through the measuring area, could have caused the high ozone event observed. Finally, simulated air mass back-trajectories can trace the probable path of the air mass causing the high ozone event, effectively locating any potential emissions sources along the path that could have directly contributed to the high ozone event observed.

5.5.1 September 6th

On September 6th, the Pandora instrument remained stationary at the La Porte Regional Airport throughout the day. Starting at 14:20 CST, the local Ozone surface concentration rose above $20 \times 10^{11} \frac{molecules}{cm^3}$. As can be seen from Figure 5.7, this event lasted from 14:30 to 17:00 CST, roughly two and a half hours. By comparing the behavior of the NO_2 VCD and the $HCHO$ VCD, the $HCHO/NO_2$ ratio indicates that the ozone production regime dropped from being NO_x limited to the transition regime twice at the beginning of this high ozone event: once at 14:20 and again at 14:50. These two times are the points of interest to determine the cause of this high Ozone event. These two dips are either due to a drop in

local $HCHO$ production or transport or due to an increase in NO_2.

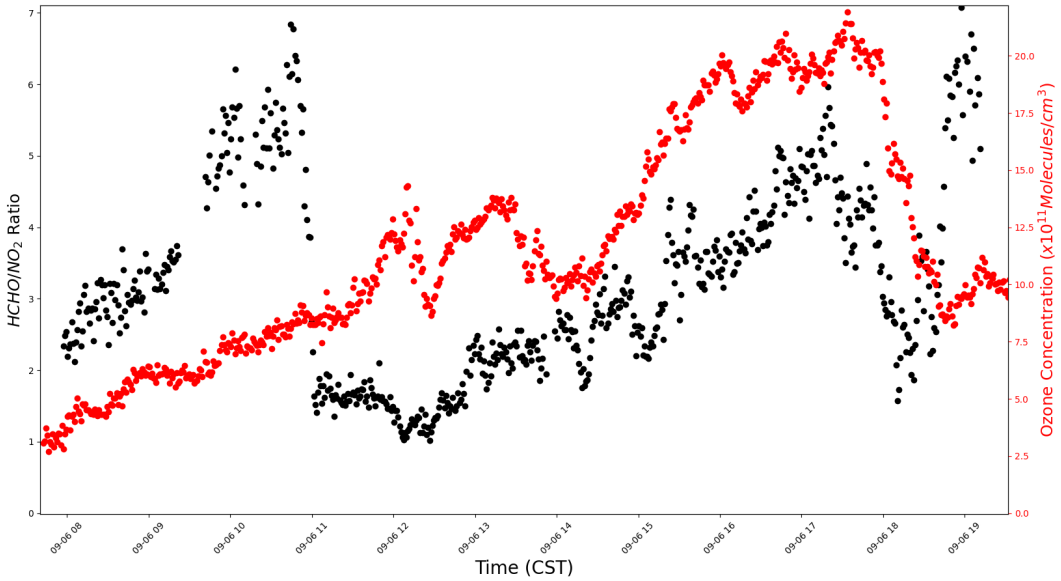


Figure 5.7: A scatter plot depicting the $HCHO/NO_2$ ratio for the VCDs retrieved on September 6, in black and the in-situ ozone concentration observed onboard MAQL1, in red. All data shown is presented as 1 minute averages.

During most of September 6th, the $HCHO$ VCD exhibited the typical inverse U shape that is typical on low $HCHO$ emissions days. However, at 14:50 CST, ther $HCHO$ VCD increases from $3-6\times10^{16}\,\frac{molecules}{cm^2}$. This time corresponds to the second dip in the $HCHO/NO_2$ ratio. However, the dips indicate that either $HCHO$ was removed or that more NO_x was added to the area. The fact that there was a spike in $HCHO$ at this time suggests that there was likely transport of both trace gases into the area, and that the relative increase in NO_2 was larger than $HCHO$. In addition, the in-situ $HCHO$ instrument was not operational on this day. As such, comparisons of the column to surface ratio for $HCHO$ are impossible, and any information on the vertical distribution of $HCHO$ must be estimated based on the behavior of NO_2.

Looking now at Figure 5.9, there are clear behaviors in both the surface concentrations and

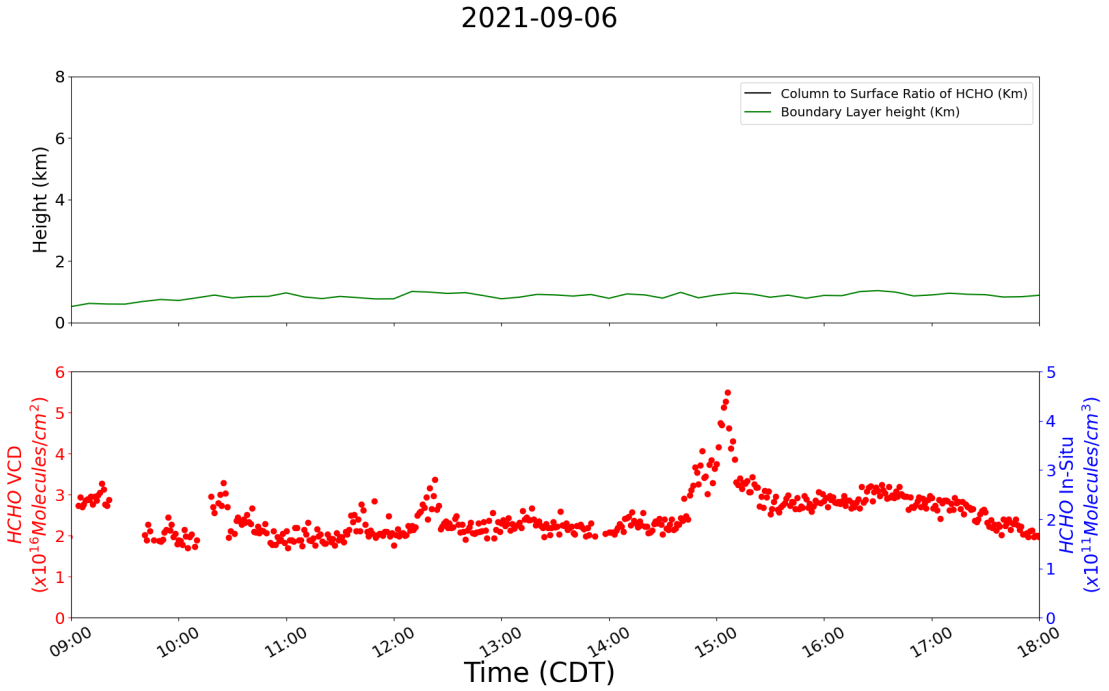


Figure 5.8: Top: The diurnal averaged Boundary Layer Height (green) on September 6. Bottom: The $HCHO$ Tropospheric Vertical Column Density (red) Aside from the boundary layer height, which is the diurnal variation averaged every 10 minutes, all data shown is presented as 1 minute averages.

VCDs that can help further understand the conditions that gave rise to the high Ozone event observed. Both the in-situ surface concentration and VCD show a sharp increase at 10:00 CST and at 11:00 CST, respectively. Both of these increases are likely tied to the same air mass, with first the surface being affected so that only the in-situ instrument recorded an increase. After the hour had passed, the high concentration of NO_2 was high enough in the atmosphere that now the Pandora instrument could measure, while at the same time the decrease in the NO_2 concentration suggests that the concentration became elevated, and wasn't directly emitted at the surface.

During this time, the column to surface ratio begins approximately at the estimated boundary layer height, suggesting that before this air mass was measured the NO_2 vertical distribution was well mixed. However, at the introduction of this air mass, the column to surface

ratio dropped well below the boundary layer threshold down to 200m, indicating the trace gas was beginning to be distributed much closer to the surface. Finally, as the NO_2 VCD began to increase while the surface concentration decreases, increasing the column to surface ratio to 3Km well above the estimated boundary layer height indicating the trace gas measured was elevated.

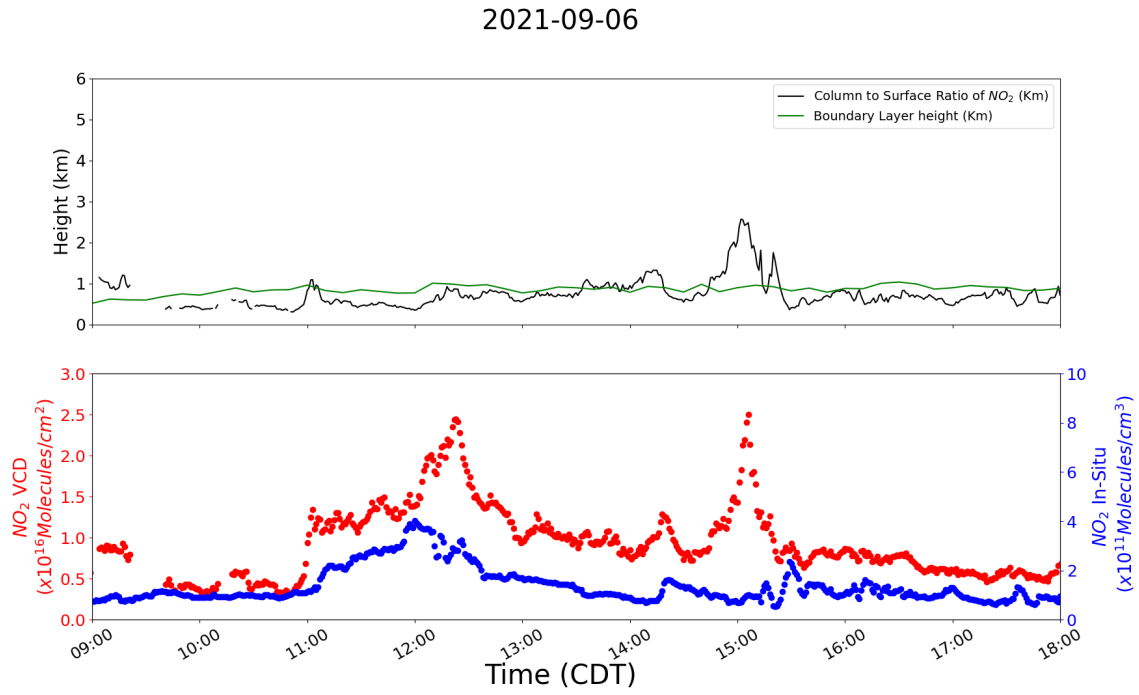


Figure 5.9: Top: The column to surface ratio of NO_2 (black) and corresponding diurnal averaged Boundary Layer Height (green) on September 6. Bottom: The NO_2 Tropospheric Vertical Column Density (red) and the in-situ surface concentration (blue). Aside from the boundary layer height, which is the diurnal variation averaged every 10 minutes, all data shown is presented as 1 minute averages.

During the time period corresponding to the high ozone event, the column to surface ratio shows two large spikes at both 14:20 and again at 14:50. the first, while only a small increase in the NO_2 VCD from $1.0 - 1.5 \times 10^{16} \frac{molecules}{cm^2}$ was recorded, the surface concentration dips from $1 - 0.5 \times 10^{11} \frac{molecules}{cm^3}$ during this first event; this causes the column to surface ratio to increase from 1.0Km to 1.5Km, indicating the likely presence of a small and discrete

air mass passing overhead with a large quantity of NO_2 present. This behavior describes a plume, where the trace gas remains contained within a relatively confined volume as it transports. In addition, at 14:50 the NO_2 VCD spikes from $1.0 - 2.7 \times 10^{16} \frac{molecules}{cm^2}$ while the NO_2 surface concentration does not significantly change. This causes the column to surface ratio to increase from 1Km, which corresponds to a well mixed distribution, to 2.7Km, once again indicating an elevated distribution. Both of these events suggest that both NO_2 and $HCHO$ were transported to the airport from some other source, with both plumes likely originating from a more distant source.

In order to determine the origin of the observed plumes, the Hybrid Single-Particle Lagrangian Integrated Trajectory (HYSPLIT)[4] was used to determine the direction from which air masses over the La Porte airport originated from earlier in the day. Figure 5.10, as well as Figures A.4 and A.5 show four back-trajectories from 17:00 CST (red) to 14:00 CST (cyan) with end altitudes of 500m, 250m, and 750m, respectively. At all three simulated altitudes, air masses during the high ozone event the transported largely from the North and Northeast directions. In particular, the area directly North of the small inlet that all four trajectories cross corresponds to one of the largest petrochemical refining complexes in the city. In addition, the 500m and 750m air masses also saw upward transport, which indicate that that the upper portion of the surface layer experienced vertical mixing, where lower air masses were elevated during transport. This is the most likely cause of the increases in both NO_2 and $HCHO$ observed: large amounts of VOCs and NO_X are produced at refineries, and as such after spending more than an hour transporting South to the airport, a lot of both trace gas groups had both reacted to form NO_2, $HCHO$, which continued to mix at the airport to cause the high ozone event observed on this day.

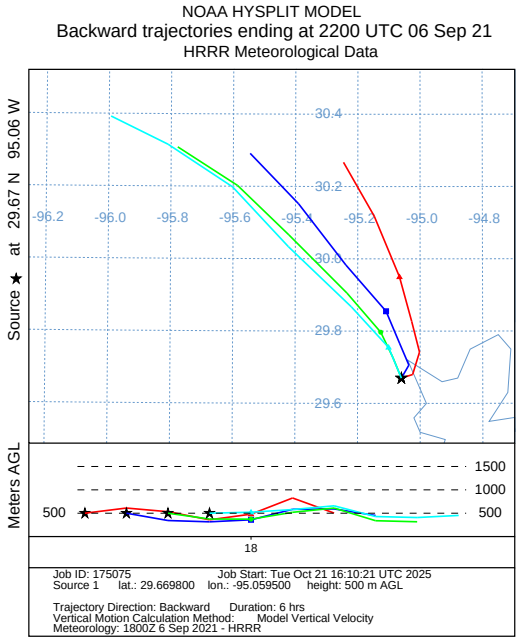


Figure 5.10: HYSPLIT [4] modeled 3 hour back-trajectory showing the path air masses at 17:00 (red), 16:00 (blue), 15:00 (green), and 14:00 (cyan) took to arrive at the la Porte Airport (starred) with an end altitude of 500m.

5.5.2 September 9th

On September 9, the Pandora instrument was driven around the suburban and rural areas to the direct South of Houston's urban core, as can be seen in Figure 5.11. This travel route differs from most of the routes traveled during TRACER-AQ1 in that the instrument did not travel close to any major industrial centers, and instead had the opportunity to measure longer range transport away from both the urban core and industrial sites. In addition, between 11:30 to 15:30, an extended high Ozone event occurred, with surface

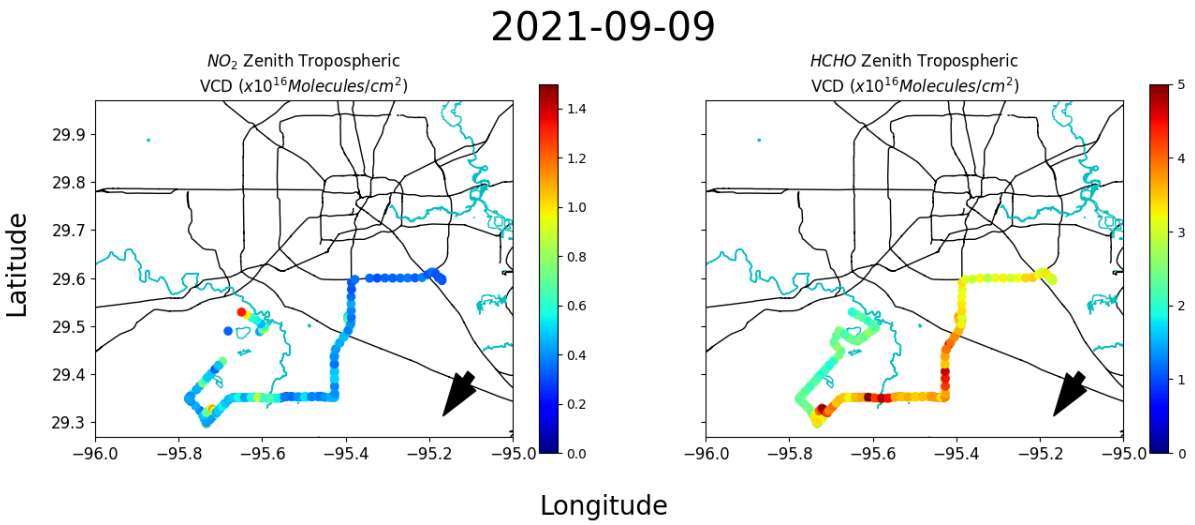


Figure 5.11: The driving route of MAQL1 on September 9 during the locally observed high Ozone event. In addition, the maps show the Zenith NO_2(a) and $HCHO$(b) VCDs retrieved during this time frame. The arrows in the bottom right of each plot shows the average wind direction collected from 5 airports located in the vicinity of the driving path. The average wind speed during this period was 3.56 m/s. All data shown is presented as 1 minute averages.

Ozone concentrations remaining consistently around $20 \times 10^{11} \frac{molecules}{cm^3}$.

Due to the more rural area where this high Ozone event was observed, the $HCHO/NO_2$ ratio during this period was much higher than on September 6, with the mean ratio increasing from 1 to 5 as the instrument traveled out of the urban core. This would correspond to the Ozone production regime shifting from a transition regime, where the amount of NO_x and VOCs present should maximize ozone production, to a NO_x limited regime, where there is not enough NO_x present to react with VOCs to generate Ozone. However, at 12:10CST and again at 13:20CST, the $HCHO/NO_2$ ratio dips below 2, which indicates that a large amount of NO_2 was likely present in the measuring area at this time.

Looking at Figure 5.13, the increase in the $HCHO/NO_2$ ratio likely corresponds with the increase in $HCHO$ from 10:00 to 13:00 CST, where the $HCHO$ VCD increases from $1 - 5 \times 10^{16} \frac{molecules}{cm^2}$ gradually over the span of 3 hours. This time period also corresponds with

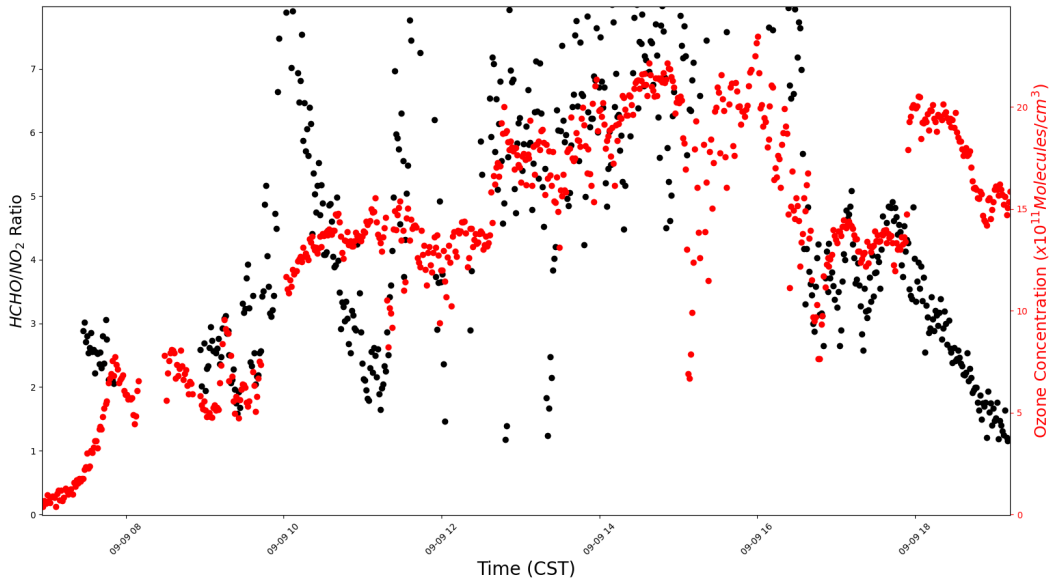


Figure 5.12: A scatter plot depicting the $HCHO/NO_2$ ratio for the VCDs retrieved on September 9. Each point is color coded to the Ozone surface concentration. All data shown is presented as 1 minute averages.

the instruments moving out of the urban core and into suburban and rural neighborhoods surrounding Houston. Therefore, this increase and subsequent consistency of high $HCHO$ VCDs is the result of secondary formation of $HCHO$ in these areas, most likely from natural VOCs, such as isoprene.

In addition, during this high ozone event, as well as directly preceding a smaller event from 17:00 to 17:40 CST, there are multiple spikes in the $HCHO$ VCD between $5-6\times 10^{16}\frac{molecules}{cm^2}$that are not present in the in-situ surface concentration. However, during the entire day the surface concentration remains elevated between $1-3\times 10^{11}\frac{molecules}{cm^3}$. This indicates that while the local $HCHO$ is well mixed and measurable by in-situ instruments, there are also elevated concentrations of $HCHO$ being transported into the area. As a result, the column to surface ratio for $HCHO$ remained well mixed for most of the morning, however during the high ozone event and after the column to surface ratio was elevated,

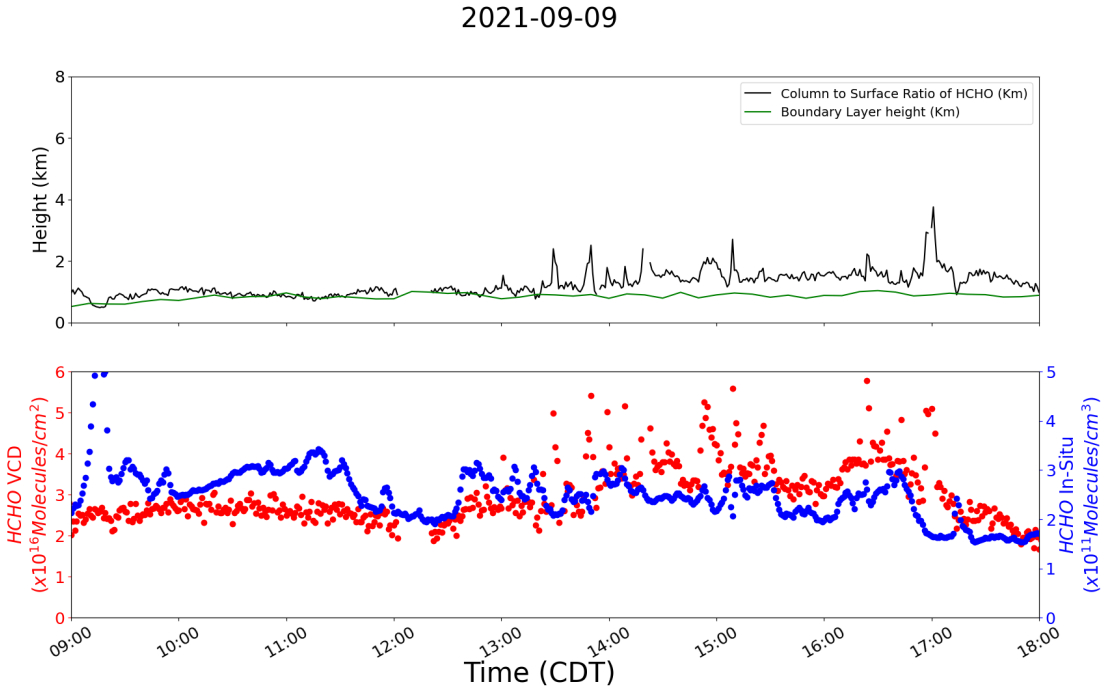


Figure 5.13: Top: The column to surface ratio of $HCHO$ (black) and corresponding diurnal averaged Boundary Layer Height (green) on September 9. Bottom: The $HCHO$ Tropospheric Vertical Column Density (red) and the in-situ surface concentration (blue). Aside from the boundary layer height, which is the diurnal variation averaged every 10 minutes, all data shown is presented as 1 minute averages.

suggesting most of the observed $HCHO$ was not interacting at the surface.

NO_2, on the other hand, did not see a large shift between 10:00 and 13:00 CST. Instead, many of the peaks seen in Figure 5.13 are also seen in Figure 5.14 such as at 13:30 and 15:00, which suggest that many of these elevated $HCHO$ concentrations were plumes that carried both VOCs and NO_x. In addition, due to the influence of on road emissions, the NO_2 in-situ concentrations for most of the day show high variation, at times oscilating between $0.5 - 8 \times 10^{11} \frac{molecules}{cm^3}$ depending on wether or not the in-situ instrument collected air from direct vehicular emissions or not. In spite of this, at many of the peaks in both $HCHO$ and NO_2 the NO_2 surface concentration maintained a low and consistent value, which in turn resulted in column to surface ratios well above the boundary layer in an elevated regime.

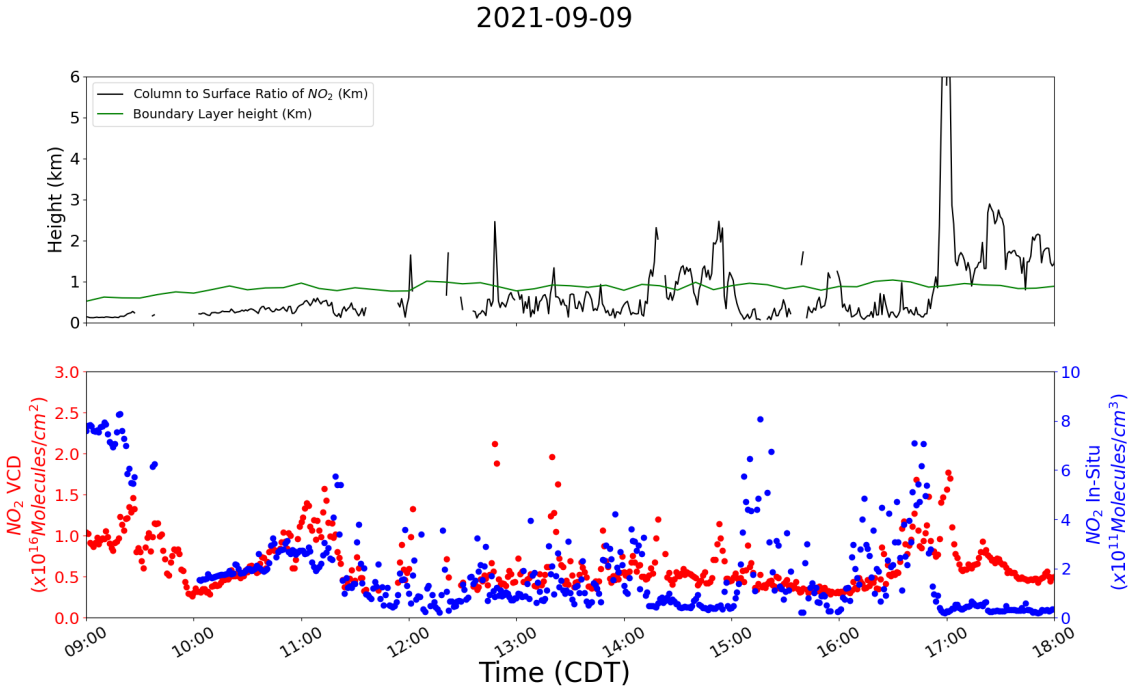


Figure 5.14: Top: The column to surface ratio of NO_2 (black) and corresponding diurnal averaged Boundary Layer Height (green) on September 9. Bottom: The NO_2 Tropospheric Vertical Column Density (red) and the in-situ surface concentration (blue). Aside from the boundary layer height, which is the diurnal variation averaged every 10 minutes, all data shown is presented as 1 minute averages.

The behavior of both trace gases during the high Ozone event suggest that there are significant quantities of both $HCHO$ and NO_2 being transported into the area and interacting with the $HCHO$ already present. In order to determine the origin of these air masses, wind data collected from five airports located near the driving path (Ellington Airport, Houston Southwest Airport(29.5065, -95.4688), Pearland Regional Airport(29.5190, -95.2421), Sugar Land Regional Airport(29.6271, -95.6556), William P. Hobby Airport (29.6442, 95.2786). These airports reported light winds between 0-5 m/s from the Northeast during the high Ozone event, with the average of these locations being 3.95m/s at 37.7°. This wind pattern indicates that the air masses likely originated from the urban core and industrial center of Houston. Emissions from these areas were likely transported into the rural communities

directly South and mixed with local $HCHO$ to produce the high amounts of Ozone observed.

5.6 Satellite Validation

Due to the different viewing geometries used, DOAS instruments have different levels of sensitivities when measuring trace gas concentrations at different altitudes. This is especially the case when comparing satellite measurements, which measure surface scattered solar irradiance and are most sensitive to near surface concentrations, and ground-based Zenith DOAS measurements, which are most sensitive to stratospheric trace gases. Because of this difference in sensitivities, there should be vertical distributions where both instruments are sufficiently sensitive to measure and others that are not. These differences in sensitivity should result in better or worse validation of Satellite-Based DOAS data products, depending on how sensitive both instruments are to the trace gases measured. In order to determine this relationship, the Pandora Zenith DOAS measurements are compared to TROPOMI, a sun-synchronous Satellite-Based DOAS instrument, in order to determine the relationship between validation and column to surface ratio. Pandora measurements within 30 minutes of each day's TROPOMI overpass are compared to the nearest TROPOMI pixel at the time of each measurement.

The Zenith DOAS sensitivity at the surface layer, as demonstrated in Chapter 7, is very consistent: while Zenith DOAS instruments are much more sensitive to stratospheric trace gases than tropospheric, Zenith DOAS instrument sensitivity to trace gases close to the surface is consistent. Therefore, it is expected that the sensitivity of the Satellite-Based DOAS instrument which is less sensitive to trace at higher altitudes, should determine how well the Ground-based DOAS instrument can perform validation.

Figure 5.15 shows the Pandora Zenith VCDs, color coded to the column to surface ratio,

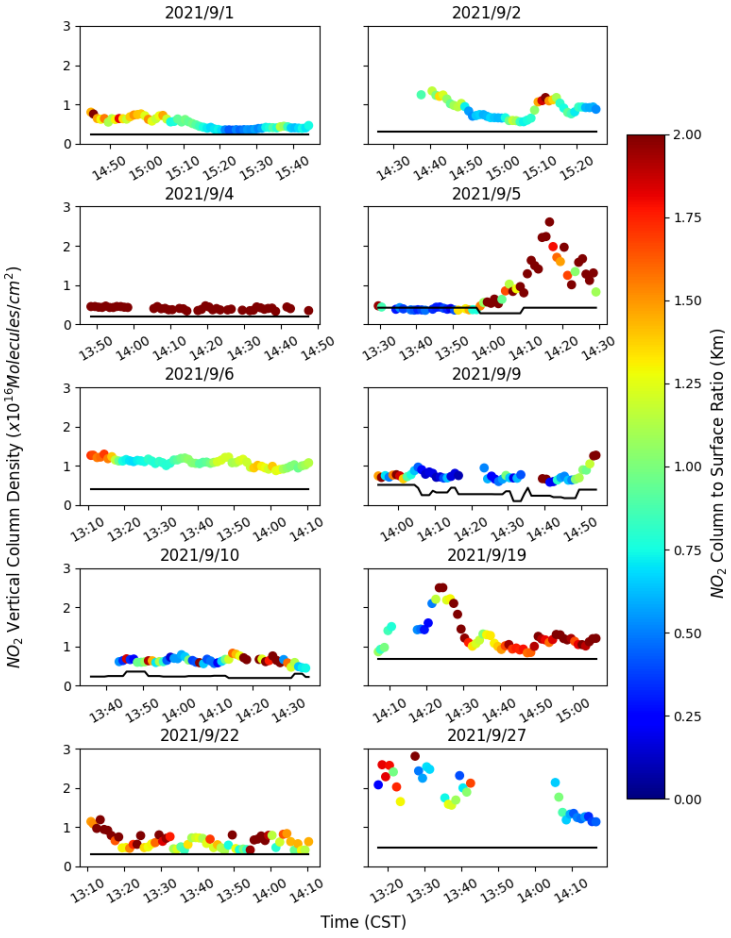


Figure 5.15: Time series plots of the TROPOMI NO_2 VCD (black) nearest the Pandora instrument and the Pandora NO_2 VCD, color coded to the column to surface ratio. The selected days correspond to days where the average column to surface ratio is larger than 1Km. All data shown is presented as 1 minute averages.

as well as the TROPOMI VCD of the nearest satellite pixel as a black line for days where the average column to surface ratio during TROPOMI overpass is greater than 750m. The difference between TROPOMI and Pandora VCDs are very high, typically between 50% to 70% difference on average. This behavior indicates that with large column to surface ratios, the TROPOMI and Pandora VCDs do not agree. In addition, time periods where there are lower column to surface ratios coincide with the best levels of agreement on the high days. For instance, September 5 saw good agreement during the first half of TROPOMI overpass,

while as time passed, the column to surface ratio increased well above 2Km as well as the Pandora VCD, causing a much larger difference between measurements.

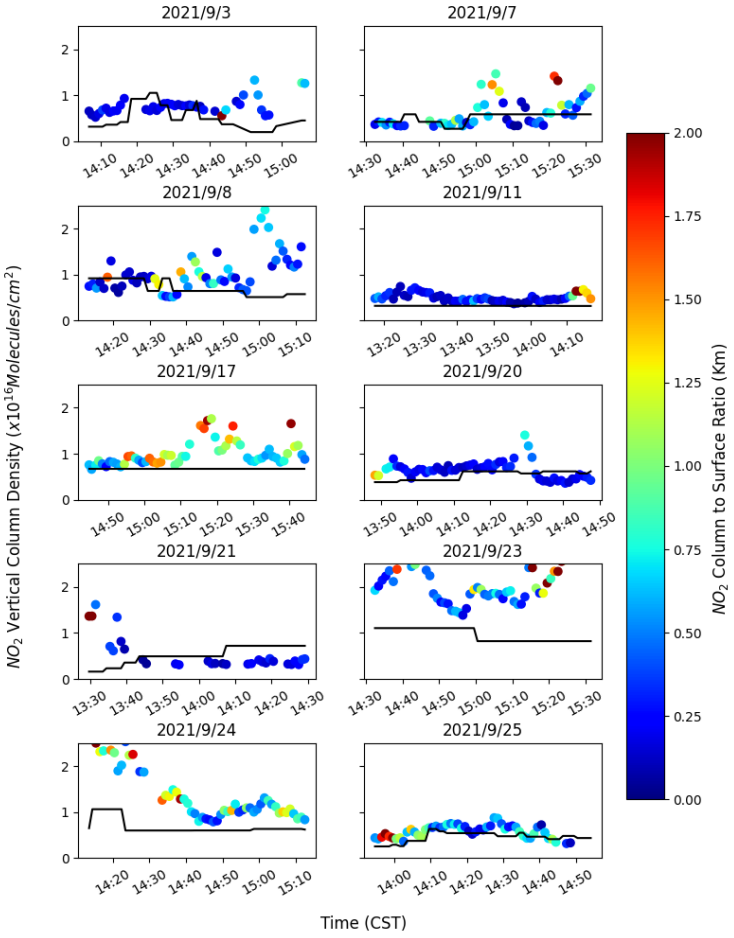


Figure 5.16: Time series plots of the TROPOMI NO_2 VCD (black) nearest the Pandora instrument and the Pandora NO_2 VCD, color coded to the column to surface ratio. The selected days correspond to days where the average column to surface ratio is less than 1Km. All data shown is presented as 1 minute averages.

Looking now to Figure 5.16, where the days shown all have average column to surface ratios less than 750m, it is clear that the days agree with TROPOMI much more consistently. On these days, the average difference between 4% to 36%, other than September 23 and 24 which were on average 56% and 53% different, respectively. Such a clear contrast between days with high column to surface ratios and low demonstrates that days where NO_2 is

distributed close to the surface, and therefore at an altitude where Satellite-Based DOAS instruments are more sensitive to, results in better validation. Similarly to the high days, days where the column to surface ration remains mostly below 1Km show good agreement while the column to surface ratio remains low, however once the column to surface ratio increases above 1Km, TROPOMI and Pandora VCDs begin to diverge. This can be seen on September 7, and 17, when at the beginning of TROPOMI overpass on the 7th and end on the 17th, the column to surface ratio rises during the middle of the TROPOMI overpass period, as does the Zenith NO_2 VCD, diverging from the TROPOMI NO_2 VCD. Finally, in order

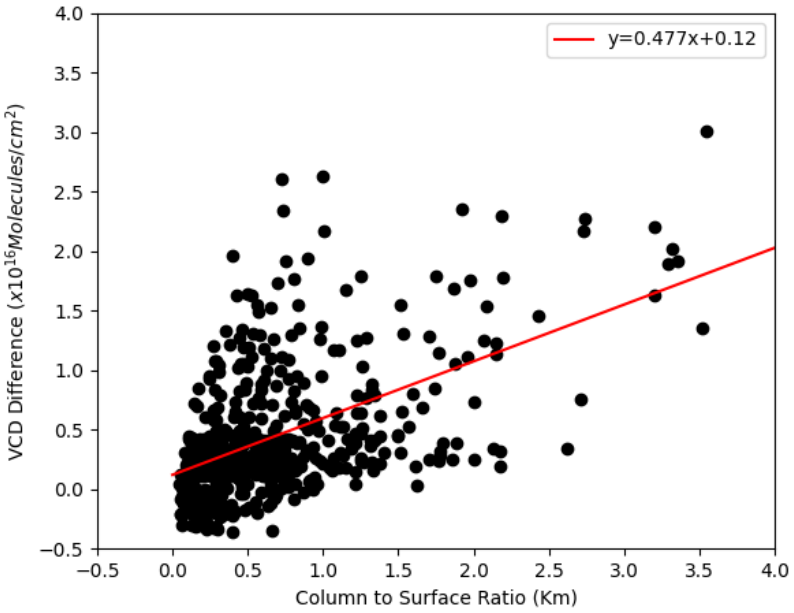


Figure 5.17: Correlation plot comparing the difference between the TROPOMI and Pandora NO_2 VCD and the column to surface ratio. All Pandora data is averaged per 1 minute.

to characterize the relationship between column to surface ratio and satellite validation, a correlation plot comparing validation differences and the column to surface ratio are plotted in Figure 5.17. While the plot is only slightly correlated, with an r value of 0.55, there is some correlation between column to surface ratio and validation. While the correlation

between the two quantities is promising, the lack of a strong link between the two is likely due to other factors, such as horizontal heterogeneity and the presence of aerosols affecting AMF calculations, that could be impacting the measurements as well. These other factors are likely what are causing the "outlier" days, such as September 19, 21, and 23, where other factors than the vertical distribution of trace gas are contributing to either better or worse validation than days with similar column to surface ratios. However, there is still a relationship between the column to surface ratio and validation, and as such should be considered when interpreting any long-term satellite validation studies.

5.7 Error Estimation

Because the Zenith DOAS VCDs shown in this chapter have been retrieved from Zenith DOAS measurements without the assistance of a single retrieval software, this means that each potential error source must be considered separately. These error sources are the retrieval uncertainty, the AMF error, and the error arising from the estimation of the reference column. In addition, due to the stratospheric component of the NO_2 column, the error related to its estimation must be considered, however this error is not present for $HCHO$. These error sources contribute to the final error estimation, following [64] according to Equation 5.1

$$\sigma_{VCD}^2 = (\frac{\sigma_{dSCD}}{AMF})^2 + (\frac{\sigma_{ref}}{AMF})^2 + (\frac{\sigma_{strat}}{AMF})^2 + (\frac{SCD}{AMF} * \frac{\sigma_{AMF}}{AMF})^2 \tag{5.1}$$

Where σ_{dSCD} represents the uncertainty of the DOAS retrieval, σ_{ref} the uncertainty of the estimation of the reference column, σ_{strat} the uncertainty of the stratospheric portion of the NO_2 column, and σ_{AMF} is the uncertainty of the Air Mass Factor estimation.

Errors relating to the DOAS retrieval were provided by QDOAS, and are related to the inability of the DOAS fit to completely account for all differential absorption measured, as well as from assumptions about the polynomial estimation for wide-band extinction, and were on average $5.80 \times 10^{14} \frac{Molecules}{cm^2}$ for Visible NO_2, $9.67 \times 10^{14} \frac{Molecules}{cm^2}$ for UV NO_2, and $4.24 \times 10^{15} \frac{Molecules}{cm^2}$ for $HCHO$. Next, errors arising from the estimation of air mass factors comes primarily due to errors in assumptions about the aerosol properties measured by the mobile Lab, as well as assumptions of the vertical profile, both error sources have been further described in Chapter 7. From this chapter, an uncertainty factor of 20% of each Air Mass Factor has been estimated, which accounts for the variability seen in AMFs through sensitivity studies. This corresponds to a mean error of $1.34 \times 10^{15} \frac{Molecules}{cm^2}$ for the Visible NO_2 retrieval, $1.23 \times 10^{15} \frac{Molecules}{cm^2}$ for the UV NO_2 retrieval, and $1.77 \times 10^{15} \frac{Molecules}{cm^2}$ for $HCHO$. There is also error from the assumptions required to estimate the trace gas column in the reference spectrum. This error arises predominantly from variations between the data used for the linear fit and fitted points themselves performed for Minimum Langley Extrapolation. This difference between the real and extrapolated data was found to be $8.69 \times 10^{14} \frac{Molecules}{cm^2}$ and $1.31 \times 10^{15} \frac{Molecules}{cm^2}$, respectively for the NO_2 Visible and UV reference columns, and$4.24 \times 10^{14} \frac{Molecules}{cm^2}$ for the $HCHO$ reference column uncertainties. The error from the estimation of the stratospheric component of the vertical column was taken from the standard deviation of the climatological stratospheric NO_2 column at , and the mean error was estimated at a latitude of 29.75°, $7.23 \times 10^{14} \frac{Molecules}{cm^2}$ for UV and $7.93 \times 10^{14} \frac{Molecules}{cm^2}$ for Visible NO_2 stratospheric columns.

In order to estimate the affect of the error estimations on the final VCDs, each error source is shown in Table 5.2 as a percentage of the mean VCD of NO_2, $6.23 \times 10^{15} \frac{Molecules}{cm^2}$ and $3.51 \times 10^{15} \frac{Molecules}{cm^2}$ for Visible and UV retrievals, respectively, and $HCHO$, $8.82 \times 10^{15} \frac{Molecules}{cm^2}$. Due to the higher $HCHO$ columns present relative to NO_2, the effect of the AMF error and

reference column error is much smaller for $HCHO$, in spite of the fact both error sources have the same values for both NO_2 and $HCHO$.

Table 5.2: Summary of Error Sources for Visible NO_2 and $HCHO$VCDs

Trace Gas	$\sigma_{\Delta SCD}$	σ_{ref}	σ_{AMF}	σ_{strat}	σ_{Total}
NO_2 Visible	9.3%	13.9%	21.4%	12.7%	31.0%
NO_2 UV	27.6%	37.4%	35.1%	20.8%	65.7%
$HCHO$	47.8%	32.2%	19.9%	N/A	64.5%

5.8 Discussion

The Mobile Zenith DOAS measurement technique is capable of observing larger areas than stationary instruments can, even with a single, fixed viewing geometry. This makes the technique ideal for short periods of intensive measurements, such as the TRACER-AQ1 field campaign, where the goal of measuring is to observe interesting trace gas events that are not necessarily regular occurrences. Mobile Zenith DOAS measurements can also be combined with collocated in-situ measurements of trace gas, to give a comparison of trace gas concentrations at the surface to the entire vertical column above the instruments. This comparison, known as the column to surface ratio, is an estimation of the effective height of the trace gas measured. The column to surface ratio can be used to estimate the proximity of the instruments to certain sources. For instance, Mobile Zenith DOAS measurements are performed primarily on roads, which when there is heavy traffic leads to NO_2 column to surface ratios remaining close to the surface, indicating the influence of nearby vehicles on the measurements. On the other hand, column to surface ratios when traveling in the proximity of industrial sources, such as the many refinery complexes in the greater Houston area, will be much higher, reflecting the height of flares and smokestacks that industrial sources emit trace gas from. Even away from urban sources, the column to surface ratio can

be used to detect the influence of the urban plume, which can help better understand the transport of trace gas into emissions free areas.

For instance, on September 6 the instruments observed multiple short spikes in the NO_2 and $HCHO$ column to surface ratio, indicating plumes transporting both trace gases into the area. These plumes likely originated from refinery complexes in the vicinity of the instruments, and were primarily responsible for the high Ozone event observed during this time. On September 9, however, the instruments measured in an emissions free area to the South of the urban core of Houston. While in this area, both NO_2 and $HCHO$ were elevated, as evidenced by the consistently high column to surface ratios over multiple hours. This behavior indicated longer range transport of trace gases, which likely originated in the urban core of Houston. The anthropogenic NO_2 and $HCHO$ emitted transported South and mixed with biogenic $HCHO$ produced through secondary formation from biogenic VOC's like isoprene. Once mixed, both trace gases produced Ozone leading to the high levels of Ozone observed during most of the day.

In addition, the column to surface ratio was found to be related to the ability of Zenith DOAS measurements to validate Satellite-Based DOAS measurements. Days in which the mean column to surface ratio was less than 0.7Km during TROPOMI overpass saw better agreement between the two instruments than days where the mean column to surface ratio was higher than 0.7Km. In addition, the difference in VCD between Satellite-Based and Zenith DOAS measurements is shown to have a linear relationship, with poorer satellite validation when the column to surface ratio is higher. However, this relationship only shows moderate correlation, with a correlation coefficient of 0.55, suggesting that while the column to surface ratio does influence satellite validation, there are likely other issues that have influenced these results.

While the column to surface ratio can estimate areas of high horizontal heterogeneity, such

as when a plume is measured, the limitations of the Zenith DOAS viewing geometry prevent a more detailed analysis of local heterogeneity. This limitation prevents more direct measurement of the origin of many of the observed high Ozone events observed, and prevents more detailed analysis of these events. However, the addition of even one MAX-DOAS viewing direction could help better understand horizontal heterogeneity. While the Zenith DOAS viewing geometry is fixed to measure vertically, MAX-DOAS measurements compare between a vertical measurement and a measurement in a chosen direction, such as looking behind or to the side of the vehicle. The comparison between VCDs retrieved by these two viewing geometries should be able to identify areas of higher heterogeneity, and with enough additional viewing directions, locate the direction of peak heterogeneity. In addition, it is possible that horizontal heterogeneity is influencing satellite validation as much, if not more, that vertical trace gas heterogeneity, and as such any analysis on satellite validation should compare the influence of vertical heterogeneity to horizontal heterogeneity on satellite validation.

Chapter 6

Mobile MAX-DOAS measurements made during TRACER-AQ2

6.1 Introduction

The TRACER-AQ1 field campaign provided a unique opportunity to study the vertical distribution of trace gas in a heterogeneous environment. By performing mobile Zenith DOAS measurements in Houston, the Zenith DOAS instrument and in-situ instruments were able to travel to regions in the Houston-Galveston-Brazoria region where the combination of meteorological processes, as well as trace gas emissions combined to form large quantities of Ozone, allowing for the major sources of the precursors to Ozone to be better understood. However, trace gas heterogeneity is not limited to the vertical direction, rather the horizontal distributions of trace gases could also give further information on the factors driving Ozone formation. The lessons learned from the TRACER-AQ1 field campaign, regarding the vertical distributions of trace gases, were expanded upon for TRACER-AQ2.

With the addition of two mobile MAX-DOAS measuring Pandora instruments, now the impact of the horizontal distributions of trace gases ln local Ozone formation could be studied. The goal of the second field campaign was to use the spatially different MAX-DOAS and Zenith DOAS measurements to identify the horizontal distribution of trace gas within a measuring area, and identify the impact on Ozone formation. To achieve this, (1) DOAS

analysis was performed not only on the two MAX-DOAS measurement sets in tandem, but also on the Zenith DOAS measurements that the MAX-DOAS instruments use as reference measurements; this analysis produces three sets of VCDs for NO_2 and $HCHO$. (2) The difference in VCD between the three datasets is used to formulate the Horizontal Heterogeneity Index, which is a measure of how heterogeneous a measurement area is. This index is then used to identify areas of high heterogeneity and determine the cause of the observed heterogeneity, such as due to plumes or nearby sources. (3) Compare the behavior of the $HCHO/NO_2$ ratio between measurement directions to determine the most probable cause of the high Ozone events observed during TRACER=AQ2.

In addition, the effect of horizontal heterogeneity on satellite validation is studied. With a similar method to that used during TRACER-AQ1, the VCDs of TROPOMI and each of the Mobile DOAS datasets are compared, using the Horizontal heterogeneity index in lieu of the Column to Surface Ratio to determine the optimal heterogeneity level that results in improved satellite validation.

6.2 TRACER-AQ2 Overview

TRACER-AQ2 was structured the same way as the first field campaign, with the intention of comparing measurements made between concurrent years. During TRACER-AQ1, there were fize days where the local Ozone concentration exceeded $20 \times 10^{11} \frac{Molecules}{cm^3}$, however September 2022 saw 10 high Ozone events, with many of these events exceeding $25 \times 10^{11} \frac{Molecules}{cm^3}$, which indicates much more Ozone was formed during 2022 than 2021. This behavior indicates that not only was TRACER-AQ1 was held in a lower Ozone year than TRACER-AQ2, but any steps to mitigate Ozone formation that were devised from the results of TRACER-AQ1 were not yet showing results.

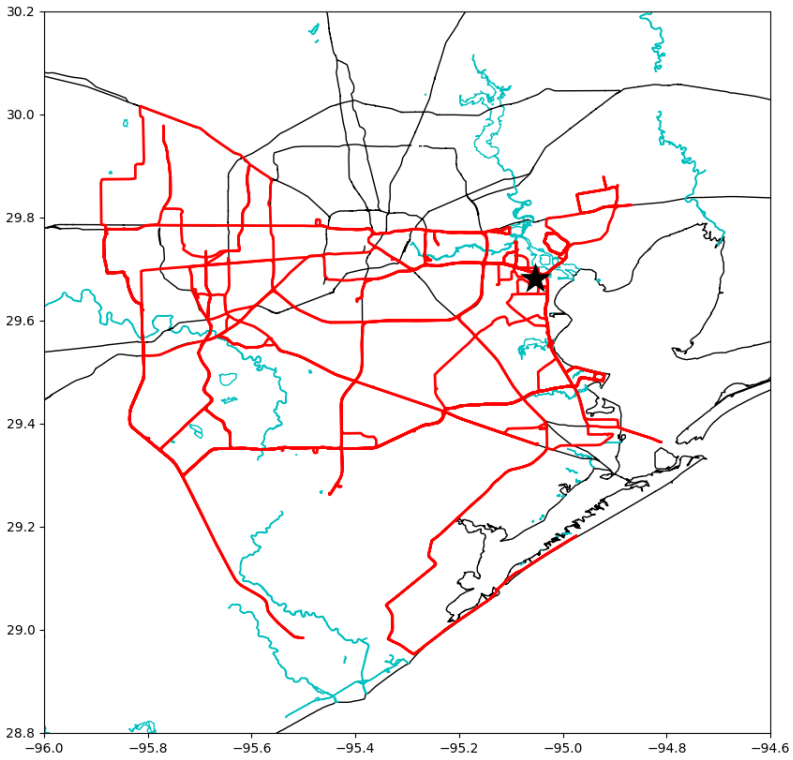


Figure 6.1: Map depicting the greater Houston Area with major roads and coastlines outlined in black, major waterways in cyan. Each path the mobile DOAS vehicle traveled during the campaign is outlined in red. The star represents la Porte airport, where the insturments remained stationary when not driving.

In order to tackle this issue, the mobile laboratory, MAQL1, was again used for TRACER-AQ2; however, instead of a single Pandora instrument fixed to measure in the Zenith direction only, two Pandora instruments were mounted with tracker systems, allowing the instruments to point in any direction while in operation. However, both instruments performed measurement schedules in fixed azimuth directions relative to the direction of motion. As can be seen in Figure 6.2, Pandora 168 measured behind MAQL1, with a measurement schedule designed to measure emissions directly above and within close vicinity to the road

MAQL1 was driving on. On the other hand Pandora 148 measured perpendicularly to the right of the vehicle; this instrument captured any major emissions and transport that was not associated with the road, likely industrial sources nearby the vehicle as well as plumes. In addition, both instruments took two Zenith measurements as references, which were used to determine the trace gas columns directly overhead the vehicle at any point in time.

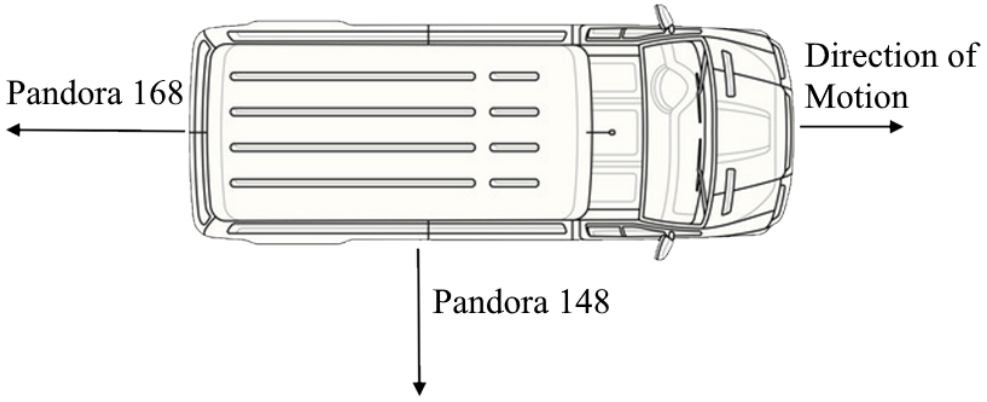


Figure 6.2: Diagram of the measuring directions of the two MAX-DOAS instruments mounted onboard MAQL1.

In addition, the driving routes of MAQL1 during TRACER-AQ2 took the Pandora instruments into rural and suburban areas much more often, as can be seen in Figure 6.1, and as such the Pandora instruments measured in the vicinity of industrial sources and in areas with high traffic flow much less often. However, due to the larger number of high Ozone events observed by the in-situ Ozone monitor onboard MAQL1, it is possible that many high Ozone events are due to interactions between urban and rural emitted trace gases.

6.3 Methodology

The data analysis for the TRACER-AQ field campaign can be separated by the methodology used to retrieve VCDs: the MAX-DOAS fast sky scanning technique and the Zenith DOAS technique. While both techniques retrieve roughly the same VCD, differences in the sensitivity of the viewing geometry to tropospheric trace gases as well as differences in the expected light path can generate discrepancies between them.

6.3.1 Zenith DOAS Analysis

The Zenith DOAS dataset was pulled from the reference measurements made by Pandora 148, after the initial Blick had made the initial corrections which convert L0 data to L1 data, but before the DOAS fit was performed. DOAS fitting of Zenith NO_2 and $HCHO$ dSCDs was performed using the QDOAS software, version 3.4.5, using the same methodology discussed in Chapter 5. The fitting procedure was separated into 2 fitting windows: NO_2 was fitted in the visible spectrum between 425 and 490nm, , and Formaldehyde was fitted in a UV window, between 328.5 and 359. The absorption cross-sections for all of these windows are summarized in Table 6.1. Please note that some of these cross-sections are used for multiple fitting windows.

In order to correct for the difference between laboratory and field cross-sections of NO_2 and O_3, I_o correction was performed on all four cross-sections, using an assumed SCD of $10^{20}\frac{Molecules}{cm^2}$ for O_3 and $10^{17}\frac{Molecules}{cm^2}$ for NO_2. This issue leads to the incomplete removal of the Fraunhofer structures from the solar reference spectrum[140], and can be corrected by correcting the solar reference spectrum with a simulated absorption spectrum generated from a given slant column density and absorption cross-sections. A Ring pseudo cross-section was generated using the Ring tool provided with the QDOAS software. A fifth order polynomial

Table 6.1: DOAS fitting parameters used to retrieve $HCHO$, NO_2, and O_2O_2 ΔSCD from Pandora zenith sky measurements.

Fitting Windows:HCHO: 328.5-359 nm, NO_2: 425-490 nm
Polynomial Order: 5
Offset and wavelength shift polynomial order: 1

Trace Gas	Temperature (K)	Source	Fitting Windows
NO_2	294, 220	Vandaele et. al.[134]	NO_2, $HCHO$
H_2O	290	Rothman et. al.[135]	NO_2
O_3	243, 223	Serdyuchenko et. al.[136]	NO_2, $HCHO$
O_2O_2	293	Thalman et. al.[137]	NO_2
$HCHO$	297	Meller and Moorgat[138]	$HCHO$
BrO	224	Fleischmann et. al.[139]	HCHO
Ring	N/A	Chanve and Spurr[49]	NO_2, HCHO

was used to estimate the wideband absorption effects, and a nonlinear shift of the measured spectrum was performed to align it with the other inputs.

The reference measurement was generated from the mean of measurements made around solar noon on September 28. In the same manner as TRACER-AQ1, the instruments were stationed on the Texas City Dike. Spectral measurements taken around solar noon were averaged together to create the reference measurement used for DOAS fitting. While the reference spectrum was measured in a relatively remote and trace gas free location, there still remains a residual amount of trace gas in this spectrum that must be removed. The NO_2 reference column was estimated using Minimum Langely Extrapolation, an example of which is shown in Figure 6.3. The reference column estimated for NO_2 was $6.78 \times 10^{15} \frac{Molecules}{cm^2}$.

In addition, because $HCHO$ again has an inverse relationship with AMF, the $HCHO$ reference column could not be estimated through Minimum Langely Extrapolation. Instead, the Bootstrap method[87] was attempted as an alternative method of estimating the $HCHO$ reference column. This method works by taking an estimated VCD of background $HCHO$, for this analysis $V_o = 1 \times 10^{14} \frac{Molecules}{cm^2}$ was used, and generated slant column densities based on each $HCHO$ dSCD's respective AMF, Then the reference column is estimated by the

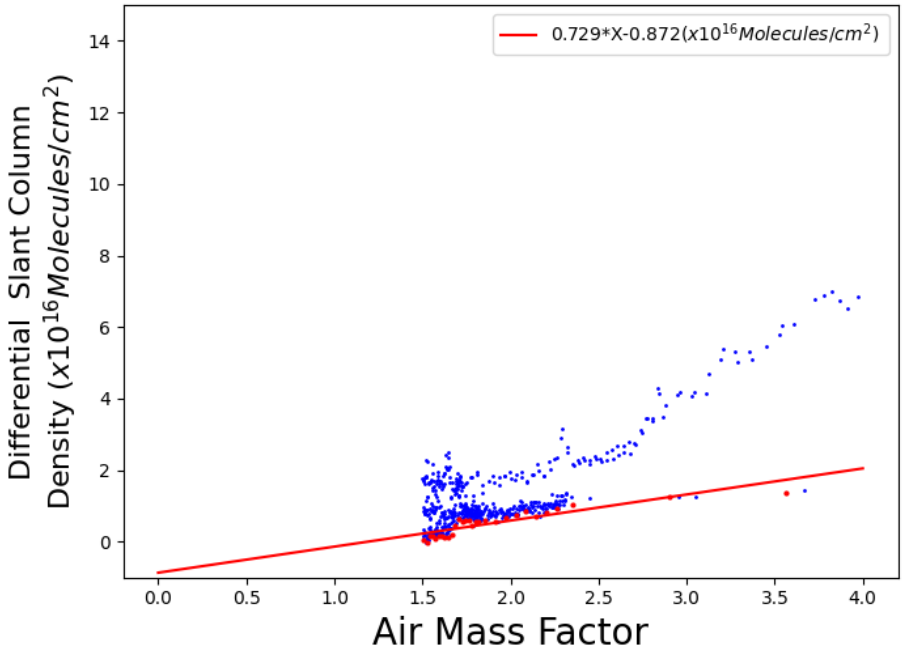


Figure 6.3: NO_2 differential slant column densities retrieved at 460 nm from measurements on the reference day, September 28, plotted as a function of the NO_2 AMF's retrieved at 460 nm from September 28. Each red dot represents the minimum ΔSCD in each bin which is used for a linear fit (red line) which is used for Minimum Langley Extrapolation. The reference column of NO_2 was estimated to be $8.72 \times 10^{15} \frac{Molecules}{cm^2}$

difference between this generated SCD and the measured dSCDs, as seen in Equation **??**. In order to account for outliers, while still finding a minimized value for the reference column, the second percentile of estimated reference columns was used as the true reference column. The reference column was estimated to be $28 \times 10^{15} \frac{Molecules}{cm^2}$.

$$dSCD_{HCHO} - AMF_{HCHO} \times V_o = -SCD_{ref} \tag{6.1}$$

However, this reference column amount proved to be too large and caused poor agreement in column amount with the two MAX-DOAS datasets. In addition, for each day the Zenith DOAS VCD's had a close to inverse U shape which typically is associated with a reference

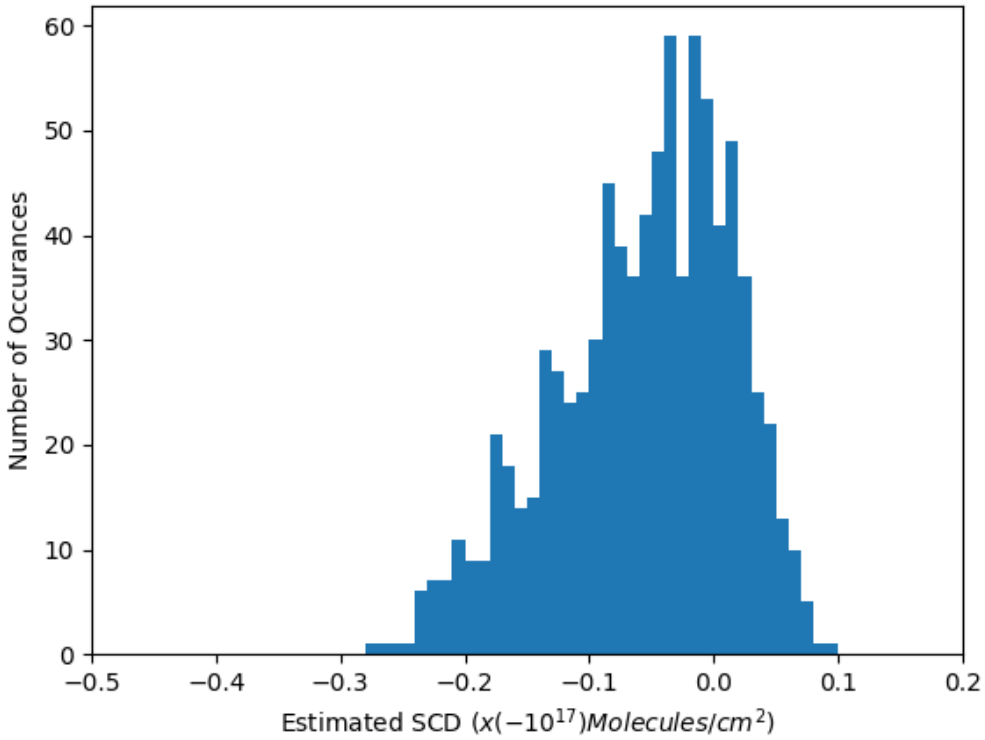


Figure 6.4: A histogram showing the results of the Bootstrap method for $HCHO$ from TRACER-AQ2. The second percentile is used as the estimated $HCHO$ reference column.

column amount that is too large. Instead, the mean MAX-DOAS VCD's between 10:00 and 14:00 on September 30, a day with little observed $HCHO$ in the MAX-DOAS datasets, was assumed to be the minimum observable VCD in the Houston area. This assumed reference column amount, $9.71 \times 10^{15} \frac{Molecules}{cm^2}$, led to improved agreement between Zenith DOAS and both MAX-DOAS datasets, not just on September 30 but for the entire field campaign.

Climatological estimations of the Stratospheric component of the NO_2 VCD[14]. These estimations are performed by the Blick software in order to estimate the contribution of the stratospheric column for total VCDs from Direct Sun measurements, allowing them to be compared to the tropospheric VCDs retrieved from MAX-DOAS measurements. Likewise, this estimation of the stratospheric component can be subtracted from Zenith DOAS total

VCDs as well, in order to estimate the Zenith tropospheric VCD.

Air Mass Factors were generated through radiative transfer simulations, which are further described in Chapter 7. The resulting box AMFs are used to generate AMFs of NO_2 and $HCHO$ using an exponential profile with an effective height of 250m and a peak concentration matching the mean concentration measured by in-situ instruments onboard MAQL1, while a box profile with a 2Km height and concentration matching the mean in-situ measurement measured by instruments onboard MAQ1 was used for HCHO. Air Mass Factors were simulated once an hour from sunrise to sunset, generating around 12 AMFs for each day. These AMFs were then linearly interpolated to match the time of each dSCD, creating a matching AMF dataset for the dSCDs.

In order to ensure high data quality, the uncertainty of each VCD was screened before use. While Pandora measurements with an uncertainty greater than 30% of the final VCD are typically considered as poor quality data, the additional uncertainties that arise due to the behavior of mobile measurements requires a higher threshold. Instead, measurements with uncertainty greater than 50% are considered as poor data quality and removed from the VCD datasets. In addition, cloud screening was performed on the Zenith DOAS measurements in the same manner as was used during TRACER-AQ1, using the O_2O_2 VCDs to determine the presence and effects of clouds.

6.3.2 MAX-DOAS Analysis

In addition to the Zenith DOAS measurements, both Pandora instruments performed fast sky scans in their respective azimuth directions. This means the instruments, wile performing the sky scanning technique, took the minimum number of measurements required to retrieve the VCD. Figure 6.5 provides a diagram of this measurement schedule. Both MAX-DOAS

instruments performed a series of five measurements at $90°, 30°, 15°, 30°, 90°$ relative to the horizon, repeating this schedule while in operation.

Each 90° and 30° measurement was scheduled to take 10 seconds, which includes the dark measurement required for dark corrections, both sets of measurement directions are then averaged together to create an average spectrum more representative of the measurement area during the measurement cycle than a single measurement. The 15° measurement, on the other hand, was scheduled to be twice as long as the 90° and 30° measurements, due to only on measurement at 15° being performed during each cycle. This leads to an expected length of each cycle being approximately one minute, however the true length of each measurement can be influenced by the amount of sunlight being measured, and can cause the measurement cycle to increase or decrease by up to ten seconds.

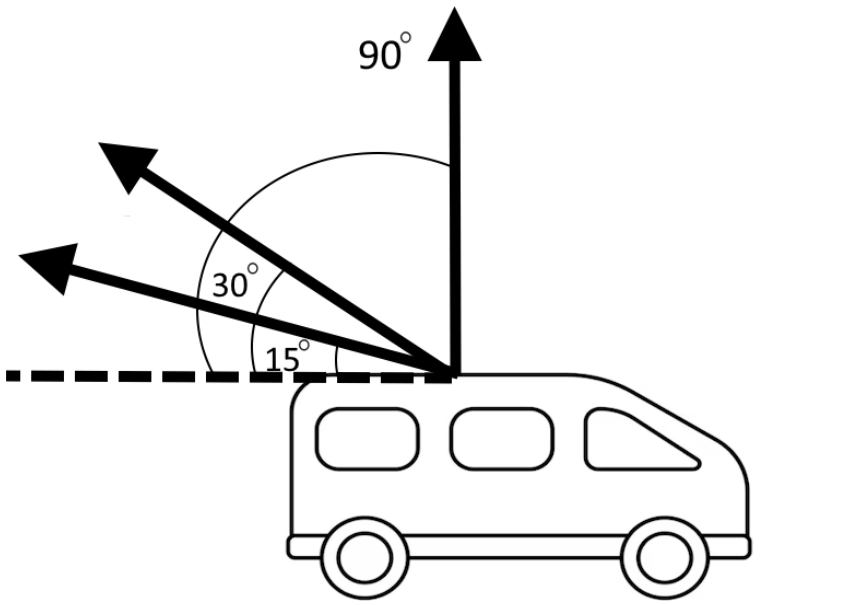


Figure 6.5: A diagram depicting the measurement schedule for the MAX-DOAS measurements over one cycle.

Both trace gases were fitted using the BlickP processing software, which is capable of performing DOAS analysis on the measured spectra and converting them into VCDs. BlickP

processed the MAX-DOAS spectra to retrieve $HCHO$ and NO_2 both in the UV wavelength. $HCHO$ was processed with a fitting window of 328.9-359.0nm and a corresponding 4th order polynomial and 1st order offset and wavelength shifting. NO_2 was processed with a fitting window of 336.0-370.0nm as well as a 5th order polynomial and 1st order offset and wavelength shifting. The absorption cross-sections used for both trace gases are listed in Table 6.2, unlike the Zenith DOAS retrievals, the MAX-DOAS retrievals fitted the same trace gases, only with different fitting parameters.

Table 6.2: Absorption Cross-Sections used for MAX-DOAS Analysis

Trace Gas	Source	Window
NO_2	Vandaele et. al.[134]	NO_2, $HCHO$
O_3	Serdyuchenko et. al.[136]	NO_2 , $HCHO$
O_2O_2	Newnham & Ballard[153]	NO_2, $HCHO$
$HCHO$	Meller and Moortgat[138]	NO_2, $HCHO$

Once the dSCDs were fitted, BlickP then converted them to VCDs using the Air-Sky Ratio algorithm. As shown in Equation 6.2, the ratio uses the retrieved dSCDs of NO_2 and $HCHO$ at 15° and 30° as well as the corresponding dSCDs of the Oxygen Collisional Complex, one of the so called air gases, to determine the VCD for each measurement cycle. The algorithm takes advantage of the well characterized O_2O_2 profile to determine what effect the scattered light path had on the O_2O_2 dSCD, which is then used to estimate what effect the same light path had on the trace of interest.

$$q_T = \frac{(qs_{15} - qs_0) \cdot q_{CLIM,AIR}}{qs_{15,AIR} - qs_{30,AIR} + 2 \cdot q_{CLIM,AIR}} = \frac{\Delta qs_{15} \cdot q_{CLIM,AIR}}{\Delta qs_{15,AIR} - \Delta qs_{30,AIR} + 2 \cdot q_{CLIM,AIR}} \quad (6.2)$$

In order to ensure high data quality, the MAX-DOAS VCDs underwent quality screening in the same manner as the Zenith DOAS VCDs. Due to the mobile nature of the measurements,

the quality flag was increased from its typical value of 30%, to 50%, in order to account for the spatial averaging that will occur from traveling one minute down a road. However, MAX-DOAS measurements are not sensitive to clouds, with only the change in the last scattering altitude affecting the VCD. Because of this, the MAX-DOAS datasets were not screened for clouds, and can be used to perform a second screening for clouds in the Zenith DOAS dataset, in order to find large deviations in trace gases between datasets that the initial cloud screening might have missed.

6.3.3 Horizontal Heterogeneity Index

The three Pandora datasets represent three distinct directions (Behind the Vehicle, to the Right of the Vehicle, and Above the Vehicle) from which measurements can be taken. While in a homogeneous environment, such as a rural region where no major sources are present, the instruments should behave similarly, however, in a heterogeneous environment, especially in the proximity to major sources of trace gases, the three Pandora datasets should record different VCDs, because the difference in measurement directions is influenced by the heterogeneous trace gas distribution. Because of this relationship between heterogeneity and the difference in VCD based on measurement direction, the difference in VCD can be used to quantify how heterogeneous a measurement area is.

Simply comparing both MAX-DOAS measuring directions will yield information about the differences between both measurement directions. The behavior of this value would, for instance, be useful in quantifying the difference between on-road and off-road emissions sources in an area. However, the MAX-DOAS viewing geometry assumes that the measurement area has a homogeneous distribution of trace gas, and the vertical profile being measured is constant along the light path, an assumption that should not hold in a suffi-

ciently heterogeneous environment. With no information about the VCD directly above the instruments, it is impossible to determine if this assumption still holds for one or both of the instruments. However, with the addition of Zenith DOAS VCDs, the trace gas distribution directly above the instruments can be used to constrain the difference between MAX-DOAS viewing direction, in order to determine which, if any, is more representative of the vertical distribution of trace gas above the instruments. Heterogeneous environments will create large differences between the at least two of the three sets of column densities. These differences can be used to indicate both how heterogeneous an area is, as well as in what direction the source of the observed heterogeneity is.In order to quantify the heterogeneity of an area, Equation 6.3 determines the root mean squared of the difference between each MAX-DOAS viewing direction and the Zenith DOAS datasets:

$$H = \sqrt{\frac{\Sigma_{i=1}^{n}(VCD_i - VCD_Z)^2}{n}} \tag{6.3}$$

Where VCD_n are the vertical column densities retrieved from MAX-DOAS measurements, and VCD_Z are the vertical column densities retrieved from ZSL-DOAS measurements. This heterogeneity value, given in $\frac{Molecules}{cm^2}$, represents the magnitude of the difference between MAX-DOAS vertical column density and Zenith vertical column density. When one, or both, measuring directions deviates from the VCD measured above the instruments, then a high Horizontal Heterogeneity Index will be recorded, indicating that the measurement area has an interesting distribution of trace gas and is likely being influenced by a nearby source. This source can be further isolated through both direct comparisons between MAX-DOAS viewing directions, indicating the direction and intensity of the source, as well as the column to surface ratio, which shows the effect of the vertical distribution on the measurements.

6.4 Results

The Pandora instruments remained in operation for 24 days during September. On September 5 and 6, Pandora 168 was not operational, and the instruments remained parked at La Porte Regional Airport; between September 16-18 the Pandora instruments remained idle at the University of Houston.

For most of September, the NO_2 VCDs remained between 0.5 and $4\times10^{16}\frac{Molecules}{cm^2}$ for all three datasets, as can be seen in Figure 6.6, with some peaks reaching upwards of $5\times10^{16}\frac{Molecules}{cm^2}$, as is the case on September 2, 3, 9, and 20. On the 2nd and 3rd, these peaks were likely due to the presence of clouds, as indicated by the O_2O_2 dSCDs shown in Figure A.1. The Zenith DOAS measurements were screened for clouds, and as such measurements made during these time periods have been omitted. What is interesting is that the MAX-DOAS datasets also see enhancements one these days also see enhancement at times the Zenith VCDs were not under the effect of clouds. This could indicate that the supposed cloud enhanced VCDs were not enhanced at all, but that high NO_2 levels in the area could indicate the presence of heightened aerosol levels as well, leading to increased scattering and enhancement of the light path length.

Outside of time periods affected by clouds, the three datasets show good agreement, with dataset differences reaching at most $2\times10^{16}\frac{Molecules}{cm^2}$. This is likely the upper limit of the effect of heterogeneous distributions in the measurement area on the MAX-DOAS VCDs, and because these differences are typically only seen when large NO_2 columns are present, are indications of nearby sources affecting measurements. In particular, the 9th, 13th, and 20th all show one set of Pandora measurements deviating from the other two sets, either higher or lower, which suggests NO_2 emissions are present in one of the directions measured, but not the other.

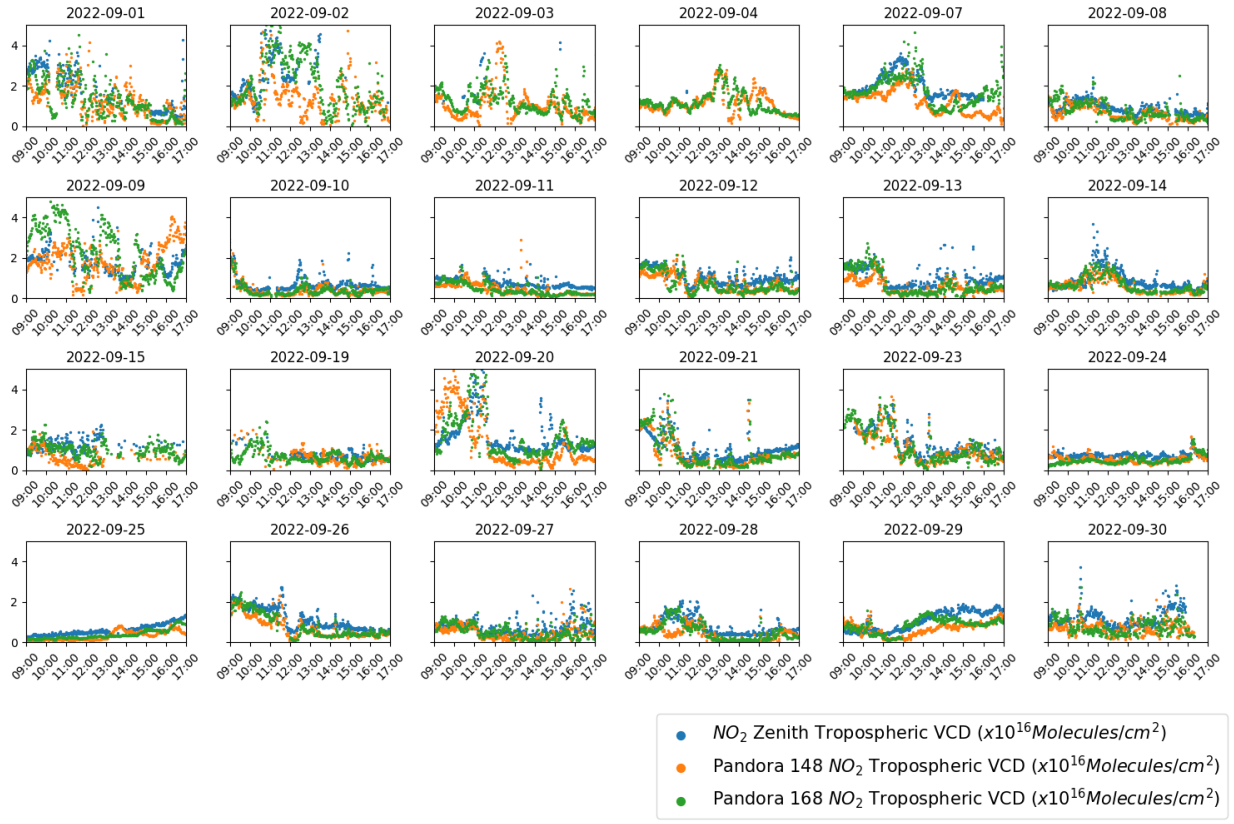


Figure 6.6: Comparison of NO_2 Tropospheric VCDs measured by both Pandora instruments, as well as columns retrieved from Zenith measurements for the Intensive Operations period of TRACER-AQ2. Time is given in local time (CDT), and columns in $\times 10^{16} \frac{Molecules}{cm^2}$

Now by incorporating the Horizontal Heterogeneity Index, the observed differences in VCD become clearer. Typical values of the NO_2 Horizontal Heterogeneity index that represent a homogeneous area range from $0 - 0.75 \times 10^{16} \frac{Molecules}{cm^2}$ and varies based on the absolute column values present; however, there are numerous instances where the index rises well above this threshold with peaks in heterogeneity reaching upwards of $3 \times 10^{16} \frac{Molecules}{cm^2}$ on days with an absence of clouds.

On some days, such as on September 10 between 12:00 and 15:00 CDT and September 21 at 14:45 CDT, rapid spikes in the heterogeneity index were observed, as can be seen in Figure A.6. These events are indicative of localized concentrations of NO_2 that increase the

heterogeneity of NO_2 in the immediate vicinity. However, because they are either isolated from other emissions sources, or remain in one particular location, they only affect the heterogeneity index for a short time. Looking back at Figure 6.6, none of the column values particularly stand out on these days, with the respective peaks not rising above $2 \times 10^{16} \frac{Molecules}{cm^2}$. However, even with such small column values, the high heterogeneity index suggests that a source nearby is impacting the measurements.

Other days, such as September 1, 7, and 20, show increases in the heterogeneity index over longer periods than were seen on the 10th and 21st. On each of these days, the peak values of the heterogeneity index were recorded while the instruments operated within either Urban Core of Houston or in other industrialized portions of the metropolitan area. In both cases, the high amount of sources led to higher levels of heterogeneity in these areas, which led to one set of MAX-DOAS measurements deviating from the other MAX-DOAS ane the Zenith measurements. This indicates that sources either behind the direction of motion or to the right are primarily responsible for the high level of heterogeneity recorded. Therefore, this indicates that measurements made in proximity to a large number of sources can result in high levels of heterogeneity, and be identified simply by the difference in VCD measurements. These differences in VCD also indicate that the trace gas emitted from industrial sources are not simply diffusing over an area, and instead remain concentrated around these source.

The Formaldehyde VCDs showed similar behaviors as NO_2.Outside of the 2nd-4th, which also were influenced by cloud enhancement, typical column values ranged from $1 - 5 \times 10^{16} \frac{Molecules}{cm^2}$. At multiple times on September 10, all three VCD datasets increased as the instruments entered and left a similar area, with Zenith VCDs rising much higher than the MAX-DOAS columns. This behavior will be further discussed in Subsection 6.5.1, however the similarities between datasets, the consistent location where the events occurred, and similar behaviors in all three NO_2 datasets, suggests that this behavior is due to some

major source impacting the measurement area, such as a ubiquitous plume originating from Houston's urban core incorporating the sources found therein.

A similar event occurred on September 8th, where between 11:00 and 13:00 CDT, all three data sets saw an increase in columns, then from 13:00 to 14:00 all three columns decreased the and rapidly increased in value, again with the zenith columns remaining larger than the MAX-DOAS columns. These shifts are likely due to the Mobile lab moving into and out of the urban plume, which tends to transport to the South of the Houston urban core in the early afternoon, followed by a major source in the Sugarland area, a major suburb of Houston.

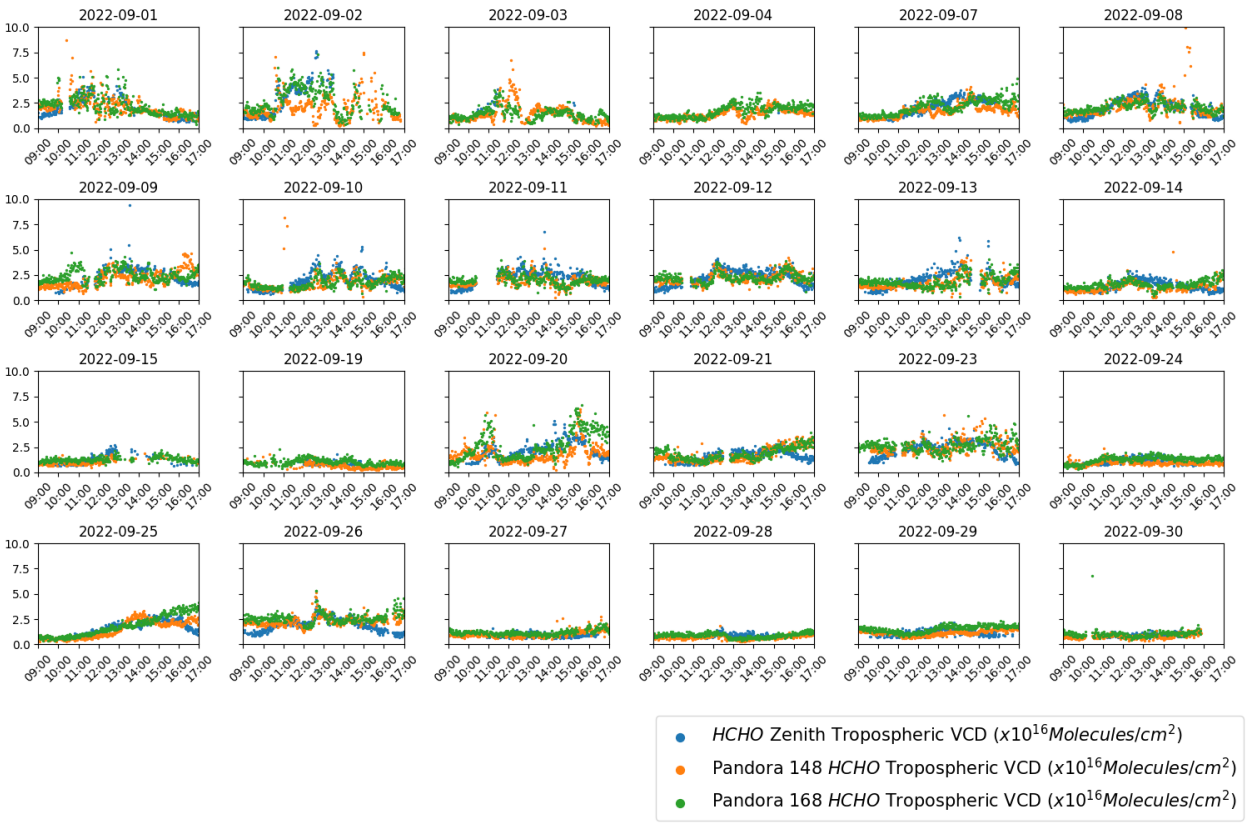


Figure 6.7: Comparison of *HCHO* Tropospheric VCDs measured by both Pandora instruments, as well as columns retrieved from Zenith measurements for the Intensive Operations period of TRACER-AQ2. Time is given in local time (CDT), and columns in $\times 10^{16} \frac{Molecules}{cm^2}$

Typical values of the heterogeneity index for $HCHO$ are larger, due to the higher levels of $HCHO$ observed when compared to NO_2. Typical values of the $HCHO$ heterogeneity Index range from $0 - 2 \times 10^{16} \frac{Molecules}{cm^2}$, with peak values of the heterogeneity index reaching up to $6 \times 10^{16} \frac{Molecules}{cm^2}$, much higher than most of the peaks seen for NO_2. In addition, most peaks in the $HCHO$ heterogeneity index are over short time periods, indicating that these peaks are due to more isolated sources of Formaldehyde.

6.5 Case Studies

6.5.1 September 10

On September 10, the Pandora instruments made multiple transects to the south of Houston, traveling East and West throughout the day through both rural as well as suburban areas, as can be seen in Figures A.8 and A.9. Due to the distance from Houston's urban cure, there were very few industrial sources present along the driving route: the closest source the instruments passed was the WA Parrish power plant, where the instruments passed at the closest 15Km to the South of the plant.

During the early afternoon, local Ozone concentrations reached upwards of $19 \times 10^{11} \frac{Molecules}{cm^3}$ and remained consistently above $16 \times 10^{11} \frac{Molecules}{cm^3}$ between 11:30 and 16:00 CDT, as shown in Figure 6.8. While this high Ozone event had a smaller magnitude than others observed during TRACER-AQ2, this event was characterized by three dips in the $HCHO/NO_2$ ratio for the Zenith DOAS dataset, a behavior also seen during TRACER-AQ1. However, this behavior is not seen in either MAX-DOAS dataset. During this time period, both MAX-DOAS datasets see a much higher degree of variability in the $HCHO/NO_2$ ratio than the Zenith DOAS dataset does. This variability could mean that there is simply too much variability in near

surface NO_2 and $HCHO$ both along the driving path as well as perpendicular to it, causing what ever event caused the dips in the Zenith DOAS $HCHO/NO_2$ ratio to be harder to detect using MAX-DOAS. Regardless, the dips in the Zenith DOAS $HCHO/NO_2$ ratio provide three time periods of interest: 12:00-13:00, 13:00-14:00, and 14:00-15:00 when the three dips occurred. These three times can be analyzed separately using the Horizontal Heterogeneity Index and Column to Surface Ratio in order to determine what mechanisms might have caused the dips seen.

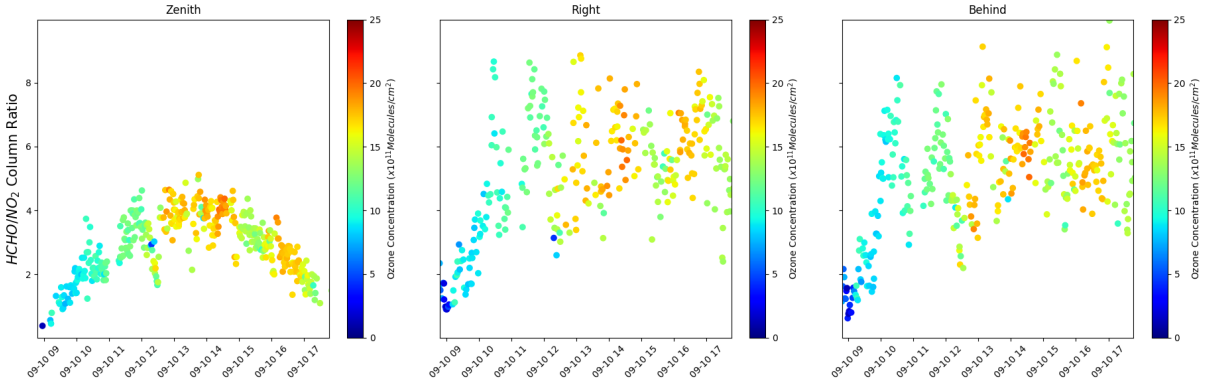


Figure 6.8: Time series of the $HCHO/NO_2$ Ratio for the Zenith DOAS (a) and MAX-DOAS datasets (b) (c). Each point is color coded to the local Ozone surface concentration($\times 10^{11} \frac{Molecules}{cm^3}$) recorded onboard MAQL1 on September 10.

Figure 6.9 shows the $HCHO$ portion of this analysis between 14:00 and 15:00 CDT. Interestingly, there are two peaks in the Zenith $HCHO$ VCDs, rather than just one to match the shift in the $HCHO/NO_2$ ratio during this time. However, the peak further West is also measured by both MAX-DOAS instruments, and as such does not significantly impact the horizontal heterogeneity index. On the other hand, the peak in the Zenith $HCHO$ VCD further East is much larger, and is not recorded by either MAX-DOAS instrument. This leads to the highest Horizontal Heterogeneity Index values concentrating in this area. In addition, most of this hour long period sees the Column to Surface Ratio remaining consistently around 2-3Km, but at the Eastern peak the ratio increases to 6Km, indicating elevated

$HCHO$ is present in the area.

Both peaks $HCHO$ correspond to the beginning (Western peak) and end (Eastern peak) of the dip in the $HCHO/NO_2$ ratio observed during this time period. Therefore, it is likely that this dip was caused by a pair of plumes transporting both $HCHO$ and NO_2. This behavior is continued in the other two hour long time periods, and can be seen in Figures A.13 and A.15, with the 13:00-14:00 time period, when the instrument is traveling Westbound, seeing much higher perpendicular VCDs of $HCHO$ than when travelling Eastbound. This behavior suggests that the origin of this $HCHO$ is located further North, and the measurement area is impacted by transport of $HCHO$ from industrial sites further North.

NO_2, as expected, showed a very similar behavior to the $HCHO$ measurements. As can be seen in Figure 6.10, as well as in Figures A.12 and A.14, peaks in the Zenith NO_2 VCDs occur at the same location as the peaks observed in the $HCHO$ VCDs. In addition, both peaks in NO_2 are marked by increases in the NO_2 Column to Surface Ratio relative to the surrounding area. This point is important because the location of both peaks is close to two major highways, where an influence by vehicular emissions would lead to large VCDs but also large surface concentrations. However the Column to Surface Ratio rises to 600m and 1.2Km in the area, as opposed to 200m in the source free areas. This behavior shows that the NO_2 measured was elevated and not due to vehicular emissions.

Due to the behavior of both NO_2 and $HCHO$, it is clear that the behavior of the $HCHO/NO_2$ ratio was due to two elevated plumes that transported both trace gases from further North during the entire time period. This estimation is further evidenced by HYSPLIT back-trajectories originating from the peaks showing air masses moving from further North during the entire period. As can be seen in Figure 6.11, A.20, and A.21, air masses below 1Km behaved similarly at the different simulated altitudes, with air masses observed at the location of interest all having likely transported from industrial and refinery complexes further

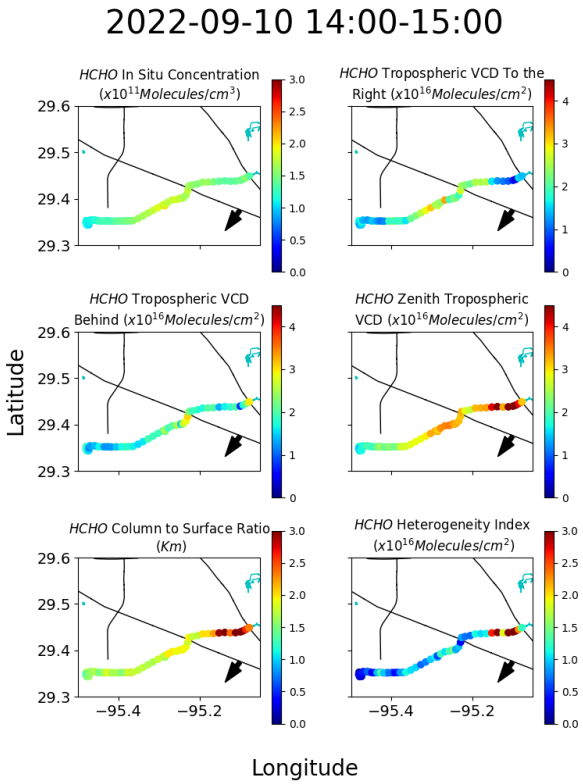


Figure 6.9: a) The 1-minute average HCHO in-situ concentrations measured on September 10 between 14:00 and 15:00 CST by the mobile lab in $\frac{Molecules}{cm^3}$ plotted at the corresponding latitude and longitude. b) The 1 minute average Pandora 148 HCHO columns plotted at the corresponding latitude and longitude. c) The 1 minute average Pandora 168 HCHO columns plotted at the corresponding latitude and longitude. d)The 1 minute average Pandora HCHO Zenith columns plotted at the corresponding latitude and longitude. e) The column to surface ratio between in-situ and Pandora Zenith columns. f) The heterogeneity index calculated from both MAX-DOAS instruments as well as Zenith columns.

North. In addition, all three altitudes simulated saw significant downward mixing of the air masses, especially the air masses from 18:00 and 19:00 UTC, which decreased in altitude from 1.25Km. The emissions from these industrial sites are known to include both VOCs and NO_x, and therefore emissions from these industrial complexes are the likely source of Ozone observed on this day.

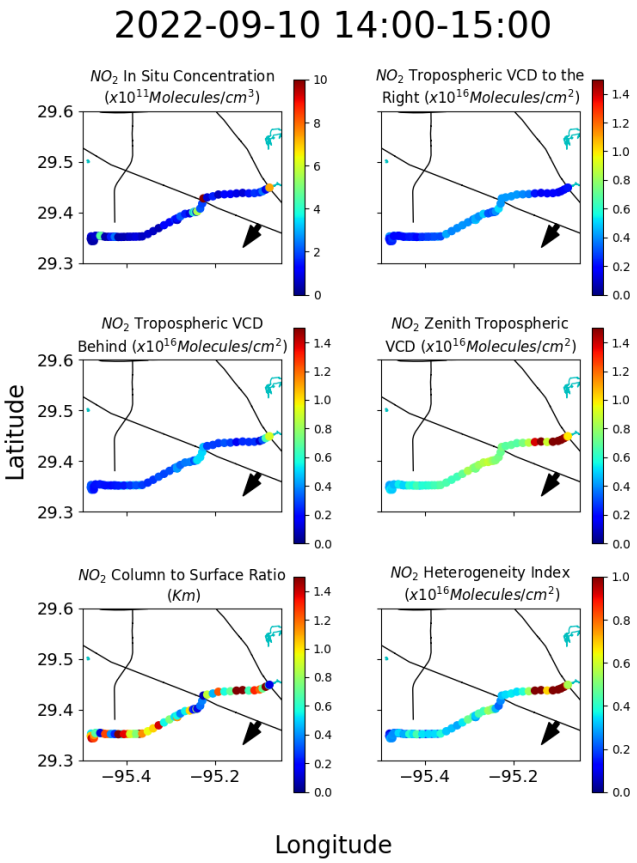


Figure 6.10: a) The 1-minute average NO_2 in-situ concentrations measured on September 10 between 14:00-15:00 CST by the mobile lab in $\frac{Molecules}{cm^3}$ b) The 1 minute average Pandora 148 NO_2 columns c) The 1 minute average Pandora 168 NO_2 columns d)The 1 minute average Pandora NO_2 Zenith columns e) The column to surface ratio between in-situ and Pandora Zenith columns. f) The heterogeneity index calculated from both MAX-DOAS instruments as well as Zenith columns.

6.5.2 September 21

September 21st saw the Pandora instruments traveling through the Southern and Western portions of the Houston-Galveston-Brazoria region, traveling West then South out of the La Porte Regional Airport into more suburban and rural areas. Between 13:00 and 17:00 CDT, as can be seen in Figure 6.12, local Ozone concentrations remained at or above $25 \times 10^{11} \frac{Molecules}{cm^3}$ for the duration of the high Ozone event, one of the largest increases in Ozone

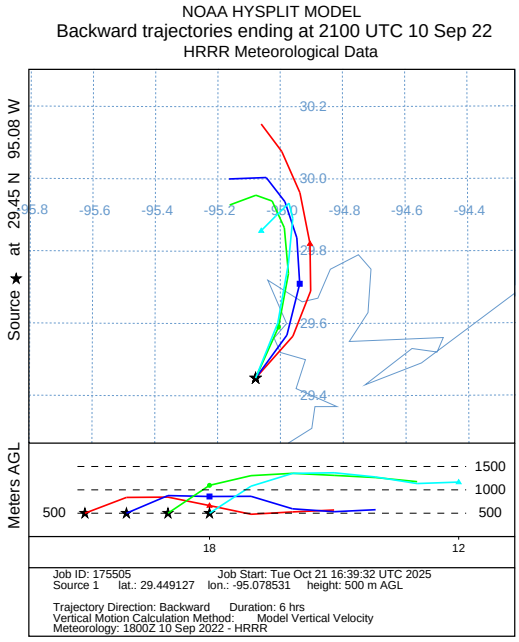


Figure 6.11: HYSPLIT modeled 3 hour back-trajectory showing the path air masses at 21:00 (red), 20:00 (blue), 19:00 (green), and 18:00 (cyan) took to transport into the high Ozone area observed, with an end altitude of 500m.

observed during both TRACER-AQ field campaigns. However, the location is well removed from any sources, and as Ozone as was measured would not normally be expected. In order to determine the combination of factors that gave rise to this high Ozone event, the Horizontal Heterogeneity Index can be used to pinpoint particular sources or transport patterns that could have impacted Ozone formation in the measuring area.

As can be seen in Figure A.2, as the Pandora instruments traveled South out of the urban core, where the NO_2 Vertical Column Density remained between $1 - 3 \times 10^{16} \frac{Molecules}{cm^2}$ for

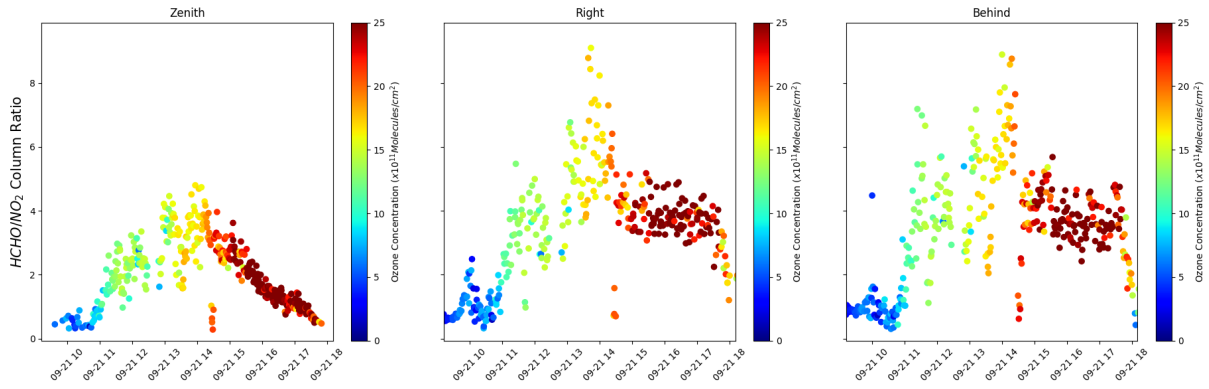


Figure 6.12: Time series of the $HCHO/NO_2$ Ratio for MAX-DOAS and Zenith DOAS datasets. Each point is color coded to the local Ozone surface concentration on September 21

all three Pandora datasets, the N_2 Vertical Column Densities decreased to between $0.1 - 1 \times 10^{16} \frac{Molecules}{cm^2}$ in all directions. This behavior is most likely due to the presence of a high volume of vehicular emissions near the instruments. All three instruments behave similarly both while traveling Westbound as well as Southbound, which indicates that the source of the NO_2 measured can not be traced from a single direction. In addition, the in-situ NO_2 surface concentrations recorded in this area are between $4 - 10 \times 10^{11} \frac{Molecules}{cm^3}$, which are some of the highest recorded over the entire day, demonstrating that the source of this trace gas is located at the surface.

Formaldehyde, on the other hand, sees very little variation while the instruments first traveled out of the city. Instead, the Formaldehyde VCDs remained between $1 - 3 \times 10^{16} \frac{Molecules}{cm^2}$ until the instruments traveled further West. In the Westernmost portion of the day's driving route, however, Formaldehyde Vertical Column Densities were much more elevated, between $2 - 5 \times 10^{16} \frac{Molecules}{cm^2}$, with corresponding column to surface ratios between 1-3Km. This behavior indicates the Formaldehyde in this area is elevated, and is likely present due to transport from Houston's urban core directly East. The Pandora instruments remained in this area from 12:00-18:00 CDT, during which time local Ozone concentrations recorded ele-

vated levels, with concentrations between $20-25\times10^{11}\,\frac{Molecules}{cm^3}$ being sustained during most of this time frame. During this high Ozone event, the Pandora instruments passed within

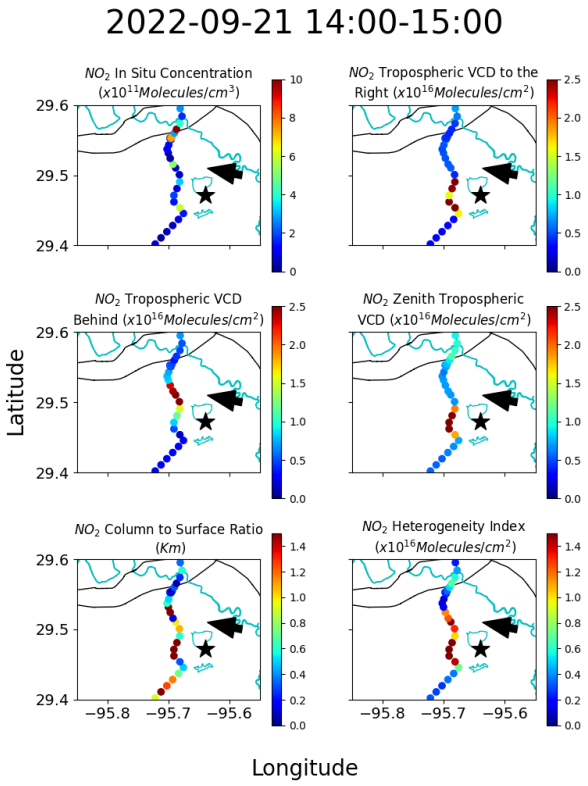


Figure 6.13: a) The 1-minute average HCHO in-situ concentrations measured on September 21 between 14:00 and 15:00 CDT while the Pandora instruments are in the proximity of the WA Parrish Power Plant (starred) by the mobile lab in $\frac{Molecules}{cm^3}$ b) The 1 minute average Pandora 148 HCHO columns c) The 1 minute average Pandora 168 HCHO columns d)The 1 minute average Pandora HCHO Zenith columns e) The column to surface ratio between in-situ and Pandora Zenith columns. f) The heterogeneity index calculated from both MAX-DOAS instruments as well as Zenith columns.

close proximity of the WA Parrish Power Plant, a coal burning power generation facility to the Southwest of Houston's Urban Core. Due to the power plant's location on the coast of Smithers lake, surrounded by farmland and forestry, the power plant is isolated from any other major sources. As can be seen in Figure 6.13, as the pandora instruments traveled Northbound past the plant, all three instruments recorded heightened Vertical Column Densities, shifting from $0.5\times10^{16}\,\frac{Molecules}{cm^2}$ to $2.5\times10^{16}\,\frac{Molecules}{cm^2}$ while in direct proximity to the

power plant. However, when directly adjacent to the power plant, the horizontal heterogeneity index reaches its peak at $1.5 \times 10^{16} \frac{Molecules}{cm^2}$, compared to $0.25 \times 10^{16} \frac{Molecules}{cm^2}$ which was observed further North and South, indicating the presence of the power plant is the most likely contributor to the elevated NO_2 columns observed in the area.

Interestingly, the Pandora instrument facing to the right, which while traveling Northbound points the instrument in the direction of the power plant, behaves similarly to the Zenith DOAS Vertical Column Densities. On the other hand, the Pandora instrument looking behind the vehicle's peak Vertical Column Densities lagged behind the other two Pandora datasets by around 5Km. This behavior shows that the NO_2 measured is elevated, likely with peak concentrations between 1-2Km. This is further evidenced by the lack of significant NO_2 surface concentrations in the area leading to column to surface ratios peaking above 1.5Km, agreeing with this estimation.

Formaldehyde, on the other hand, is much more well mixed in the entire area around the power plant, as shown in Figure A.3. All three Pandora instruments show similar Vertical Column Densities, between $2-4 \times 10^{16} \frac{Molecules}{cm^2}$ through the entire section of the days travel. This behavior resulted in the Horizontal Heterogeneity Index through the area remaining between $1-2 \times 10^{16} \frac{Molecules}{cm^2}$ and Column to Surface Ratios between 2-3Km. Indicating Formaldehyde was very well mixed horizontally but elevated vertically. Due to this behavior, it is likely that the dip in the Zenith DOAS $HCHO/NO_2$ ratio at 13:00 behaves the opposite of the spike in the $HCHO/NO_2$ ratio seen in both MAX-DOAS viewing directions is the result of the instrument's proximity to the WA Parrish Power plant. Even while the instruments remained over 10Km away from the power plant, the impact of the elevated NO_2 emitted from the power plant is causing the MAX-DOAS instruments, which are more sensitive to near surface concentrations, is clear, indicating that the power plant's emissions were influencing Ozone production at a distance away from the source.

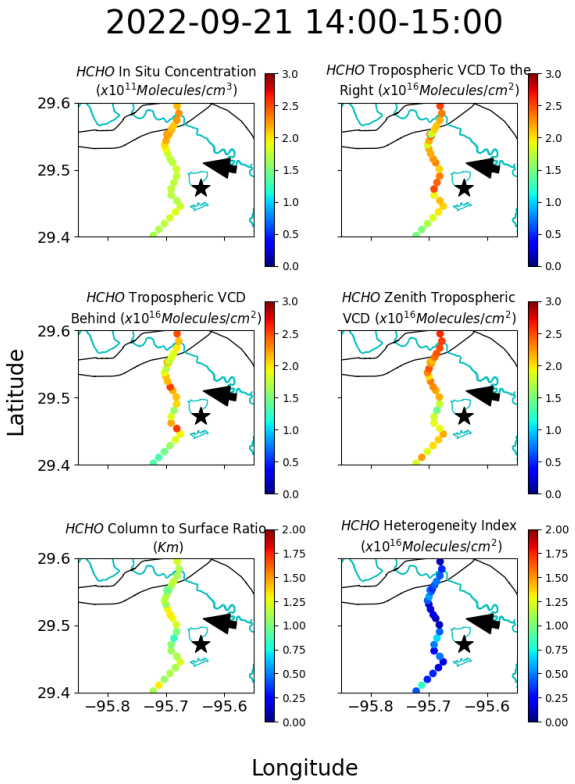


Figure 6.14: a) The 1-minute average HCHO in-situ concentrations measured on September 21 between 14:00 and 15:00 CDT while the Pandora instruments are in the proximity of the WA Parrish Power Plant (starred) by the mobile lab in $\frac{Molecules}{cm^3}$ b) The 1 minute average Pandora 148 HCHO columns c) The 1 minute average Pandora 168 HCHO columns d)The 1 minute average Pandora HCHO Zenith columns e) The column to surface ratio between in-situ and Pandora Zenith columns. f) The heterogeneity index calculated from both MAX-DOAS instruments as well as Zenith columns.

Figures 6.15, A.22, and A.23 show the air masses during the high Ozone event originating from the Northeast of the power plant, and traveling due West after passing the power plant. This places the air masses originally from Houston's urban core, which likely means that the large amount of $HCHO$ observed in the area is a combination of secondary formation from natrual VOC sources as well as transport from the urban core. In addition, after passing the power plant, the air masses began to move due West, aligning with the observations from the heterogeneity analysis that emissions from the power plant transported to the West. These air masses also mixed vertically from near the surface at all simulated altitudes. This

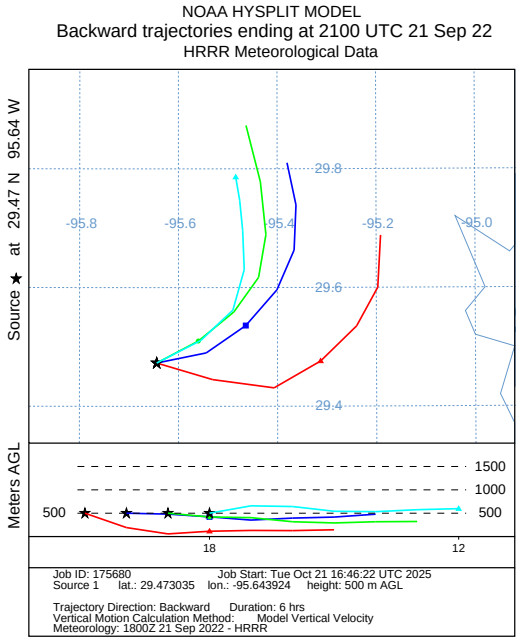


Figure 6.15: HYSPLIT modeled 3 hour back-trajectory showing the path air masses at 21:00 (red), 20:00 (blue), 19:00 (green), and 18:00 (cyan) took to transport into the high Ozone area observed at an altitude of 500m.

indicates that the observed $HCHO$ likely originated close to the surface before rising in altitude. Therefore, the transport of both NO_x and $HCHO$ from the urban core increased the base NO_2 and $HCHO$ during the high Ozone event, and mixing of these air masses with emissions from the power plant increased the rate of Ozone formation in the area to create one of the worst high Ozone events observed during both TRACER-AQ field campaigns.

6.6 Satellite Validation

The second TRACER-AQ field campaign provided a second opportunity to determine the relationship between the Column to surface Ratio and how effective Ground-Based DOAS validation of Satellite-Based DOAS measurements can be. In addition, the Horizontal heterogeneity Index can be used in the same manner. The index provides an estimate to how heterogeneous the measurement area is, and therefore can demonstrate how the heterogeneity of the air mass covered by each Satellite-Based DOAS pixel swath can influence the representativeness of the air mass as well as the ability of Ground-Based DOAS instruments to perform validation. In addition, the MAX-DOAS datasets are also used for validation, and are compared to the Horizontal Heterogeneity Index. These results can be seen in Figures A.16-A.19, however the difference in measurement direction did not result in a significant change in behavior. As a result, only the Zenith DOAS results are presented in this section.

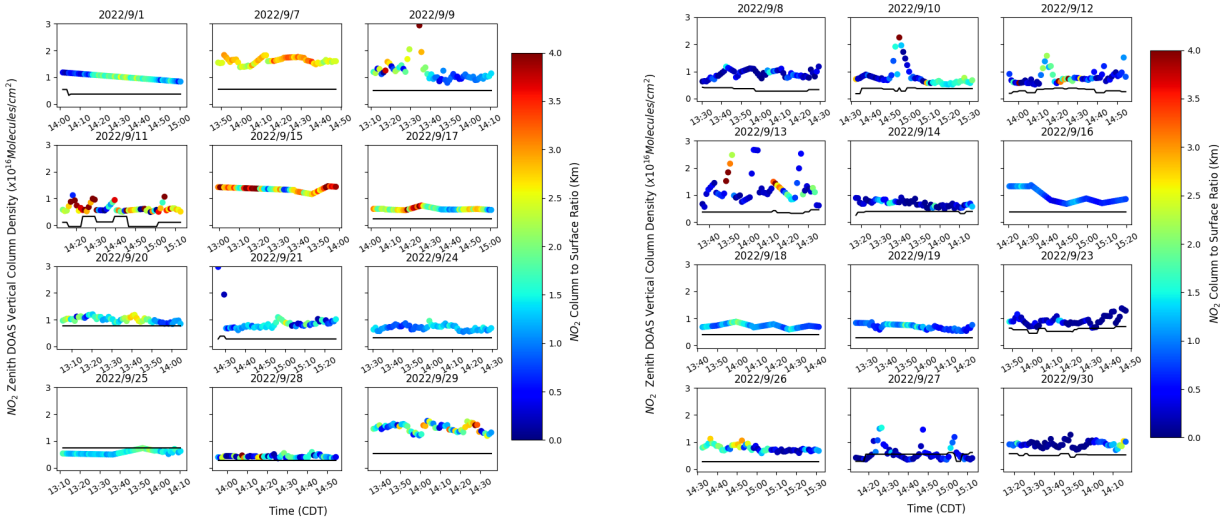


Figure 6.16: (Left) A collection of Scatter plots on days with a column to surface ratio >1Km comparing TROPOMI NO_2 VCDs (black) to Zenith DOAS VCDs, color coded to each measurement's column to surface ratio. (Right) A collection of Scatter plots on days with a column to surface ratio <1Km comparing TROPOMI NO_2 VCDs (black) to Zenith DOAS VCDs, color coded to each measurement's column to surface ratio

Figure 6.16 shows how the Column to Surface Ratio impacted validation using the Zenith DOAS dataset during the TRACER-AQ2 field campaign. Similar to TRACER-AQ1, the days were separated into days with a high average Column to Surface Ratio (left) and low average Column to Surface Ratio (right). The behavior between days is consistent to TRACER-AQ1, with the mean difference between Zenith DOAS and TROPOMI VCDs for days with high column to surface ratios once again remaining around 70%, while the difference between VCD datasets on low Column to Surface Ratio days once again resting at 20%. The consistent behavior between field campaigns indicates that the vertical distribution of trace gas consistently impacts Satellite-Based DOAS measurements. Interestingly, many of the high Column to Surface Ratio days showed good agreement between datasets, such as on September 20 and 28, when the mean difference between Pandora Zenith and TROPOMI VCDs were only 2.8% and 27%, respectively; one other day of interest is September 25, when TROPOMI actually overestimated the Pandora Zenith VCD, at a -70% difference. These days show that the column to surface ratio, while a good indicator for satellite validation, is not the main driver for issues in satellite validation.

This point is further reinforced in Figure 6.17, which showcases the relationship between the Column to Surface Ratio and the difference in VCD datasets. The red line represents the linear fit of the scatter plot, and with a slope of only 0.1010, it is clear that while larger column to surface ratios do result in larger differences between Ground-Based and Satellite-Based DOAS VCD measurements, the relationship is not that strong. This is further demonstrated by the correlation coefficient of the fit, r=0.42, which demonstrates that while there is a clear relationship between Column to Surface Ratio and Validation differences, there are likely other factors at play influencing the differences between DOAS instrument measurements.

One other possible factor influencing satellite validation are heterogeneities present within

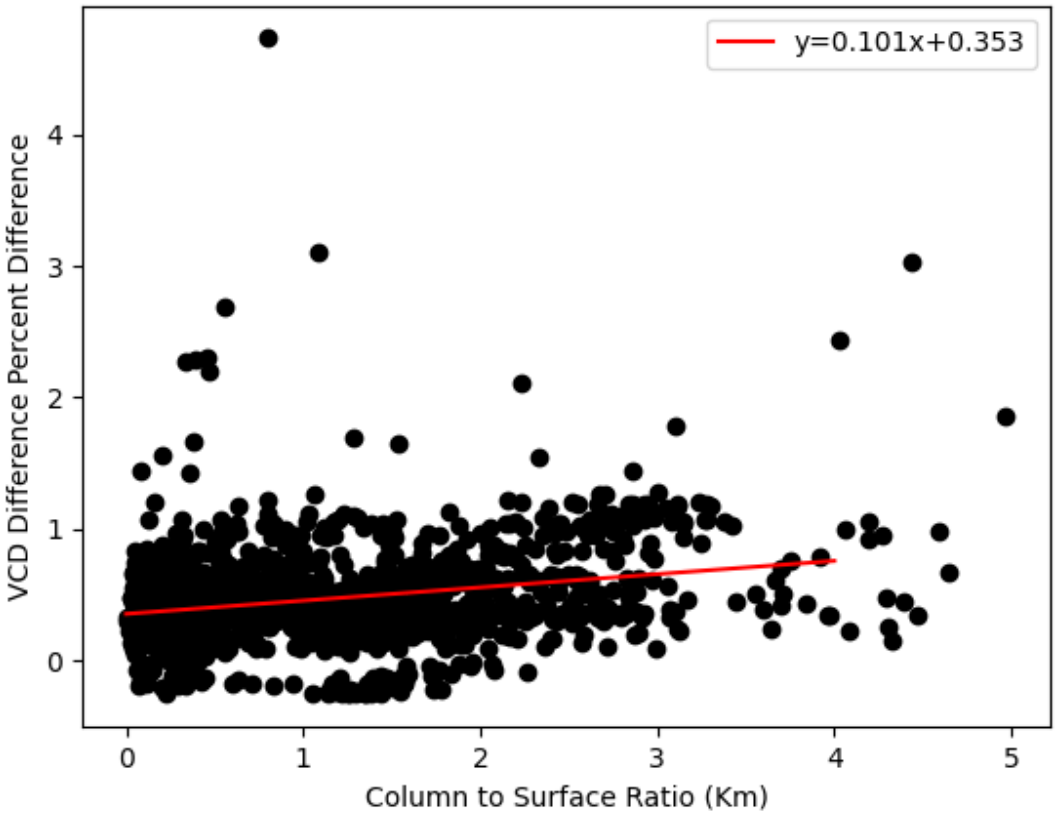


Figure 6.17: Correlation plot showing the linear relationship between the Column to Surface Ratio and the difference between the TROPOMI and Zenith DOAS VCDs during TROPOMI overpass. The correlation coefficient of this linear fit is r=0.42.

a measuring area. The spatial averaging that Satellite-Based DOAS instruments perform when taking measurements could impact the instrument's ability to measure smaller scale trace gas distributions. With that in mind, the Horizontal Heterogeneity Index can also be used to determine how well Satellite-Based DOAS measurements can be validated. Figure 6.18 shows the TRACER-AQ Zenith DOAS measurements during TROPOMI overpass each day of the field campaign. These scatter plots are separated by their mean Horizontal heterogeneity Index, with the left plots having mean Horizontal Heterogeneity Index values greater than $0.25 \times 10^{16} \frac{Molecules}{cm^2}$, with the plots on the right side having less than this value.

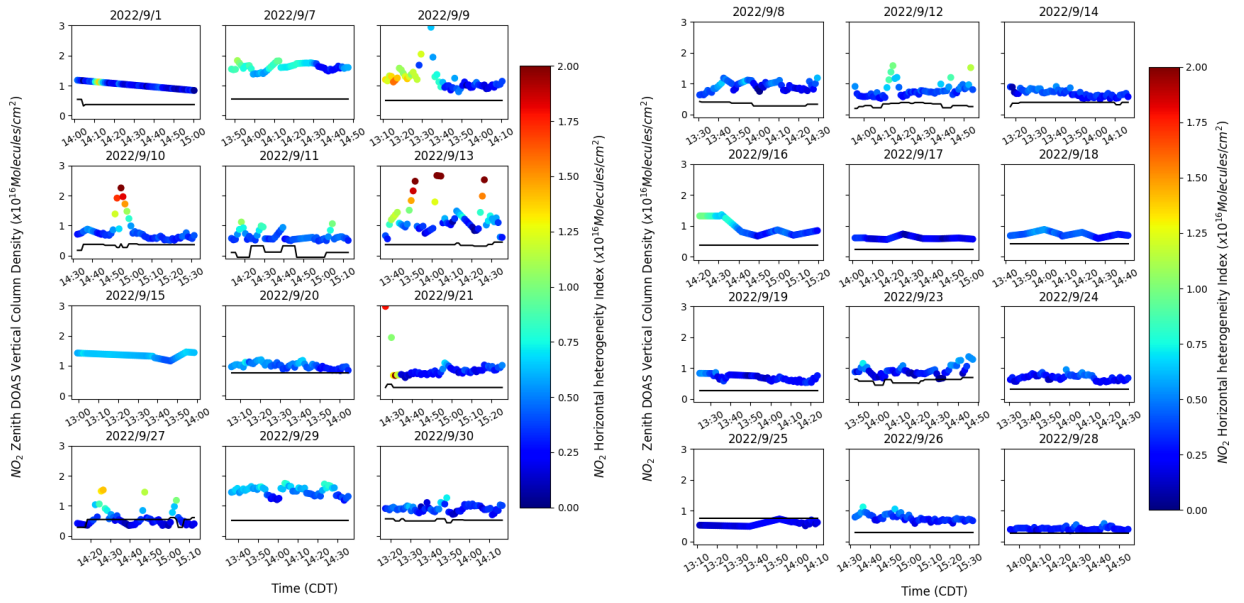


Figure 6.18: (Left) A collection of Scatter plots on days with a column to Horizontal heterogeneity Index $> 0.25 \times 10^{16} \frac{Molecules}{cm^2}$ comparing TROPOMI NO_2 VCDs (black) to Zenith DOAS VCDs, color coded to each measurement's column to surface ratio. (Right) A collection of Scatter plots on days with a Horizontal heterogeneity Index $< 0.25 \times 10^{16} \frac{Molecules}{cm^2}$ comparing TROPOMI NO_2 comparing TROPOMI NO_2 VCDs (black) to Zenith DOAS VCDs, color coded to each measurement's column to surface ratio

it becomes quite clear that the horizontal distribution of trace gas plays a critical role in satellite validation, with the left plots showing much larger differences, typically between 60-100%, than the right plots which have differences between 1-50%. In addition, increases in horizontal heterogeneity can be directly linked to increases in differences between the VCD datasets, as is clearly the case on September 8, 10, 12, 13, and 27. On these days, increases in the Zenith DOAS NO_2 VCD correspond to increases in the Horizontal Heterogeneity Index, demonstrating that heterogeneity directly relates to higher Zenith DOAS NO_2 VCDs with no corresponding increase in the TROPOMI VCDs.

This relationship is further reinforced by Figure 6.19,which showcases the correlation plot between the NO_2 Horizontal Heterogeneity Index and the difference between TROPOMI and Pandora Zenith DOAS VCD. This relationship is much more linear than the relationship

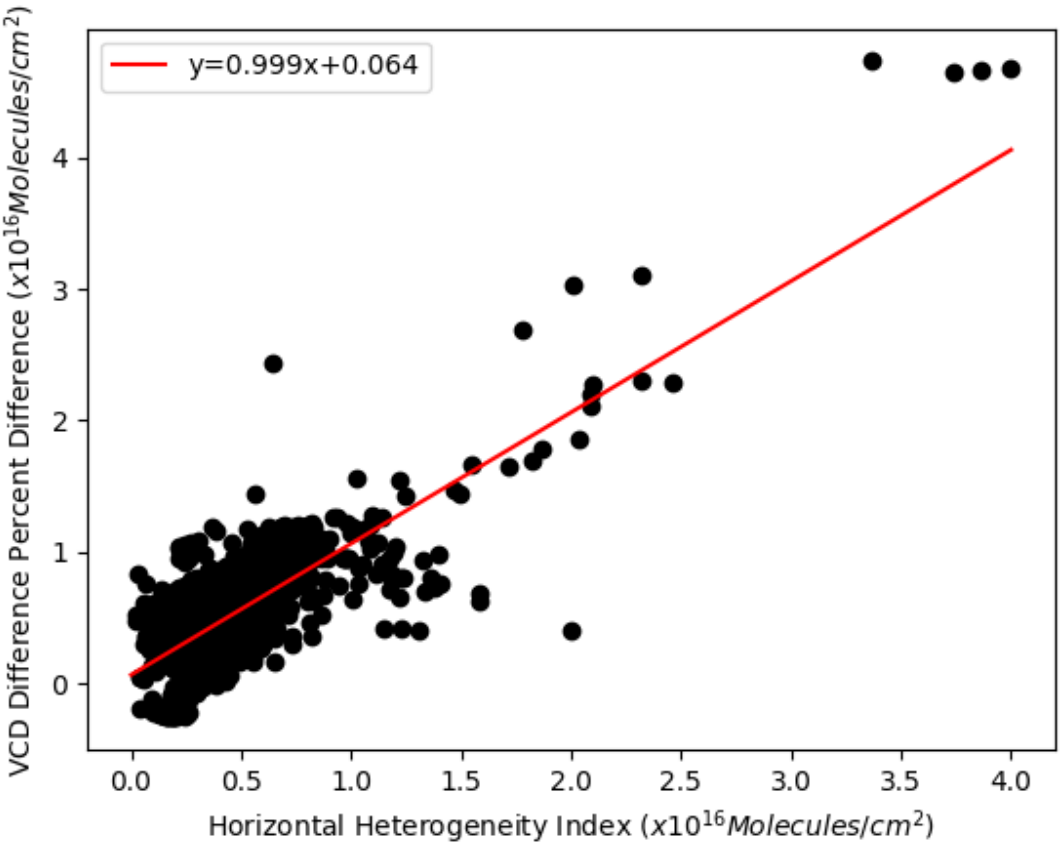


Figure 6.19: Correlation plot showing the linear relationship between the Horizontal heterogeneity Index and the difference between the TROPOMI and Zenith DOAS VCDs during TROPOMI overpass.The correlation coefficient of this linear fit is r=0.78.

between the NO_2 Column to Surface Ratio and difference between TROPOMI and Pandora Zenith DOAS VCD, with a slope of 0.99 being much closer to unity than when comparing validation results using the Column to Surface Ratio. In addition, the correlation between the NO_2 Horizontal Heterogeneity Index and difference between TROPOMI and Pandora Zenith DOAS VCD is much higher, with a correlation coefficient of 0.78, over twice that of the correlation coefficient between Column to Surface Ratio and the difference between TROPOMI and Pandora Zenith DOAS VCD. This relationship provides compelling evidence that satellite validation is primarily influenced by horizontal heterogeneities present within a

measuring area; while this relationship is far from the only factor influencing satellite validation, it is, however, the most prominent, and is the most likely source of any inconsistencies between measurements. In addition, the relationship between Zenith DOAS VCD and the Horizontal Heterogeneity Index suggests that only certain measurements are affected by high heterogeneity, and rather than discounting entire days where the mean Horizontal heterogeneity Index is too large, specific high heterogeneity measurements could be filtered out, improving validation efforts without sacrificing individual days.

6.7 Discussion

The addition of the horizontal heterogeneity index, when used in conjunction with the column to surface ratio, provides more robust methodology for identifying sources of VOC's and NO_x, as well as their contribution to Ozone production. The high Ozone event observed on September 6 was found to be due to transport of the Houston Urban Plume by up to 20Km to the South of the urban core into a suburban area with no nearby sources of $HCHO$ and NO_2 to explain the increase in trace gas. This conclusion was demonstrated based on the behavior of both the horizontal heterogeneity index and column to surface ratio, and validated by local wind patterns. While the urban plume was observed in one location, this plume likely also produced Ozone along its path, causing Ozone nonattainment in large swaths of Houston on this day.

On September 21, the WA Parrish power plant, an isolated coal burning power plant in a rural area to the south of the urban core, was observed to be a significant source of NO_2. The isolated nature of the power plant made this an ideal case for identification, with NO_2 columns surrounding the power plant at a minimum, while the pattern of columns adjacent the plant demonstrating that the plant is a significant source of NO_2. In addition, the

behavior of the two MAX-DOAS directions can be used to validate the column to surface ratio. Using the peak in the right facing MAX-DOAS instrument and the peak in the rear facing MAX-DOAS instrument as the bottom of a right triangle, and assuming the observed plume is between 15° and 30°, the two MAX-DOAS zenith viewing directions, then the altitude of the plume could be between 0.85Km and 1.84Km. The observed column to surface ratio in this area is between both of these values, indicating that this assumed effective height is a reasonable estimation of the true height of the plume. However, this is a single instance where an isolated plume was observed, and might not be indicative of the typical plume behavior. In order to fully understand the behavior of the column to surface ratio when estimating plume heights, other plumes from other isolated sources need to be observed.

Finally, the horizontal heterogeneity index provides a more compelling estimation of the ability of Ground-Based DOAS instruments to validate Satellite-Based DOAS instruments. The column to surface ratio when compared to TROPOMI NO_2 measurements during TRACER-AQ2 behaved similarly to TRACER-AQ1, further proving that the altitude of the observed trace gas plays a part in poor validation results, but that other factors play a role in poor validation. On the other hand, the horizontal heterogeneity index is much more correlated to the difference between Ground-Based DOAS and Satellite-Based DOAS instrument, with an r^2 value of 0.7, indicating a much more direct relationship between horizontal trace gas heterogeneity and satellite validation. While the relationship between horizontal trace gas heterogeneity and satellite validation is likely the major driver of poor validation, it is still clear that there are many factors other than trace gas heterogeneity that are influencing satellite validation. However, the relationship between the horizontal heterogeneity index and the difference in satellite validation data products is clear enough that the horizontal heterogeneity index can be used to filter out poor measurements for satellite validation. This

means, with the addition of a single additional MAX-DOAS viewing direction to the typical Pandora stationary operation, these high heterogeneity measurements can be avoided when comparing Pandora data to satellite data, resulting in improved satellite validation.

Chapter 7

Radiative Transfer Simulations

7.1 Introduction

Typically, Mobile DOAS studies are not concerned with the conversion of dSCDs into VCDs; instead of the typical radiative transfer modeling of air mass factors that most other Zenith DOAS studies perform[64], most studies have made assumptions about the air mass factors of each measurement to simplify the conversion of DOAS measurements into VCDs[151][112]. These studies have justified this decision due to the unavailability of aerosol data available along the driving path of the vehicle, or the study instead focused on other, more significant error sources, such as the error of a wind profile used for emission flux measurements. In addition, some studies have performed radiative transfer modeling of Zenith AMFs, but only focused the sensitivity of aerosol loading and column density on their radiative transfer models[107][154].

The two studies presented in this dissertation make direct comparisons to other quantities: both TRACER-AQ1&2 compare Zenith VCDs to in-situ surface concentrations while TRACER-AQ2 also makes comparisons between Zenith DOAS VCDs and MAX-DOAS VCDs. Both of these comparisons result in information about the spatial distribution of trace gas in the measuring area, and as such require the Zenith VCDs to have a similar amount of uncertainty as the other measurements they are being compared to. Houston, Texas presents a unique challenge to perform these radiative transfer simulations: due to

large amounts of trace gas and heterogeneity in the Houston-Galveston Area, high levels of aerosols are also present and are distributed heterogeneously throughout the area. This prevents any of the assumptions used in previous Zenith DOAS studies from being usable, and requires radiative transfer modeling of Zenith AMFs in order to produce sufficient estimations of VCDs. At the same time, the inability to collect sufficient information on the aerosol conditions at each measurement is mitigated by a small sub-network of aerosol measuring instruments scattered around the area as well, which can be used to determine what the average aerosol conditions in the area are in lieu of a direct measurement.

This chapter describes the data preparations and processing of aerosol information into AMFs through radiative transfer simulations. In addition, three sensitivity studies are presented to understand the uncertainty introduced into the AMFs through the assumptions made about local Single Scatter Albedo & Asymmetry Parameter, Aerosol Optical Depth and profile, as well as the a priori profile used to convert box AMFs into AMFs for each trace gas.

7.2 Data Preparation

Radiative transfer simulations determine the most probable light path of photons based on estimated scattering in the atmosphere. While Rayleigh scattering is easy to estimate due to overwhelming scattering by Oxygen and Nitrogen molecules, Mie scattering requires information on aerosol scattering in order to simulate. Aerosol scattering can be described by three quantities: Aerosol Optical Depth (AOD) which describes the total light extinction due to aerosols, Single Scatter Albedo (SSA), which describes how much extinction is due to scattering, and Asymmetry Parameter (ASY) which describes how uniform aerosol scattering is, for 1D simulations, the Asymmetry Parameter describes how much up-scattering and down-scattering occurs.

In order to obtain these quantities, a sub-network of six AERONET instruments are used to collect information on AOD, ASY, and SSA at Aldine, Liberty, Sugarland the University of Houston Coastal Research Center, as well as the University of Houston Main Campus, and an Atmospheric Radiation Measurement (ARM) site located at La Porte Regional Airport). These six sites provide aerosol scattering information at a wide range of locations both in the Houston Metro area, near industrial sites, as well as in rural and suburban communities. This wide range of locations can be expected to yield a mean set of aerosol scattering information for every hour of operation that is a reasonable estimate of the scattering properties of aerosols present anywhere in the region. Figure 7 shows the hourly averaged AOD values for the six sites used.



Figure 7.1: Map showing the AERONET instruments in operation around the Houston-Galveston-Brazoria area during TRACER-AQ1&2.

However, while Aerosol Optical Depth is retrieved multiple times each hour, Single Scatter Albedo and Asymmetry Parameter are secondary retrievals from AERONET measurements. As such, these typically require multiple measurements to retrieve, and can be very difficult. As such, there are not enough of either quantity to average every hour; instead, a daily mean of both quantities is used, and the additional uncertainty caused by the daily mean is investigated in Section 7.3. Each daily set of Single Scatter Albedo and Asymmetry parameter included mean values, as well as high and low values determined by twice the standard deviation of each daily set of measurements. Furthermore, each aerosol quantity was linearly interpolated to the correct wavelength before use.

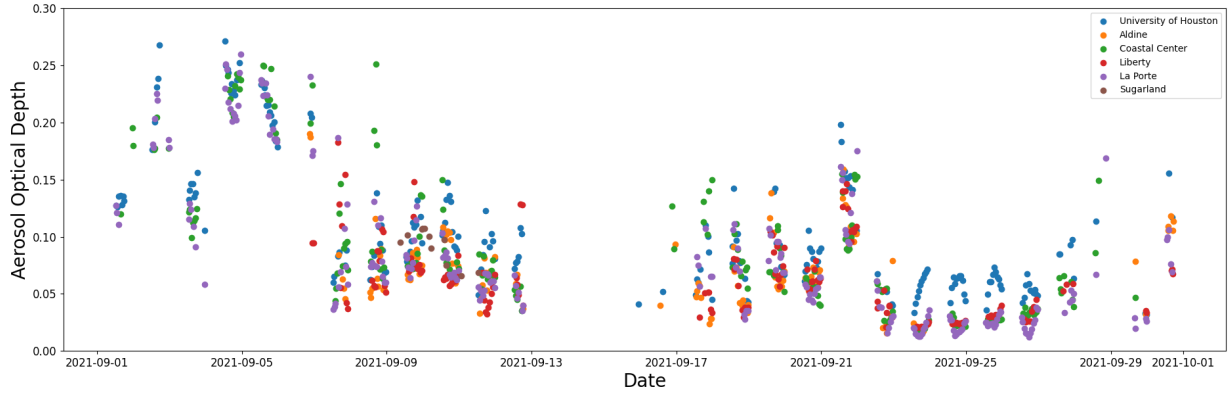


Figure 7.2: Hourly averaged L2 Aerosol Optical Depth values retrieved at 870nm from six AERONET sites in the Houston-Galveston-Brazoria area during TRACER-AQ

In addition to Aerosol Optical Depth, the profile of aerosol particles present must also be considered. This profile describes the light extinction at each atmospheric layer simulated, and at a location like Houston is critical to accurately describe Mie scattering. Prior studies have demonstrated that the aerosol profile is proportional to the backscatter profile collected from LIDAR instruments[155], one of which was operating onboard MAQL1 during both field campaigns. The backscatter profiles collected can the be converted into aerosol profiles to be used for radiative transfer simulations.

The first step in this conversion is to average the backscatter profiles together in order to smooth the profiles; similar to how the AOD is averaged hourly, the backscatter profiles are averaged each hour of operation. Further smoothing is applied on the upper portion of the profile, between 500m and 2Km using a first order Savitzky-Golay filter to account for the additional instrument noise present at higher altitudes.In addition, by 4Km all smooth profiles begin to be overwhelmed by high noise, and will report backscatter values in the negatives, which indicates a low signal to noise ratio brought on by a lack of aerosols at these altitudes. Because of this high noise 4Km has been set as the upper limit of each profile, and any values above are assumed to be 0. However, many profiles begin to be affected by noise, such as the profiles seen in Figure 7.4, these profiles are set to 0 starting at a lower altitude, when the smoothed profile becomes less than 0.

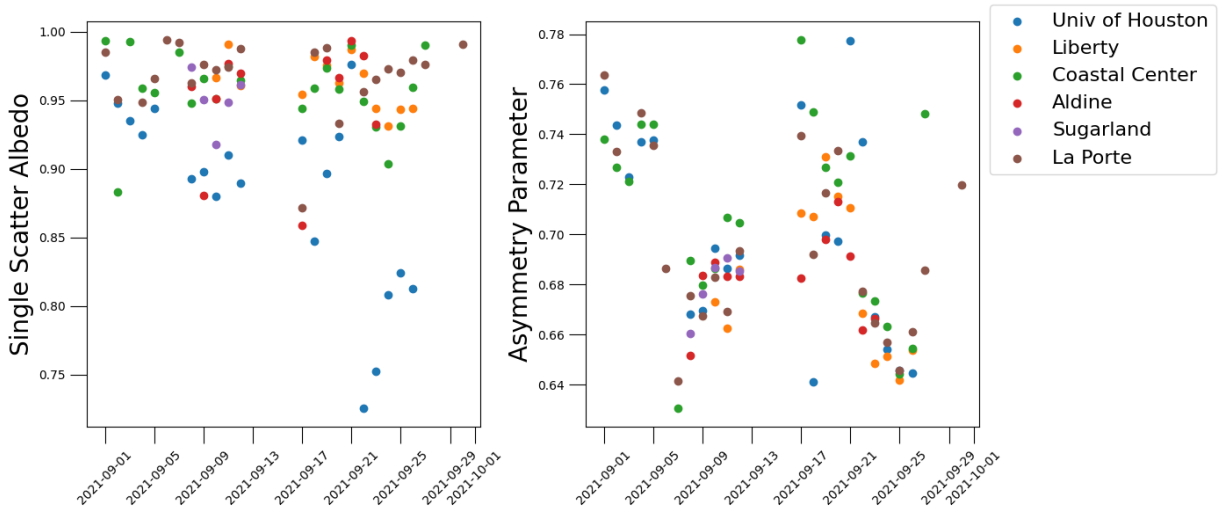


Figure 7.3: Daily mean values for single scatter albedo(a) and asymmetry parameter(b) retrieved from six AERONET instruments at 440nm in the Houston-Galveston-Brazoria area during September 2021.

In addition, the LIDAR instrument has a minimum detection limit of 100m, which means that the backscatter profile below this altitude is not accurate. This portion of the backscatter profile is removed after smoothening, and a replacement is linearly extrapolated below 100m

at twice the slope as measured from 100m to 200m. Figure 7.4 a) shows these first few steps starting with the original backscatter profile, in blue and the smoothed and corrected profile, in red. Above 1Km, the original profile begins to vary much more wildly as the effect of noise becomes more pronounced, however the smoothed profile instead begins to shift toward 0 at higher altitudes, until it crosses 0 at around 3.2Km. This altitude is set as the upper limit of this profile.

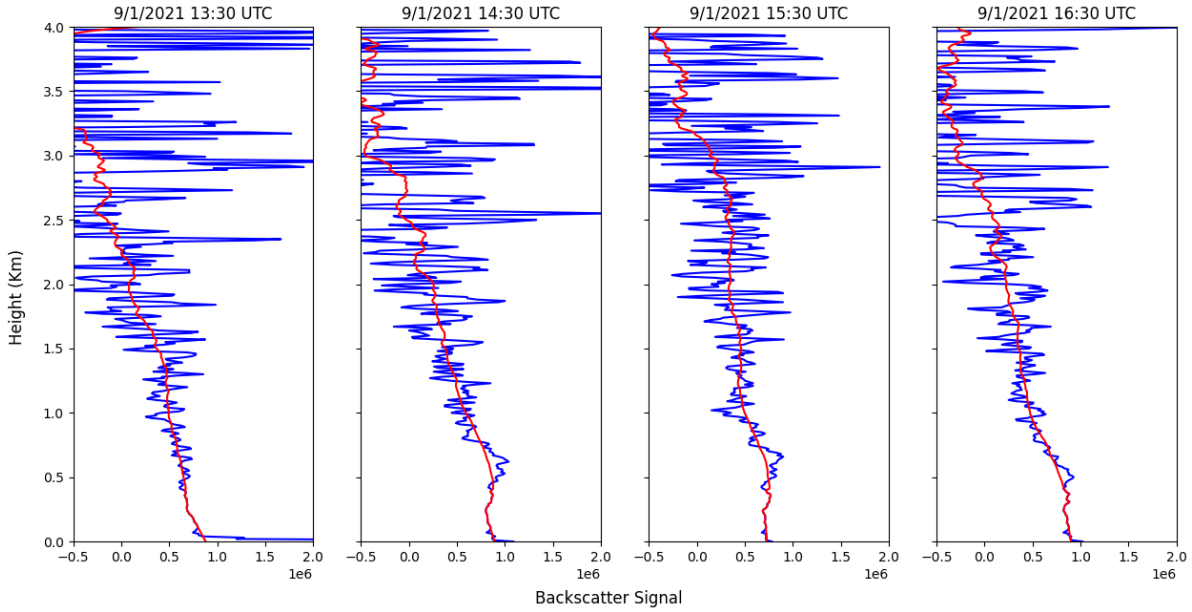


Figure 7.4: Four backscatter profiles (blue) temporally averaged over a one hour period. The red line represents the corrected backscatter profile, where further smoothing has been applied, and the bottom 40m has been corrected by linearly extrapolating the backscatter signal in the 100-40m range.

Once the smoothed profile are prepared, the backscatter profiles must first be converted to aerosol profiles at the LIDAR's operating wavelength of 910nm:

$$X_{scale} = AOD_{910}/B_{int} \tag{7.1}$$

Where AOD_{910} is the AOD value at 910nm, B_{int} is the integrated backscatter profile over

height. One issue, however, is that AERONET instruments do not retrieve AOD at 910nm. Instead, the AOD at 870nm and 1020nm must be used to calculate the angstrom exponent, which can scale the AOD retrieved from 870nm to 910nm

$$\alpha = -\frac{ln(\frac{AOD_{1020}}{AOD_{870}})}{ln(\frac{1020}{870})} \tag{7.2}$$

$$AOD_{910} = AOD_{870} \cdot (\frac{910nm}{870nm})^{\alpha} \tag{7.3}$$

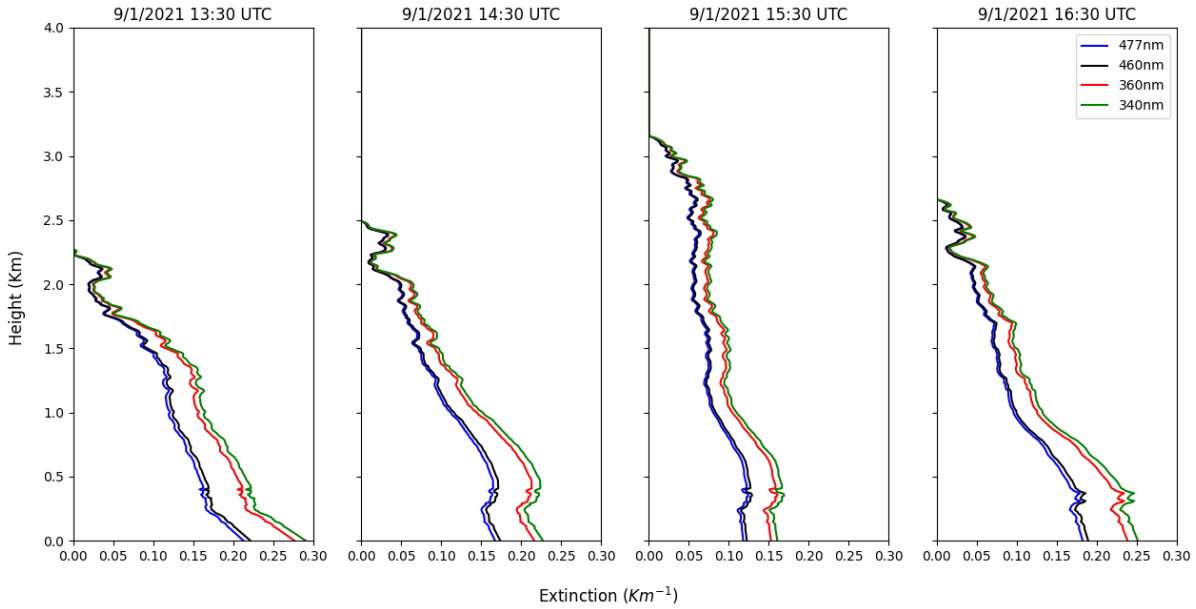


Figure 7.5: The aerosol extinction profiles of the four corrected backscatter profiles from Figure 7.4, scaled to 477nm (blue), 460nm (red), 360nm (red) and 340nm (green).

Where α is the angstrom exponent between 870nm and 1020nm which is profided as part of AERONET retrievals, and AOD_{870} is the AOD at 870nm. Now that the aerosol profile at 910nm has been processed, the profile can be scaled to the four wavelengths used for the sensitivity study: 477nm, 460nm, 360nm, and 340nm. This scaling is performed in the same way as the previous step, with angstrom coefficients available between 1020 and 320nm. The 460nm and 477nm wavelengths are used to simulate at the center wavelength of the NO_2

Visible DOAS retrieval, and at a strong absorption line of $O2O2$, respectively; the 360nm wavelength was selected as the center wavelength for the NO_2 UV DOAS retrievals, however since O_2O_2 shows high absorption at this wavelength as well a separate UV wavelength was not needed. Finally, the 340nm wavelength was selected due to it being the center wavelength of the $HCHO$ DOAS retrievals.

Finally, in order to ensure the altitude grid matched the other inputs into the radiative transfer simulator, the aerosol extinction profiles are interpolated onto the same grid as the atmospheric profiles. The atmosphere profiles used for the simulations includes profiles of air temperature, pressure, and relative humidity, as well as certain trace gases like Ozone and NO_2 that were collected from Ozonesonde flights launched during the TRACER-AQ field campaign approximately once per day.

Figure 7.5 shows the final extinction profiles of the backscatter profiles shown in Figure 7.4 scaled by the AOD at 477, 460, 360, and 340nm. In order to perform the sensitivity study on the effect of the aerosol profile, three sets of aerosol profiles were created, the first representing mean aerosol conditions using the mean AOD, the second representing high aerosol conditions using the twice the standard deviation of AOD measurements added to the mean AOD, and one representing low aerosol conditions using twice the standard deviation of AOD measurements subtracted from the mean AOD.

7.3 Effect of Single Scatter Albedo & Asymmetry Parameter

Due to the lack of data for Single Scatter Albedo and Asymmetry Parameter from the AERONET sites, an hourly average of both properties is not feasible to be used for radiative

transfer simulations. On the other hand, there is enough data to provide daily averages of both properties. This daily average introduces further complications, however, chiefly the larger range of aerosol conditions that a mobile instrument can measure in over an entire day as opposed to a single hour. Therefore, in order to understand how the daily changes in Single Scatter Albedo and Asymmetry Parameter can impact radiative transfer simulations, an initial sensitivity study was performed to gauge the impact of both input parameters on the uncertainty of the output.

This sensitivity study analyzes the sensitivity of the radiative transfer model to the Single Scatter Albedo and the Asymmetry Parameter while using a standard aerosol configuration[156], to determine much the output AMF can change. The Single Scatter Albedo and the Asymmetry Parameter measurements, while not originally retrieved at 440nm, are linearly interpolated using retrievals of Single Scatter Albedo and Asymmetry Parameter at higher wavelengths to 460 and 360nm. The resulting values are averaged together in order to determine what the mean value of both parameters are across the local network, while the upper and lower bounds each day are taken from twice the standard deviation of each day's set of measurements.

Figure 7.3 shows the daily averaged Single Scatter Albedo and Asymmetry values retrieved from the six AERONET sites during TRACER-AQ. Typically, the asymmetry parameter can range from 0.625 to 0.8 in Houston, however the difference between high and low values on individual days ranges only between 0.05 and 0.15. Aside from the AERONET site at the University of Houston Main Campus, which is considered an urban location, the Single Scatter Albedo retrieved from the other instruments remain close to 1.0, with almost all retrieved SSA's being above 0.7. The typical differences in daily instrument retrievals, however, range between 0.05 and 0.2, University of Houston Main Campus instrument determining the standard deviation of each day's dataset.

Using these ranges of values, the effect of the daily estimation of Single Scatter Albedo and Asymmetry parameter can be investigated by altering a typical atmosphere, as defined by [156], provided with the Libradtran library. The aerosol Single Scatter Albedo and Asymmetry Parameter were then changed from their observed minimum to maximum for all of September in ten steps individually, and the model was run at each step at 477nm and 360nm for ten SZA's from 0° to 90°. The retrieved box air mass factors were then used to retrieve air mass factors of O_2O_2, a trace gas with a consistent profile dependent on the vertical profile of air and as such the impact of the vertical profile in the retrieval of the AMF should be minimal. Finally, for all parts of the sensitivity study, the surface albedo was assumed to be 0.15, representing the estimated albedo of both asphalt and concrete [74], which the instrument can be expected to be operating above at any point in time.

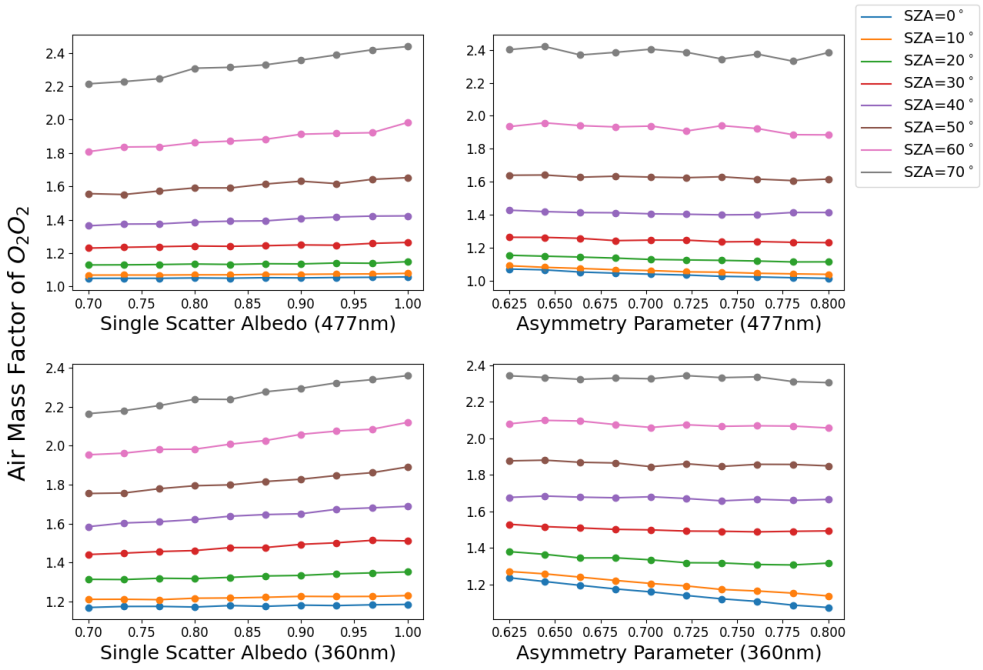


Figure 7.6: The AMF for O_2O_2 as the single scatter albedo was increased from 0.7 to 1.0, for 477nm(a) and 360nm(c), as well as AMFs for O_2O_2 as the asymmetry parameter was increased from 0.625 to 0.8 for 477nm(b) and 360nm(d). Each line corresponds to the solar zenith angle used to retrieve AMFS, from 0° to 70° in 10° increments.

Figure 7.6 shows the shift in the Air Mass Factors for O_2O_2 as both Single Scatter Albedo and Asymmetry Parameter are increased from minimum values. At both UV and Visible wavelengths, single scatter albedo increasingly deviated from the minimum AMF, with solar zenith angles closer to the horizon seeing larger deviations than solar zenith angles closer to zenith. In spite of this, AMFs at both wavelengths only deviate at a maximum of 0.2 using the limits found for September. At each solar zenith angle, the deviation is linear, with increasing solar zenith angle increasing the slope of this deviation. Because of this linear nature, it is evident that the error that can occur on a daily basis, with a maximum deviation of the single scatter albedo of 0.2, the error due to an incorrect single scatter albedo estimate is closer to 5%.

The Asymmetry Parameter, on the other hand, has an inverse linear relation to increasing values, and is much more sensitive to the retrieval wavelength than the single scatter albedo, with maximum differences in the AMF at 360nm reaching up to 0.15. In addition, low solar zenith angles, in particular 0° and 10° show much larger deviations than larger solar zenith angles. However, the minimum solar zenith angle in Houston in September is close to 20° which show much lower deviations, behaving much more similarly to the rest of the solar zenith angles tested. As such, the maximum deviation of the retrieved air mass factors due to errors in the asymmetry parameter estimation amount to 2.5% at 477nm, and 5% at 360nm.

7.4 Effect of the Aerosol Profile

The second portion of the sensitivity study focused on the effect of averaging both the aerosol profile as well as the spatially averaged AOD on retrieved air mass factors. The averaging of both every hour leads to aerosol information from a wide variety of locations being averaged

together, and while is represented by the averaging of both the aerosol profile and AOD, there will be some uncertainty due to deviations in the assumed behavior of the averaged aerosol conditions and the true conditions.The high, low, and mean aerosol profiles and AOD were passed through the radiative transfer simulator and the resulting box Air Mass Factors were converted into O_2O_2 air mass factors in the same manner as in Section 7.3 for both UV and Visible wavelengths. The difference in air mass factors between the high and low aerosol conditions and the mean aerosol conditions are presented as a function of solar zenith angle in Figure 7.7.

The resulting box air mass factors represent the highest case, and average case scenario for aerosol conditions, which were then converted into air mass factors for NO_2 using the mean profile measured by ozonesondes launched during the TRACER-AQ campaign. Figure 7.7 shows the deviation of air mass factors for NO_2 of under high and low aerosol loadings compared to the mean aerosol conditions. Deviations from mean aerosol conditions are very consistent for most solar zenith angles, however at high solar zenith angles ($> 70°$), the error begins to compound, as the light begins to travel more and more through the troposphere. AMF retrieval errors at 477nm remain consistently less than ± 0.05 outside of large solar zenith angles, and are not sensitive to solar zenith angle. This behavior indicates that, outside of twilight, deviations of air mass factor are not sensitive to the solar zenith angle. The retrievals at 360nm, however, are much more sensitive to the potential differences in aerosol conditions, with differences in both the high and mean conditions as well as the low and mean conditions being twice as large as their visible counterparts, close to ± 0.1 outside of high solar zenith angles. For all of the aerosol scenarios tested, the standard deviation (2σ) was approximately 5% at 477nm and 7.5% at 360nm, which means that error due to incorrect aerosol profiles is expected to remain below 5% for visible AMFs and 7.5% for UV AMFs.

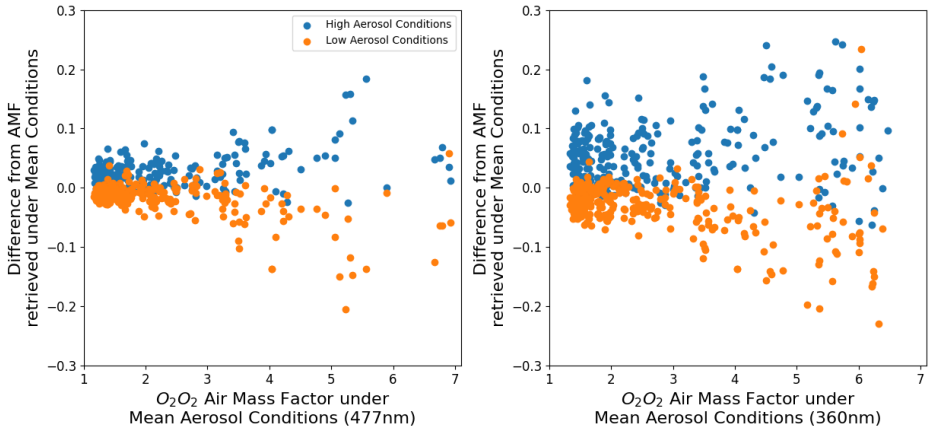


Figure 7.7: The absolute difference between O_2O_2 Air Mass Factors retrieved from high and mean aerosol conditions (blue) and from low and mean aerosol conditions (orange) plotted as a function of O_2O_2 Air Mass Factor retrieved from mean aerosol conditions for 477nm retrievals(a) and 360nm retrievals(b).

7.5 Effect of the A Priori Profile

While the uncertainty of the input aerosol information has been quantified, this uncertainty only includes the data processing up to the calculation of box Air Mass Factors. The estimation of Air Mass Factors also requires an assumed profile, to be used in the estimation of partial VCDs at each atmospheric layer simulated. This a priori profile is typically difficult to estimate, due to the wide range of possible trace gas vertical distributions, which is compounded in both TRACER-AQ field campaigns by the mobile nature of the measurements. Because of this additional uncertainty, a single a priori profile could lead to significant error if the true vertical profile deviates too far from the assumed profile. On the other hand, Zenith DOAS and MAX-DOAS fast sky scan measurements are unable to retrieve vertical profiles, and any estimation of what profile was present requires the VCD to be able to estimate vertical distributions with the Column to Surface Ratio.

The O_2O_2 profile, which is directly proportional to the profile of air, could potentially suffice as an alternative for an a priori profile. The O_2O_2 can be both estimated from surface

measurements of weather conditions[141] and directly measured by atmospheric soundings, which were taken at multiple points throughout both field campaigns. In order to determine how effective this method might be, the O_2O_2 profile is tested as an alternative to estimating an a priori profile, and an average of profiles measured from 24 ozonesondes launched during TRACER-AQ1 is used as the baseline profile for the sensitivity study.

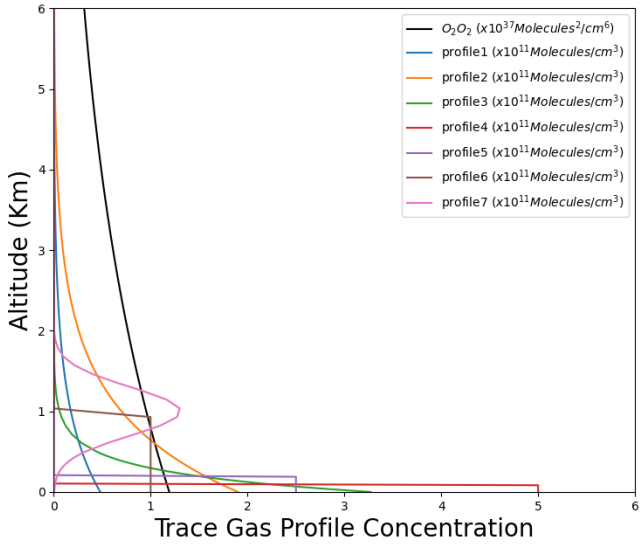


Figure 7.8: The vertical profiles used in the 2019 MAX-DOAS profile inter-comparison study[5]. These profiles serve as the basis for the profile-based prtion of the sensitivity study. Details on the profile shape are provided in Table 7.1. In addition, the vertical profile of O_2O_2 (black) is included, which is derived from the mean atmospheric conditions measured by balloon sondes launched during TRACER-AQ.

Table 7.1: Description of trace gas profiles used for sensitivity study

Profile	Description	VCD ($\times 10^{15} \frac{Molecules}{cm^2}$)	Max Concentration($\times 10^{11} \frac{Molecules}{cm^3}$)
Profile 1	Exponential, 1Km Scale Height	5.00	0.48
Profile 2	Exponential, 1Km Scale Height	19.99	1.90
Profile 3	Exponential, 0.250 Km Scale Height	9.93	3.27
Profile 4	Box Profile, 100m Height	5.00	5.00
Profile 5	Box Profile, 200m Height	5.00	2.50
Profile 6	Box Profile, 1Km Height	10.00	1.00
Profile 7	Gaussian at 1Km, 300m FWHM	10.00	1.31

For the a priori sensitivity study, a set of trace gas profiles was selected from the first

seven profiles used in the 2019 MAX-DOAS profile inter-comparison study conduced by Udo Fries[5], more information can be found in Figure 7.8 and Table 7.1. These profiles represent seven likely configurations of both NO_2 and $HCHO$ that can be present in a high source environment like Houston. In addition, a mean O_2O_2 profile was created from the average profile of air measured by 24 ozonesondes launched during September, which can be approximated by an exponential profile with a maximum concentration of $1.19\times10^{37}\,\frac{Molecules^2}{cm^6}$ and a scale height of 4.5Km. The air mass factors retrieved from the seven profiles are then compared to the air mass factors retrieved using the O_2O_2 profile, and the diurnal average of the percent differences relative to the O_2O_2 profile are plotted in Figure 7.9.

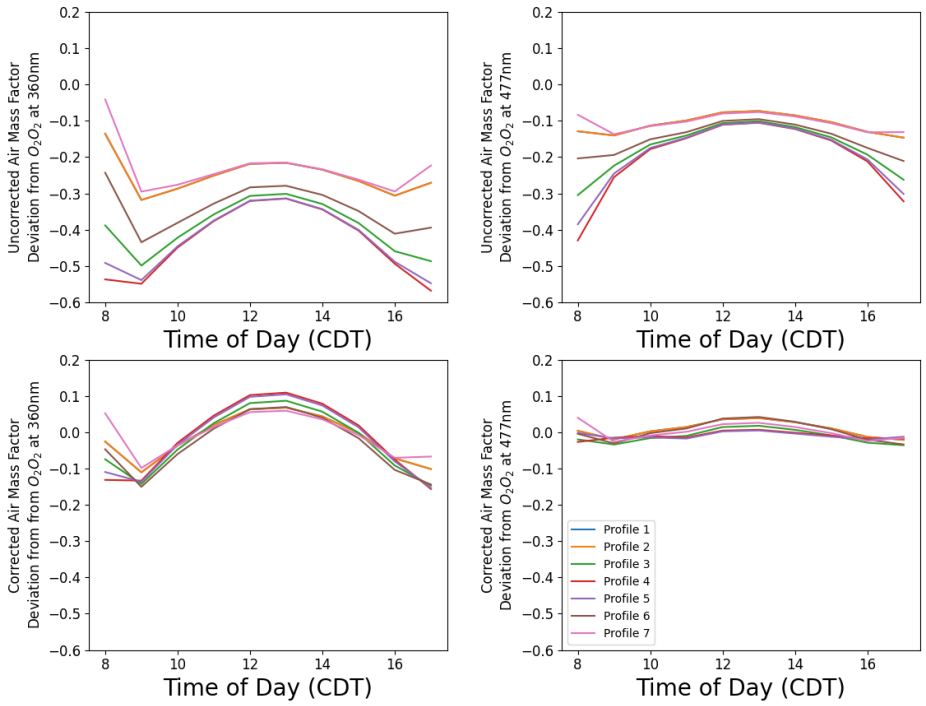


Figure 7.9: The diurnal average of uncorrected differences between the air mass factors retrieved from the seven profiles and the O_2O_2 profile in the UV band (a) and Visible band (b), as well as the diurnal average of corrected differences between the air mass factors retrieved from the seven profiles and the O_2O_2 profile at 360nm(c) 477nm(d).

The O_2O_2 profile overestimates the air mass factor at both 360 and 477nm, and at all solar

zenith angles, as can be seen in Figure 7.9 a) and b). Outside of high solar zenith angles, UV O_2O_2 AMFs remain between 0.2-0.4 larger than the AMF retrieved from the other trace gas profiles, with a clear solar zenith angle dependency. Visible air mass factor differences are much smaller, with O_2O_2 AMFs remaining between -0.08 and -0.2 outside of high solar zenith angles.

The errors due to potential profile mismatch are much larger than the errors from the aerosol inputs, and shows that the O_2O_2 profile leads to too different of an Air Mass Factor to be used to retrieve the AMFs of other trace gases by itself. However, the differences between air mass factors has a linear relation, as can be seen in Figure 7.10. For both UV and Visible wavelengths, the air mass factors retrieved from the O_2O_2 profile and the other profiles are closely correlated ($r^2 > 0.97$) and similar linear behaviors. As such, it is feasible to correct the O_2O-2 air mass factors to agree with the air mass factors retrieved from the profiles. Figures 7.9 c) and d) show the differences between the corrected O_2O_2 air mass factors and air mass factors retrieved from the profiles. Now, the maximum difference is closer to ± 0.1 for UV and ± 0.05 for Visible wavelengths, with a clear solar zenith angle dependence. In addition in individual profiles deviations are less than 5% from other profiles, which shows that the seven profiles chosen likely agree with each other better than with the O_2O_2 profile. This indicates that the changing of the vertical profile will impact the air mass factor by no more that 10%, which when combined with the assumptions made for the aerosol conditions, leads to a total estimated uncertainty of 20% for Visible air mass factor retrievals. UV retrievals, on the other hand, were consistently higher than the Visible counterparts. This leads to a higher expected uncertainty due to the assumed aerosol properties, at 25%.

7.6 Discussion

While the difference between the air mass factors retrieved from the O_2O_2 profile correlate well with the other seven profiles used for the study, the difference in retrieved air mass factor is too large for the O_2O_2 profile to be effectively used in place of an assumed a priori profile. Because the differences between each of the profiles in smaller than the difference between any of the seven profiles and the O_2O_2 profile, it is still more effective to assume a vertical profile that closely matches the behavior of the trace gas being analyzed than to use an easily measurable profile that does not behave similarly to the trace gas measured, such as O_2O_2.

However, with sufficient knowledge of the trace gas profile present during measurement, the O_2O_2 profile could be used as a substitute, however prior knowledge of even the general shape of the trace gas profile would be still a preferable alternative to the O_2O_2 profile.

The increase in UV AMF uncertainty compared to the Visible retrievals results in an increase in the mean uncertainty for both the NO_2 and $HCHO$ VCDs. Not only does the larger AMF uncertainty result in poorer quality data, but increased uncertainty in the UV dSCDs is also propagated through the analysis, resulting in far more of both $HCHO$ and UV NO_2 VCDs not meeting the quality standard set for the datasets. As such, it is not recommended to average aerosol properties from a local aerosol measurement network to retrieve UV AMFs. On the other hand, the issue could reside in the increased variability of aerosol scattering properties in a polluted city such as Houston. In order to determine how valid this AMF retrieval technique is, other, less polluted cities should also be used as test locations, in order to determine if this variability in aerosol conditions is the primary cause of the higher uncertainty.

Uncertainty could also be further reduced by limiting the measurement area to locations

within close proximity of an aerosol measuring instrument. For instance, Wu et. al. [154] performed radiative transfer calculations based on aerosol conditions measured within close proximity to a power plant. Because the mobile DOAS measurements were performed on public roads that remained close to the plant, it is reasonable to conclude that the measurements made by the instrument at the power plant are the only measurements of aerosol optical properties to perform radiative transfer calculations.

Retrievals of Visible AMFs are still of high enough quality to be used for processing dSCDs into VCDs, without introducing unacceptable amounts of uncertainty into the measurements. By using only visible retrieval windows, it is feasible to produce VCDs from mobile DOAS measurements with a sufficient network of aerosol measuring instruments, providing these instruments provide enough measurements at enough locations to generate mean values of the aerosol optical properties.

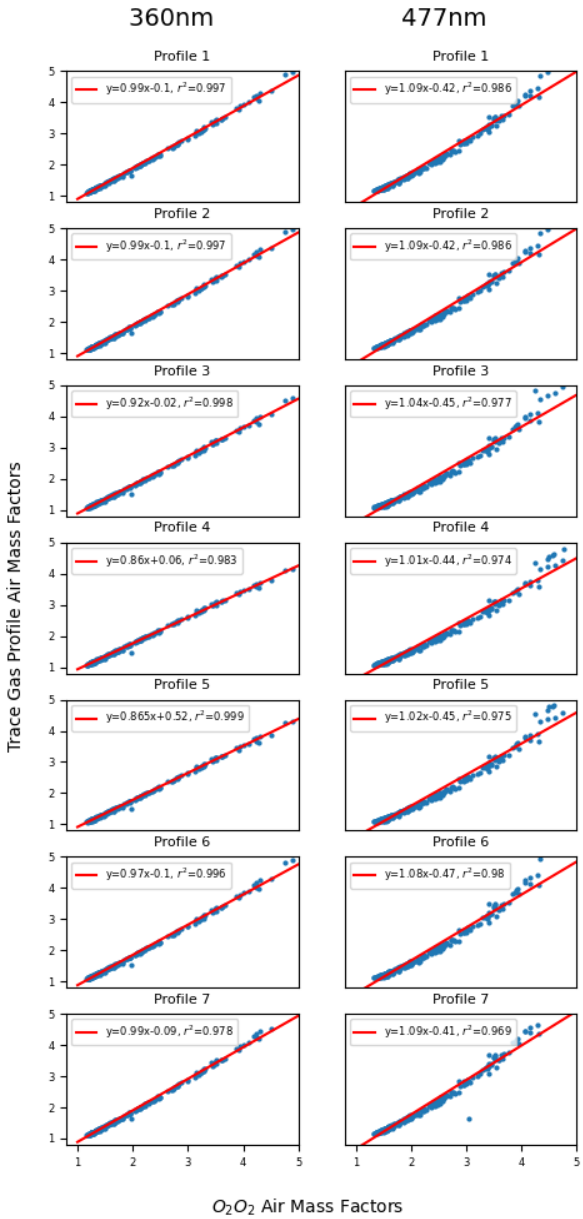


Figure 7.10: Linear fits of the air mass factors retrieved from the seven profiles and the air mass factors retrieved from the O_2O_2 profile at 360nm(column a) and 477nm(column b)

Chapter 8

Conclusions

This dissertation presents analysis techniques to determine the spatial distribution of trace gas, both vertically and horizontally, as well as a demonstration of further information that can be gained from these techniques. The results shown have accomplished the dissertation objectives by 1) demonstrating through sensitivity study the uncertainty added to estimations of Air Mass Factors through estimations of aerosol scattering properties in a heterogeneous environment, 2) used the column to surface ratio to identify the vertical distribution of trace gas, and relate these distributions to sources as well as estimate the impact of these sources on Ozone production on high Ozone days observed during the TRACER-AQ1 field campaign, 3) used the Horizontal Heterogeneity Index to determine the horizontal heterogeneity of trace gases in a measuring area, and used this index, along with the column to surface ratio, to triangulate sources and determine how the mixing of trace gases from various sources led to increased Ozone on days where high Ozone was observed during the TRACER-AQ2 field campaign, and 4) used the column to surface ratio and Horizontal Heterogeneity Index to identify which distributions of trace gas lead to poor satellite validation by Ground-Based DOAS instruments.

By comparing Zenith DOAS measurements to in-situ surface concentrations, an estimation of the vertical distribution of trace gas is obtained. This value, known as the column to surface ratio, is an easily measurable quantity, with only a single Zenith DOAS and in-situ measurement required for calculation. This provides a rapid estimation of the effective height

of the trace gas vertical profile, without requiring a large set of measurements as are typically used by other DOAS instruments for profile retrieval. The column to surface ratio is also highly influenced by local sources, such as industrial and vehicular emissions, and can be used to estimate the proximity and influence of sources on local air quality. In particular, two high ozone events during the TRACER-AQ field campaign in 2021 were used as case studies, and the sources most likely responsible for the observed increase in Ozone, as well as the approximate height of the plumes responsible for transporting the trace gas, were identified. In addition, the column to surface ratio was found to be an effective at estimating the ability of Ground-Based DOAS instruments to validate Satellite-Based DOAS measurements. Days in which the mean column to surface ratio were less than 0.7 Km during TROPOMI overpass times saw improved comparisons between TROPOMI and Zenith DOAS measurements than when the mean column to surface ratio was greater than 0.7 Km. This behavior is likely due to the sensitivity of Satellite-Based DOAS instruments decreasing at higher altitudes, leading to worse satellite measurements when trace gas is distributed above the surface. However, these two quantities are only mildly correlated, which indicates that there are other factors influencing Satellite-Based DOAS and Ground-Based DOAS measurements. Regardless, consideration of the column to surface ratio when making comparisons between Satellite-Based DOAS and Ground-Based DOAS measurements can ensure that only trace gas that both instruments are sufficiently sensitive to are used for comparisons.

In addition, Zenith DOAS can also be compared between MAX-DOAS measurements measured at at least two different azimuth angles can be used to estimate the horizontal distribution of trace gas around the instruments. This estimation, called the Horizontal Heterogeneity Index, uses the difference between MAX-DOAS and Zenith DOAS VCDs to estimate how different, or how heterogeneous, a trace gas is in the measurement area. This analysis technique provides a more effective estimation of nearby sources and their impact on trace

gases in a measurement area, with additional comparisons between MAX-DOAS viewing directions the source of heterogeneity can be triangulated. During the TRACER-AQ2 field campaign in 2022, two high Ozone events were used as a pair of case studies to both identify what sources contributed to the observed increase in Ozone, as well as how these sources interacted with their surroundings to produce Ozone. However, while it is clear that meteorological patterns on both days dictated the transport of trace gas into the measurements areas, however a pair of days is not enough time to understand the full impact of meteorology on the high Ozone events observed. A longer study on high Ozone events in Houston would be better suited to make these types of conclusions than a short term field campaign. In addition, the Horizontal Heterogeneity Index showed a much closer correlation to poor satellite validation than the column to surface ratio. This behavior is due to the spatial averaging that Satellite-Based DOAS measurements undergo due to the limitations on spatial resolution of these instruments. This means that spatial averaging of regions of high horizontal heterogeneity at the surface by Satellite-Based DOAS instruments will lead to very different measurements than Ground-Based DOAS measurements. However, the correlation between validation error and the Horizontal Heterogeneity Index is, while higher than the correlation between validation error and column to surface ratio, only moderately high, indicating the influence of not just the vertical distribution of trace gas but also other factors influencing satellite validation. While other potential limiting factors to satellite validation should be explored, the horizontal heterogeneity of trace gas within a measurement area is likely the primary driver of poor satellite validation, and filtering out high heterogeneity measurements measured by Ground-Based DOAS measurements will lead to improved validation efforts.

Finally, in order to compare Zenith DOAS measurements to both in-situ concentrations and MAX-DOAS measurements, the absolute vertical column density that the Zenith DOAS instrument measured needed to be estimated. However, calculation of the Zenith DOAS VCD

requires radiative transfer simulations which make use of aerosol scattering properties that can not be measured effectively onboard a mobile platform. In order to overcome this limitation, a novel approach to estimating the scattering properties of aerosols was devised using aerosol measuring instruments scattered around Houston, Texas to generate an estimation of the mean aerosol conditions at a given time. However, due to the heterogeneous nature of an urban environment, especially one with as high emissions of both trace gas and aerosols like Houston, serious consideration needed to be taken to understand how much uncertainty this estimation of aerosol conditions introduced into the radiative transfer simulations. A sensitivity study was performed using the aerosol data collected during TRACER-AQ1, which was used to devise reasonable limits on how much aerosol conditions could vary in the city, and these limits were used to test the impact of incorrect aerosol information being used to estimate air mass factors. This included the single scatter albedo, asymmetry parameter, aerosol vertical profile, and aerosol optical depth. In addition, the assumed a priori trace gas profile, which is used to convert the results of radiative transfer simulations to a trace gas specific air mass factor, was also used as a parameter to analyze the sensitivity of the AMF uncertainty to an incorrect profile being used. When combined, the uncertainty from all parameters tested totaled less than 20%. This is an acceptable amount of uncertainty, which when compared with other Zenith DOAS studies which do not make considerations on changing aerosol conditions or make assumptions about the AMF to avoid radiative transfer simulations, is less than similar studies. Because the uncertainty is within acceptable levels, this technique of estimating aerosol conditions allows for a lower uncertainty VCD to be retrieved from Zenith DOAS measurements than previous studies, making the technique a more effective measurement in locations where nearby aerosol information might not be available and on mobile platforms, where Zenith DOAS's rapid measurement technique is more desirable.

This dissertation serves as a proof of concept that demonstrates how making considerations about how the spatial behavior of measurements can yield information on the spatial distribution of trace gas. Even using a small number of different measurement directions and instruments, the vertical and horizontal distribution of trace gas can be estimated and used to determine the sources of trace gases, as well as how these gases are interacting to produce other harmful trace gases, such as ozone. However, the work presented in this dissertation is the result of two month long field campaigns which were both held in September of 2021 and 2022. Because of this, the conclusions that can be drawn from analysis of the spatial distribution of trace gas is limited to short term behaviors observed during case studies. In order to fully understand the impact of spatial trace gas distributions, future studies should be held over longer periods of time in order to more effectively understand the diurnal, weekly, seasonal, and even yearly patterns that emerge in trace gas distributions. To accomplish this, future studies would likely need to rely on a network of stationary instruments collecting data in a diverse set of locations within a heterogeneous environment, such as a major city or industrial hub. However, mobile DOAS measurements can serve as an effective tool to identify locations of interest where high trace gas heterogeneity is observed, which can better inform long term projects in the same area. Regardless, this dissertation serves as a blueprint for future strategies regarding trace gas heterogeneity, and can be used to inform future projects dedicated to trace gas measurement, not just in a polluted environment like Houston, Texas, but in any location in the world.

Appendices

Appendix A

Additional Figures

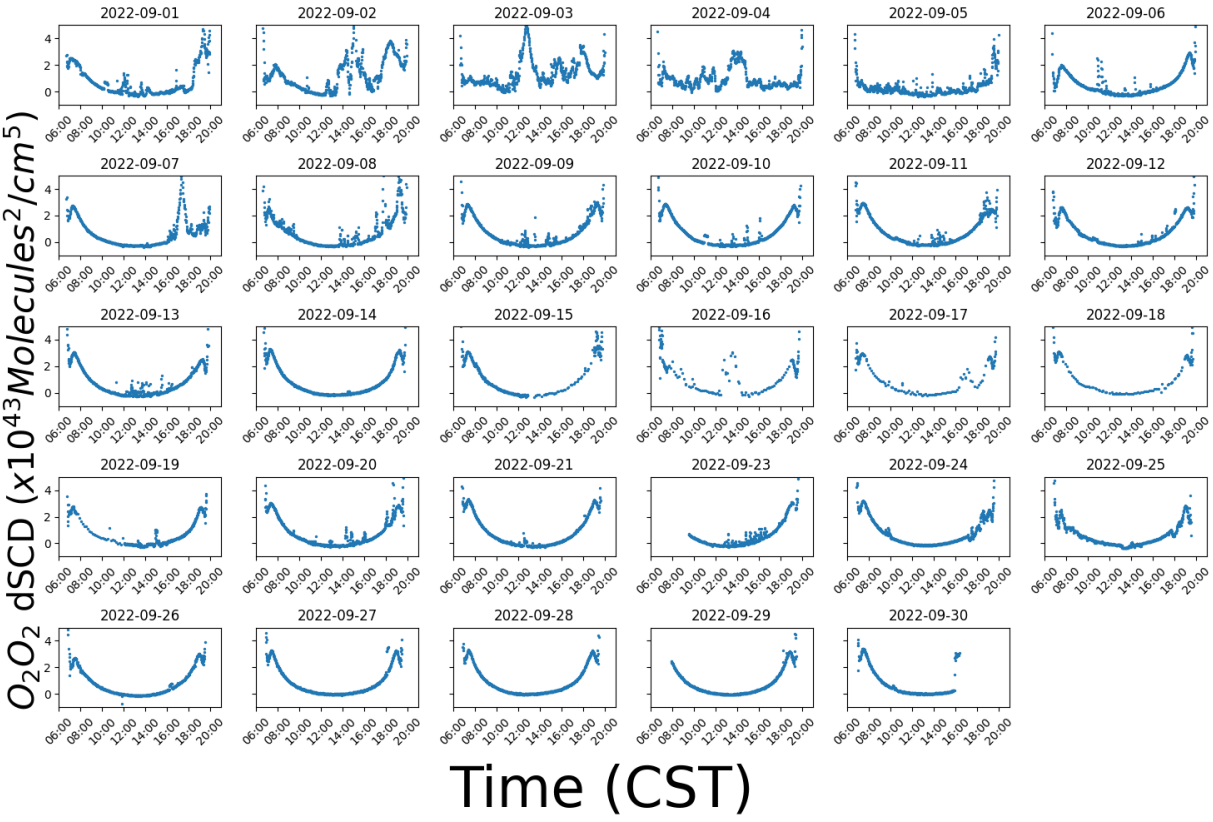


Figure A.1: Comparison of O_2O_2 dSCDs retrieved from Zenith measurements for the Intensive Operations period of TRACER-AQ2. Time is given in local time (CST), and columns in $\times 10^{43} \frac{Molecules^2}{cm^5}$

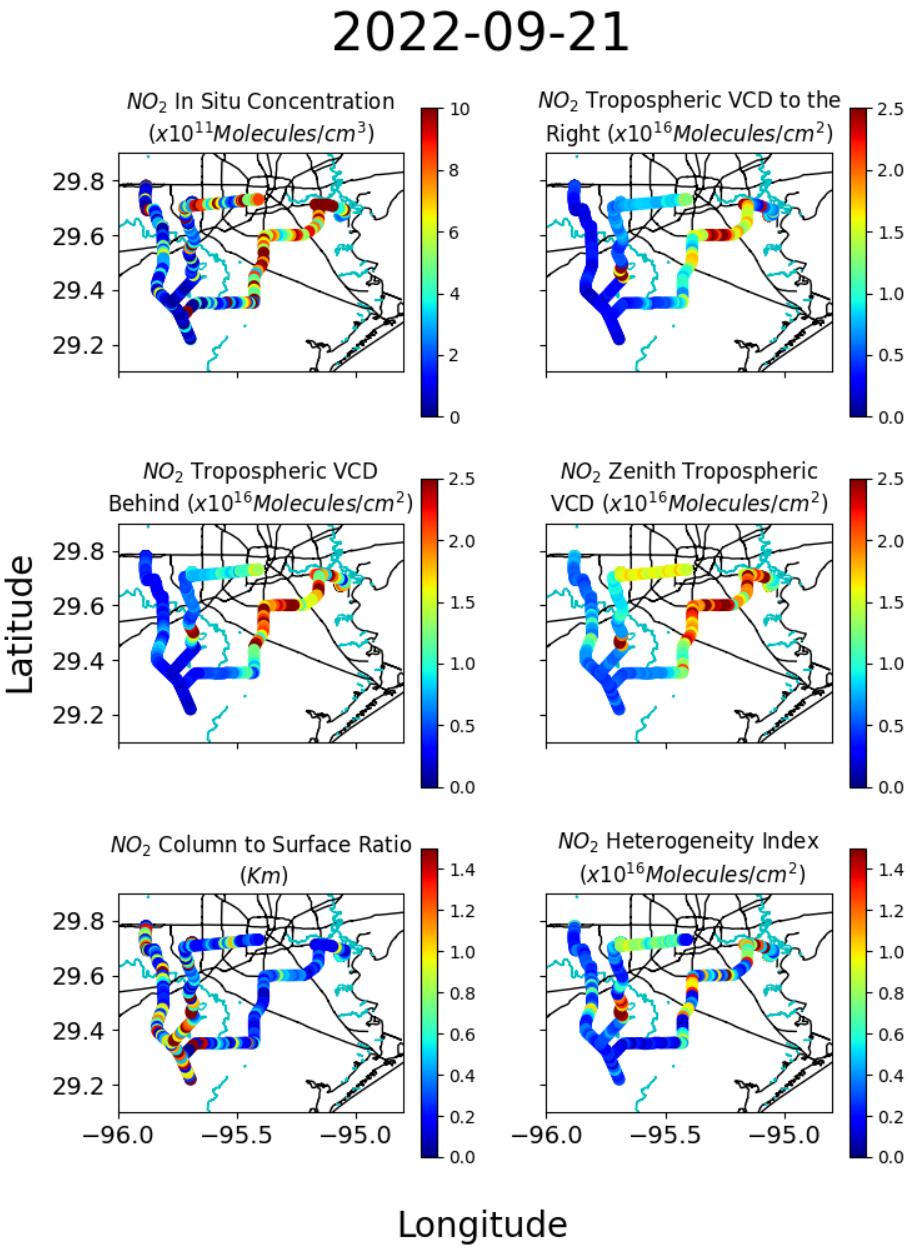


Figure A.2: a) The 1-minute average HCHO in-situ concentrations measured on September 21 by the mobile lab in $\frac{Molecules}{cm^3}$ b) The 1 minute average Pandora 148 HCHO columns c) The 1 minute average Pandora 168 HCHO columns d)The 1 minute average Pandora HCHO Zenith columns e) The column to surface ratio between in-situ and Pandora Zenith columns. f) The heterogeneity index calculated from both MAX-DOAS instruments as well as Zenith columns.

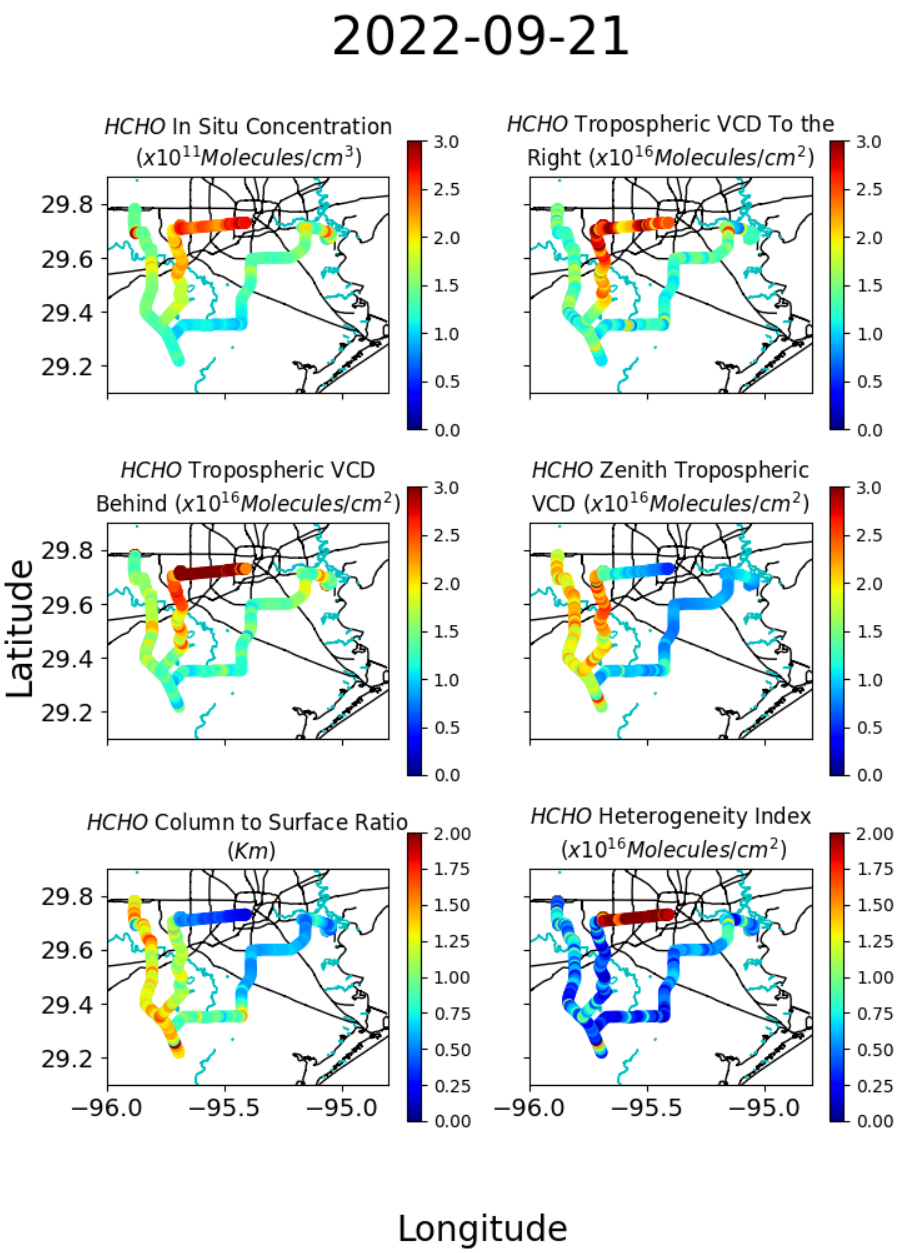


Figure A.3: a) The 1-minute average HCHO in-situ concentrations measured on September 21 by the mobile lab in $\frac{Molecules}{cm^3}$ b) The 1 minute average Pandora 148 HCHO columns c) The 1 minute average Pandora 168 HCHO columns d)The 1 minute average Pandora HCHO Zenith columns e) The column to surface ratio between in-situ and Pandora Zenith columns. f) The heterogeneity index calculated from both MAX-DOAS instruments as well as Zenith columns.

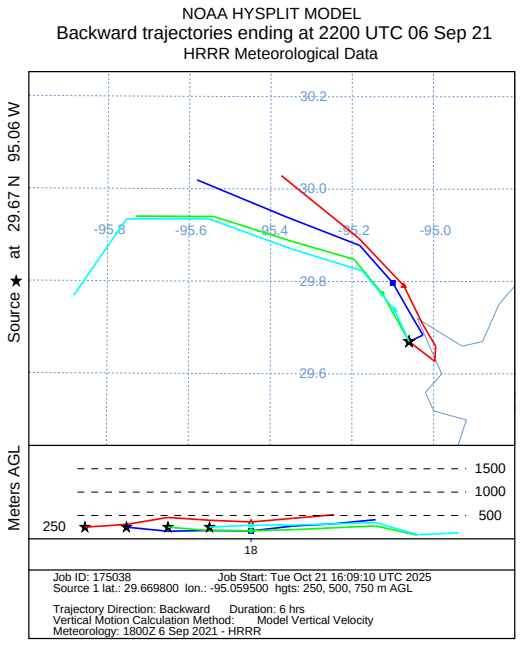


Figure A.4: HYSPLIT [4] modeled 3 hour back-trajectory showing the path air masses at 17:00 (red), 16:00 (blue), 15:00 (green), and 14:00 (cyan) took to arrive at the la Porte Airport (starred) with an end altitude of 250m.

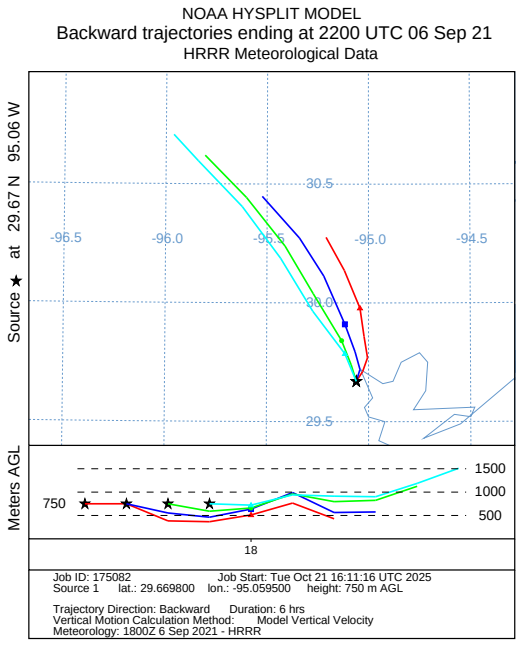


Figure A.5: HYSPLIT [4] modeled 3 hour back-trajectory showing the path air masses at 17:00 (red), 16:00 (blue), 15:00 (green), and 14:00 (cyan) took to arrive at the la Porte Airport (starred) with an end altitude of 750m.

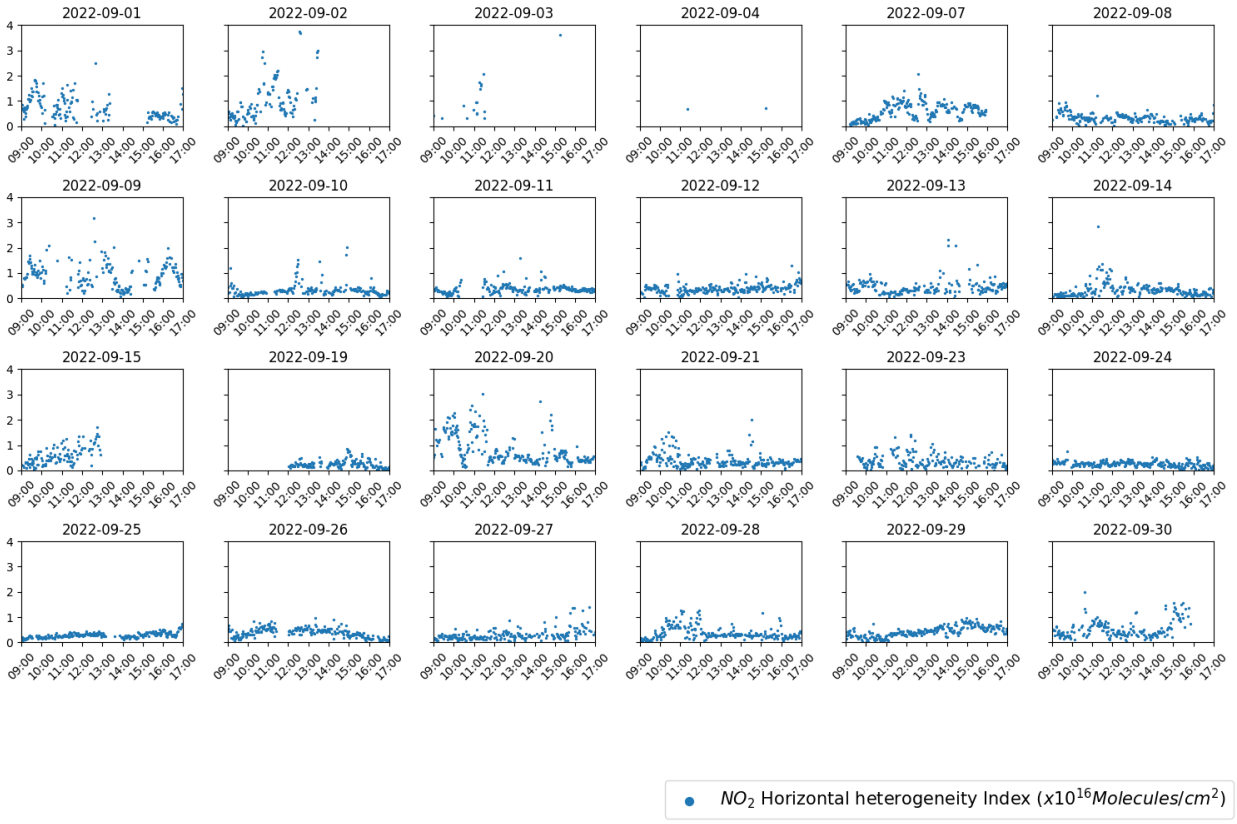


Figure A.6: The Horizontal heterogeneity Index of each day's set of measurements for the Intensive Operations period of TRACER-AQ2. Time is given in local time (CST), and index in $\times 10^{16} \frac{Molecules}{cm^2}$

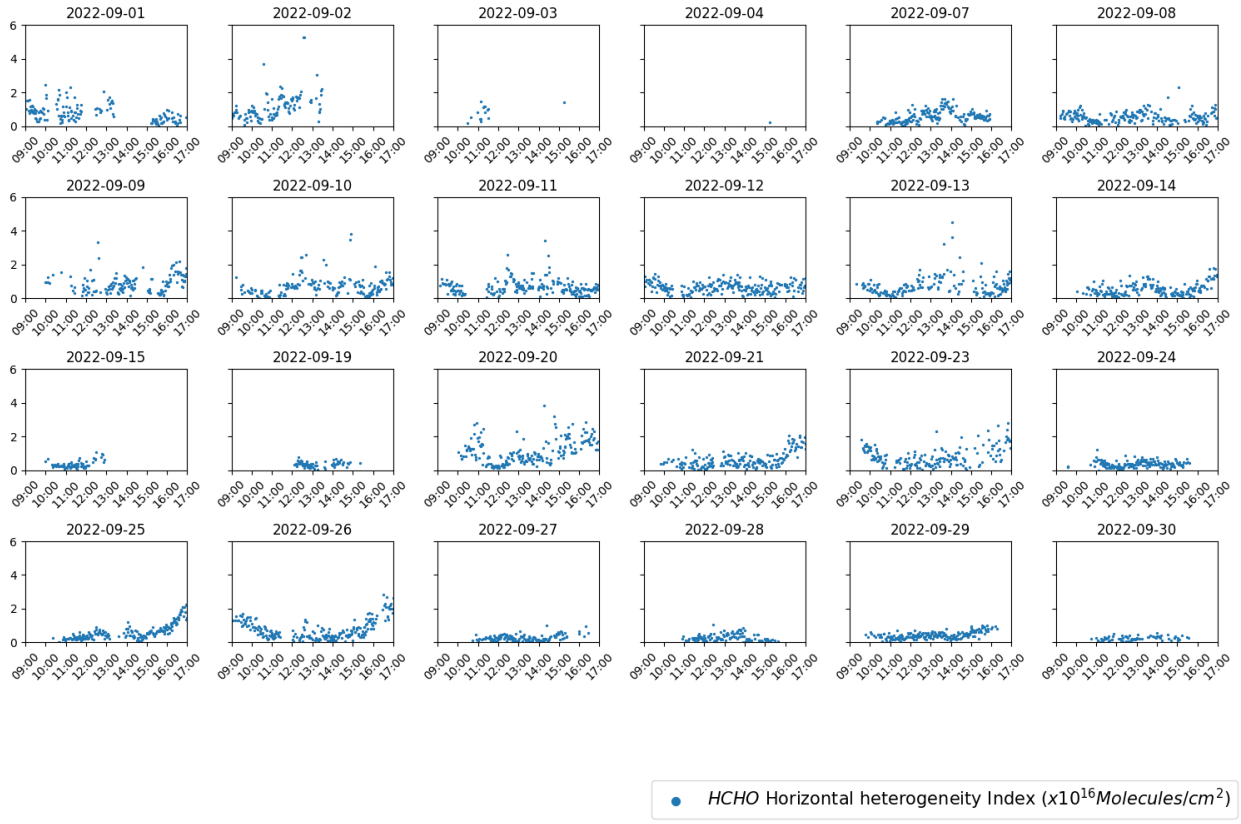


Figure A.7: The Horizontal heterogeneity Index of each day's set of measurements for the Intensive Operations period of TRACER-AQ2. Time is given in local time (CST), and index in $\times 10^{16} \frac{Molecules}{cm^2}$

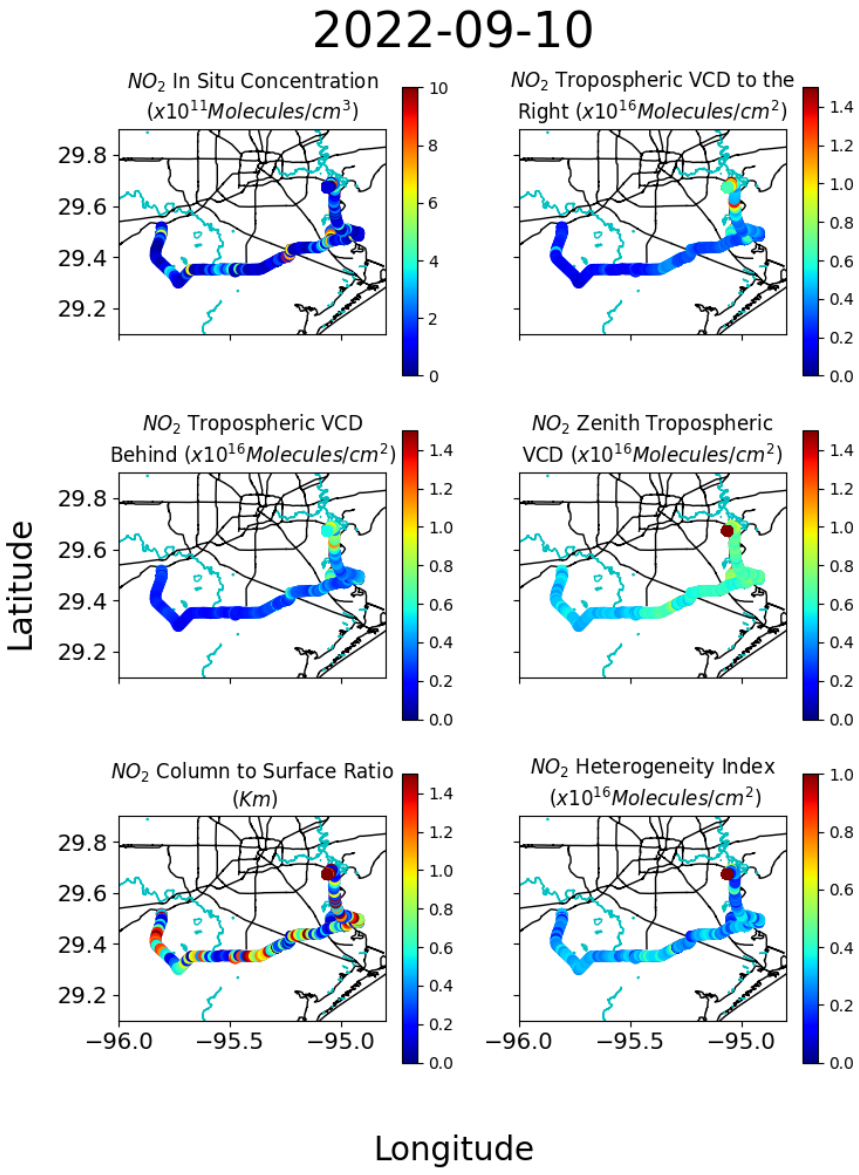


Figure A.8: a) The 1-minute average NO_2 in-situ concentrations measured on September 10 by the mobile lab in ppb plotted at the corresponding latitude and longitude. b) The 1 minute average Pandora 148 NO_2 columns plotted at the corresponding latitude and longitude. c) The 1 minute average Pandora 168 NO_2 columns plotted at the corresponding latitude and longitude. d)The 1 minute average Pandora NO_2 Zenith columns plotted at the corresponding latitude and longitude. e) The column to surface ratio between in-situ and Pandora Zenith columns. f) The heterogeneity index calculated from both MAX-DOAS instruments as well as Zenith columns.

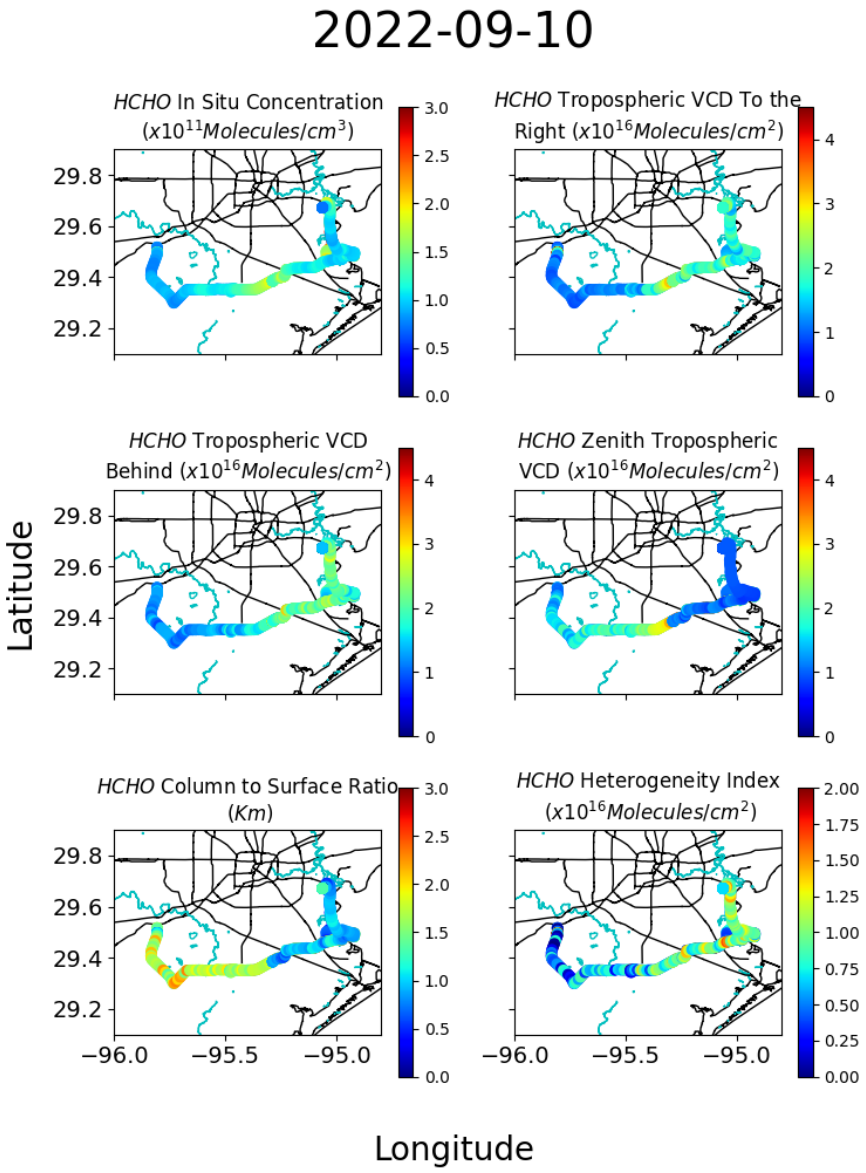


Figure A.9: a) The 1-minute average $HCHO$ in-situ concentrations measured on September 10 by the mobile lab in ppb plotted at the corresponding latitude and longitude. b) The 1 minute average Pandora 148 $HCHO$ columns plotted at the corresponding latitude and longitude. c) The 1 minute average Pandora 168 $HCHO$ columns plotted at the corresponding latitude and longitude. d)The 1 minute average Pandora $HCHO$ Zenith columns plotted at the corresponding latitude and longitude. e) The column to surface ratio between in-situ and Pandora Zenith columns. f) The heterogeneity index calculated from both MAX-DOAS instruments as well as Zenith columns.

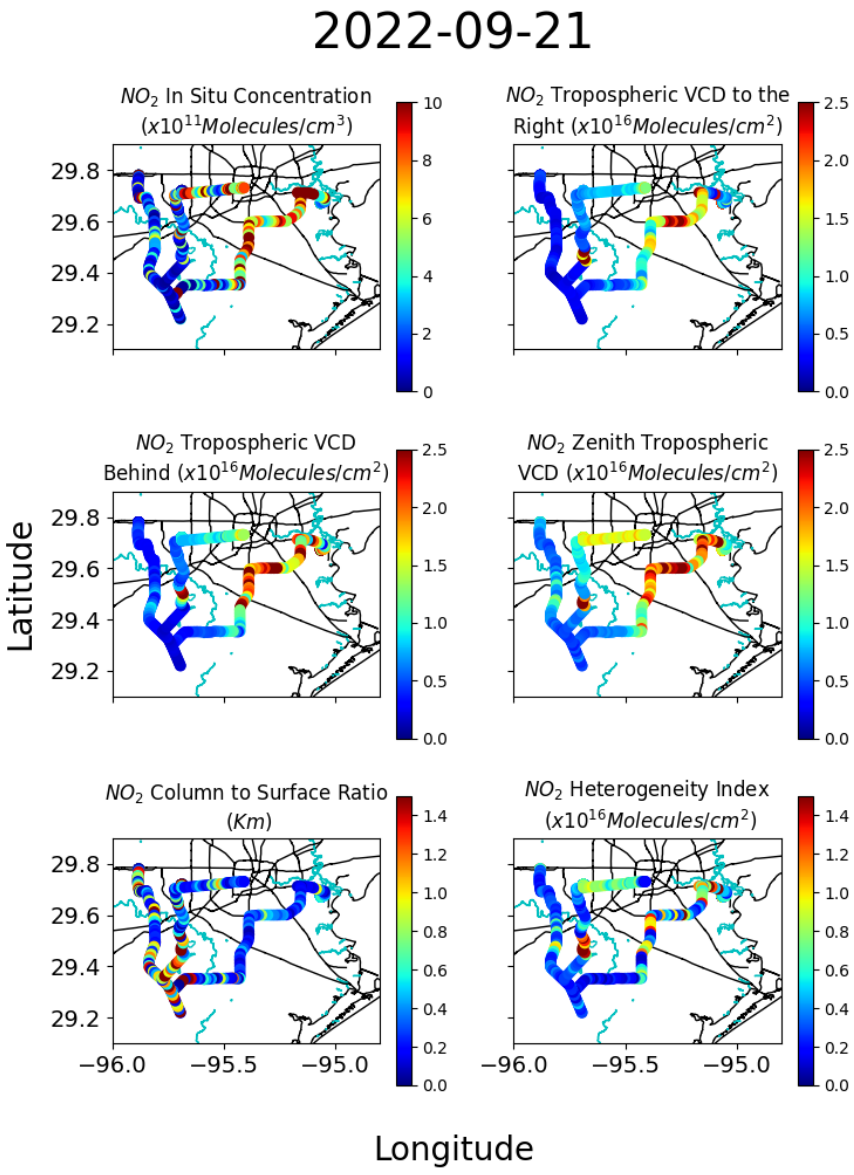


Figure A.10: a) The 1-minute average NO_2 in-situ concentrations measured on September 21 by the mobile lab in ppb b) The 1 minute average Pandora 148 NO_2 columns c) The 1 minute average Pandora 168 NO_2 columns d)The 1 minute average Pandora NO_2 Zenith columns e) The column to surface ratio between in-situ and Pandora Zenith columns. f) The heterogeneity index calculated from both MAX-DOAS instruments as well as Zenith columns.

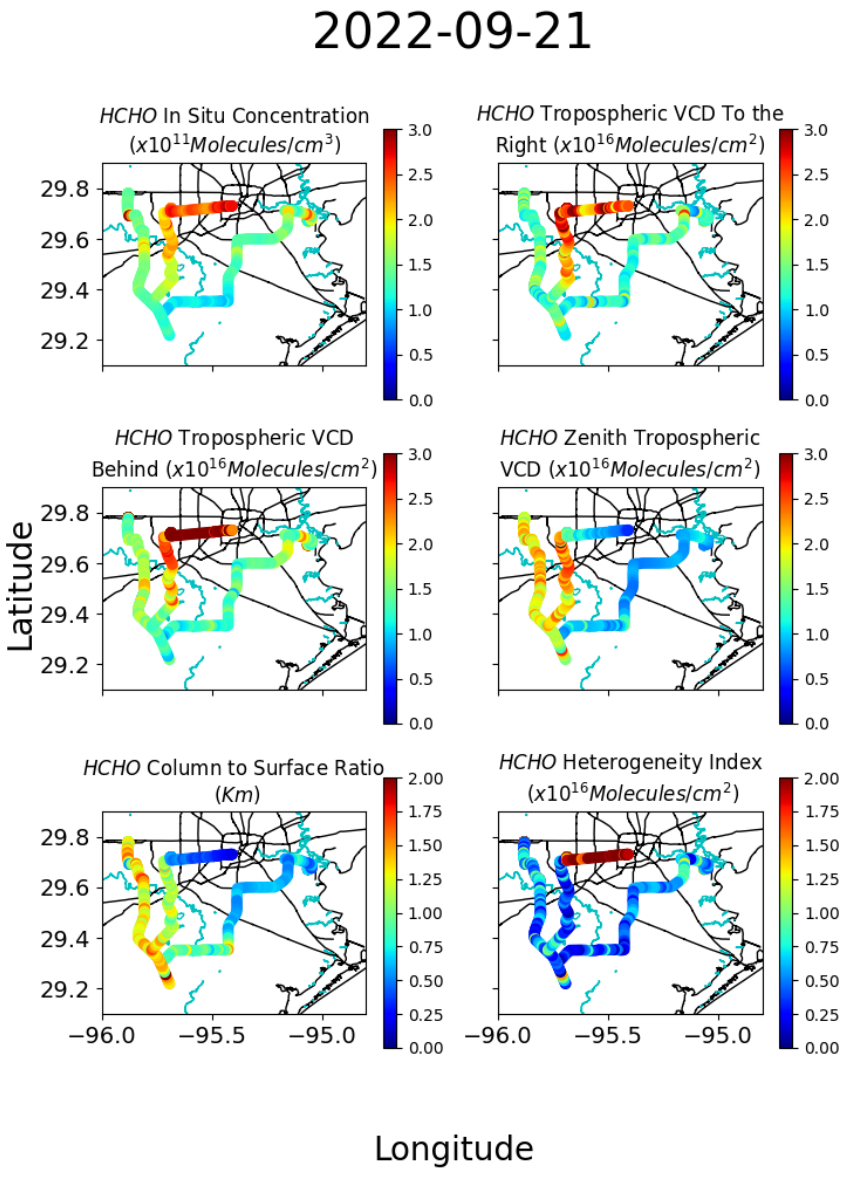


Figure A.11: a) The 1-minute average $HCHO$ in-situ concentrations measured on September 21 by the mobile lab in ppb b) The 1 minute average Pandora 148 $HCHO$ columns c) The 1 minute average Pandora 168 $HCHO$ columns d)The 1 minute average Pandora $HCHO$ Zenith columns e) The column to surface ratio between in-situ and Pandora Zenith columns. f) The heterogeneity index calculated from both MAX-DOAS instruments as well as Zenith columns.

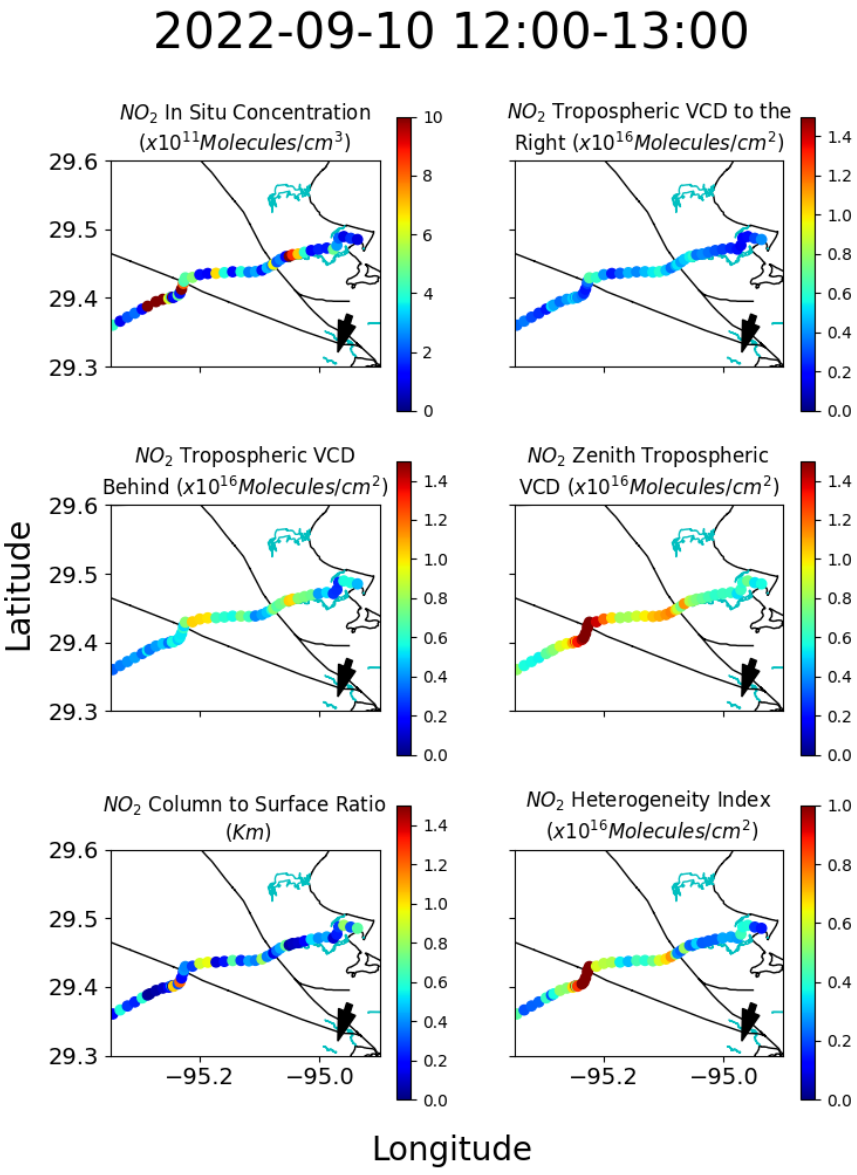


Figure A.12: a) The 1-minute average NO_2 in-situ concentrations measured on September 10 between 12:00-13:00 CST by the mobile lab b) The 1 minute average Pandora 148 NO_2 columns c) The 1 minute average Pandora 168 NO_2 columns d)The 1 minute average Pandora NO_2 Zenith columns e) The column to surface ratio between in-situ and Pandora Zenith columns. f) The heterogeneity index calculated from both MAX-DOAS instruments as well as Zenith columns.

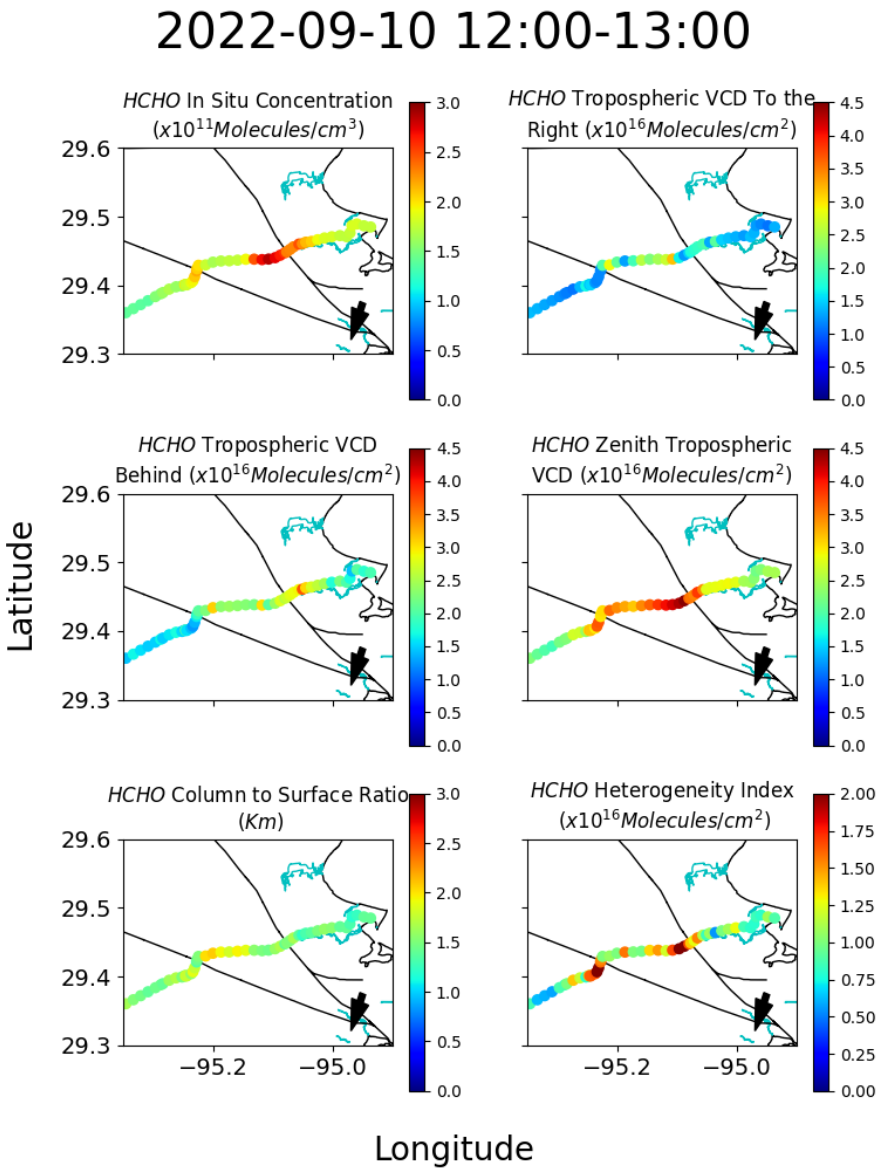


Figure A.13: a) The 1-minute average HCHO in-situ concentrations measured on September 10 between 12:00-13:00 CST by the mobile lab b) The 1 minute average Pandora 148 HCHO columns c) The 1 minute average Pandora 168 HCHO columns d)The 1 minute average Pandora HCHO Zenith columns e) The column to surface ratio between in-situ and Pandora Zenith columns. f) The heterogeneity index calculated from both MAX-DOAS instruments as well as Zenith columns.

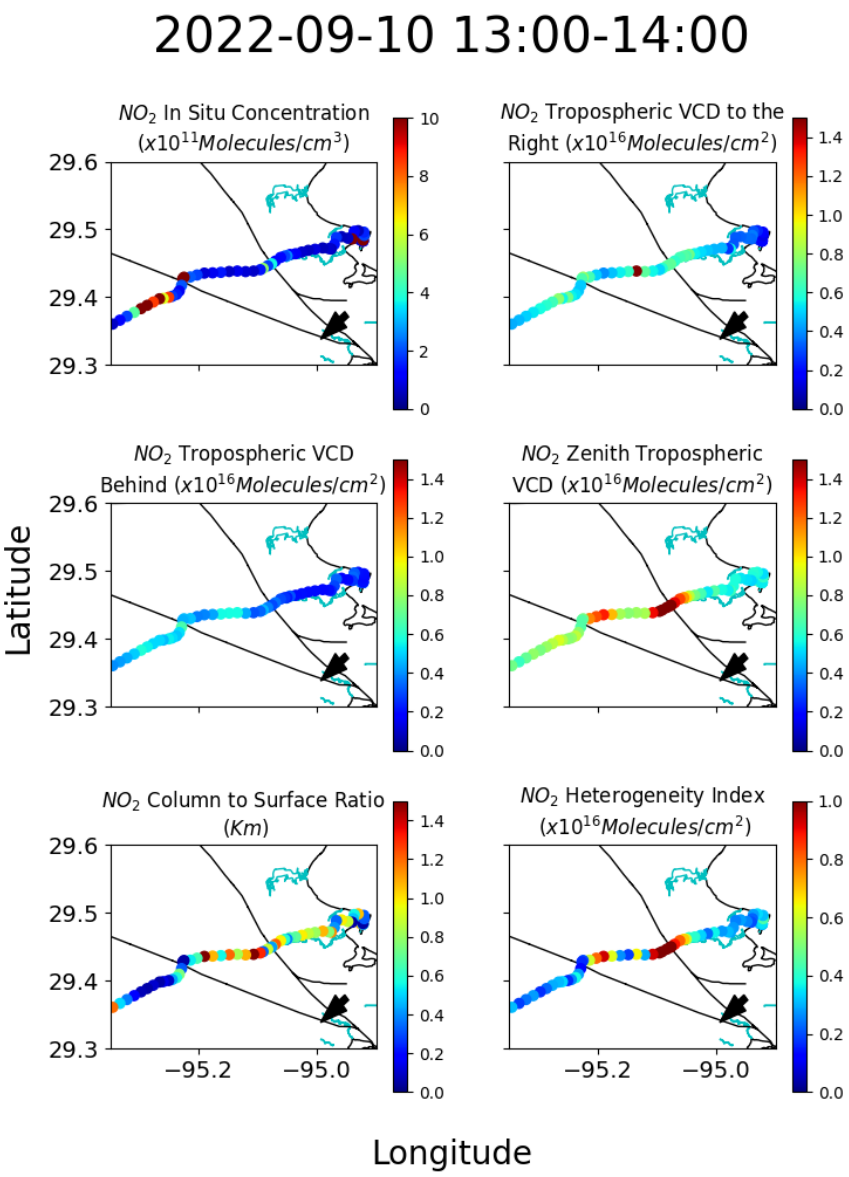


Figure A.14: a) The 1-minute average NO_2 in-situ concentrations measured on September 10 between 13:00-14:00 CST by the mobile lab b) The 1 minute average Pandora 148 NO_2 columns c) The 1 minute average Pandora 168 NO_2 columns d)The 1 minute average Pandora NO_2 Zenith columns e) The column to surface ratio between in-situ and Pandora Zenith columns. f) The heterogeneity index calculated from both MAX-DOAS instruments as well as Zenith columns.

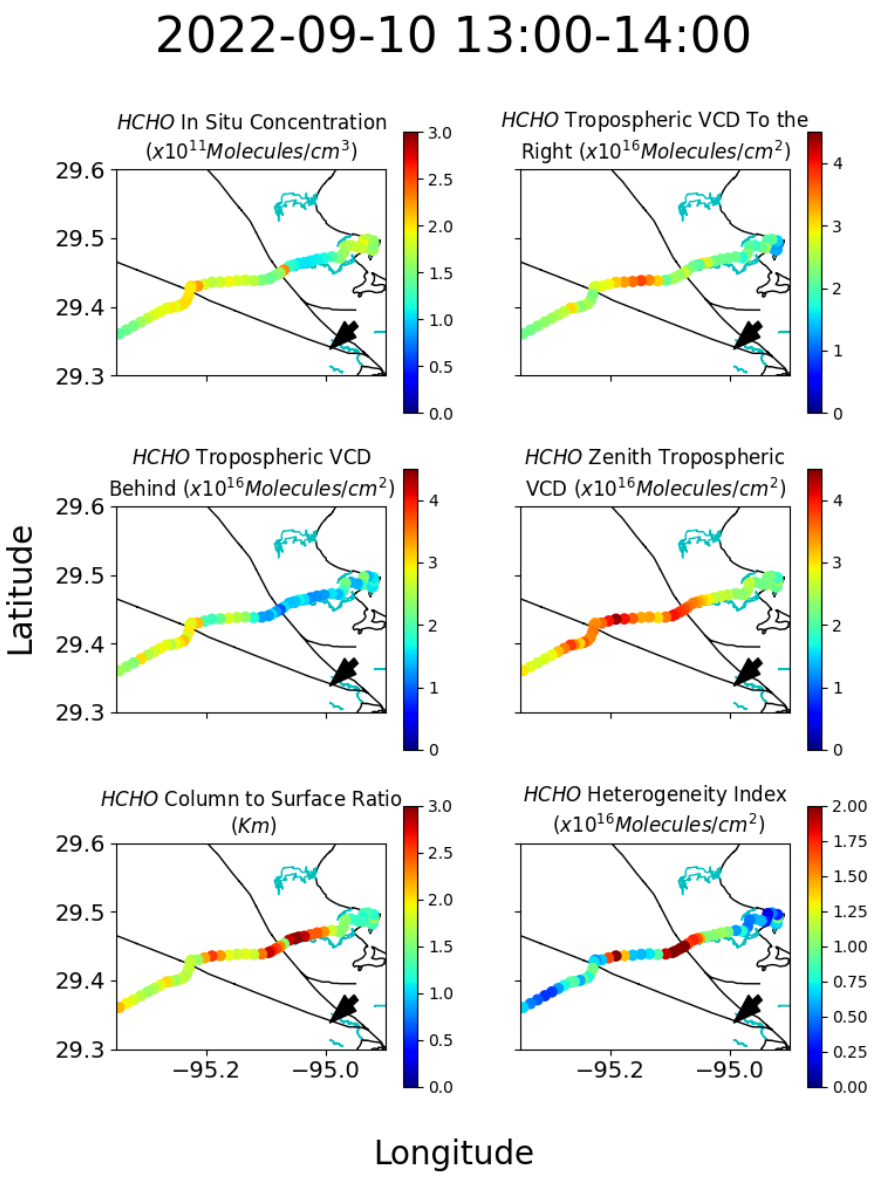


Figure A.15: a) The 1-minute average HCHO in-situ concentrations measured on September 10 between 13:00-14:00 CST by the mobile lab b) The 1 minute average Pandora 148 HCHO columns c) The 1 minute average Pandora 168 HCHO columns d)The 1 minute average Pandora HCHO Zenith columns e) The column to surface ratio between in-situ and Pandora Zenith columns. f) The heterogeneity index calculated from both MAX-DOAS instruments as well as Zenith columns.

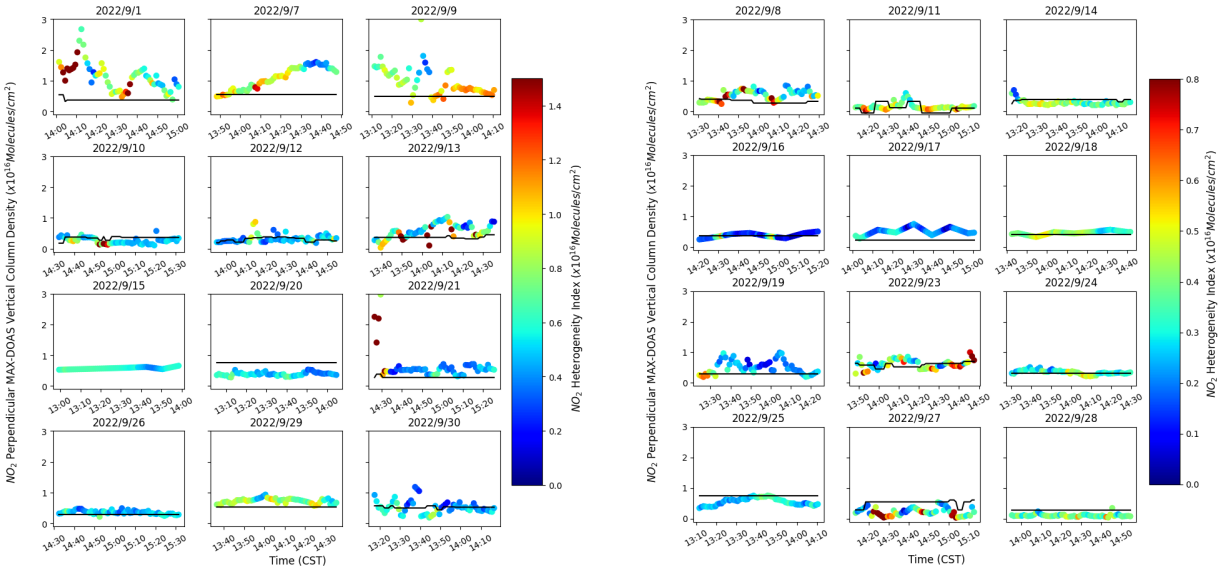


Figure A.16: (Left) A collection of Scatter plots on days with a column to Horizontal heterogeneity Index $> 0.25\times10^{16}\,\frac{Molecules}{cm^2}$ comparing TROPOMI NO_2 VCDs (black) to Pandora 148 MAX-DOAS VCDs, color coded to each measurement's column to surface ratio. (Right) A collection of Scatter plots on days with a Horizontal heterogeneity Index $< 0.25\times10^{16}\,\frac{Molecules}{cm^2}$ comparing TROPOMI NO_2 VCDs (black) to Pandora 148 MAX-DOAS VCDs, color coded to each measurement's column to surface ratio

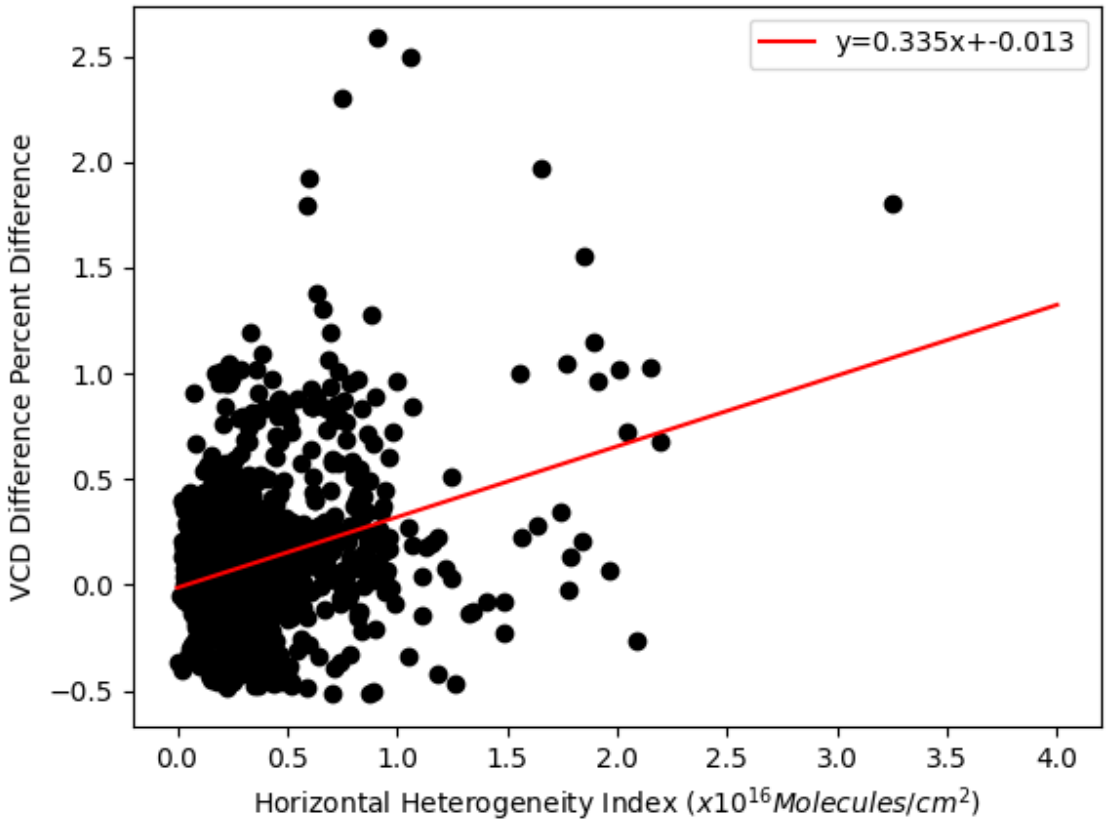


Figure A.17: Correlation plot showing the linear relationship between the Horizontal heterogeneity Index and the difference between the TROPOMI and Pandora 148 MAX-DOASS VCDs during TROPOMI overpass.The correlation coefficient of this linear fit is r=0.30.

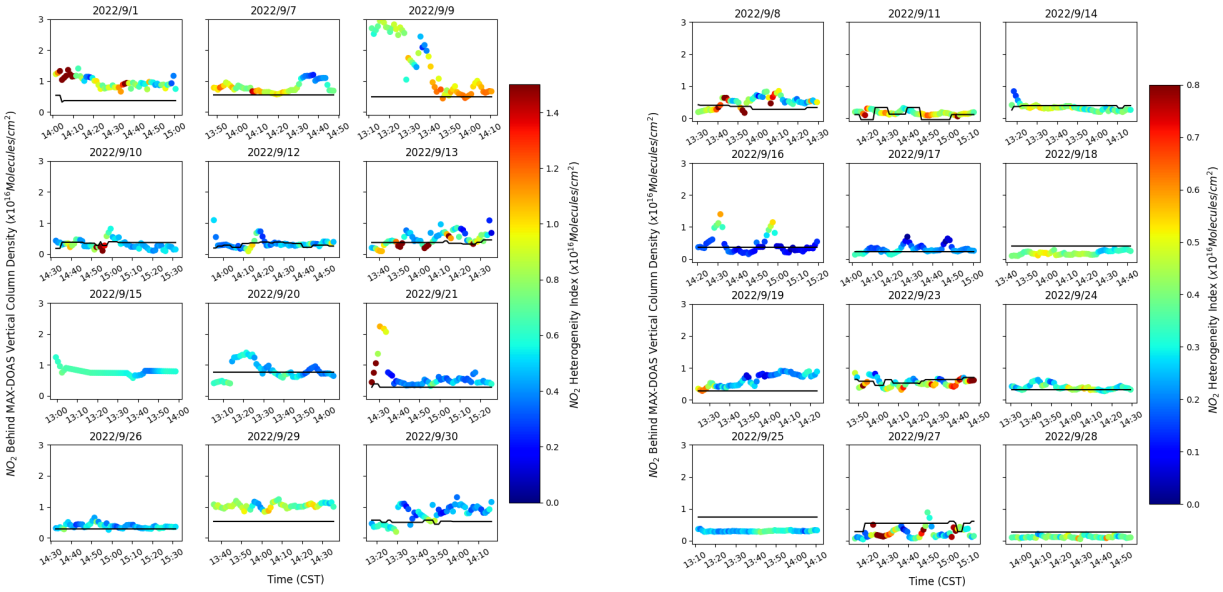


Figure A.18: (Left) A collection of Scatter plots on days with a column to Horizontal heterogeneity Index $> 0.25\times10^{16}\,\frac{Molecules}{cm^2}$ comparing TROPOMI NO_2 VCDs (black) to Pandora 168 MAX-DOAS VCDs, color coded to each measurement's column to surface ratio. (Right) A collection of Scatter plots on days with a Horizontal heterogeneity Index $< 0.25\times10^{16}\,\frac{Molecules}{cm^2}$ comparing TROPOMI NO_2 VCDs (black) to Pandora 168 MAX-DOAS VCDs, color coded to each measurement's column to surface ratio

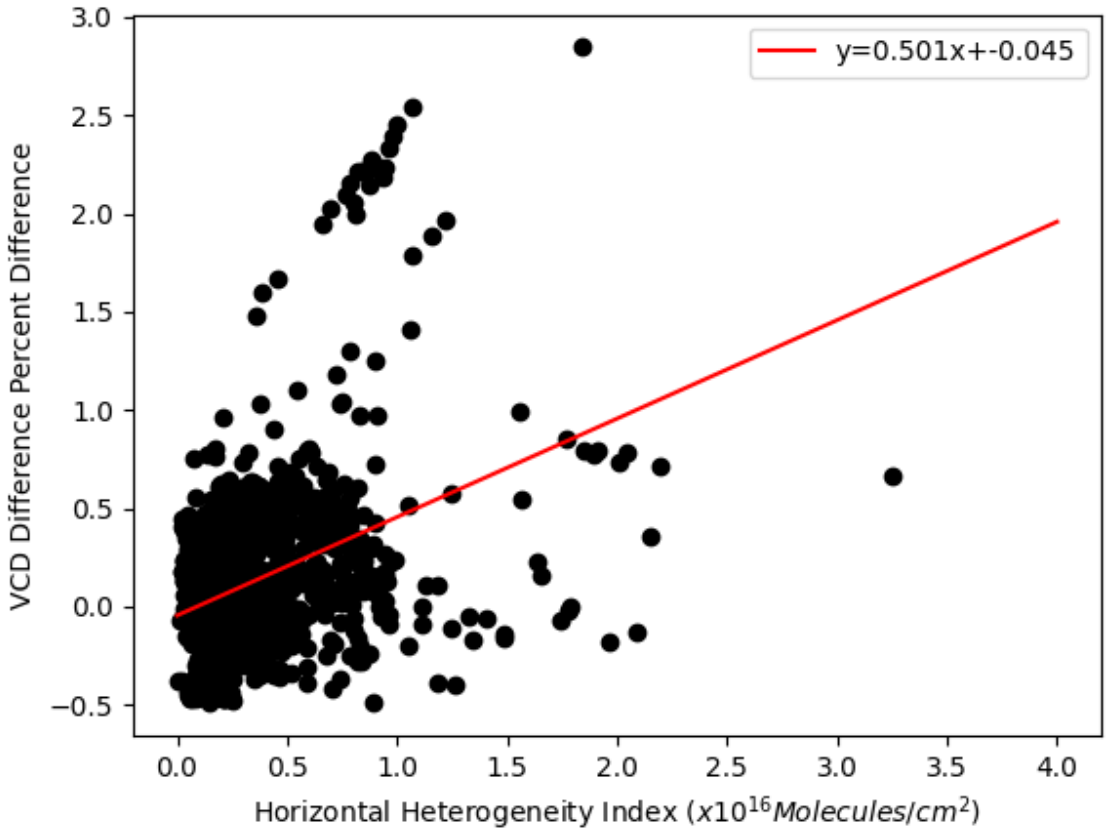


Figure A.19: Correlation plot showing the linear relationship between the Horizontal heterogeneity Index and the difference between the TROPOMI and Pandora 168 MAX-DOASS VCDs during TROPOMI overpass.The correlation coefficient of this linear fit is r=0.37.

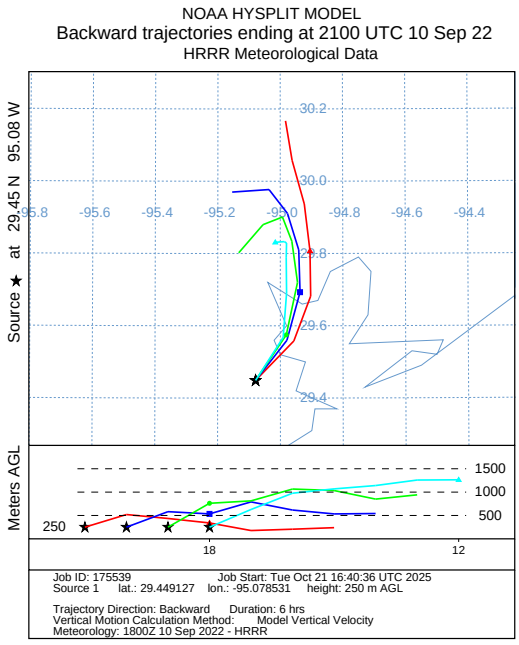


Figure A.20: HYSPLIT modeled 3 hour back-trajectory showing the path air masses at 21:00 (red), 20:00 (blue), 19:00 (green), and 18:00 (cyan) took to transport into the high Ozone area observed, with an end altitude of 250m.

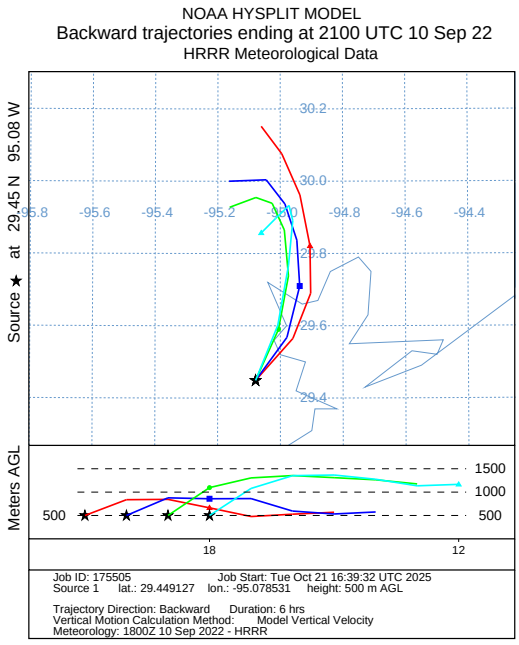


Figure A.21: HYSPLIT modeled 3 hour back-trajectory showing the path air masses at 21:00 (red), 20:00 (blue), 19:00 (green), and 18:00 (cyan) took to transport into the high Ozone area observed, with an end altitude of 750m.

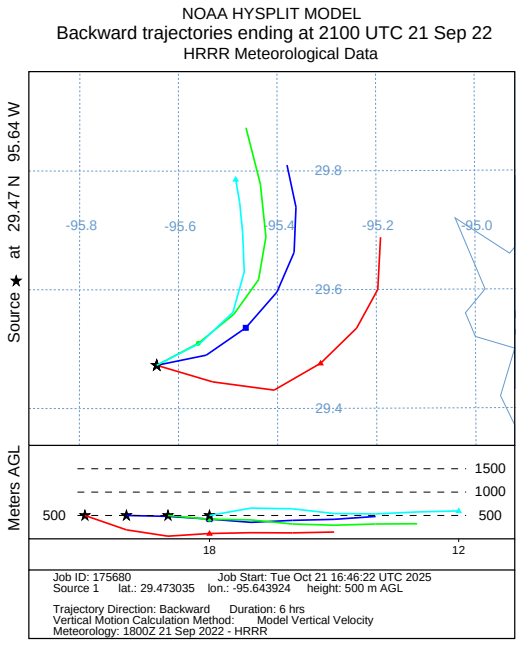


Figure A.22: HYSPLIT modeled 3 hour back-trajectory showing the path air masses at 21:00 (red), 20:00 (blue), 19:00 (green), and 18:00 (cyan) took to transport into the high Ozone area observed at an altitude of 250m.

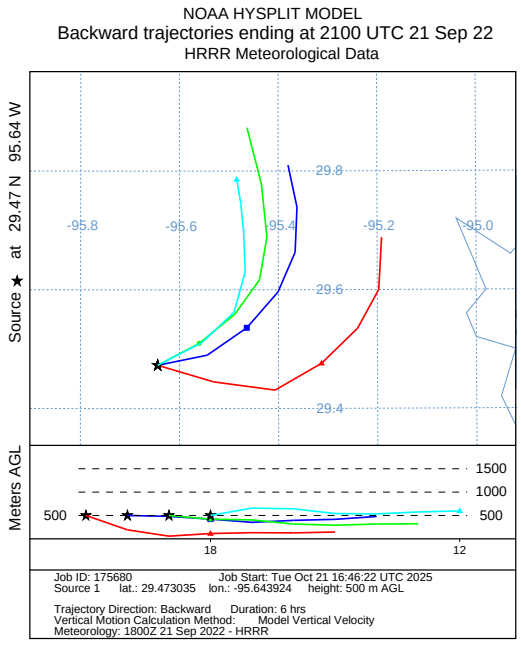


Figure A.23: HYSPLIT modeled 3 hour back-trajectory showing the path air masses at 21:00 (red), 20:00 (blue), 19:00 (green), and 18:00 (cyan) took to transport into the high Ozone area observed at an altitude of 750m.

Bibliography

[1] John Seinfeld and Pandis Spyros. *Atmospheric Chemistry and Physics*. John Wiley and Sons Inc., third edition, 2016.

[2] Alexander Cede. Manual for Blick Software Suite 1.8, April 2021.

[3] Ulrich Platt and Jochen Stutz. *Differential Optical Absorption Spectroscopy*. Springer-Verlag Berlin Heidelberg, 1st edition, 2008.

[4] A. F. Stein, R. R. Draxler, G. D. Rolph, B. J. B. Stunder, M. D. Cohen, and F. Ngan. NOAA's HYSPLIT Atmospheric Transport and Dispersion Modeling System. December 2015. Section: Bulletin of the American Meteorological Society.

[5] Udo Frieß, Steffen Beirle, Leonardo Alvarado Bonilla, Tim Bösch, Martina M. Friedrich, François Hendrick, Ankie Piters, Andreas Richter, Michel van Roozendael, Vladimir V. Rozanov, Elena Spinei, Jan-Lukas Tirpitz, Tim Vlemmix, Thomas Wagner, and Yang Wang. Intercomparison of MAX-DOAS vertical profile retrieval algorithms: studies using synthetic data. *Atmospheric Measurement Techniques*, 12(4):2155–2181, April 2019.

[6] Elmer Robinson and Robert C. Robbins. Gaseous Nitrogen Compound Pollutants from Urban and Natural Sources. *Journal of the Air Pollution Control Association*, 20(5):303–306, May 1970.

[7] Thomas W. Hesterberg, William B. Bunn, Roger O. McClellan, Ali K. Hamade, Christopher M. Long, and Peter A. Valberg. Critical review of the human data on

short-term nitrogen dioxide (NO $_2$) exposures: Evidence for NO $_2$ no-effect levels. *Critical Reviews in Toxicology*, 39(9):743–781, October 2009.

[8] OAR US EPA. Nitrogen Dioxide (NO2) Pollution, March 2016.

[9] M. Schaap, C. Cuvelier, C. Hendriks, B. Bessagnet, J.M. Baldasano, A. Colette, P. Thunis, D. Karam, H. Fagerli, A. Graff, R. Kranenburg, A. Nyiri, M.T. Pay, L. Rouïl, M. Schulz, D. Simpson, R. Stern, E. Terrenoire, and P. Wind. Performance of European chemistry transport models as function of horizontal resolution. *Atmospheric Environment*, 112:90–105, July 2015.

[10] Michael J. Prather, Lucien Froidevaux, and Nathaniel J. Livesey. Observed changes in stratospheric circulation: decreasing lifetime of N_2O, 2005–2021. *Atmospheric Chemistry and Physics*, 23(2):843–849, January 2023. Publisher: Copernicus GmbH.

[11] Robert W. Portmann and Susan Solomon. Indirect radiative forcing of the ozone layer during the 21st century. *Geophysical Research Letters*, 34(2), 2007. _eprint: https://onlinelibrary.wiley.com/doi/pdf/10.1029/2006GL028252.

[12] C. E. Randall, J. D. Lumpe, R. M. Bevilacqua, K. W. Hoppel, E. P. Shettle, D. W. Rusch, L. L. Gordley, K. Kreher, K. Pfeilsticker, H. Boesch, G. Toon, F. Goutail, and J.-P. Pommereau. Validation of POAM III NO2 measurements. *Journal of Geophysical Research: Atmospheres*, 107(D20):ACH 6–1–ACH 6–15, 2002. _eprint: https://onlinelibrary.wiley.com/doi/pdf/10.1029/2001JD001520.

[13] B. Funke, M. López-Puertas, T. von Clarmann, G. P. Stiller, H. Fischer, N. Glatthor, U. Grabowski, M. Höpfner, S. Kellmann, M. Kiefer, A. Linden, G. Mengistu Tsidu, M. Milz, T. Steck, and D. Y. Wang. Retrieval of stratospheric NO from 5.3 and 6.2 m nonlocal thermodynamic equilibrium emissions measured by Michelson Interferometer for Passive Atmospheric Sounding (MIPAS) on

Envisat. *Journal of Geophysical Research: Atmospheres*, 110(D9), 2005. _eprint: https://onlinelibrary.wiley.com/doi/pdf/10.1029/2004JD005225.

[14] Samuel M. Brohede, Craig S. Haley, Chris A. Mclinden, Christopher E. Sioris, Donal P. Murtagh, Svetlana V. Petelina, Edward J. Llewellyn, Ariane Bazureau, Florence Goutail, Cora E. Randall, Jerry D. Lumpe, Ghassan Taha, Larry W. Thomasson, and Larry L. Gordley. Validation of Odin/OSIRIS stratospheric NO_2 profiles. *Journal of Geophysical Research: Atmospheres*, 112:D07310, 2007. Publisher: American Geophysical Union.

[15] Jean Pierre Pommereau and Florence Goutail. O_3 and NO_2 ground-based measurements by visible spectrometry during Arctic winter and spring 1988. *Geophysical Research Letters*, 15(8):891–894, August 1988.

[16] Jean-Pierre Pommereau and Jacques Piquard. Ozone and nitrogen dioxide vertical distributions by UV-visible solar occultation from balloons. *Geophysical Research Letters*, 21(13):1227–1230, June 1994.

[17] IPCC(2013). Climate Change 2013: The Physical Science Basis. Technical report, Cambridge Univ. Press, Cambridge, UK.

[18] Matthieu Pommier. Estimations of NO_x emissions, NO_2 lifetime and their temporal variation over three British urbanised regions in 2019 using TROPOMI NO_2 observations. *Environmental Science: Atmospheres*, 3(2):408–421, 2023.

[19] Sagar V Krupa and William J Manning. Atmospheric ozone: Formation and effects on vegetation. *Environmental Pollution*, 50(1-2):101–137, 1988.

[20] B.J. Finlayson-Pitts and J.N. Pitts. Atmospheric Chemistry of Tropospheric Ozone

Formation: Scientific and Regulatory Implications. *Air & Waste*, 43(8):1091–1100, August 1993.

[21] Peng Wang, Yuan Chen, Jianlin Hu, Hongliang Zhang, and Qi Ying. Attribution of Tropospheric Ozone to NO $_x$ and VOC Emissions: Considering Ozone Formation in the Transition Regime. *Environmental Science & Technology*, 53(3):1404–1412, February 2019.

[22] Yizhen Wu, Juntao Huo, Gan Yang, Yuwei Wang, Lihong Wang, Shijian Wu, Lei Yao, Qingyan Fu, and Lin Wang. Measurement report: Production and loss of atmospheric formaldehyde at a suburban site of Shanghai in summertime. *Atmospheric Chemistry and Physics*, 23(5):2997–3014, March 2023. Publisher: Copernicus GmbH.

[23] Kei Toda, Satoru Yunoki, Akira Yanaga, Masaki Takeuchi, Shin-Ichi Ohira, and Purnendu K. Dasgupta. Formaldehyde Content of Atmospheric Aerosol. *Environmental Science & Technology*, 48(12):6636–6643, June 2014.

[24] Alex Guenther, C. Nicholas Hewitt, David Erickson, Ray Fall, Chris Geron, Tom Graedel, Peter Harley, Lee Klinger, Manuel Lerdau, W. A. Mckay, Tom Pierce, Bob Scholes, Rainer Steinbrecher, Raja Tallamraju, John Taylor, and Pat Zimmerman. A global model of natural volatile organic compound emissions. *Journal of Geophysical Research: Atmospheres*, 100(D5):8873–8892, May 1995.

[25] A. Guenther, T. Karl, P. Harley, C. Wiedinmyer, P. I. Palmer, and C. Geron. Estimates of global terrestrial isoprene emissions using MEGAN (Model of Emissions of Gases and Aerosols from Nature). *Atmospheric Chemistry and Physics*, 6(11):3181–3210, August 2006. Publisher: Copernicus GmbH.

[26] Thomas Staffelbach, Albrecht Neftel, Bernhard Stauffer, and Daniel Jacob. A record

of the atmospheric methane sink from formaldehyde in polar ice cores. *Nature*, 349(6310):603–605, February 1991.

[27] T. D. Sharkey, A. E. Wiberley, and A. R. Donohue. Isoprene Emission from Plants: Why and How. *Annals of Botany*, 101(1):5–18, October 2007.

[28] Dana A. Brewer, Michael A. Ogliaruso, Tommy R. Augustsson, and Joel S. Levine. The oxidation of isoprene in the troposphere: Mechanism and model calculations. *Atmospheric Environment (1967)*, 18(12):2723–2744, January 1984.

[29] Paul I. Palmer, Daniel J. Jacob, Arlene M. Fiore, Randall V. Martin, Kelly Chance, and Thomas P. Kurosu. Mapping isoprene emissions over North America using formaldehyde column observations from space. *Journal of Geophysical Research: Atmospheres*, 108(D6), 2003. _eprint: https://onlinelibrary.wiley.com/doi/pdf/10.1029/2002JD002153.

[30] Changsub Shim, Yuhang Wang, Yunsoo Choi, Paul I. Palmer, Dorian S. Abbot, and Kelly Chance. Constraining global isoprene emissions with Global Ozone Monitoring Experiment (GOME) formaldehyde column measurements. *Journal of Geophysical Research: Atmospheres*, 110(D24), 2005. _eprint: https://onlinelibrary.wiley.com/doi/pdf/10.1029/2004JD005629.

[31] D. D. Parrish, T. B. Ryerson, J. Mellqvist, J. Johansson, A. Fried, D. Richter, J. G. Walega, R. A. Washenfelder, J. A. de Gouw, J. Peischl, K. C. Aikin, S. A. McKeen, G. J. Frost, F. C. Fehsenfeld, and S. C. Herndon. Primary and secondary sources of formaldehyde in urban atmospheres: Houston Texas region. *Atmospheric Chemistry and Physics*, 12(7):3273–3288, April 2012. Publisher: Copernicus GmbH.

[32] Ricardo Suarez-Bertoa, Tommaso Selleri, Roberto Gioria, Anastasios D. Melas, Christian Ferrarese, Jacopo Franzetti, Bertold Arlitt, Naoki Nagura, Takaaki Hanada, and

Barouch Giechaskiel. Real-Time Measurements of Formaldehyde Emissions from Modern Vehicles. *Energies*, 15(20):7680, October 2022.

[33] Michael I Mishchenko. Vector radiative transfer equation for arbitrarily shaped and arbitrarily oriented particles: a microphysical derivation from statistical electromagnetics.

[34] Knut Stamnes. The theory of multiple scattering of radiation in plane parallel atmospheres. *Reviews of Geophysics*, 24(2):299–310, May 1986.

[35] Arne Dahlback. A new spherical model for computing the radiation field available for photolysis and heating at twilight. *Planetary and Space Science*, 39(5):671–683, 1991.

[36] Ulrich Platt. Differential Optical Absorption Spectroscopy (DOAS). *Air Monitoring by Spectroscopic Techniques*, 127:27–83, 1994.

[37] D. Perner and U. Platt. Detection of nitrous acid in the atmosphere by differential optical absorption. *Geophysical Research Letters*, 6(12):917–920, 1979. _eprint: https://onlinelibrary.wiley.com/doi/pdf/10.1029/GL006i012p00917.

[38] U. Platt, D. Perner, G. W. Harris, A. M. Winer, and J. N. Pitts. Observations of nitrous acid in an urban atmosphere by differential optical absorption. *Nature*, 285(5763):312–314, May 1980. Publisher: Nature Publishing Group.

[39] D. Perner, D. H. Ehhalt, H. W. Pätz, U. Platt, E. P. Röth, and A. Volz. OH - Radicals in the lower troposphere. *Geophysical Research Letters*, 3(8):466–468, 1976. _eprint: https://onlinelibrary.wiley.com/doi/pdf/10.1029/GL003i008p00466.

[40] J. F. Noxon, E. C. Whipple, and R. S. Hyde. Stratospheric NO_2 : 1. Observational method and behavior at mid-latitude. *Journal of Geophysical Research: Oceans*, 84(C8):5047–5065, August 1979.

[41] MARCEL V. Migeotte. Lines of Methane at 7.7\ensuremath{\mu} in the Solar Spectrum. *Physical Review*, 74(1):112–113, July 1948. Publisher: American Physical Society.

[42] Marcel V. Migeotte. The Fundamental Band of Carbon Monoxide at $4.7\ensuremath{\mu}$ in the Solar Spectrum. *Physical Review*, 75(7):1108–1109, April 1949. Publisher: American Physical Society.

[43] W.N. Hartley. On the Absorption of Solar Rays by Atmospheric Ozone. *Journal of the Chemical Society*, 39:111–128, 1881.

[44] J. Chappius. Sur le spectre d'absorption de l'ozone. *Comptes Rendus de I'Académie des Sciences*, 91:985–986, 1880.

[45] G. Hönninger, H. Leser, O. Sebastián, and U. Platt. Ground-based measurements of halogen oxides at the Hudson Bay by active longpath DOAS and passive MAX-DOAS. *Geophysical Research Letters*, 31(4), 2004. _eprint: https://onlinelibrary.wiley.com/doi/pdf/10.1029/2003GL018982.

[46] Olga Pikelnaya, Stephen C. Hurlock, Sebastian Trick, and Jochen Stutz. Intercomparison of multiaxis and long-path differential optical absorption spectroscopy measurements in the marine boundary layer. *Journal of Geophysical Research: Atmospheres*, 112(D10), 2007. _eprint: https://onlinelibrary.wiley.com/doi/pdf/10.1029/2006JD007727.

[47] J. F. Grainger and J. Ring. Anomalous Fraunhofer Line Profiles. *Nature*, 193(4817):762–762, February 1962.

[48] D. J. Fish and R. L. Jones. Rotational Raman scattering and the ring effect in

zenith-sky spectra. *Geophysical Research Letters*, 22(7):811–814, 1995. _eprint: https://onlinelibrary.wiley.com/doi/pdf/10.1029/95GL00392.

[49] Kelly V. Chance and Robert J. D. Spurr. Ring effect studies: Rayleigh scattering, including molecular parameters for rotational Raman scattering, and the Fraunhofer spectrum. *Applied Optics*, 36(21):5224–5230, July 1997. Publisher: Optica Publishing Group.

[50] Thomas Wagner. Satellite Observations of Atmospheric Halogen Oxides. 2000. Publisher: Heidelberg University Library.

[51] G. Hönninger, C. von Friedeburg, and U. Platt. Multi axis differential optical absorption spectroscopy (MAX-DOAS). *Atmospheric Chemistry and Physics*, 4(1):231–254, February 2004. Publisher: Copernicus GmbH.

[52] Gerd Hönninger and U. Platt. Observations of BrO and its vertical distribution during surface ozone depletion at Alert. *Atmospheric Environment*, 36(15-16):2481–2489, May 2002.

[53] A Heckel, A Richter, T Tarsu, F Wittrock, C Hak, I Pundt, W Junkermann, and J P Burrows. MAX-DOAS measurements of formaldehyde in the Po-Valley. *Atmos. Chem. Phys.*, page 10, 2005.

[54] Tim Bösch, Vladimir Rozanov, Andreas Richter, Enno Peters, Alexei Rozanov, Folkard Wittrock, Alexis Merlaud, Johannes Lampel, Stefan Schmitt, Marijn de Haij, Stijn Berkhout, Bas Henzing, Arnoud Apituley, Mirjam den Hoed, Jan Vonk, Martin Tiefengraber, Moritz Müller, and John Philip Burrows. BOREAS – a new MAX-DOAS profile retrieval algorithm for aerosols and trace gases. *Atmospheric Measurement Techniques*, 11(12):6833–6859, December 2018. Publisher: Copernicus GmbH.

[55] H. Irie, Y. Kanaya, H. Akimoto, H. Iwabuchi, A. Shimizu, and K. Aoki. First retrieval of tropospheric aerosol profiles using MAX-DOAS and comparison with lidar and sky radiometer measurements. *Atmospheric Chemistry and Physics*, 8(2):341–350, January 2008.

[56] H. Irie, H. Takashima, Y. Kanaya, K. F. Boersma, L. Gast, F. Wittrock, D. Brunner, Y. Zhou, and M. Van Roozendael. Eight-component retrievals from ground-based MAX-DOAS observations. *Atmospheric Measurement Techniques*, 4(6):1027–1044, June 2011.

[57] Sk Nabil Nowak. *Remote Sensing of the Lower Atmosphere: From Surface Concentration to Mixing Layer Height*. PhD thesis, Virginia Tech, 2022.

[58] A. W. Brewer, C. T. Mcelroy, and J. B. Kerr. Nitrogen Dioxide Concentrations in the Atmosphere. *Nature*, 246(5429):129–133, November 1973. Publisher: Nature Publishing Group.

[59] R. L. McKenzie, P. V. Johnston, C. T. McElroy, J. B. Kerr, and S. Solomon. Altitude distributions of stratospheric constituents from ground-based measurements at twilight. *Journal of Geophysical Research: Atmospheres*, 96(D8):15499–15511, 1991. _eprint: https://onlinelibrary.wiley.com/doi/pdf/10.1029/91JD01361.

[60] Florence Goutail, Jean Pierre Pommereau, Alain Sarkissian, Esko Kyro, and Valery Dorokhov. Total nitrogen dioxide at the Arctic Polar Circle since 1990. *Geophysical Research Letters*, 21(13):1371–1374, 1994. _eprint: https://onlinelibrary.wiley.com/doi/pdf/10.1029/93GL01783.

[61] S. Solomon, R. W. Portmann, R. W. Sanders, J. S. Daniel, W. Madsen, B. Bartram, and E. G. Dutton. On the role of nitrogen dioxide in the absorption of solar radiation.

Journal of Geophysical Research: Atmospheres, 104(D10):12047–12058, 1999. _eprint: https://onlinelibrary.wiley.com/doi/pdf/10.1029/1999JD900035.

[62] F. Hendrick, B. Barret, M. Van Roozendael, H. Boesch, A. Butz, M. De Mazière, F. Goutail, C. Hermans, J.-C. Lambert, K. Pfeilsticker, and J.-P. Pommereau. Retrieval of nitrogen dioxide stratospheric profiles from ground-based zenith-sky UV-visible observations: validation of the technique through correlative comparisons. *Atmospheric Chemistry and Physics*, 4(8):2091–2106, October 2004. Publisher: Copernicus GmbH.

[63] U. Platt, L. Marquard, T. Wagner, and D. Perner. Corrections for zenith scattered light DOAS. *Geophysical Research Letters*, 24(14):1759–1762, 1997. _eprint: https://onlinelibrary.wiley.com/doi/pdf/10.1029/97GL01693.

[64] F. Tack, F. Hendrick, F. Goutail, C. Fayt, A. Merlaud, G. Pinardi, C. Hermans, J.-P. Pommereau, and M. Van Roozendael. Tropospheric nitrogen dioxide column retrieval from ground-based zenith–sky DOAS observations. *Atmospheric Measurement Techniques*, 8(6):2417–2435, June 2015.

[65] D Chen, B Zhou, S Beirle, L M Chen, and T Wagner. Tropospheric NO2 column densities deduced from zenith-sky DOAS measurements in Shanghai, China, and their application to satellite validation. *Atmos. Chem. Phys.*, page 22, 2009.

[66] T. Kerzenmacher, M. A. Wolff, K. Strong, E. Dupuy, K. A. Walker, L. K. Amekudzi, R. L. Batchelor, P. F. Bernath, G. Berthet, T. Blumenstock, C. D. Boone, K. Bramstedt, C. Brogniez, S. Brohede, J. P. Burrows, V. Catoire, J. Dodion, J. R. Drummond, D. G. Dufour, B. Funke, D. Fussen, F. Goutail, D. W. T. Griffith, C. S. Haley, F. Hendrick, M. Höpfner, N. Huret, N. Jones, J. Kar, I. Kramer, E. J. Llewellyn, M. López-Puertas, G. Manney, C. T. McElroy, C. A. McLinden, S. Melo, S. Mikuteit,

D. Murtagh, F. Nichitiu, J. Notholt, C. Nowlan, C. Piccolo, J.-P. Pommereau, C. Randall, P. Raspollini, M. Ridolfi, A. Richter, M. Schneider, O. Schrems, M. Silicani, G. P. Stiller, J. Taylor, C. Tétard, M. Toohey, F. Vanhellemont, T. Warneke, J. M. Zawodny, and J. Zou. Validation of NO_2 and NO from the Atmospheric Chemistry Experiment (ACE). *Atmospheric Chemistry and Physics*, 8(19):5801–5841, October 2008. Publisher: Copernicus GmbH.

[67] J. W. Leitch, T. Delker, W. Good, L. Ruppert, F. Murcray, K. Chance, X. Liu, C. Nowlan, S. J. Janz, N. A. Krotkov, K. E. Pickering, M. Kowalewski, and J. Wang. The GeoTASO airborne spectrometer project. page 92181H, San Diego, California, United States, October 2014.

[68] Caroline R. Nowlan, Xiong Liu, James W. Leitch, Kelly Chance, Gonzalo González Abad, Cheng Liu, Peter Zoogman, Joshua Cole, Thomas Delker, William Good, Frank Murcray, Lyle Ruppert, Daniel Soo, Melanie B. Follette-Cook, Scott J. Janz, Matthew G. Kowalewski, Christopher P. Loughner, Kenneth E. Pickering, Jay R. Herman, Melinda R. Beaver, Russell W. Long, James J. Szykman, Laura M. Judd, Paul Kelley, Winston T. Luke, Xinrong Ren, and Jassim A. Al-Saadi. Nitrogen dioxide observations from the Geostationary Trace gas and Aerosol Sensor Optimization (GeoTASO) airborne instrument: Retrieval algorithm and measurements during DISCOVER-AQ Texas 2013. *Atmospheric Measurement Techniques*, 9(6):2647–2668, June 2016. Publisher: Copernicus GmbH.

[69] Laura M. Judd, Jassim A. Al-Saadi, James J. Szykman, Lukas C. Valin, Scott J. Janz, Matthew G. Kowalewski, Henk J. Eskes, J. Pepijn Veefkind, Alexander Cede, Moritz Mueller, Manuel Gebetsberger, Robert Swap, R. Bradley Pierce, Caroline R. Nowlan, Gonzalo González Abad, Amin Nehrir, and David Williams. Evaluating Sentinel-5P TROPOMI tropospheric NO_2 column densities with airborne and Pandora spectrom-

eters near New York City and Long Island Sound. *Atmospheric Measurement Techniques*, 13(11):6113–6140, November 2020. Publisher: Copernicus GmbH.

[70] Theano Drosoglou, Alkiviadis F. Bais, Irene Zyrichidou, Natalia Kouremeti, Anastasia Poupkou, Natalia Liora, Christos Giannaros, Maria Elissavet Koukouli, Dimitris Balis, and Dimitrios Melas. Comparisons of ground-based tropospheric NO_2 MAX-DOAS measurements to satellite observations with the aid of an air quality model over the Thessaloniki area, Greece. *Atmospheric Chemistry and Physics*, 17(9):5829–5849, May 2017. Publisher: Copernicus GmbH.

[71] Iolanda Ialongo, Henrik Virta, Henk Eskes, Jari Hovila, and John Douros. Comparison of TROPOMI/Sentinel-5 Precursor NO_2 observations with ground-based measurements in Helsinki. *Atmospheric Measurement Techniques*, 13(1):205–218, January 2020. Publisher: Copernicus GmbH.

[72] Ka Lok Chan, Matthias Wiegner, Jos van Geffen, Isabelle De Smedt, Carlos Alberti, Zhibin Cheng, Sheng Ye, and Mark Wenig. MAX-DOAS measurements of tropospheric NO₂ and HCHO in Munich and the comparison to OMI and TROPOMI satellite observations. *Atmospheric Measurement Techniques*, 13(8):4499–4520, August 2020.

[73] Ermioni Dimitropoulou, François Hendrick, Gaia Pinardi, Martina M. Friedrich, Alexis Merlaud, Frederik Tack, Helene De Longueville, Caroline Fayt, Christian Hermans, Quentin Laffineur, Frans Fierens, and Michel Van Roozendael. Validation of TROPOMI tropospheric NO_2 columns using dual-scan multi-axis differential optical absorption spectroscopy (MAX-DOAS) measurements in Uccle, Brussels. *Atmospheric Measurement Techniques*, 13(10):5165–5191, October 2020. Publisher: Copernicus GmbH.

[74] H. Li, J. Harvey, and A. Kendall. Field measurement of albedo for different land cover materials and effects on thermal performance. *Building and Environment*, 59:536–546, January 2013.

[75] Martine De Mazière, Anne M. Thompson, Michael J. Kurylo, Jeannette D. Wild, Germar Bernhard, Thomas Blumenstock, Geir O. Braathen, James W. Hannigan, Jean-Christopher Lambert, Thierry Leblanc, Thomas J. McGee, Gerald Nedoluha, Irina Petropavlovskikh, Gunther Seckmeyer, Paul C. Simon, Wolfgang Steinbrecht, and Susan E. Strahan. The Network for the Detection of Atmospheric Composition Change (NDACC): history, status and perspectives. *Atmospheric Chemistry and Physics*, 18(7):4935–4964, April 2018.

[76] E. A. Celarier, E. J. Brinksma, J. F. Gleason, J. P. Veefkind, A. Cede, J. R. Herman, D. Ionov, F. Goutail, J.-P. Pommereau, J.-C. Lambert, M. van Roozendael, G. Pinardi, F. Wittrock, A. Schönhardt, A. Richter, O. W. Ibrahim, T. Wagner, B. Bojkov, G. Mount, E. Spinei, C. M. Chen, T. J. Pongetti, S. P. Sander, E. J. Bucsela, M. O. Wenig, D. P. J. Swart, H. Volten, M. Kroon, and P. F. Levelt. Validation of Ozone Monitoring Instrument nitrogen dioxide columns. *Journal of Geophysical Research: Atmospheres*, 113(D15), 2008. _eprint: https://onlinelibrary.wiley.com/doi/pdf/10.1029/2007JD008908.

[77] Cheng Liu, Chengzhi Xing, Qihou Hu, Qihua Li, Haoran Liu, Qianqian Hong, Wei Tan, Xiangguang Ji, Hua Lin, Chuan Lu, Jinan Lin, Hanyang Liu, Shaocong Wei, Jian Chen, Kunpeng Yang, Shuntian Wang, Ting Liu, and Yujia Chen. Ground-Based Hyperspectral Stereoscopic Remote Sensing Network: A Promising Strategy to Learn Coordinated Control of O3 and PM2.5 over China. *Engineering*, 19:71–83, December 2022.

[78] Y. Kanaya, H. Irie, H. Takashima, H. Iwabuchi, H. Akimoto, K. Sudo, M. Gu, J. Chong, Y. J. Kim, H. Lee, A. Li, F. Si, J. Xu, P.-H. Xie, W.-Q. Liu, A. Dzhola, O. Postylyakov, V. Ivanov, E. Grechko, S. Terpugova, and M. Panchenko. Long-term MAX-DOAS network observations of NO_2 in Russia and Asia (MADRAS) during the period 2007–2012: instrumentation, elucidation of climatology, and comparisons with OMI satellite observations and global model simulations. *Atmospheric Chemistry and Physics*, 14(15):7909–7927, August 2014. Publisher: Copernicus GmbH.

[79] A Richter, D Adukpo, S Fietkau, A Heckel, A Ladstätter-Weißenmayer, A Löwe, T Medeke, H Oetjen, F Wittrock, and J P Burrows. SCIAMACHY VALIDATION USING GROUND-BASED DOAS MEASUREMENTS OF THE UNIVERSITY OF BREMEN BREDOM NETWORK.

[80] Bo Galle, Mattias Johansson, Claudia Rivera, Yan Zhang, Manne Kihlman, Christoph Kern, Thomas Lehmann, Ulrich Platt, Santiago Arellano, and Silvana Hidalgo. Network for Observation of Volcanic and Atmospheric Change (NOVAC)—A global network for volcanic gas monitoring: Network layout and instrument description. *Journal of Geophysical Research: Atmospheres*, 115(D5), 2010. _eprint: https://onlinelibrary.wiley.com/doi/pdf/10.1029/2009JD011823.

[81] Alexander Cede, Jay Herman, Andreas Richter, Nickolay Krotkov, and John Burrows. Measurements of nitrogen dioxide total column amounts using a Brewer double spectrophotometer in direct Sun mode. *Journal of Geophysical Research: Atmospheres*, 111(D5):2005JD006585, March 2006.

[82] Debora Griffin, Xiaoyi Zhao, Chris A. McLinden, Folkert Boersma, Adam Bourassa, Enrico Dammers, Doug Degenstein, Henk Eskes, Lukas Fehr, Vitali Fioletov, Katherine Hayden, Shailesh K. Kharol, Shao-Meng Li, Paul Makar, Randall V. Martin, Cris-

tian Mihele, Richard L. Mittermeier, Nickolay Krotkov, Maarten Sneep, Lok N. Lamsal, Mark ter Linden, Jos van Geffen, Pepijn Veefkind, and Mengistu Wolde. High-Resolution Mapping of Nitrogen Dioxide With TROPOMI: First Results and Validation Over the Canadian Oil Sands. *Geophysical Research Letters*, 46(2):1049–1060, 2019. _eprint: https://onlinelibrary.wiley.com/doi/pdf/10.1029/2018GL081095.

[83] Lim-Seok Chang, Donghee Kim, Hyunkee Hong, Deok-Rae Kim, Jeong-Ah Yu, Kwangyul Lee, Hanlim Lee, Daewon Kim, Jinkyu Hong, Hyun-Young Jo, and Cheol-Hee Kim. Evaluation of correlated Pandora column NO_2 and in situ surface NO_2 measurements during GMAP campaign. *Atmospheric Chemistry and Physics*, 22(16):10703–10720, August 2022. Publisher: Copernicus GmbH.

[84] Andra J. Reed, Anne M. Thompson, Debra E. Kollonige, Douglas K. Martins, Maria A. Tzortziou, Jay R. Herman, Timothy A. Berkoff, Nader K. Abuhassan, and Alexander Cede. Effects of local meteorology and aerosols on ozone and nitrogen dioxide retrievals from OMI and pandora spectrometers in Maryland, USA during DISCOVER-AQ 2011. *Journal of Atmospheric Chemistry*, 72(3-4):455–482, September 2015.

[85] Jay Herman and Jianping Mao. Seasonal Variation of Total Column Formaldehyde, Nitrogen Dioxide, and Ozone Over Various Pandora Spectrometer Sites with a Comparison of OMI and Diurnally Varying DSCOVR-EPIC Satellite Data, May 2024.

[86] Elena Spinei, Andrew Whitehill, Alan Fried, Martin Tiefengraber, Travis N. Knepp, Scott Herndon, Jay R. Herman, Moritz Müller, Nader Abuhassan, Alexander Cede, Dirk Richter, James Walega, James Crawford, James Szykman, Lukas Valin, David J. Williams, Russell Long, Robert J. Swap, Youngjae Lee, Nabil Nowak, and Brett Poche. The first evaluation of formaldehyde column observations by improved Pandora spec-

trometers during the KORUS-AQ field study. *Atmospheric Measurement Techniques*, 11(9):4943–4961, August 2018.

[87] Jay Herman, Alexander Cede, Elena Spinei, George Mount, Maria Tzortziou, and Nader Abuhassan. NO2 column amounts from ground-based Pandora and MFDOAS spectrometers using the direct-sun DOAS technique: Intercomparisons and application to OMI validation. *Journal of Geophysical Research: Atmospheres*, 114(D13), 2009. _eprint: https://onlinelibrary.wiley.com/doi/pdf/10.1029/2009JD011848.

[88] J. Herman, R. Evans, A. Cede, N. Abuhassan, I. Petropavlovskikh, and G. McConville. Comparison of ozone retrievals from the Pandora spectrometer system and Dobson spectrophotometer in Boulder, Colorado. *Atmospheric Measurement Techniques Discussions*, 8(3):3049–3085, March 2015. Publisher: Copernicus Gesellschaft mbH.

[89] Tijl Verhoelst, Steven Compernolle, Gaia Pinardi, Jean-Christopher Lambert, Henk J. Eskes, Kai-Uwe Eichmann, Ann Mari Fjæraa, José Granville, Sander Niemeijer, Alexander Cede, Martin Tiefengraber, François Hendrick, Andrea Pazmiño, Alkiviadis Bais, Ariane Bazureau, K. Folkert Boersma, Kristof Bognar, Angelika Dehn, Sebastian Donner, Aleksandr Elokhov, Manuel Gebetsberger, Florence Goutail, Michel Grutter de la Mora, Aleksandr Gruzdev, Myrto Gratsea, Georg H. Hansen, Hitoshi Irie, Nis Jepsen, Yugo Kanaya, Dimitris Karagkiozidis, Rigel Kivi, Karin Kreher, Pieternel F. Levelt, Cheng Liu, Moritz Müller, Monica Navarro Comas, Ankie J. M. Piters, Jean-Pierre Pommereau, Thierry Portafaix, Cristina Prados-Roman, Olga Puentedura, Richard Querel, Julia Remmers, Andreas Richter, John Rimmer, Claudia Rivera Cárdenas, Lidia Saavedra de Miguel, Valery P. Sinyakov, Wolfgang Stremme, Kimberly Strong, Michel Van Roozendael, J. Pepijn Veefkind, Thomas Wagner, Folkard Wittrock, Margarita Yela González, and Claus Zehner. Ground-based validation of the Copernicus Sentinel-5P TROPOMI NO_2 measurements with the NDACC ZSL-DOAS,

MAX-DOAS and Pandonia global networks. *Atmospheric Measurement Techniques*, 14(1):481–510, January 2021. Publisher: Copernicus GmbH.

[90] Jörg Heland, Hans Schlager, Andreas Richter, and John P. Burrows. First comparison of tropospheric NO2 column densities retrieved from GOME measurements and in situ aircraft profile measurements. *Geophysical Research Letters*, 29(20):44–1–44–4, 2002. _eprint: https://onlinelibrary.wiley.com/doi/pdf/10.1029/2002GL015528.

[91] D. G. Loyola, M. E. Koukouli, P. Valks, D. S. Balis, N. Hao, M. Van Roozendael, R. J. D. Spurr, W. Zimmer, S. Kiemle, C. Lerot, and J.-C. Lambert. The GOME-2 total column ozone product: Retrieval algorithm and ground-based validation. *Journal of Geophysical Research: Atmospheres*, 116(D7), 2011. _eprint: https://onlinelibrary.wiley.com/doi/pdf/10.1029/2010JD014675.

[92] Randall V. Martin. An improved retrieval of tropospheric nitrogen dioxide from GOME. *Journal of Geophysical Research*, 107(D20):4437, 2002.

[93] Rosemary Munro, Rüdiger Lang, Dieter Klaes, Gabriele Poli, Christian Retscher, Rasmus Lindstrot, Roger Huckle, Antoine Lacan, Michael Grzegorski, Andriy Holdak, Alexander Kokhanovsky, Jakob Livschitz, and Michael Eisinger. The GOME-2 instrument on the Metop series of satellites: instrument design, calibration, and level 1 data processing – an overview. *Atmospheric Measurement Techniques*, 9(3):1279–1301, March 2016.

[94] D.V. Ionov, Valery P. Sinyakov, and V.K. Semenov. Validation of GOME (ERS-2) NO2 vertical column data with ground-based measurements at ISSyk-Kul (Kyrgyzstan). *Advances in Space Research*, 37:2254–2260, November 2005.

[95] Gaia Pinardi, Michel Van Roozendael, François Hendrick, Nicolas Theys, Nader Abuhassan, Alkiviadis Bais, Folkert Boersma, Alexander Cede, Jihyo Chong, Sebastian

Donner, Theano Drosoglou, Anatoly Dzhola, Henk Eskes, Udo Frieß, José Granville, Jay R. Herman, Robert Holla, Jari Hovila, Hitoshi Irie, Yugo Kanaya, Dimitris Karagkiozidis, Natalia Kouremeti, Jean-Christopher Lambert, Jianzhong Ma, Enno Peters, Ankie Piters, Oleg Postylyakov, Andreas Richter, Julia Remmers, Hisahiro Takashima, Martin Tiefengraber, Pieter Valks, Tim Vlemmix, Thomas Wagner, and Folkard Wittrock. Validation of tropospheric NO₂ column measurements of GOME-2A and OMI using MAX-DOAS and direct sun network observations. *Atmospheric Measurement Techniques*, 13(11):6141–6174, November 2020.

[96] H. Bovensmann, J. P. Burrows, M. Buchwitz, J. Frerick, S. Noel, V. V. Rozanov, K. V. Chance, and A. P. H. Goede. SCIAMACHY: Mission Objectives and Measurement Modes. *JOURNAL OF THE ATMOSPHERIC SCIENCES*, 56(2):127–150, January 1999.

[97] A J M Piters and K Bramstedt. Overview of SCIAMACHY validation: 2002–2004. *Atmos. Chem. Phys.*, page 22, 2006.

[98] Yunsoo Choi and Amir Hossein Souri. Chemical condition and surface ozone in large cities of Texas during the last decade: Observational evidence from OMI, CAMS, and model analysis. *Remote Sensing of Environment*, 168:90–101, October 2015.

[99] Pieternel F. Levelt, Joanna Joiner, Johanna Tamminen, J. Pepijn Veefkind, Pawan K. Bhartia, Deborah C. Stein Zweers, Bryan N. Duncan, David G. Streets, Henk Eskes, Ronald van der A, Chris McLinden, Vitali Fioletov, Simon Carn, Jos de Laat, Matthew DeLand, Sergey Marchenko, Richard McPeters, Jerald Ziemke, Dejian Fu, Xiong Liu, Kenneth Pickering, Arnoud Apituley, Gonzalo González Abad, Antti Arola, Folkert Boersma, Christopher Chan Miller, Kelly Chance, Martin de Graaf, Janne Hakkarainen, Seppo Hassinen, Iolanda Ialongo, Quintus Kleipool, Nickolay Krotkov,

Can Li, Lok Lamsal, Paul Newman, Caroline Nowlan, Raid Suleiman, Lieuwe Gijsbert Tilstra, Omar Torres, Huiqun Wang, and Krzysztof Wargan. The Ozone Monitoring Instrument: overview of 14 years in space. *Atmospheric Chemistry and Physics*, 18(8):5699–5745, April 2018.

[100] J. H. G. M. van Geffen, K. F. Boersma, M. Van Roozendael, F. Hendrick, E. Mahieu, I. De Smedt, M. Sneep, and J. P. Veefkind. Improved spectral fitting of nitrogen dioxide from OMI in the 405–465 nm window. *Atmospheric Measurement Techniques*, 8(4):1685–1699, April 2015.

[101] J.P. Veefkind, I. Aben, K. McMullan, H. Förster, J. De Vries, G. Otter, J. Claas, H.J. Eskes, J.F. De Haan, Q. Kleipool, M. Van Weele, O. Hasekamp, R. Hoogeveen, J. Landgraf, R. Snel, P. Tol, P. Ingmann, R. Voors, B. Kruizinga, R. Vink, H. Visser, and P.F. Levelt. TROPOMI on the ESA Sentinel-5 Precursor: A GMES mission for global observations of the atmospheric composition for climate, air quality and ozone layer applications. *Remote Sensing of Environment*, 120:70–83, May 2012.

[102] Daniel L. Goldberg, Susan C. Anenberg, Gaige Hunter Kerr, Arash Mohegh, Zifeng Lu, and David G. Streets. TROPOMI NO2 in the United States: A Detailed Look at the Annual Averages, Weekly Cycles, Effects of Temperature, and Correlation With Surface NO2 Concentrations. *Earth's Future*, 9(4):e2020EF001665, 2021. _eprint: https://onlinelibrary.wiley.com/doi/pdf/10.1029/2020EF001665.

[103] Jos van Geffen, Henk Eskes, Steven Compernolle, Gaia Pinardi, Tijl Verhoelst, Jean-Christopher Lambert, Maarten Sneep, Mark ter Linden, Antje Ludewig, K. Folkert Boersma, and J. Pepijn Veefkind. Sentinel-5P TROPOMI NO_2 retrieval: impact of version v2.2 improvements and comparisons with OMI and ground-based data. *Atmo-*

spheric Measurement Techniques, 15(7):2037–2060, April 2022. Publisher: Copernicus GmbH.

[104] Xiaoyi Zhao, Debora Griffin, Vitali Fioletov, Chris McLinden, Alexander Cede, Martin Tiefengraber, Moritz Müller, Kristof Bognar, Kimberly Strong, Folkert Boersma, Henk Eskes, Jonathan Davies, Akira Ogyu, and Sum Chi Lee. Assessment of the quality of TROPOMI high-spatial-resolution NO_2 data products in the Greater Toronto Area. *Atmospheric Measurement Techniques*, 13(4):2131–2159, April 2020. Publisher: Copernicus GmbH.

[105] P. Zoogman, X. Liu, R.M. Suleiman, W.F. Pennington, D.E. Flittner, J.A. Al-Saadi, B.B. Hilton, D.K. Nicks, M.J. Newchurch, J.L. Carr, S.J. Janz, M.R. Andraschko, A. Arola, B.D. Baker, B.P. Canova, C. Chan Miller, R.C. Cohen, J.E. Davis, M.E. Dussault, D.P. Edwards, J. Fishman, A. Ghulam, G. González Abad, M. Grutter, J.R. Herman, J. Houck, D.J. Jacob, J. Joiner, B.J. Kerridge, J. Kim, N.A. Krotkov, L. Lamsal, C. Li, A. Lindfors, R.V. Martin, C.T. McElroy, C. McLinden, V. Natraj, D.O. Neil, C.R. Nowlan, E.J. O'Sullivan, P.I. Palmer, R.B. Pierce, M.R. Pippin, A. Saiz-Lopez, R.J.D. Spurr, J.J. Szykman, O. Torres, J.P. Veefkind, B. Veihelmann, H. Wang, J. Wang, and K. Chance. Tropospheric Emissions: Monitoring of Pollution (TEMPO). *Journal of quantitative spectroscopy & radiative transfer*, 186:17–39, January 2017.

[106] Jeffrey A. Geddes, Randall V. Martin, Eric J. Bucsela, Chris A. McLinden, and Daniel J. M. Cunningham. Stratosphere–troposphere separation of nitrogen dioxide columns from the TEMPO geostationary satellite instrument. *Atmospheric Measurement Techniques*, 11(11):6271–6287, November 2018.

[107] Shanshan Wang, Bin Zhou, Zhuoru Wang, Suna Yang, Nan Hao, Pieter Valks,

Thomas Trautmann, and Limin Chen. Remote sensing of NO2 emission from the central urban area of Shanghai (China) using the mobile DOAS technique. *Journal of Geophysical Research: Atmospheres*, 117(D13), 2012. _eprint: https://onlinelibrary.wiley.com/doi/pdf/10.1029/2011JD016983.

[108] Daniel-Eduard Constantin, Alexis Merlaud, Michel Van Roozendael, Mirela Voiculescu, Caroline Fayt, François Hendrick, Gaia Pinardi, and Lucian Georgescu. Measurements of Tropospheric NO2 in Romania Using a Zenith-Sky Mobile DOAS System and Comparisons with Satellite Observations. *Sensors*, 13(3):3922–3940, March 2013. Number: 3 Publisher: Multidisciplinary Digital Publishing Institute.

[109] Daniel-Eduard Constantin, Alexis Merlaud, Mirela Voiculescu, Michel VAN Roozendael, Maxim Arseni, Adrian Rosu, and Lucian Georgescu. NO2 AND SO2 OBSERVATIONS IN SOUTHEAST EUROPE USING MOBILE DOAS OBSERVATIONS.

[110] Dmitry V. Ionov, Maria V. Makarova, Vladimir S. Kostsov, and Stefani C. Foka. Assessment of the NO integral emission from the St.Petersburg megacity by means of mobile DOAS measurements combined with dispersion modelling. *Atmospheric Pollution Research*, 13(12):101598, December 2022.

[111] John K. E. Johansson, Johan Mellqvist, Jerker Samuelsson, Brian Offerle, Jana Moldanova, Bernhard Rappenglück, Barry Lefer, and James Flynn. Quantitative measurements and modeling of industrial formaldehyde emissions in the Greater Houston area during campaigns in 2009 and 2011. *Journal of Geophysical Research: Atmospheres*, 119(7):4303–4322, 2014. _eprint: https://onlinelibrary.wiley.com/doi/pdf/10.1002/2013JD020159.

[112] T Wagner, O Ibrahim, R Shaiganfar, and U Platt. Mobile MAX-DOAS observations of tropospheric trace gases. *Atmos. Meas. Tech.*, page 12, 2010.

[113] Siyang Cheng, Xinghong Cheng, Jianzhong Ma, Xiangde Xu, Wenqian Zhang, Jinguang Lv, Gang Bai, Bing Chen, Siying Ma, Steffen Ziegler, Sebastian Donner, and Thomas Wagner. Mobile MAX-DOAS observations of tropospheric NO_2 and HCHO during summer over the Three Rivers' Source region in China. *Atmospheric Chemistry and Physics*, 23(6):3655–3677, March 2023. Publisher: Copernicus GmbH.

[114] O Ibrahim, R Shaiganfar, R Sinreich, T Stein, U Platt, and T Wagner. Car MAX-DOAS measurements around entire cities: quantification of NOx emissions from the cities of Mannheim and Ludwigshafen (Germany). *Atmos. Meas. Tech.*, page 13, 2010.

[115] Wei Tan, Shaohua Zhao, Cheng Liu, Ka Lok Chan, Zhouqing Xie, Yu Zhu, Wenjing Su, Chengxin Zhang, Haoran Liu, Chengzhi Xing, and Jianguo Liu. Estimation of winter time NOx emissions in Hefei, a typical inland city of China, using mobile MAX-DOAS observations. *Atmospheric Environment*, 200:228–242, March 2019.

[116] Ang Li, Jie Zhang, Pinhua Xie, Zhaokun Hu, Jin Xu, Fusheng Mou, Fengcheng Wu, Jiangguo Liu, and Wenqing Liu. Variation of temporal and spatial patterns of NO2 in Beijing using OMI and mobile DOAS. *Science China Chemistry*, 58(9):1367–1376, September 2015.

[117] F. C. Wu, P. H. Xie, A. Li, K. L. Chan, A. Hartl, Y. Wang, F. Q. Si, Y. Zeng, M. Qin, J. Xu, J. G. Liu, W. Q. Liu, and M. Wenig. Observations of SO_2 and NO_2 by mobile DOAS in the Guangzhou eastern area during the Asian Games 2010. *Atmospheric Measurement Techniques*, 6(9):2277–2292, September 2013. Publisher: Copernicus GmbH.

[118] Fengcheng Wu, Pinhua Xie, Ang Li, Fusheng Mou, Hao Chen, Yi Zhu, Tong Zhu, Jianguo Liu, and Wenqing Liu. Investigations of Temporal and Spatial Distribution

of Precursors SO₂ and NO₂ Vertical Columns in North China Plain by Mobile DOAS, September 2017.

[119] A. Merlaud, M. Van Roozendael, N. Theys, C. Fayt, C. Hermans, B. Quennehen, A. Schwarzenboeck, G. Ancellet, M. Pommier, J. Pelon, J. Burkhart, A. Stohl, and M. De Mazière. Airborne DOAS measurements in Arctic: vertical distributions of aerosol extinction coefficient and NO₂ concentration. *Atmospheric Chemistry and Physics*, 11(17):9219–9236, September 2011.

[120] Laura M. Judd, Jassim A. Al-Saadi, Lukas C. Valin, R. Bradley Pierce, Kai Yang, Scott J. Janz, Matthew G. Kowalewski, James J. Szykman, Martin Tiefengraber, and Moritz Mueller. The Dawn of Geostationary Air Quality Monitoring: Case Studies From Seoul and Los Angeles. *Frontiers in Environmental Science*, 6, August 2018. Publisher: Frontiers.

[121] Mary Angelique G. Demetillo, Aracely Navarro, Katherine K. Knowles, Kimberly P. Fields, Jeffrey A. Geddes, Caroline R. Nowlan, Scott J. Janz, Laura M. Judd, Jassim Al-Saadi, Kang Sun, Brian C. McDonald, Glenn S. Diskin, and Sally E. Pusede. Observing Nitrogen Dioxide Air Pollution Inequality Using High-Spatial-Resolution Remote Sensing Measurements in Houston, Texas. *Environmental Science & Technology*, 54(16):9882–9895, August 2020.

[122] Daniel-Eduard Constantin, Alexis Merlaud, Mirela Voiculescu, Carmelia Dragomir, Lucian Georgescu, Francois Hendrick, Gaia Pinardi, and Michel Van Roozendael. Mobile DOAS Observations of Tropospheric NO2 Using an UltraLight Trike and Flux Calculation. *Atmosphere*, 8(78), April 2017.

[123] Wenfu Tang, David P. Edwards, Louisa K. Emmons, Helen M. Worden, Laura M. Judd, Lok N. Lamsal, Jassim A. Al-Saadi, Scott J. Janz, James H. Crawford, Merritt N.

Deeter, Gabriele Pfister, Rebecca R. Buchholz, Benjamin Gaubert, and Caroline R. Nowlan. Assessing sub-grid variability within satellite pixels using airborne mapping spectrometer measurements. preprint, Gases/Remote Sensing/Data Processing and Information Retrieval, January 2021.

[124] F. Klappenbach, M. Bertleff, J. Kostinek, F. Hase, T. Blumenstock, A. Agusti-Panareda, M. Razinger, and A. Butz. Accurate mobile remote sensing of XCO₂ and XCH₄ latitudinal transects from aboard a research vessel. *Atmospheric Measurement Techniques*, 8(12):5023–5038, December 2015.

[125] Ping Wang, Ankie Piters, Jos van Geffen, Olaf Tuinder, Piet Stammes, and Stefan Kinne. Shipborne MAX-DOAS measurements for validation of TROPOMI NO₂ products. *Atmospheric Measurement Techniques*, 13(3):1413–1426, March 2020.

[126] Xianxin Li, Zhangjun Wang, Libin Du, Xingtao Liu, Xiufen Wang, Chao Chen, Xiangqian Meng, Hui Li, Quanfeng Zhuang, Wei Deng, Xin Pan, and Xinzhao Chu. Shipborne MAX-DOAS Observations of Tropospheric Trace Gases over a Coastal City and the Yellow Sea near Qingdao, China. *Journal of Atmospheric and Oceanic Technology*, 37(3):365–380, March 2020. Publisher: American Meteorological Society Section: Journal of Atmospheric and Oceanic Technology.

[127] Maria Tzortziou, Christopher P. Loughner, Daniel L. Goldberg, Laura Judd, Dilchand Nauth, Charlotte F. Kwong, Tong Lin, Alexander Cede, and Nader Abuhassan. Intimately tracking NO2 pollution over the New York City - Long Island Sound land-water continuum: An integration of shipboard, airborne, satellite observations, and models. *Science of The Total Environment*, 897:165144, November 2023.

[128] US EPA. Green Book | US EPA.

[129] P. H. Daum, L. I. Kleinman, S. R. Springston, L. J. Nunnermacker, Y.-N. Lee, J. Weinstein-Lloyd, J. Zheng, and C. M. Berkowitz. Origin and properties of plumes of high ozone observed during the Texas 2000 Air Quality Study (TexAQS 2000). *Journal of Geophysical Research: Atmospheres*, 109(D17), 2004. _eprint: https://onlinelibrary.wiley.com/doi/pdf/10.1029/2003JD004311.

[130] A. O. Langford, C. J. Senff, R. M. Banta, R. M. Hardesty, R. J. Alvarez II, Scott P. Sandberg, and Lisa S. Darby. Regional and local background ozone in Houston during Texas Air Quality Study 2006. *Journal of Geophysical Research: Atmospheres*, 114(D7), 2009. _eprint: https://onlinelibrary.wiley.com/doi/pdf/10.1029/2008JD011687.

[131] E. J. Williams, B. M. Lerner, P. C. Murphy, S. C. Herndon, and M. S. Zahniser. Emissions of NOx, SO2, CO, and HCHO from commercial marine shipping during Texas Air Quality Study (TexAQS) 2006. *Journal of Geophysical Research: Atmospheres*, 114(D21), 2009. _eprint: https://onlinelibrary.wiley.com/doi/pdf/10.1029/2009JD012094.

[132] Eduardo P. Olaguer, Charles E. Kolb, Barry Lefer, Bernhard Rappenglück, Renyi Zhang, and Joseph P. Pinto. Overview of the SHARP campaign: Motivation, design, and major outcomes. *Journal of Geophysical Research: Atmospheres*, 119(5):2597–2610, 2014. _eprint: https://onlinelibrary.wiley.com/doi/pdf/10.1002/2013JD019730.

[133] Karin Kreher, Michel Van Roozendael, Francois Hendrick, Arnoud Apituley, Ermioni Dimitropoulou, Udo Frieß, Andreas Richter, Thomas Wagner, Johannes Lampel, Nader Abuhassan, Li Ang, Monica Anguas, Alkis Bais, Nuria Benavent, Tim Bösch, Kristof Bognar, Alexander Borovski, Ilya Bruchkouski, Alexander Cede, Ka Lok Chan,

Sebastian Donner, Theano Drosoglou, Caroline Fayt, Henning Finkenzeller, David Garcia-Nieto, Clio Gielen, Laura Gómez-Martín, Nan Hao, Bas Henzing, Jay R. Herman, Christian Hermans, Syedul Hoque, Hitoshi Irie, Junli Jin, Paul Johnston, Junaid Khayyam Butt, Fahim Khokhar, Theodore K. Koenig, Jonas Kuhn, Vinod Kumar, Cheng Liu, Jianzhong Ma, Alexis Merlaud, Abhishek K. Mishra, Moritz Müller, Monica Navarro-Comas, Mareike Ostendorf, Andrea Pazmino, Enno Peters, Gaia Pinardi, Manuel Pinharanda, Ankie Piters, Ulrich Platt, Oleg Postylyakov, Cristina Prados-Roman, Olga Puentedura, Richard Querel, Alfonso Saiz-Lopez, Anja Schönhardt, Stefan F. Schreier, André Seyler, Vinayak Sinha, Elena Spinei, Kimberly Strong, Frederik Tack, Xin Tian, Martin Tiefengraber, Jan-Lukas Tirpitz, Jeroen van Gent, Rainer Volkamer, Mihalis Vrekoussis, Shanshan Wang, Zhuoru Wang, Mark Wenig, Folkard Wittrock, Pinhua H. Xie, Jin Xu, Margarita Yela, Chengxin Zhang, and Xiaoyi Zhao. Intercomparison of NO₂, O₄, O₃ and HCHO slant column measurements by MAX-DOAS and zenith-sky UV–visible spectrometers during CINDI-2. *Atmospheric Measurement Techniques*, 13(5):2169–2208, May 2020.

[134] A. C. Vandaele, C. Hermans, P. C. Simon, M. Carleer, R. Colin, S. Fally, M. F. Mérienne, A. Jenouvrier, and B. Coquart. Measurements of the NO2 absorption cross-section from 42 000 cm−1 to 10 000 cm−1 (238–1000 nm) at 220 K and 294 K. *Journal of Quantitative Spectroscopy and Radiative Transfer*, 59(3):171–184, 1998.

[135] L. S. Rothman, I. E. Gordon, Y. Babikov, A. Barbe, D. Chris Benner, P. F. Bernath, M. Birk, L. Bizzocchi, V. Boudon, L. R. Brown, A. Campargue, K. Chance, E. A. Cohen, L. H. Coudert, V. M. Devi, B. J. Drouin, A. Fayt, J.-M. Flaud, R. R. Gamache, J. J. Harrison, J.-M. Hartmann, C. Hill, J. T. Hodges, D. Jacquemart, A. Jolly, J. Lamouroux, R. J. Le Roy, G. Li, D. A. Long, O. M. Lyulin, C. J. Mackie, S. T.

Massie, S. Mikhailenko, H. S. P. Müller, O. V. Naumenko, A. V. Nikitin, J. Orphal, V. Perevalov, A. Perrin, E. R. Polovtseva, C. Richard, M. A. H. Smith, E. Starikova, K. Sung, S. Tashkun, J. Tennyson, G. C. Toon, Vl G. Tyuterev, and G. Wagner. The HITRAN2012 molecular spectroscopic database. *Journal of Quantitative Spectroscopy and Radiative Transfer*, 130:4–50, 2013.

[136] A. Serdyuchenko, V. Gorshelev, M. Weber, W. Chehade, and J. P. Burrows. High spectral resolution ozone absorption cross-sections – Part 2: Temperature dependence. *Atmospheric Measurement Techniques*, 7(2):625–636, February 2014.

[137] Ryan Thalman and Rainer Volkamer. Temperature dependent absorption cross-sections of o 2–o 2 colli sion pairs between 340 and 630 nm and at atmospherically relevant pressure. *Physical Chemistry Chemical Physics*, (37), 2013.

[138] Richard Meller and Geert K. Moortgat. Temperature dependence of the absorption cross sections of formaldehyde between 223 and 323 K in the wavelength range 225–375 nm. *Journal of Geophysical Research: Atmospheres*, 105(D6):7089–7101, 2000. _eprint: https://onlinelibrary.wiley.com/doi/pdf/10.1029/1999JD901074.

[139] Oliver C. Fleischmann, Matthias Hartmann, John P. Burrows, and Johannes Orphal. New ultraviolet absorption cross-sections of BrO at atmospheric temperatures measured by time-windowing Fourier transform spectroscopy. *Journal of Photochemistry and Photobiology A: Chemistry*, 168(1-2):117–132, November 2004.

[140] K. Chance and R.L. Kurucz. An improved high-resolution solar reference spectrum for earth's atmosphere measurements in the ultraviolet, visible, and near infrared. *Journal of Quantitative Spectroscopy and Radiative Transfer*, 111(9):1289–1295, June 2010.

[141] Steffen Beirle, Christian Borger, Steffen Dörner, Vinod Kumar, and Thomas Wagner. Calculating the vertical column density of O₄ during day-

time from surface values of pressure, temperature, and relative humidity. *Atmospheric Measurement Techniques*, 15(4):987–1006, February 2022.

[142] T. Wagner, A. Apituley, S. Beirle, S. Dörner, U. Friess, J. Remmers, and R. Shaiganfar. Cloud detection and classification based on MAX-DOAS observations. *Atmospheric Measurement Techniques*, 7(5):1289–1320, May 2014. Publisher: Copernicus GmbH.

[143] L. N. Lamsal, R. V. Martin, A. van Donkelaar, M. Steinbacher, E. A. Celarier, E. Bucsela, E. J. Dunlea, and J. P. Pinto. Ground-level nitrogen dioxide concentrations inferred from the satellite-borne Ozone Monitoring Instrument. *Journal of Geophysical Research: Atmospheres*, 113(D16), 2008. _eprint: https://onlinelibrary.wiley.com/doi/pdf/10.1029/2007JD009235.

[144] L. N. Lamsal, N. A. Krotkov, E. A. Celarier, W. H. Swartz, K. E. Pickering, E. J. Bucsela, J. F. Gleason, R. V. Martin, S. Philip, H. Irie, A. Cede, J. Herman, A. Weinheimer, J. J. Szykman, and T. N. Knepp. Evaluation of OMI operational standard NO_2 column retrievals using in situ and surface-based NO_2 observations. *Atmospheric Chemistry and Physics*, 14(21):11587–11609, November 2014. Publisher: Copernicus GmbH.

[145] Anne M. Thompson, Ryan M. Stauffer, Tyler P. Boyle, Debra E. Kollonige, Kazuyuki Miyazaki, Maria Tzortziou, Jay R. Herman, Nader Abuhassan, Carolyn E. Jordan, and Brian T. Lamb. Comparison of Near-Surface NO2 Pollution With Pandora Total Column NO2 During the Korea-United States Ocean Color (KORUS OC) Campaign. *Journal of Geophysical Research: Atmospheres*, 124(23):13560–13575, December 2019. Publisher: John Wiley & Sons, Ltd.

[146] K. F. Boersma, D. J. Jacob, M. Trainic, Y. Rudich, I. DeSmedt, R. Dirksen, and H. J. Eskes. Validation of urban NO_2 concentrations and their diurnal and seasonal

variations observed from the SCIAMACHY and OMI sensors using in situ surface measurements in Israeli cities. *Atmospheric Chemistry and Physics*, 9(12):3867–3879, June 2009. Publisher: Copernicus GmbH.

[147] Daewon Kim, Hanlim Lee, Hyunkee Hong, Wonei Choi, Yun Gon Lee, and Junsung Park. Estimation of Surface NO2 Volume Mixing Ratio in Four Metropolitan Cities in Korea Using Multiple Regression Models with OMI and AIRS Data. *Remote Sensing*, 9(6):627, June 2017. Number: 6 Publisher: Multidisciplinary Digital Publishing Institute.

[148] Taylor J. Adams, Jeffrey A. Geddes, and Elena S. Lind. New Insights Into the Role of Atmospheric Transport and Mixing on Column and Surface Concentrations of NO2 at a Coastal Urban Site. *Journal of Geophysical Research: Atmospheres*, 128(12):e2022JD038237, 2023. _eprint: https://onlinelibrary.wiley.com/doi/pdf/10.1029/2022JD038237.

[149] Clare M. Flynn, Kenneth E. Pickering, James H. Crawford, Lok Lamsal, Nickolay Krotkov, Jay Herman, Andrew Weinheimer, Gao Chen, Xiong Liu, James Szykman, Si-Chee Tsay, Christopher Loughner, Jennifer Hains, Pius Lee, Russell R. Dickerson, Jeffrey W. Stehr, and Lacey Brent. Relationship between column-density and surface mixing ratio: Statistical analysis of O3 and NO2 data from the July 2011 Maryland DISCOVER-AQ mission. *Atmospheric Environment*, 92:429–441, August 2014.

[150] Claudia Rivera, Johan Mellqvist, Jerker Samuelsson, Barry Lefer, Sergio Alvarez, and Monica R. Patel. Quantification of NO2 and SO2 emissions from the Houston Ship Channel and Texas City industrial areas during the 2006 Texas Air Quality Study. *Journal of Geophysical Research: Atmospheres*, 115(D8), 2010. _eprint: https://onlinelibrary.wiley.com/doi/pdf/10.1029/2009JD012675.

[151] M. Johansson, C. Rivera, B. de Foy, W. Lei, J. Song, Y. Zhang, B. Galle, and L. Molina. Mobile mini-DOAS measurement of the outflow of NO₂ and HCHO from Mexico City. *Atmospheric Chemistry and Physics*, 9(15):5647–5653, August 2009.

[152] Yeyuan Huang, Ang Li, Pinhua Xie, Zhaokun Hu, Jin Xu, Xiaoyi Fang, Hongmei Ren, Xiaomei Li, and Bing Dang. NOx Emission Flux Measurements with Multiple Mobile-DOAS Instruments in Beijing. *Remote Sensing*, 12(16):2527, January 2020. Number: 16 Publisher: Multidisciplinary Digital Publishing Institute.

[153] David A. Newnham and John Ballard. Visible absorption cross sections and integrated absorption intensities of molecular oxygen (O2 and O4). *Journal of Geophysical Research: Atmospheres*, 103(D22):28801–28815, 1998. _eprint: https://onlinelibrary.wiley.com/doi/pdf/10.1029/98JD02799.

[154] Fengcheng Wu, Ang Li, Pinhua Xie, Hao Chen, Zhaokun Hu, Qiong Zhang, Jianguo Liu, and Wenqing Liu. Emission Flux Measurement Error with a Mobile DOAS System and Application to NOx Flux Observations. *Sensors (Basel, Switzerland)*, 17(2):231, January 2017.

[155] Thomas Wagner, Steffen Beirle, Nuria Benavent, Tim Bösch, Ka Lok Chan, Sebastian Donner, Steffen Dörner, Caroline Fayt, Udo Frieß, David García-Nieto, Clio Gielen, David González-Bartolome, Laura Gomez, François Hendrick, Bas Henzing, Jun Li Jin, Johannes Lampel, Jianzhong Ma, Kornelia Mies, Mónica Navarro, Enno Peters, Gaia Pinardi, Olga Puentedura, Janis Puķīte, Julia Remmers, Andreas Richter, Alfonso Saiz-Lopez, Reza Shaiganfar, Holger Sihler, Michel Van Roozendael, Yang Wang, and Margarita Yela. Is a scaling factor required to obtain closure between measured and modelled atmospheric O_4 absorptions? An assessment of uncertainties of mea-

surements and radiative transfer simulations for 2 selected days during the MAD-CAT campaign. *Atmospheric Measurement Techniques*, 12(5):2745–2817, May 2019. Publisher: Copernicus GmbH.

[156] Eric Shettle. Models of aerosols, clouds, and precipitation for atmospheric propagation studies. In *no. 454 in AGARD Conference Proceedings*, March 1990. Publication Title: In AGARD.